Influence of Mg and Si Content in Aluminum Alloys on Dynamically Recrystallized Microstructure During Solid-state Joining Using Friction Surfacing

Von der Fakultät für Ingenieurwissenschaften, Abteilung Maschinenbau und Verfahrenstechnik der

Universität Duisburg-Essen

zur Erlangung des akademischen Grades

eines

Doktors der Ingenieurwissenschaften

Dr.-Ing.

genehmigte Dissertation

von

Jonas Ehrich
aus
Mülheim an der Ruhr

Gutachter: Univ. Prof. Dr.-Ing. Stefanie Hanke, Universität Duisburg-Essen
Univ. Prof. Dr.-Ing. habil. Benjamin Klusemann, Leuphana Universität Lüneburg

Tag der mündlichen Prüfung: 20.09.2023

Abstract

Friction Surfacing is a friction-based solid-state joining technology with the potential to locally modify component properties. During Friction Surfacing, the joining partners, consumable stud and substrate, are joined in solid phase. In this process, the deposited material undergoes severe plastic deformation at elevated temperatures ($\approx 0.8\ T_{liquidus}$) and is dynamically recrystallized. In addition to fundamental material properties such as heat capacity and strength, material-specific dynamic microstructural mechanisms have a major impact on the effective flow stresses. The influence of alloying elements in metals on the under these extreme thermal and mechanical loading conditions has not been sufficiently investigated to date. Furthermore, the stacking fault energy are affected by the alloying elements, which influence the sliding properties of dislocations as well as the plastic formability and recrystallization behavior. The hypothesis is that the stacking fault energy and secondary phases play a crucial role in the Friction Surfacing process properties, coating characteristics, and the onset of dynamic recrystallization.

Custom-made cast aluminum alloys are processed using Friction Surfacing. In this context, the alloys differ only in Si and Mg content, and so this influence can be investigated. Process characteristics, coating geometries, and material deposition efficiencies are all determined in experimental welds, which are carried out at the Helmholtz-Zentrum Hereon in Geesthacht. The correlations of these characteristics with the microstructural events in the alloys, in particular dynamic recrystallization, are analyzed by optical light microscopy and electron microscopy methods at the University of Duisburg-Essen. The precipitation and dissolution processes of phases in the solid solution occurring are investigated by analytical methods such as differential scanning calorimetry and energy dispersive X-ray spectroscopy, and correlated with the respective Al-Mg-Si alloy and its processing state.

Pronounced shear flow localization is observed for increasing content of alloying elements, yielding fine-grained flow lines with preferred crystal orientations. Further, the change in stacking fault energy with increasing content of alloying elements resulted in lower recrystallized grain size and higher grain orientation differences, due to a lower tendency for dislocation annihilation by recovery. Secondary phase particles increase with Mg or Si content, spheroidize during processing and influence the formation of the dislocation cell structure through both particle-stimulated nucleation and Zener pinning. Dissolution and re-precipitation of strength-enhancing precipitates take place, while dislocation loops in the microstructure being an indicator of dynamic precipitation, which influences the mechanical properties of the Friction Surfacing coating.

A structured investigation of the effects on the processing behavior and resulting microstructure when a single alloying element, Mg or Si, is changed in an Al-based alloy is carried out. This novel approach is based on the assumption that in otherwise similar alloys the stacking fault energy and secondary phase particle interactions are crucial for the Friction Surfacing process characteristics, the coating properties and the recrystallized microstructure. The results show the validity of this assumption and are discussed in terms of additional possible impacts of the alloy composition.

Kurzfassung

Friction Surfacing ist eine reibbasierte Festphase-Fügetechnologie mit dem Potential Bauteileigenschaften lokal zu modifizieren. Beim Friction Surfacing werden die Fügepartner, Reibbolzen und Substrat, in fester Phase miteinander verbunden. Dabei erfährt das Auftragsmaterial extreme plastische Verformung (Severe Plastic Deformation) bei erhöhten Temperaturen ($\approx 0.8\ T_{liquidus}$) und wird dynamisch rekristallisiert. Neben grundlegenden Werkstoffeigenschaften wie Wärmekapazität und Festigkeit, wirken sich werkstoffspezifische dynamische mikrostrukturelle Mechanismen stark auf die aktiven Fließspannungen aus. Der Einfluss der Legierungselemente in Metallen unter diesen extremen thermischen und mechanischen Belastungsbedingungen ist bis heute nicht ausreichend erforscht. Die Hypothese ist, dass die Stapelfehlerenergie und die sekundären Phasen eine entscheidende Rolle für die Eigenschaften des Friction Surfacing-Prozesses, die Beschichtungseigenschaften und den Beginn der dynamischen Rekristallisation spielen.

Maßgefertigte speziell gegossene Aluminiumlegierungen werden unter Verwendung von Friction Surfacing verarbeitet. Hierbei unterscheiden sich die Legierungen im Si- und Mg-Gehalt, sodass der Einfluss des Legierungsgehaltes untersucht werden kann. In Versuchsschweißungen, welche am Helmholtz-Zentrum Hereon in Geesthacht durchgeführt werden, werden Prozesscharakteristika, Schichtgeometrien und Materialeffizienzen ermittelt. Die Zusammenhänge dieser Größen mit den mikrostrukturellen Vorgängen in den Legierungen, insbesondere der dynamischen Rekristallisation, werden mittels Optischer Lichtmikroskopie und Elektronen-Mikroskopie an der Universität Duisburg-Essen analysiert. Die im Zuge der hohen Wärmegradienten auftretenden Ausscheidungs- und Auflösungsprozesse von Phasen im Mischkristall werden mittels Analysemethoden wie Dynamischer Differenzkalorimetrie und Energiedispersiver Röntgenspektroskopie untersucht und mit der jeweiligen Al-Mg-Si Legierung und dessen Zustand korreliert.

Mit zunehmendem Gehalt an Legierungselementen wird eine ausgeprägte Scherflusslokalisierung beobachtet, die zu feinkörnigen Fließlinien mit bevorzugten Kristallorientierungen führt. Darüber hinaus führt die Änderung der Stapelfehlerenergie mit zunehmendem Gehalt an Legierungselementen zu einer geringeren rekristallisierten Korngröße und höheren Unterschieden in der Kornorientierung, was auf eine geringere Tendenz zur Versetzungsannihilation durch Erholung zurückzuführen ist. Sekundärphasenteilchen nehmen mit dem Mg- oder Si-Gehalt zu, sphäroidisieren während der Verarbeitung und beeinflussen die Bildung der Versetzungszellenstruktur sowohl durch teilchenstimulierte Keimbildung als auch durch Zener-Pinning. Die Auflösung und Wiederausscheidung von festigkeitssteigernden Ausscheidungen findet statt, während Versetzungsschleifen im Gefüge ein Indikator für dynamische Ausscheidungsbildung sind, die die mechanischen Eigenschaften der Friction Surfacing Beschichtung beeinflussen.

Es wird eine strukturierte Untersuchung der Auswirkungen auf das Verarbeitungsverhalten und das resultierende Mikrogefüge durchgeführt, wenn ein einzelnes Legierungselement, Mg oder Si, in einer

Al-Basislegierung verändert wird. Dieser neuartige Ansatz basiert auf der Annahme, dass in ansonsten ähnlichen Legierungen die Stapelfehlerenergie und die Wechselwirkungen der Sekundärphasenteilchen entscheidend für die Prozessmerkmale des Friction Surfacing, die Schichteigenschaften und das rekristallisierte Gefüge sind. Die Ergebnisse zeigen die Gültigkeit dieser Annahme und werden im Hinblick auf weitere mögliche Auswirkungen der Legierungszusammensetzung diskutiert.

Contents

Nomenclature

Symbol	
a	Lattice constant
α	Rotation angle (ideal shear texture)
$b/\vec{b_i}$	Burgers vector
$\beta, \beta', \beta'', U1, U2, B'$	Phases in the precipitation sequence of Al-Mg-Si
β_H	Heating rate
c_p	Excess specific heat capacity
γ_{SFE}	Stacking fault energy
γ_{GB}	Specific grain boundary energy
d	Coating thickness
d_0	stacking fault width
d_B	Lattice space distance (Bragg equation)
d_{eff}	Effective coating thickness (height of the shear zone)
d_m	Mean grain diameter
d_{offset}	Distance of deposition offset
d_{stud}	Diameter of the consumable stud
E_i	Dislocation energy
e_s	Specific energy input per deposited material unit volume
$\dot{\varepsilon}$	Strain rate
$\varepsilon(t)$	Time-dependent shear strain
ε_{cr}	Critical strain
$\dot{\varepsilon}_{eff}$	Effective shear strain rate
ε_v	Von-Mises strain
F_z	Axial force
G	Shear modulus
g	Orientation matrix
η	Deposition efficiency
η^*	Particle size
θ	Misorientation angle
θ_B	Bragg angle
θ', θ''	Phases in the precipitation sequence of Al-Cu
k_y	Grain boundary resistance
λ_B	Wavelength of primary electrons (Bragg equation)
λ_{crit}	Critical size of the deformation zone

m	Sample mass
n	Rotational speed
n_B	Diffraction order (Bragg equation)
n_{mf}	Average material flow rate
P	Introduced energy
p_D	Driving pressure for recrystallization
P_T	Torsional energy component
P_x	Transverse energy component
P_z	Axial energy component
p_Z	Zener pressure
ρ_{cr}	Dislocation density
σ_0	Constant of starting stress
σ_y	Yield stress
$\Delta\sigma$	Stress difference
Q	Lattice activation energy
$\dot{Q}_{baseline}$	Heat flow of the baseline
$\dot{Q}_{sample}$	Heat flow of the sample
R	Gas constant
r_c	Corrected radius
r_{eff}	Effective radius of the shear surface
Δs_z	Consumed stud length difference
T	Torque
T_z	Temperature (Zener-Hollomon equation)
Δt	Time difference
$\varphi(t)$	Time dependent angle of rotation
$V_{consumed}$	Consumed stud volume
v_{CR}	Consumption rate
$V_{deposited}$	Deposited material volume
v_x	Translational speed
w	Coating width
Z	Zener-Hollomon parameter

Abbreviation	
AA	Aluminum alloy
AR	Aspect ratio
ARB	Accumulative-Roll Bonding
AS	Advancing side
bcc	Body centered cubic
BM	Base material
BSE	Backscattered electrons
CCD	Charge-coupled device
CI	Confidence index
DD	Deposition direction
DFT	Density functional theory
DP	Dynamic Precipitation
DRV	Dynamic Recovery
DRX	Dynamic recrystallization
dDRX	Discontinuous dynamic recrystallization
cDRX	Continuous dynamic recrystallization
gDRX	Geometric dynamic recrystallization
mDRX	Meta-dynamic recrystallization
pDRX	Post-dynamic recrystallization
DSC	Differential scanning calorimetry
ECAP	Equal-channel angular pressing
EDX	Energy dispersive X-ray spectroscopy
EBSD	Electron backscattered diffraction
fcc	Face centered cubic
FS	Friction Surfacing
FSE	Forward scattered electrons
FSSW	Friction Stir Spot Welding
FSW	Friction Stir Welding
GNB	Geometrically necessary boundary
GP	Guinier-Preston
HAGB	High angle grain boundary
HAZ	Heat-affected zone
HFDB	Hybrid Friction Diffusion Bonding
HPT	High-pressure torsion
HR-STEM	High-resolution scanning transmission electron microscopy
HV	Vickers hardness

IDB	Incidental dislocation boundaries
IPF	Inverse pole figure
IR	Infrared camera
IQ	Image quality
KAM	Kernel average misorientation
LAGB	Low angle grain boundary
Mg	Magnesium
MO	Misorientation angle
ND	normal direction
OLM	Optical light microscopy
PF	Pole figure
PNS	Particle stimulated nucleation
RD	Reference/rolling direction
RFSSW	Refill friction stir spot welding
RS	Retreating side
RT	Room temperature
SD	Shear direction
SE	Secondary electrons
SEM	Scanning electron microscope
SFE	Stacking fault energy
SPD	Severe plastic deformation
SPN	Shear plane normal
SRV	Static recovery
SRX	Static recrystallization
dSRX	Discontinuous static recrystallization
cSRX	Continuous static recrystallization
SSSS	Supersaturated solid solution
tc	Thermocouple
TD	Transverse direction
TE	Twist Extrusion
TEM	Transmission electron microscope
TMAZ	Thermo-mechanically affected zone
TMP	Thermomechanical processing
UFG	Ultrafine-grained
WDS	Wavelength-dispersive spectroscopy
XRD	X-ray diffraction

1 Introduction

Research and development of novel technologies that are economical, resource-efficient, and consume less energy and materials is an urgent challenge to reduce the carbon footprint worldwide. Considering the increasingly pressing environmental issues, there is a growing need for resource-efficient production, especially in industry. The transportation sector, including aerospace, automotive, and shipping, is also a major contributor to global greenhouse gas emissions, and reducing its impact on the environment is a serious concern. One promising way to achieve this is to use preferably recycled aluminum alloys with tailored material properties. Aluminum is an excellent material for recycling because it can be recycled repeatedly without losing its properties or quality. Recycling aluminum requires only about 5% [1] of the energy needed to produce primary aluminum from bauxite ore, thus contributing to the reduction of greenhouse gases. The motivation behind the use of aluminum alloys lies in the increasing demand for lightweight materials. Lightweight materials offer advantages such as lower fuel consumption, better performance and higher payload. Taking into account the dismantling and circular economy in the design of new components made of recycled aluminum alloys ensures a sustainable impact on the environment. Aluminum alloys, in particular hardenable alloys, are a preferred choice due to their good strength-to-weight ratio and excellent corrosion resistance.

Solid-state technologies can be employed to modify the material properties of aluminum components locally. Solid-state joining processes have gained considerable attention in recent years due to their advantages over conventional welding techniques, such as lower thermal distortion and enhanced material properties through severe plastic deformation (SPD) and its resulting ultra fine-grained microstructure. One of these processes is Friction Surfacing, which uses a rotating consumable stud to deposit a coating of material onto a substrate using frictional heat and plastic deformation. This process has been successfully applied to various materials, including aluminum alloys, titanium alloys, carbon steel, tool steels, Ni-based alloys etc. and additionally allows the fabrication of composite materials by depositing a coating of one material onto another, such as Al-steel, Al-Cu etc. [2]. This opens up new possibilities for designing high-performance components with tailored material properties, such as improved strength, fracture toughness, or wear resistance. In addition, Friction Surfacing can also be used to repair weld damaged or worn components, reducing the need for costly replacement. This technology is also suitable for additive manufacturing [3], which enables the production of parts featuring complex designs with SPD microstructures. Another significant advantage of Friction Surfacing is its environmental friendliness. Because it is a solid-state joining process, there is no need for additives or shielding gas, reducing waste and pollution. The process is also highly efficient as it can be performed at relatively low temperatures, resulting in lower energy consumption, and can thus be considered a green manufacturing technology. In the future, the promising energy-related functional properties of SPD or nano-SPD materials, such as hydrogen storage in bulk material, improvement of superconducting parameters, or homogeneously distributed corrosion, are expected to make an important contribution to energy-related issues, especially to the reduction of CO_2 emissions [4].

Friction surfacing is also of interest for materials science based fundamental research, in particular to gain a deeper insight into the material specific thermal and micromechanical characteristics under extreme thermo-mechanical conditions, and how the resulting microstructure responds to specific alloying elements. In this study, the influence of Mg and Si on the dynamically recrystallized microstructure by thermomechanical processing using FS of Al-Mg-Si alloys will be thoroughly investigated.

Friction Surfacing offers a promising alternative to conventional fusion welding, as it is a solid-state joining technology, which additionally works as an additive manufacturing technology that generates coatings with ultra-fine-grained microstructures and improved material and functional properties operating at relatively low heat input and reduced distortion.

2 Objectives

The major objective of this research is to gain a more thorough understanding of the influence of alloying elements and material properties on the microstructural processes with respect to dynamically recrystallized microstructures during severe plastic deformation at elevated temperatures of Al-base alloys. Particular attention is given to the investigation of the assumption that when only one of the alloying elements Mg or Si is changed in aluminum alloys, the process behavior, flow stresses during plastic deformation and the resulting microstructures alter considerably. These property changes are attributed to the micromechanisms, which in turn are significantly influenced by the stacking fault energy and the secondary phases. To address this hypothesis, the following methods are applied. Friction Surfacing is used as an SPD technique and allows extremely high strain rates and strains at high temperature. Magnesium is a key element in aluminum alloys that leads to solid solution strengthening. It is known that Mg can strongly affect diffusion processes in aluminum by causing vacancies in the crystal lattice and influencing the dynamic recrystallization mechanisms [1]. Dynamic recrystallization has a significant influence on the process properties and material flow in frictional solid-state joining processes. Preliminary results from the study by Hanke et al. [5] have shown distinct differences regarding the processing behavior and the process parameters used for AA6082 and AA5083. These two alloys have a 4 wt.% difference in Mg content. Silicon is of particular interest as it can produce a high proportion of hard Si secondary phases in cast alloys. From an engineering point of view, thermomechanical processing of Al alloys with high silicon content by Friction Surfacing is of high interest as it leads to a material state with advantageous properties. The combination of Mg and Si leads to strength enhancing Mg_2Si precipitates in Al alloys. It is not fully understood how the precipitation kinetics is affected by the thermal cycle as well as high strains and strain rates during deposition. It is hypothesized that precipitate formation is influenced by the additional plastic deformation and associated dislocation motion. To understand the influence of a particular alloying element, it is necessary to keep constant the concentration of the other elements in the alloys studied. This is hardly possible in commercial alloys since many alloying elements are used in different combinations in Al alloys. In this research, the initial alloy AA6060 from a single production batch is melted and either Mg or Si is added to different amounts. In addition to the initial alloy AA6060, a total of six Mg-rich and three Si-rich alloys are the focus of these investigations.

In the course of this research thesis, the following technological and scientific questions are additionally addressed:

- Does the high content of Si secondary phase particles with hardness values of about 1200 HV0.2 influence the internal friction during plastic deformation, thus affecting the temperature development or the evolution of flow stresses?
- Do high concentrations of Mg-containing secondary phases in Al alloys lead to embrittlement during extreme plastic deformation at elevated temperatures?

- How do different amounts of Mg and Si affect the material behavior under SPD at high temperatures during stable FS deposition?
- How does the presence of secondary phases affect the plasticization and recrystallization behavior?
- How do Mg and Si influence the microstructural and mechanical properties after SPD at elevated temperatures?
- Does a correlation exist between different Mg and Si contents and recrystallization mechanisms?
- How do Mg and Si influence dislocation mechanisms and interactions during FS?
- How is the (dynamic) precipitation formation of Mg_2Si influenced by different amounts of Mg and Si?

3 State of the art

In this chapter, the fundamental principles, and the state of the art of the Friction Surfacing process, as well as its superordinate process severe plastic deformation are introduced. The focus lies on the investigation of microstructure evolution through dynamic recrystallisation and the prevailing micromechanisms during severe plastic deformation at elevated temperatures of Al-Mg-Si alloys. The theoretical fundamentals of the main lattice defects and micromechanisms as influencing factors on the dynamic recrystallisation are presented in this chapter.

3.1 Friction Surfacing

Friction surfacing (FS) is a solid-state joining process patented by Klopstock and Neelands in 1941 [6]. FS coatings are deposited by severe plastic deformation at elevated temperatures ($\approx$ 0.8 $T_{liquidus}$), requiring different process parameters for different alloys. Since the 1980s, Friction Surfacing has been increasingly investigated as a form of coating deposition for ultrafine-grained homogeneous coatings with good wear and corrosion properties [2]. FS technology enables the processing of alloys that are difficult to join by e.g. conventional fusion welding methods. Joining dissimilar metals is also possible using FS as reported in previous studies. For example, FS of AA6063 onto AISI 1018 carbon steel was reported by Seidi and Miller [7]. Rafi et al. [8] studied the coating characteristics and integrity of tool steel (H13) over low carbon steel. Hanke et al. [9] studied the dynamic recrystallization (DRX) behavior of Ni-based alloy 625 deposited onto 42CrMo4. Due to the low energy consumption, environmental friendliness and high deposition efficiency, which were demonstrated by Hanke and dos Santos [5] by a parameter study using different Al-alloys, FS can be considered as a green manufacturing process.

Dilip et al. [10] show in their study that FS provides reproducible process conditions, which enables the fabrication of three-dimensional parts in single and multi-track processes and thus can be used as an additive manufacturing method. In a study Shen et al. [3] have demonstrated the feasibility of Friction Surfacing Layer Deposition (FSLD) and its flexibility required for the deposition of multiple layers. The process can be an effective alternative to melt-based additive manufacturing processes for certain applications. A schematic representation of the process can be found in Figure 1. The length and width of a deposit is determined by the availability of coating material from the stud, the process parameters, the environmental conditions, and the material pairings.

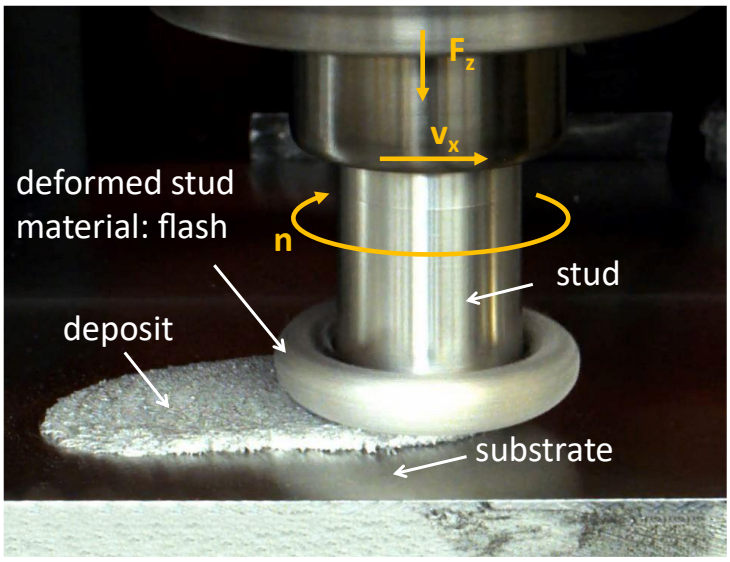

Figure 1: Friction Surfacing process (AA6060 onto AA2024)

3.1.1 FS process

The single-layer surfacing process starts with a pre-heating phase, during which a rotating stud made from the coating material is pressed with a defined axial force onto the substrate to be coated. The relative sliding in contact generates frictional heating of the stud and substrate material. The tip of the stud begins to adhere to the substrate surface, and the frictional torque causes shear deformation of the thermally softened stud material. The soft, plastically deforming stud material is often referred to as a "quasi-liquid layer" in the pertinent literature [11] [12]. The transverse motion is superimposed, and along the trajectory, soft material from the stud tip is deposited on the substrate, leaving a layer with a width in the order of the stud diameter. In addition, some of the soft material at the edge of the stud is forced out of the contact zone by the axial force and pushed up around the stud, forming a flash [11] [13]. The process steps are represented in Figure 2 (a). Additionally, a schematic depiction of the process is shown in Figure 2 (b).

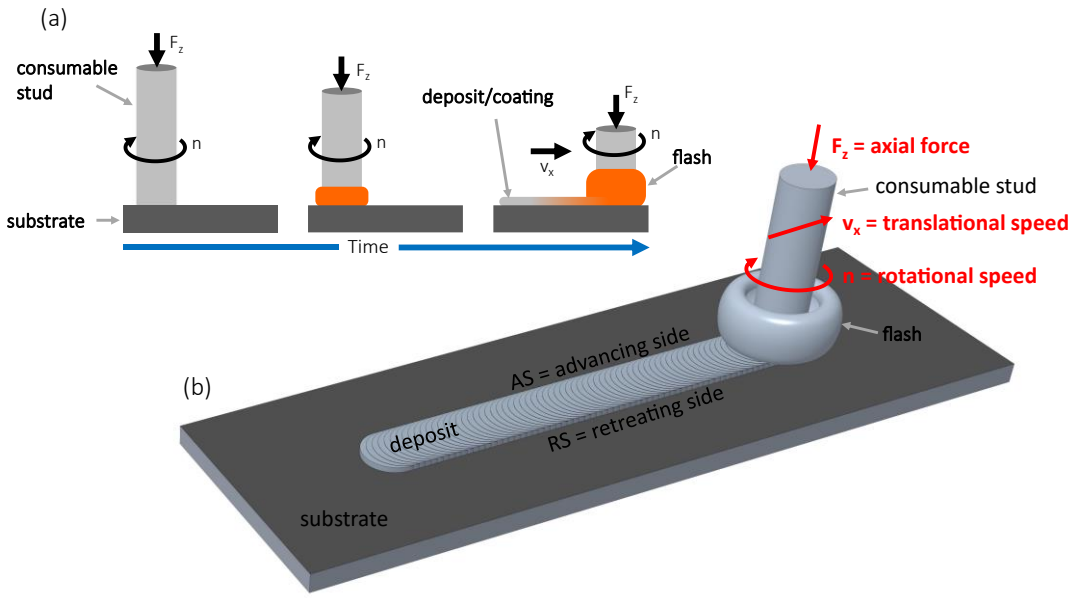

Figure 2: (a) FS process steps, and (b) schematic illustration of the FS process.

In coating deposition, a distinction is made between characteristic regions. The advancing side, AS, is defined as the side of the coating on which the relative circumferential speed and the translational speed of the rotating stud add up. The opposite side of the coating, where the relative circumferential speed and the translational speed act in opposite directions, is called the retreating side, RS. The area in between is called the center section, see Figure 2 (b). The most decisive factors for stable FS processing behavior are the rotational speed n, the axial force F_z and the translational speed v_x. The parameter window in which FS runs with stable process forces and torques and leads to coatings with homogeneous width, thickness, and defect-free bonding, depends mainly on the material pairing used.

During FS, the deposited material is processed under specific conditions such as large strains at high temperatures, so little is known about material properties under these extreme conditions. For this reason, the application of new materials is based on both experience and trial and error. Small changes in microstructure and alloy composition can have large effects on plastic flow behavior [5]. After successfully elaborating a stable parameter window, the relationships between several variables can be investigated by means of the response surface methodology .A possible statistical method for this would be a three-level factorial design of experiments approach according to Box-Behnken [14]. This includes, among others, the coating geometry. The typical influences of the process parameters on the reaction forces and torques as well as on the coating development have been widely investigated. For the aluminum alloys AA6082 and AA5083, Hanke and dos Santos [5] have found that the torque decreases with increasing rotational speed, with increasing feed rate and with decreasing axial force. It has been reported, e.g. for stainless steel [11] [15] and for aluminum alloy AA5052 [16], that with higher axial force and lower rotational speed the coatings' thickness and width decrease. Reducing the translational speed resulted in increased coating width and thickness according to the studies by Shinoda [15] and Sakahima [16]. For Ti-6Al-4V on the other hand, within a range of rotational speeds from 300 to 6000

min^{-1}, an initial increase followed by a decrease in deposited coating volume was observed [17]. The tendencies of the process responses according to the process parameters with respect to coating width, thickness and reaction torque are summarized in Table 1.

Table 1: Process responses of Al & stainless steel according to [5] [15] [11].

process parameters	width & thickness reaction torque
↑ axial force [kN]	↑
↑ rotational speed [min^{-1}]	↓
↑ translational speed [mm s^{-1}]	↓

The parameter window in which FS runs with stable process forces and torques under the same conditions and leads to coatings with homogeneous width, thickness and defect-free joint depends on the material pairings and in particular on the alloying elements of the consumable stud material. Eventually, if certain FS parameters exhibit steady-state deposition behavior, studies can be used in which prediction of the effects on thickness, width, and bond strength is provided. So far, no studies have been published that investigate applying FS to cast aluminum alloys with specific compositions, in particular high Si and Mg contents, as stud material.

Due to the thermo-mechanical conditions experienced by the plasticized material during FS, diffusion as a bonding mechanism for complete contact of the interface between coating material and substrate is not required, as is the case with diffusion bonding. The bonding in FS is achieved mainly via metallurgical bonding. The phenomena of material flow during FS have been investigated in several studies, showing that the flash is mainly composed of material near the cylindrical surface of the stud, while the material in the center of the stud is predominantly deposited and responsible for the formation of the coating [11]. It has been shown for various materials that dynamic recrystallization (DRX) occurs during FS [9] [5] [2]. DRX is defined as the simultaneous introduction of crystallographic defects by deformation and their elimination by recrystallization (described in detail in chapter 3.4.1). It is the main reason for the formation of ultrafine or nanocrystalline microstructures during severe plastic deformation (SPD) at low temperatures and is necessary to achieve the very large strains required for FS. Dislocations and stacking fault energy play an important role in the process of DRX. The interaction and movement of dislocations as well as the presence of stacking faults contribute to the local loading and stress conditions required for nucleation and growth of new grains during DRX.

3.2 Dislocations interactions & stacking fault energy

From a crystallographic point of view, a distinction is made between edge dislocations and screw dislocations, which are both introduced during the plastic deformation of metallic materials [18]. An edge dislocation can be illustrated by inserting an additional half lattice plane into the crystal lattice. The end of this half plane creates a distortion of the surrounding lattice and thus represents a site of

higher internal energy. A screw dislocation turns the crystal planes into a continuous screw-shaped surface. The distortion energy of an edge dislocation is about 1.5 times larger than that of a shear stress-based screw dislocation, due to both shear and compressive stresses [19]. However, very few dislocations occur as pure edge or screw dislocations, but rather as a mixture of both forming an elliptical dislocation ring. The proportion of segments of screw dislocations in elliptical dislocation rings is higher than that of segments of edge dislocations [19] [1]. The dislocation energy for a dislocation line consisting of edge and screw dislocations depends on the shear modulus G and is quadratically proportional to the Burgers vector b; the energy can be summarized in good approximation as follows:

$$E \cong \frac{1}{2} G b^2 \tag{1}$$

The measure of the direction and magnitude of the distortion introduced by dislocation lines is the Burgers vector b, which is related to the lattice constant a, and the direction [uvw]. It is obtained according to the following procedure. In a defective crystal, an encompassing line is drawn around the dislocation (Burgers circulation). This circulation is now transferred to a perfect crystal. At one point, the circulation cannot be closed. The connection necessary to close the circulation is the Burgers vector [18]. Dislocations move under the condition of shear forces on certain slip planes and in preferred directions [1]. When a dislocation moves from one slip plane to another by performing cross slip, this is called "wavy slip". Lattice defects that cannot be cut, such as stationary dislocations or semi- and incoherent secondary phase particles, are bypassed by cross slip. Cross slip is the predominant sliding mode of dislocations in aluminum alloys and is a prerequisite for the development of dislocation cell structures. Obstruction of cross slip leads to "planar slip", which delays the formation of dislocation cell structures. The factors influencing the wavy slip behavior of aluminum alloys are of considerable importance [1]. Wavy slip characteristics can be hindered by either separable precipitate particles or dissociation of dislocations into partial dislocations. Thus, the complexity of dislocations is further increased by the fact that dislocations can be split into two partial dislocations and subsequently form a stacking fault.

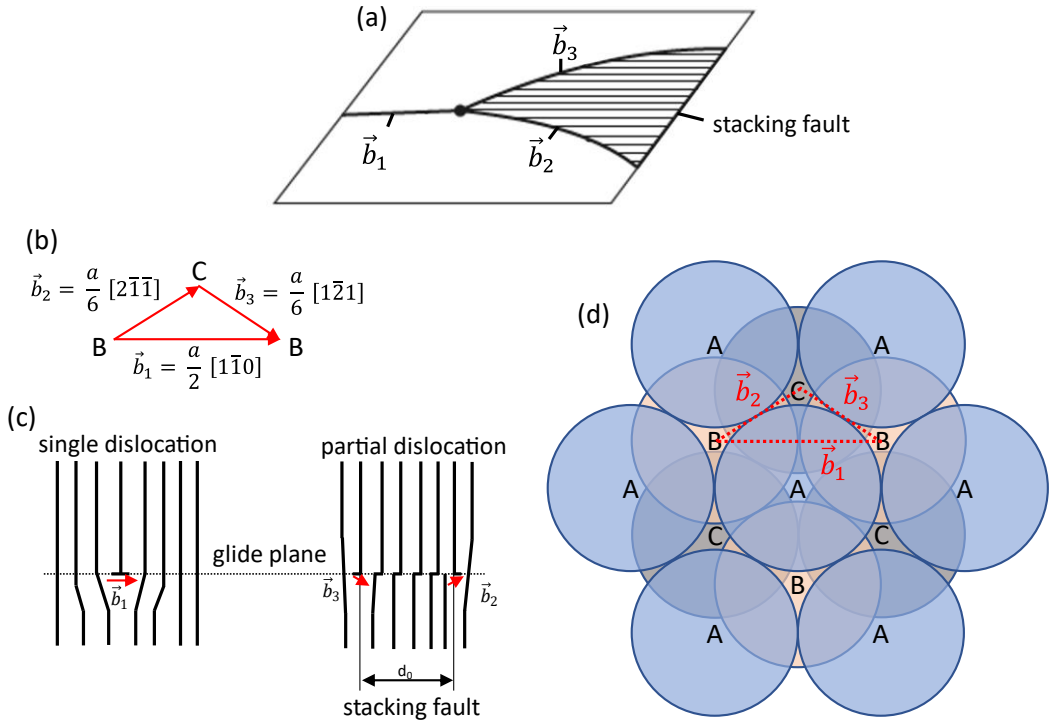

Figure 3: (a) Dissociation of a single dislocation into two partial dislocations; (b) Possible split of dislocations according to Burgers vectors; (c) stacking sequence in the fcc lattice; (d) Dissociation of an edge dislocation in the fcc into Shockley dislocations [19] [18] [20].

A stacking fault is a fault in the stacking order of the atoms, e.g., in the stacking of the close-packed {111} slip planes in the face-centered cubic lattice of aluminum alloys of the order ABCABC. Planes A, B, and C are each offset from each other by a/6 in the <112> direction. Stacking faults can also result from a single dislocation being split into a so-called (a/6) Shockley partial if this reduces its energy [19]. The principle of dislocation split is outlined in Figure 3. For example, if a dislocation with Burgers vector b splits into two partial dislocations with Burgers vector b/2, the energy E_2 of the partial dislocation pair would thus be half the energy E_1 of the single dislocation according to the following equation [19]:

$$E_2 = 2 \cdot \frac{1}{2} G \left(\frac{b}{2}\right)^2 = \frac{1}{2} \cdot \left(\frac{1}{2} G b^2\right) = \frac{1}{2} E_1 \tag{2}$$

The width between the resulting partial dislocations is the stacking fault. In general, the larger the width d_0, the higher the energy reduction due to dislocation split. However, in cubic lattices, there are decompositions of the Burgers vectors into smaller vectors that allow stacking fault constellations of lower energy. In the fcc lattice, on the slip plane (111), a complete dislocation with Burgers vector $\vec{b}_1 = \frac{a}{2}[1\bar{1}0]$ can be split into two partial Shockley dislocations according to [19]:

$$\vec{b}_1 = \vec{b}_2 + \vec{b}_3 = \frac{a}{2}[1\bar{1}0] = \frac{a}{6}[2\bar{1}\bar{1}] + \frac{a}{6}[1\bar{2}1] \tag{3}$$

The formation of partial dislocations is directly related to the stacking fault energy γ_{SFE} (energy per unit area) and to the energy balance of the dislocation split. With lower stacking fault energy and larger stacking fault width, more dislocations can move on their preferred slip planes, an effect which has been described as planar slip. Cross slip and climb are then more difficult to obtain and can only be achieved at higher strain rates and elevated temperatures, leading to higher dislocation density. Dislocation split in aluminum alloys is more difficult to achieve due to its high stacking fault energy. The smaller the γ_{SFE}, the easier dislocations split into Shockley partial dislocations, so the stacking fault width (d_0) of the splitting is inversely proportional to the stacking fault energy. The decisive factor here is the balance between the repulsive forces acting on the partial dislocations and the attractive forces caused by the stacking fault energy [19] [20].

$$\gamma_{SFE} = \frac{Ga^2}{24\pi}\frac{1}{d_0} \tag{4}$$

The values for stacking fault energy for several elements vary significantly according to the pertinent literature. The stacking fault energy for some common elements is listed in Table 2.

Table 2: SFE / surface tension of common elements and boundaries at room temperature.

Element	Energy γ & γ_{SFE} [mJm^{-2}]	Reference
HAGB	≈ 500	[18]
LAGB	0 … 100	[18]
Twin grain boundary	160	[18]
Aluminum	166 - 250	[20] [19] [1]
Magnesium	125	[20]
Copper	78 - 100	[21]
Silicon	50 - 60	[22]
Zirconium	240	[20]

Since it is difficult to measure the stacking fault energy, the exact values in the literature vary, e.g., for pure aluminum, they range from 166 to 250 mJm^{-2}. Two likely reasons for the high scatter of the stacking fault energy values are the general measurement conditions and the purity of the material used because the stacking fault energy reacts sensitively to foreign element additions.

Since aluminum has an increased cross-slip ability due to its high stacking fault energy, the probability of forming a stacking fault is low, and thus strain-hardening is not very pronounced. At the same time, the high cross-slip capacity also impedes the formation of crystal twins [1] [20]. Figure 4 (a) schematically illustrates the cross-slip of a dislocation from the (111) to the (11-1) plane in the fcc lattice.

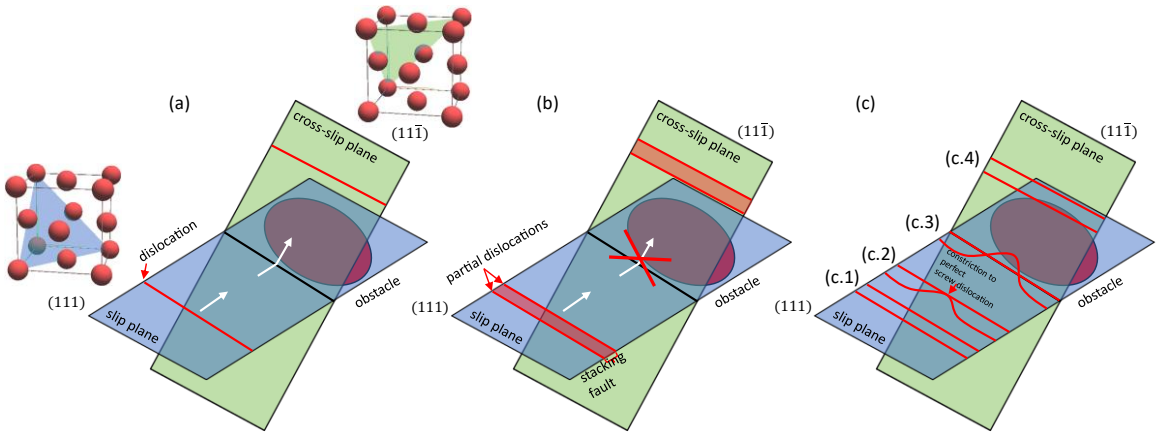

Figure 4: (a) Cross-slip of a dislocation from the (111) to the (11-1) plane in the fcc lattice. (b) Cross-slip of a single Shockley partial dislocation is not possible. (c) Cross-slip through constriction of an extended dislocation.

Figure 4 (b) shows that a single Shockley partial dislocation cannot cross-slip and is thus constrained to glide in its plane. However, it is possible for an extended screw dislocation to form a constriction, and then move freely in other planes at this region of perfect dislocation. The energy required to develop a constriction is lower in metals with high stacking fault energy, such as aluminum. In addition, constriction of dislocations is favored by thermal activation, so the ability to cross-slip increases with the rise in temperature. The formation of a constriction is shown in Figure 4 (c). An extended dislocation glides in the (111) slip plane in (c.1) and has constricted along a short length in (c.2). The constriction is screw-like in character, can cross-slip, and is formed by internal stresses that compress the partial dislocations. Figure 4 (c.3) illustrates how the dislocation dissociates into two separate partial dislocations with a stacking fault on the (11-1) plane. The new dislocation (c.4) is free to move in the cross-slip plane and has transferred to the (11-1) plane through the constriction mechanism [23].

3.3 Ultrafine-grained structure created by severe plastic deformation

The features of a material are not exclusively determined by its composition, but also to a considerable degree by its microstructural state. This is exploited in a variety of ways, most notably through heat treatments or forging of previously cast material. Severe plastic deformation (SPD) is a method of certain metal forming processes in which extremely high strain is introduced into bulk materials. The development of the principles underlying SPD techniques is concerned with the effects on solid materials when combining large hydrostatic pressures with simultaneous shear deformation [24]. SPD is one possible approach for creating homogeneous zones of ultrafine-grained (d_m<500 nm) and nanocrystalline (d_m<100 nm) structures in materials. Conventional SPD processes such as High-Pressure Torsion (HPT) [25], Equal Channel Angular Pressing (ECAP) [26], Accumulative-Roll Bonding (ARB) [27] and Twist Extrusion (TE) [28] are common processes for the production of ultrafine-grained metallic materials. There are now over 100 SPD processes and their modifications, including friction stir processes such as Friction Stir Welding (FSW) [29] [30], Hybrid Friction Diffusion Bonding (HFDB), Friction Stir Spot Welding (FSSW) or Friction Surfacing (FS) [31] [4].

By introducing extremely large strains into the solid material, the density of lattice defects in the material increases accordingly, resulting in grain refinement and large fractions of high-angle grain boundaries. When large plastic strains (>2) are introduced, hydrostatic pressure is simultaneously applied to the material through the geometrically constrained setup. This is necessary to prevent cracks from forming at high strains. As a result of ultrafine-grained microstructure, the mechanical and physical properties change significantly compared to conventional materials. Due to the increased dislocation density with simultaneous grain refinement during plastic deformation, the strength increases. This is because more grain boundaries and static dislocations occur, which serve as a barrier to the sliding of dislocations. The Hall-Petch relationship represents a linear relationship between the mean grain diameter d_m and the yield stress σ_y. The yield stress increases with decreasing grain size [32]:

$$\sigma_y = \sigma_0 + k_y \cdot {d_m}^{-1/2} \tag{5}$$

$$\Delta\sigma = k_y \cdot {d_m}^{-1/2} \tag{6}$$

$\Delta\sigma$ is the stress difference, σ_0 is the constant of starting stress for dislocation movement and k_y is an empirical material constant called grain boundary resistance. This can be interpreted as the contribution of grain boundaries to strength [32]. The validity of the Hall-Petch relationship is limited down to a grain size of approx. 10 nm. When the grain size decreases further, the yield stress also decreases, since sliding at the grain boundary and/or creep seem to be the predominant deformation modes in these size ranges. Experimental confirmation is not yet available at this stage. This phenomenon is also known as the inverse Hall-Petch effect [33] [34].

Conventionally, refinement of the initial microstructure of crystalline metals is achieved by recrystallization, i.e., annealing treatment after plastic deformation. However, in SPD-processed materials, grain refinement is already observed in the SPD-deformed state without annealing [35]. The

detailed microstructure evolution and grain refinement during SPD is still subject of research. With increasing deformation, the misorientation of the grains in the microstructure increases and so-called substructures or dislocation cell structures form.

During e.g. HPT, the initial formation of the substructures can be expected at a von-Mises strain of ε_v=0.5-1. With an increasing von-Mises strain, further subgrains are formed in the initial grains, which transform into large angle grain boundaries. This effect continues until no further grain refinement is possible (ε_v=8) and, finally, a saturation region is established [36] [37]. At a higher von-Mises strain, no further grain refinement is achievable, and instead a reorientation of the grains is achieved. The micro-mechanism of subgrain evolution, which is responsible for the formation of ultrafine-grained (UFG) microstructures, is described in the literature as grain subdivision [38]. The progress of grain subdivision is schematically shown in Figure 5. In the first step, slip lines form depending on the material-related slip systems; these slip lines then evolve into characteristic slip patterns with increasing plastic deformation (Figure 5 (a)). The differences in slip patterns cause different crystal rotations in different local areas, leading to the development of misorientations between neighboring areas. Such misorientations are sustained by the geometrically necessary boundaries (GNBs), which are dislocation boundaries with planar morphology introduced by plastic deformation [38] (Figure 5 (b)).

In the intermediate regions, domains develop in which random dislocation boundaries are formed. These are called incidental dislocation boundaries (IDBs). A typical example of IDBs are dislocation cell boundaries in deformed microstructures as they also occur during dynamic recrystallization at high temperatures. Tsuji et al. [38] consider that grain subdivision is the common mechanism for the formation of ultrafine microstructures at high shear deformations during SPD. The forming process is sometimes referred to by other terms, e.g., grain fragmentation, in-situ recrystallisation, continuous dynamic recrystallisation, etc. At both high temperatures and ambient temperature, recovery processes can occur during or after deformation, and recrystallisation can occur to a higher or lower degree, especially in materials with a relatively low melting temperature. In Figure 5 (b), it can be seen that the original grains are first subdivided by GNBs and additionally by IDBs within the domains, a process which is consequently called grain subdivision. With increasing plastic deformation, the number of grain subdivision processes increases and leads to further refinement of the crystals (Figure 5 (c)). It was experimentally discovered that the degree of misorientation of GNBs increases monotonically with increasing plastic strain and GNBs even become HAGBs with an MO > 15°while the misorientation of IDBs does not increase so much and IDBs remain between an MO of 2-5 ° or reach an MO of LAGBs between 5 and 15° [38]. At very high monotonic plastic strains, as occurs in SPD methods, lamellar boundary structures (Figure 5 (d)) with very high misorientation densities and GNBs form [35] [38].

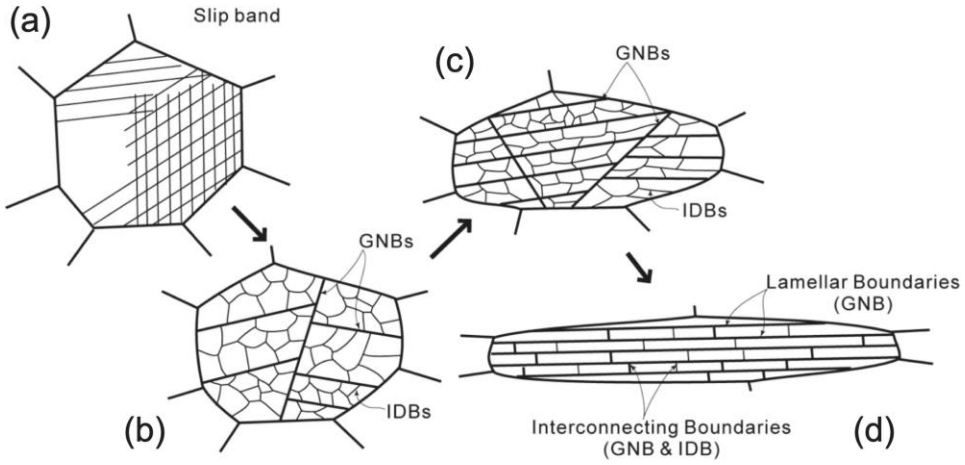

Figure 5: Schematic illustration showing progress of the grain subdivision within a grain. (a) Evolution of slip band/slip lines and slip pattern, (b) Development of GNBs and IDBs, (c) Grain refinement through increase of GNBs and IDBs grain subdivision, (d) Evolution of lamellar boundaries at very high strains [38].

Gholizadeh et al. [39] conducted systematic investigations on SPD at different temperatures and strain rates and came to the following conclusions. When deformation occurs under high flow stress, at low temperatures and/or high strain rates, the mechanism of grain subdivision dominates in the formation of UFG microstructures. When deformation occurs under low flow stress, at high temperatures and/or low strain rates, recovery inhibits the development of HAGBs through the mechanism of grain subdivision, resulting in a heterogeneous distribution of HAGBs. Consequently, the microstructures can be recognized as typical (discontinuous) dynamic recrystallization structures characterized by nucleation and growth of recrystallized domains. In this case, it would be difficult to obtain ultrafine grain sizes. Various combinations of different processes, i.e. grain subdivision, grain boundary migration and recovery, which are constituents of dynamic recrystallisation (see Dynamic Recrystallization), lead to varying pronounced microstructures.

The average grain diameter in the saturation state depends on the alloying elements of the sample as well as on the temperature at which SPD is performed. On the other hand, the grain size of the initial material before deformation has a minor influence on the grain size in the saturation range [36] [40]. SPD-deformed materials tend to exhibit grain sizes in the micrometer or nanometer range and have a high proportion of large-angle grain boundaries. SPD materials feature high strength combined with satisfactory ductility. With conventional deformation methods, such as rolling, similarly high strengths can be achieved, but in this case the ductility is reduced due to the preferred direction of the grains and texture formation [41] [42]. Compared to conventionally deformed materials, an enhanced ratio between yield strength and elongation can be obtained for nanocrystalline SPD-deformed specimens [35].

SPD deformed materials can provide exceptional mechanical and functional properties. SPD-processed materials are already used for biomedical applications, e.g., dental implants made of nanostructured titanium. SPD materials are expected to be in higher demand in biomedical applications due to their increased life expectancy [4]. Moreover, SPD deformed materials offer in some cases better

performance especially in the field of energy applications. Skripnyuk et al. [43] have investigated the magnesium-based alloy ZK60 in terms of its hydrogen storage properties. They found that the alloy processed by ECAP had increased hydrogen storage capacity and enhanced hydrogen desorption kinetics compared to the unprocessed coarse-grained ZK60 variant. Dobatkin et al. [44] showed that for HPT-processed Cu-Cr alloys with subsequent heat treatments, high hardness with good electrical conductivity can be achieved. Nishizaki et al. [45] found that the superconducting parameters namely, the critical temperature, the critical current density, and the critical field of niobium could be improved by the HPT process. Gao et al. [46] describe in their study that a Mg-Zn-Ca alloy treated by HPT shows a homogeneously distributed and uniform corrosion, whereas the as-cast alloy displays mainly inhomogeneous areas of pitting corrosion. Schütte et al. [47] show that Al-Si alloys processed by Friction Surfacing exhibit an improvement in wear resistance compared to as-cast Al-Si alloys. Hanke [48] has demonstrated in her thesis that the resistance to surface fatigue of NiAl bronze can be increased through FS. The superalloy Cr60Ni40 also exhibits an improved wear resistance and also a superior wear behaviour in sliding wear compared to the conventional as-cast condition. Consequently, it is expected that the promising functional properties of SPD or nano-SPD materials achieved by grain subdivision and/or dynamic recrystallisation will significantly contribute to energy-related issues in the future, especially the reduction of CO_2 emissions.

3.4 Recrystallization

Deformation of crystalline materials introduces defects such as dislocations and new interfaces, resulting in a metastable state. These defects can be healed out at elevated temperatures and associated accelerated diffusion processes. Thermally activated processes reduce the free energy of the system by annihilating and rearranging dislocations during recovery, without migration of high-angle boundaries (HAGBs). Recovery processes that occur during annealing are called static recovery (SRV), and those that occur during high temperature deformation are called dynamic recovery (DRV) [20].

The term static recrystallization (SRX) describes the formation of new crystallographic microstructures in deformed metals by subsequent heat treatment, via a reduction in the energy of the crystal structure in conjunction with grain boundary migration. Increasing deformation results in an accumulation of dislocations, causing an increase in internal stored energy which is the driving force for recrystallization [19] [1]. Nuclei, from which the formation of new grains initiates, form in regions with the highest density of accumulated dislocations. During annealing, the nuclei sites evolve into subgrains or low-angle boundaries (LAGBs), whose misorientations gradually increase until they reach values typical of HAGBs [49]. These HAGBs migrate and newly formed grains grow until they collide, resulting in a homogeneous, almost defect free microstructure. The stronger the deformation, the more dislocations are introduced into the material, causing more nuclei to grow and grains to collide faster, processes which in turn result in a finer grain size. This phenomenon is also known as primary recrystallization. It is a discontinuous process that depends strongly on the degree of deformation and the subsequent

annealing temperature and duration. Therefore, this process is also referred to as discontinuous static recrystallization (dSRX).

Primary recrystallization can also occur continuously without clear nucleation and growth stage. Some aluminum alloys contain dispersoids finely distributed in the microstructure. Fine particles precipitate along the subgrain boundaries. During the subsequent annealing, a gradual subgrain growth takes place due to the coarsening of the dispersoids, and thus the misorientations of the LAGBs increase until they are transformed into HAGBs [49]. This process is continuous and also results in a homogeneous recrystallized microstructure, which is called continuous static recrystallization (cSRX) or extended recovery [49] [50]. Precipitates in the lattice structure stabilize the primary recrystallized microstructure. If the annealing temperatures are excessively high or the annealing times are prolonged, the lattice-stabilizing precipitates can dissolve, so that finely recrystallized grains can grow heterogeneously. This process serves to further reduce the internal energy of the material, as the total grain boundary length in the material is reduced. This process is referred to as continuous grain growth. As a grain boundary tends to shorten, a migration of the grain boundaries occurs, so small grains shrink and are finally consumed, resulting in an increased average grain size. A special case is described by secondary recrystallisation, in which the continuous grain growth is hindered by precipitates, for instance, and discontinuous grain growth occurs. This results in a microstructure containing a few very large and many fine crystals. This phenomenon is undesirable in technical cases [51].

3.4.1 Dynamic Recrystallization

Recrystallization can also occur during deformation processes at elevated temperatures, so a distinction is made between static and dynamic recrystallization (DRX) [19]. DRX is defined as the simultaneous introduction of crystallographic defects by deformation, their restoration by dynamic recovery and recrystallization of the grain structure. For DRX to take place, sufficient strain and temperature are required. In the pertinent literature the critical strain (ε_{cr}) or the critical dislocation density (ρ_{cr}) required for the onset of DRX of various materials is frequently determined [20]. DRX can be divided into three different types, i.e., discontinuous dynamic recrystallization (dDRX), continuous dynamic recrystallization (cDRX) and geometric dynamic recrystallization (gDRX). Different types of DRX mechanisms and processes act in different materials, depending also on the loading conditions, and are extensively described in the literature [52] [53] [54] [55]. In general, the acting DRX type and its mechanisms are a function of thermomechanical processing (TMP) conditions including strain, strain rate and temperature gradient, as well as material properties including the lattice structure, shear modulus, initial grain size, secondary phase particles, and especially the stacking fault energy (SFE) [20]. In particular the mobility of dislocations plays a crucial role in plastic deformation, and recovery and recrystallization. In dDRX, recrystallization occurs discontinuously during TMP. The dislocations accumulate in the early deformation stages predominantly near initial HAGBs. If DRV does not proceed fast enough to annihilate the dislocations formed during work hardening, the dislocation density increases to a critical dDRX state where the first groups of nuclei forms [20]. Here they lead to the

formation of nuclei for the following grain growth when sufficient dislocation density is reached with ongoing deformation. In the process, bulging of grain boundaries takes place. The bulging of a grain boundary occurs in the direction from the side with the lower dislocation density to the side with the higher density (Figure 6, middle row). The bulge is surrounded by dislocations, which develop and grow into subgrains by migration into the surrounding deformed material and rotation [56]. The resulting subgrains and grains preferentially form a chain structure typical of dDRX along the initial grain boundaries or at precipitates. The resulting microstructure is characterized by the formation of necklace-like arranged grains [20] [52]. Regarding dDRX, there are particular phenomena that can occur. When the critical strain required for dDRX is interrupted, but the elevated temperature is not reduced fast enough, the recrystallization nuclei generated grow without incubation time. In the literature, this process is also called meta-dynamic recrystallization (mDRX) or post-dynamic recrystallization (pDRX) [20] [52].

Another type of DRX is continuous dynamic recrystallization (cDRX), which is much less studied than dDRX since it has long been assumed that DRV is the only softening mechanism in materials with high SFE [20]. cDRX is mostly observed in materials of higher SFE, which facilitates cross-slipping and climbing of dislocations. The term "continuous" is used because cDRX is dominated by the formation of dislocation cells during deformation [55]. The new grains develop as a result of the increase in density of dislocations trapped by the subgrain boundaries during deformation [52]. Thus, with increasing dislocation accumulation, subgrain boundaries develop from the dislocation cells, which are eventually transformed by rotational processes and further dislocation accumulation into recrystallized LAGB grains and, finally, into HAGB grains (Figure 6, top row). Compared to dDRX, cDRX is less dependent on the parent grain size because the cell structures can form efficiently independent of the parent grain boundaries due to the higher mobility of the dislocations [20]. The resulting grain structure usually contains equiaxed grains of homogeneous size, which is determined by the size of the initial dislocation cells.

The third type of DRX is the so-called geometric dynamic recrystallization (gDRX) and is described by McQueen [57] [58]. In gDRX, the new microstructure is the result of a geometric change in shape of the original grains and is therefore dependent on the initial grain size and on the strain. gDRX is sometimes described in the literature as a subcategory of cDRX [20]. For example, in hot deforming, large parent grains are stretched during rolling, subsequently forming serrations in the grain boundaries by DRV with a wavelength that reflects the subgrain size. Thus, the parent grain is segmented and thinned out in the course of substantial elongation, resulting in a significant increase in grain boundary length. As the deformation increases, the grains are further compressed, and the serrations on opposite sides of the parent grains meet (HAGB impingement), resulting in the fragmentation of the parent grains (pinch-off) and the formation of new grains as shown in Figure 6 [59] [56]. When the remaining LAGBs continue to absorb dislocations and transform into bands of small equiaxed HAGB grains, gDRX is

complete. For FS, incomplete gDRX was observed in the flash remaining at the studs after coating deposition from Al-alloy 6082 [60].

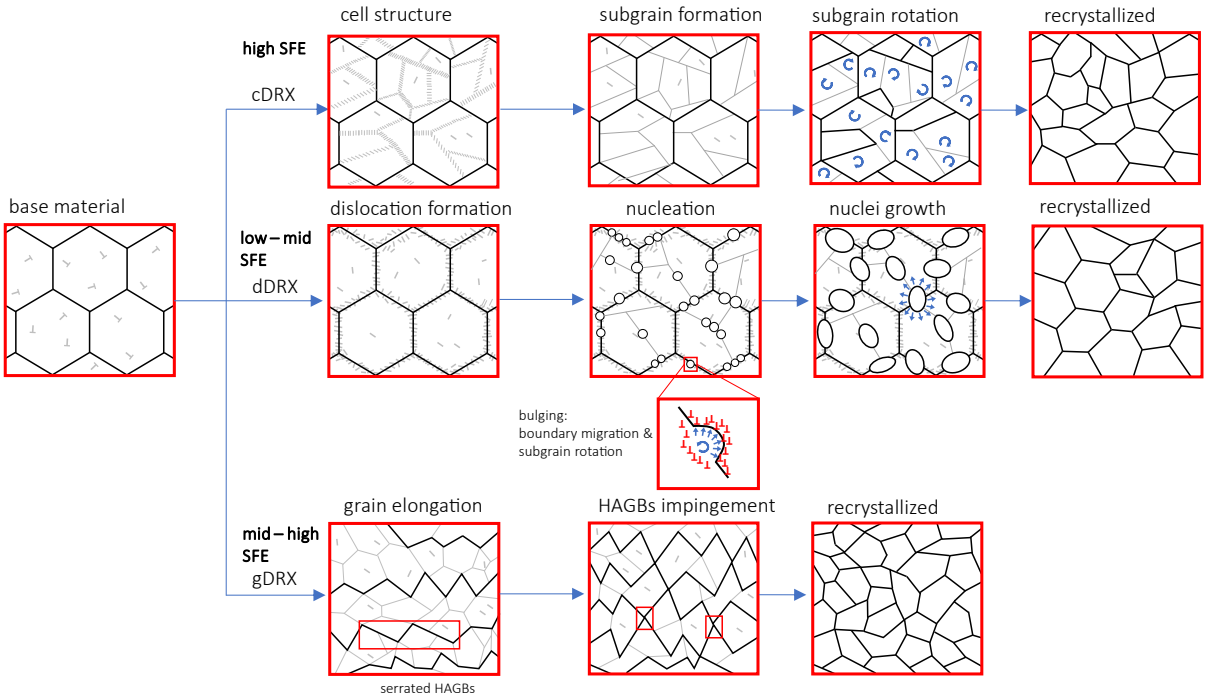

Figure 6: Schematic illustration of the development of the new grains for the cDRX, dDRX & gDRX mechanisms (adapted from: [56] [61] [49] [52] [20]).

The ability for strain hardening by dislocation accumulation decreases with increasing temperature and increases with increasing strain rate. The reason for this lies in the increased diffusion rates and dislocation mobility, and thus acceleration of the thermally activated restoration processes, and at the same time the reduced time to allow them to take place. The general Zener-Hollomon principle is in fact a time-temperature equivalence, which can be used to describe thermally activated phenomena such as recrystallization. The Zener-Hollomon equation describes the relationship between strain rate, lattice activation energy, gas constant and the temperature. The Zener-Hollomon parameter can be calculated through [62]:

$$Z = \dot{\varepsilon} \exp\left(\frac{Q}{R\,T_Z}\right) \tag{7}$$

where $\dot{\varepsilon}$ is the strain rate, Q is the lattice activation energy, R is the gas constant, and T_Z is the temperature. In the work of Dialami et al. [63] and of Chang et al. [64] AZ31 Mg alloy was processed using FSW, and the dynamically recrystallized grain size was correlated with Zener-Hollomon parameters [62]. The dynamically recrystallized grain size decreases with increasing Z value [65]. TMP involves multiple, complex, and interrelated mechanisms occurring in the microstructure. How interactions on a multiscale level influence the sub-mechanisms, especially in their intensity and sequential order, is not fully understood to date, hence further research is required [20].

3.4.2 Factors influencing DRX

The main factors influencing DRX are thermo-mechanical processing (TMP) conditions, initial grain size, dislocation characteristics and associated stacking fault energies and secondary phase particles.

The initial grain size influences the dDRX mechanism. Since grain boundaries act as nucleation sites during dDRX, recrystallization kinetics slows down for large initial grains. Besides this, grain boundaries hinder the dislocation movement, so by varying the grain size, the dislocation movement is affected, independent of the different DRX types. However, the influence of initial grain size during cDRX/gDRX has not been sufficiently understood to date [20].

Depending on the stacking fault energy, the dislocation density increases during plastic deformation, causing dislocations to accumulate, form dislocation tangles, and envelop 3-D structures with dislocation-free crystal regions, the so-called dislocation cell structure. The cell walls represent rotational boundaries. At the same time, dislocations annihilate themselves with increasing deformation on the cell walls, a process which is supported by dislocation climbing, i.e., migration of a dislocation to another slip plane by rearrangements of vacancies [66]. Depending on the temperature and strain rate, further deformation leads to an equilibrium state of forming new and old dislocations; this results in an equilibrium state of DRV and DRX [1], taking into account the phenomenon that stacking fault energy increases with increasing temperature [67]. The stacking fault energy can be lowered by substitutionally dissolved foreign atoms in fcc metals. For example, Al-Mg alloy tends to have planar sliding behavior due to its lower stacking fault energy [66]. In summary, the SFE determines the width of a stacking fault, which affects the level of dislocation dissociation into partial dislocations. A low SFE promotes such a dissociation reaction, which hinders the capacity of cross-slip and climb of dislocations and thus influence DRX [20].

It is known that secondary phase particles can significantly influence recrystallization. On the one hand, large particles such as intermetallics with a diameter larger than 1µm can promote recrystallization [68]. These particles can accelerate the interactions between dislocations and particles in zones with local deformation gradients [69], and thus act as nuclei sites. This process is called Particle Stimulated Nucleation (PSN) [20]. On the other hand, finely distributed secondary phase precipitates (< 1µm) strongly impede the dislocation movement and migration of grain boundaries. Due to the so-called Zener drag effect, recrystallization is slowed down, and grain growth is promoted. Another Zener effect with similar effects which can be observed, e.g. on very fine dispersoids, is the so-called Zener pinning [20], [70] [71]. The influence on the grain boundary and dislocation motion is due to a repulsive force on the grain boundary/dislocation. Contact with particles stores interfacial energy, which must be reapplied when detaching from the particles again. The corresponding restoring pressure is called the Zener pressure p_Z [19]. With respect to recrystallization, recovery, and grain growth, Zener effects counteract PSN. Assuming that the critical size of the deformation zone λ_{crit} is twice the particle size η^*, Engler et

al. [68] describe the ability of large particles to serve as nuclei sites considering the Zener effects by the following equation:

$$\eta^* = \frac{1}{2}\lambda_{crit} = \frac{2\,\gamma_{GB}}{p_D - p_Z} \tag{8}$$

where γ_{GB} is the specific grain boundary energy, p_D is the driving pressure for recrystallization and p_Z is the Zener pressure [68].

In summary, DRX depends not only on the type and size of secondary phase particles, but also on whether phases are present before recrystallization begins, or are formed during recrystallization, or are formed after processing through post dynamic recrystallization.

Dynamic precipitation (DP) during DRX depends on the plastic strain and strain rate acting parallel to the thermal cycle. Strain induced precipitates during TMP can differ from precipitates caused by conventional aging of an undeformed metal [72] [73]. In addition, depending on the thermo-mechanical process, precipitation sequences may not proceed entirely or even more than once. For example, in a single friction stir welding process, precipitates can first dissolve, but later reprecipitate again [74]. However, DRX promotes dynamic precipitation [75], while at the same time dynamic precipitation may inhibit DRX due to the Zener pinning effect [76] [71]. Since the interactions of DRX and secondary phase particles are highly dynamic and complex, mathematical models have been developed in previous studies, which Huang et al. present in review publications [20] [71].

3.5 Precipitation hardening

Precipitation hardening can achieve an increase in strength through the interaction of particles with dislocations and resulting restriction of mobility. Dislocations are likely to cut coherent precipitates and bypass semi-coherent and incoherent precipitates according to the Orowan mechanism, which is present in Al alloys [1]. The process utilizes the decreasing solubility of one or more of the elements in a solution with decreasing temperature. Heat treatment in several steps is necessary for the implementation. In the first step, the alloying elements are dissolved in the solid solution entirely, or partially if required so. Subsequently, the temperature is rapidly lowered, so that a thermodynamically stable state cannot be established. The resulting solid solution is supersaturated. In the final step, the material is heat treated again so that the solid solution approaches the equilibrium state by reducing the supersaturation through the formation of finely distributed precipitates. In suitable alloys, these precipitates are responsible for the strength increase achieved, depending on their size, strength and the spacing between them [77]. Excessively prolonged ageing treatments cause small particles to dissolve and deposit on larger particles. This process is called Ostwald ripening and has a softening effect on the material due to the larger particle sizes and large distances between them. Precipitates are secondary phases. In contrast to primary phases, they are not formed during the casting process but during subsequent heat treatment as a result of segregation in the solid state. While primary phases are thermally stable, this does not

generally apply to secondary phases. If the secondary phases are thermally stable and have low solubility at elevated temperatures, they are classified as dispersoid phases. Both secondary phases and primary phases can have an influence on recrystallization, as described in chapter 2.3.2, “Factors influencing DRX”. Precipitates differ from dispersoid phases in terms of their high solubility at elevated temperatures and from the steeply declining solubility on cooling. Thus, precipitate phases are thermally less stable, but have greater influence on the strength of the material by hindering the dislocation movement [1].

3.6 Precipitation kinetics of Al-Mg-Si

In this thesis Al-Mg-Si alloys are studied, which are mainly precipitation strengthened by the precipitation formation of Mg_2Si. For this reason, the theory of precipitation strengthening is described within this chapter for Mg_2Si precipitation hardening. The Al-Mg-Si system is a ternary system from which the quasi-binary system Al-Mg_2Si can be derived. Depending on the ratio of Mg to Si, the alloys are classified as "balanced" or "excess". This classification is based on the stoichiometric composition of Mg_2Si (2/1). If the amounts of Mg and Si contained in the alloy in relation to each other correspond to this ratio, the alloy is balanced. If the ratio is <2, there is a Si excess; if it is >2, there is a Mg excess. The equilibrium phase Mg_2Si (β-phase) has a high formation enthalpy of 6.4 kcal/mol and a maximum solubility of 1.85 wt.% at 595 °C. An excess of Si affects the solubility of Mg_2Si much less compared to an excess of Mg. Furthermore, an excess of Si increases the achievable strengthening effects by a higher percentage than an equal excess of Mg or an equal increase of the Mg_2Si content [1]. Al-Mg-Si alloys follow the general precipitation sequence [78] [79] [80]:

SSSS α-Al → atomic clusters → Mg/Si co-clusters GP I zones (spheroidal) → β″ GP II zones (needle-shaped) → β′ (rod-shaped) (U1, U2, B′) → β (plate-shaped)

involving the equilibrium phases α-Al, β-Mg_2Si and Si. If sufficient Cu is added in Al-Mg-Si systems, further complex precipitation phases with as yet unexplored compositions result. Since the alloys used in this study have a low Cu content, the Cu-containing precipitates are neglected. Thus, according to [80] [81], the following precipitation phases result listed in Table 3.

Table 3: Overview of known precipitation phases in the Al–Mg–Si system [80] [81].

phase	morphology	composition	unit cell
GP zones	1 to 3 nm spherical particles 2 x 20 nm needles	$Mg_{2+x}Al_{7-x-y}Si_{2+y}$	monoclinic
β″	4 x 50 nm needles	Mg_5Si_6	monoclinic
β′	rods several hundred nm long, with 10 nm diameter	$Mg_{1.8}Si$	hexagonal
U1	needles several hundred nm long, with 15 nm diameter	$MgAl_2Si$	trigonal
U2	needles several hundred nm long, with 15 nm diameter	MgAlSi	orthorhombic
B′	laths up to 1 µm long	$Mg_9Al_3Si_7$	hexagonal
β	Plates up to 10-20 µm across	Mg_2Si	fcc

The actual precipitation hardening follows a more complex sequence of numerous metastable phases, depending on temperature, time, and exact alloy composition [82]. In the solid solution, separate clusters of silicon and magnesium atoms form at the beginning of the precipitation hardening process, evolving into Mg/Si clusters and GP zones [79]. Clusters are collections of alloying elements that do not follow any pattern in their arrangement. If an internal structure develops, these clusters are called GP zones. Depending on their orientation or correspondence with the surrounding crystal structure, GP zones or precipitates are considered coherent, semi-coherent, or incoherent [1]. As the process continues, the β″-phase, as well as the β′-phase are formed. The hardness maximum corresponds to the transition from β″ to β′, with additional uniform distribution of GP zones. The β′-phase has an ordered structure corresponding to the composition Mg_2Si and transforms into the β-equilibrium phase by a diffusionless transformation during further growth [1]. Besides the β″-phase and the β′-phase, various other phases can form in the temperature interval of 200-300 °C. It is possible that several of these phases exist in parallel in the combination β′ (Mg_2Si), U2 (MgAlSi), U1 ($MgAl_2Si_2$), B′(MgSi) or β″ (Mg_2Si), β′ (Mg_2Si), U2 (MgAlSi), U1 ($MgAl_2Si_2$). Each of these phases has its own morphology and stoichiometric composition [79]. However, aside from the equilibrium phase β-Mg_2Si, Cu additions in Al-Mg-Si alloys can cause, for example, the equilibrium phase Q-$Al_5Cu_2Mg_8Si_6$ and its precursor phases (Q″, Q′) or the equilibrium phase θ-Al_2CuMg and its precursors (θ″, θ′). Consequently, the complexity and potential amount of precipitation phases rises with increasing alloying elements [1].

3.6.1 Dynamic precipitation

Precipitates can form at a higher rate during plastic flow in the deformed microstructure compared to static conditions. This phenomenon is referred to in the literature as dynamic precipitation (DP) and has been observed and described by scientists in previous studies [83] [84] [85] [86].

Microstructural mobility occurs by a vacancy exchange. For thermally activated processes, the temperature controls both mobility and driving forces. Microstructural mobility in metals can also be induced by plasticity. Since plasticity generates vacancies and interstitials through nucleation and dislocation-dislocation interactions, thus lowering the temperature required for microstructure transformations to room temperature or even below. These mechanisms create kinks and jogs within the dislocations. Kinks and jogs are steps in dislocations lines. Kinks can be viewed as a subset of jogs. The reason for the appearance of a kink is that, from an energetic point of view, it is much easier to overcome energy barriers just locally by kinking than by sliding the entire screw dislocation (Figure 7 (a)). A kink therefore lies within the slip plane. A jog on the other hand lies outside of the slip plane (Figure 7 (b)). The creation of jogs proceeds via dislocation-dislocation interaction and is displayed in Figure 7 (c) & (d). In Figure 7 (c) two dislocation lines, X-Y and A-B, lie perpendicular to each other. In the same way, the Burgers vectors b_1 and b_2 are orthogonal to one another. While the dislocation X-Y is mobile, A-B is stationary. After the dislocation interaction (Figure 7 (d)), the dislocation X-Y remains unchanged, while in the case of the dislocation A-B an edge or so-called jog with edge length b_1 has been created. This edge no longer lies on the original slip plane P_{AB}. Depending on the orientation of the Burgers vectors of the crossing dislocations, e.g. parallel to each other, a jog is generated for both the moving dislocation and the stationary dislocation. Since the dislocation motion on its slip plane is energetically more favorable than climbing onto another slip plane, the dislocation motion is slowed down by the dislocation interaction effects. Thus, if a screw dislocation contains a jog, the part of the dislocation that lies within the slip plane bows out due to the pinning, while the more immobile jog remains stationary (Figure 7 (e), (f)) [23]. fcc materials like aluminum alloys contain a certain concentration of thermal jogs by deformation. When the dislocations move through the material, the dragging of those jogs leads to a generation of vacancies by geometric effects [85]. Moreover, these vacancies can organize into nanoscale dislocation loops and turn into a Frank-Read source [23]. During plasticity, non-equilibrium vacancy concentration occurs through jog dragging effects. The resulting vacancies can lead to the mediation of mass transfer. As a result, clusters can be diffused more rapidly in the high vacancy concentration areas, leading to acceleration of precipitation through strain-induced plasticity [85] [86].

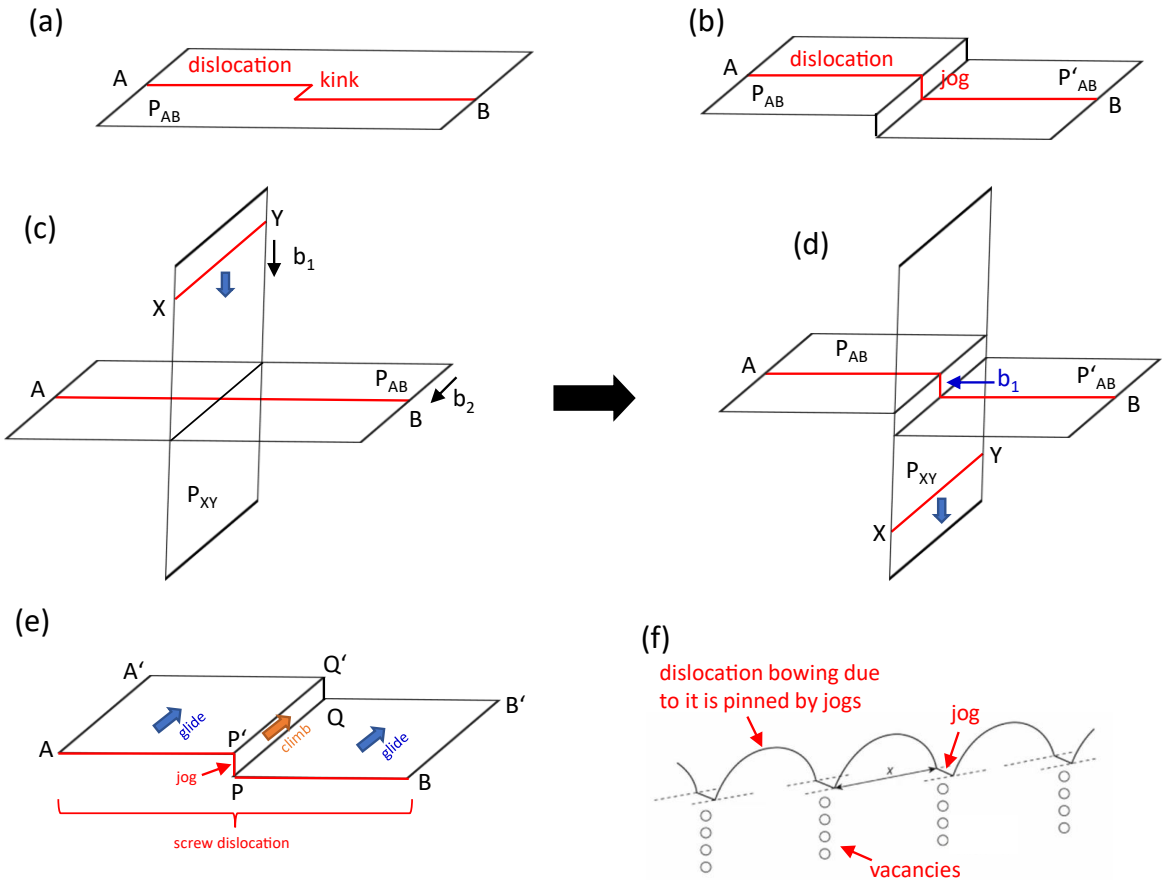

Figure 7: (a): Dislocation containing a kink. (b): Dislocation containing a jog. (c): Dislocation XY moving on its slip plane P_{xy}. (d): Dislocation XY has cut through AB and produced a jog PP′ in AB. (e): Movement of a screw dislocation containing a jog PP′. Movement of dislocation to A′–Q′–Q–B′ would require a climb of the jog PP′ to QQ′. (f): Glide of jogged screw dislocation producing trails of vacancies [23].

By in-situ small angle X-ray scattering, Deschamps et al. [86] were able to show that at elevated temperature deformation accelerated precipitate growth can be rationalized by strain-induced vacancies in an Al-Zn-Mg alloy (AA7449). The precipitate growth rate was shown to increase linearly with strain and to be relatively independent of strain rate. TMP affect precipitation in two ways. On the one hand, the local vacancy concentrations near the jogs force mass transfer and accelerate precipitation kinetics [85] [86]. On the other hand, spherical β″ phases with diameters in the nanometer range are more likely to be found in an Al-Mg-Si alloy during TMP than β′ and stable β-Mg_2Si. TEM investigations suggested that needle-shaped β″-phases are fragmented to spherical shape by the high effective shear strain during the SPD process, leading to the formation of spherical β″-phases and affecting the precipitation kinetics [72]. The details of the mechanisms and sub-mechanisms controlling dynamic precipitation are yet unclear and the subject of current research.

3.7 Crystallographic notation & stereographic projection

Crystallographic orientation refers to the relative orientation of the three crystal axes of a crystal in a cubic system [87]. In the practical description of crystallographic orientation of a technical material, the three axes of the crystal reference frame are often specified for the reference/rolling direction (RD), the

normal direction (ND) of the rolling surface, and the transverse direction (TD) of a rolled sheet – interpreted for comparable directions applicable to any specific, non-rolled sample. For the analysis in Friction Surfacing coatings, the reference coordinate system is the sample coordinate system [87] with the three perpendicular axes in normal direction (ND), deposition direction (DD) and transverse direction (TD). The mathematical relationship between the two systems, the crystal coordinate system and the reference coordinate system, consists of a pure rotation due to the orthonormality of these systems [87]. The orientation matrix g reads:

$$g = \begin{bmatrix} \cos\alpha_1 & \cos\beta_1 & \cos\gamma_1 \\ \cos\alpha_2 & \cos\beta_2 & \cos\gamma_2 \\ \cos\alpha_3 & \cos\beta_3 & \cos\gamma_3 \end{bmatrix} \tag{9}$$

In this context, the rotation is uniquely determined by the direction cosines of the unrotated coordinate axes in the rotated coordinate system. By multiplying the first and third columns of the orientation matrix g divided by the least common divisor, the Miller indices {hkl} <uvw> are calculated. The notation {hkl} denotes all symmetrically equivalent planes of a crystallographic plane, while <uvw> describes all symmetrically equivalent directions [88]. In crystallography, a three-dimensional orientation sphere is employed to represent the spatial location or orientation of crystallographic axes. Each point on the sphere corresponds to a penetration point of a plane normal. When projected onto a two-dimensional plane, the sphere is transformed using a stereographic projection. To accomplish this, a reference sphere is placed around a crystal, which is penetrated at point P by the normal of a crystal plane E [89]. When point P is connected to the projection center, which is the south pole of the sphere, the resulting intersection point P′ with the equatorial plane of the sphere becomes the projection plane. Point P′ represents the pole of the plane E and is defined by two angles, α and β, as shown in Figure 8. The value of α ranges from 0° at the center to 90° at the edge, while β ranges from 0° to 360° [88]. Stereographic projection cannot represent planes with normals in the southern hemisphere, but these planes are equivalently represented by normals with a reversed sign. To determine an orientation, only the specification of at least two poles {hkl} is required in the cubic lattice because of the fixed angular relationships between planes and directions. Therefore, the location of a crystal orientation can be described by a pole figure (PF). Although a {hkl} pole figure only reflects the position of the {hkl} poles, all crystallographic directions parallel to the sample axes can be determined from the angles α_i and β_i. There are two types of pole figures, the pole figure and the inverse pole figure (IPF). The pole figure describes the position of the crystal axes with respect to the sample coordinate system whereas the inverse pole figure describes the position of the sample axes in the crystal coordinate system [89].

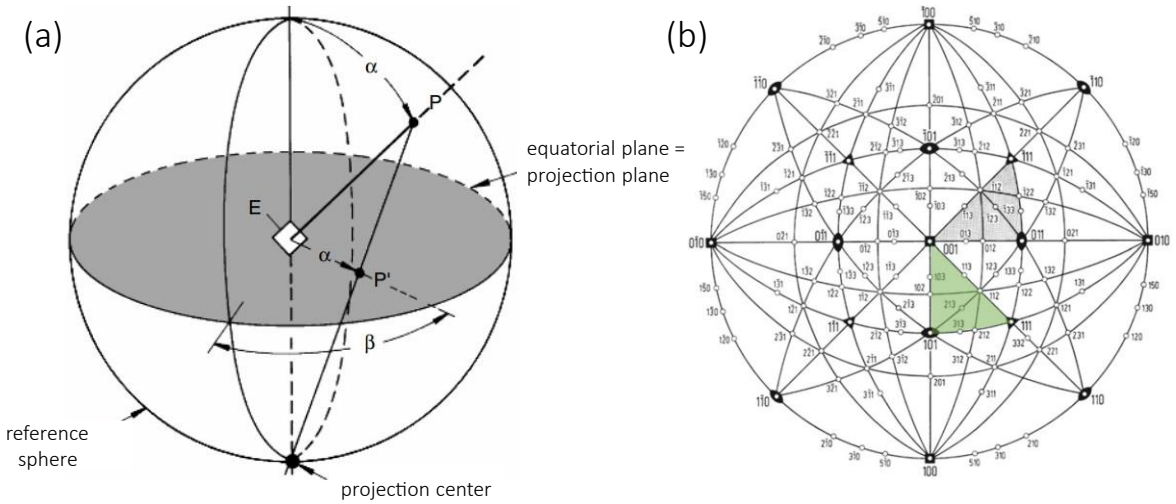

Figure 8: (a): Principle of stereographic projection of the pole P' of a crystallographic plane E (b): Stereographic projection of a cubic crystal in (001) position; The green triangle indicates the partial section of the stereographic representation for application in inverse pole figure maps [19].

3.7.1 Ideal shear texture in fcc materials

The phenomenon of grain orientation of polycrystals concentrated in the vicinity of one or few orientations is called preferred orientation, and the preferred orientations of polycrystals is known as texture [90]. Formation of textures leads to anisotropy of the material characteristics [91]. It is known that the material flow in conventional solid-state joining technologies, such as Friction Stir Welding or Friction Surfacing, is dominated by shear deformation. Therefore, the generated {111}-PF plots are compared with those of an ideal simple shear orientation of face-centered cubic (fcc) materials. As is well known, fcc crystals slide preferentially along the 4 x {111} slip planes in 3 x <1-10> directions and thus have 12 different slip systems, something that makes fcc materials generally favorable for plastic deformation [19]. Here, the crystallographic planes {hkl} and directions <uvw> are the same direction as the shear plane and shear direction [92]. In their research, Li et al.[93] studied and simulated the ideal shear texture components using ECAP (equal channel angular pressing) experiments. The ideal shear textures of fcc materials consist of the following three main components:

Partial fiber:	A Fiber	{111}<uvw>
	B Fiber	{hkl}<110>
Component:	C	{001}<110>

Figure 9 reveal the projections of the ideal simple shear texture for fcc metals onto the 111-pole figures [94] in (a), A-fiber: {111}<uvw> [95] in (b), B-fiber: {hkl}<110> [95] in (c) and C-component texture in (d). Table 4 lists the exact Miller indices as well as Euler angles of the achievable ideal shear texture components. The ideal shear textures that develop in fcc materials are formed by continuous lattice rotation, where the alignment of the {111}-slip plane with the shear plane and/or the <110>-slip direction with the shear direction is favored. This leads to the formation of the A- and B-fiber

orientations, respectively. Aluminum alloys predominantly form a {112} <110> texture as the fcc lattice, which corresponds to B or $\overline{B}$ components of the ideal shear texture. In these shear textures, the closest-packed <110> direction is aligned with the shear direction, and the closest-packed plane {111} is aligned with the shear rotation direction, which is perpendicular to the shear direction (SD) and shear plane normal (SPN) [92].

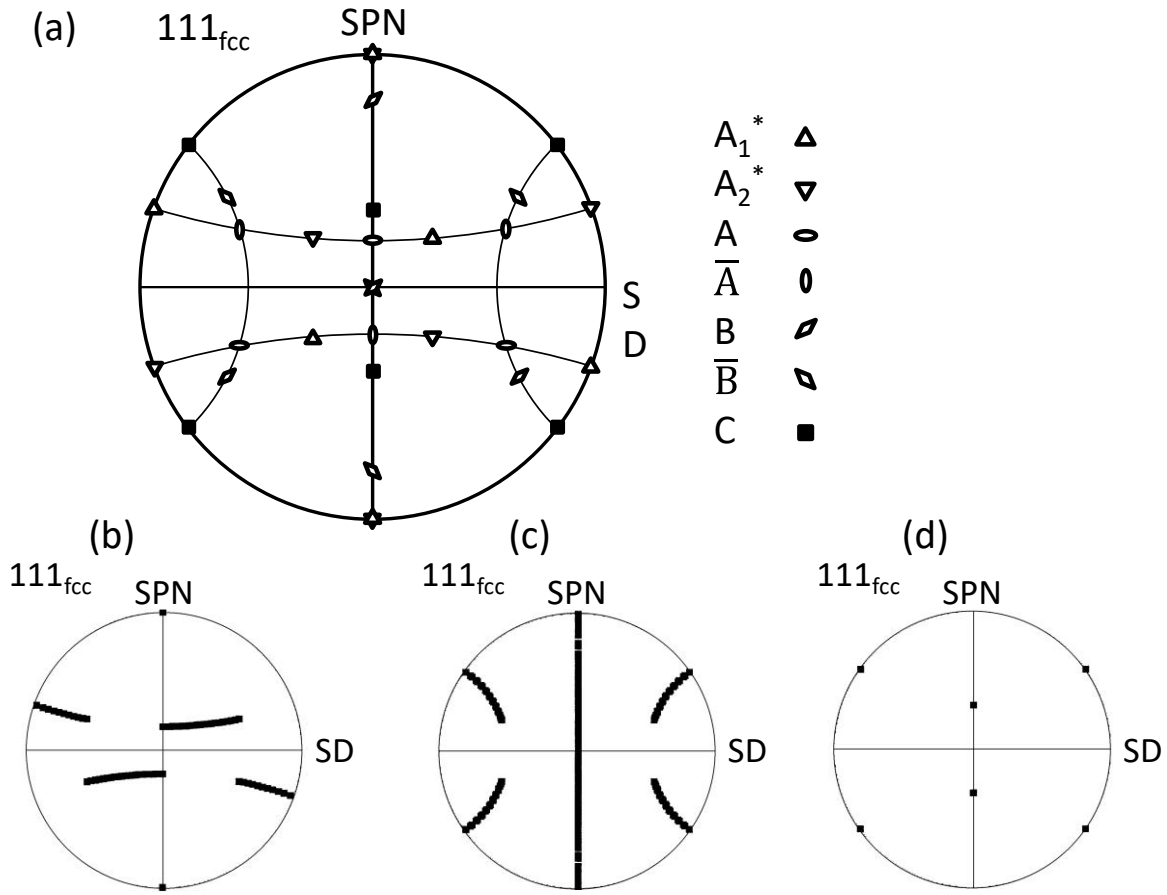

Figure 9: (a) Projections of the ideal simple shear texture for fcc metals onto the 111-pole figures [91] (b) A-fiber: {111}<uvw> [95] (c) B-fiber: {hkl}<110> [95] (d) C-component texture.

Table 4: Ideal crystallographic orientation of fcc simple shear deformation textures including Miller indices and Euler angles [92].

Crystal structure	Shear component texture	{hkl} <uvw>	Euler angles [°]		
			ϕ_1	ϕ	ϕ_2
fcc	A_1^*	{111} <$\bar{1}1\bar{2}$>	35.3 / 215.3	45	0
			125.3 / 305.3	90	45
	A_2^*	{111} <$11\bar{2}$>	144.7 / 324.7	45	0
			54.7 / 234.7	90	45
	A	{1$\bar{1}$1} <110>	0	35.3	45
	$\bar{A}$	{1$\bar{1}$1} <$\bar{1}\bar{1}$0>	180	35.3	45
	B	{1$\bar{1}$2} <110>	0 / 120 / 240	54.7	45
	$\bar{B}$	{$\bar{1}1\bar{2}$} <$\bar{1}\bar{1}$0>	60 / 180 / 300	54.7	45
	C	{001} <110>	90 / 270	45	0
			0 / 180	90	45

4 Materials and methods

This chapter provides an overview of the friction-based solid-state joining process Friction Surfacing and equipment, as well as the materials and analytical methods used in this thesis.

4.1 Custom-made Al-Mg-Si cast alloys

Aluminum alloys were custom-made by remelting the precipitation hardenable alloy AA6060 from a single production batch and adding either Mg or Si in varying amounts. A total of 10 different alloys were produced and compared for this study. The initial alloy AA6060 and 6 different Al alloys with Mg additions of 2 wt.% and 3.5 wt.% were provided by the company Erbslöh Aluminium GmbH (Velbert, Germany). Furthermore, 4 Al alloys with Mg additions of 6.4 wt.%, 8.9 wt.%, 10.6 wt.% and 12.1 wt.% were produced at the Chair of Metallurgy of Iron and Steel Production at the University of Duisburg-Essen. 3 Different Al alloys with Si contents of 6.6 wt.%, 10.4 wt.% and 14.6 wt.% were also produced by Erbslöh Aluminium GmbH. The modified alloys and a sample of the original AA6060 were cast in small, slightly conical molds, resulting in as-cast rods 80-110 mm long and 25 mm in diameter; from each of these a consumable stud for FS could be machined (see Figure 10).

Figure 10: Cast rods & machined consumable studs.

All cast rods underwent a homogenization heat treatment at 535 °C for 72 hours to adjust a uniformly distributed microstructure in all materials. For comparison purposes, wrought rods from the same batch of the original AA6060 in the T6 condition were also used in this study. For practical reasons, small variations in other alloying contents could not be avoided. Still, differences are very small and therefore neglected in the discussions in this study. The chemical compositions of the ten cast alloys were measured by optical emission spectroscopy and are listed in Table 5.

Table 5: Chemical composition of studied Al alloys (stud material).

consumable stud material

	Al	Si	Fe	Cu	Mn	Mg	Cr	Zn	Ti
AA6060 (DIN EN 573, 2013)	bal	**0.3-0.6**	0.1-0.3	0.1	0.1	**0.35-0.6**	0.05	0.15	0.1
AA 6060-T6	bal	**0.37**	0.17	0.013	0.009	**0.27**	0.002	0.009	0.018
2 wt.% Mg	bal	0.38	0.19	0.012	0.009	**1.94**	0.003	0.003	0.016
3.5 wt.% Mg	bal	0.39	0.19	0.014	0.009	**3.48**	0.003	0.007	0.015
6.4 wt.% Mg	bal	0.37	0.17	0.009	0.010	**6.44**	0.002	0.001	0.014
8.9 wt.% Mg	bal	0.41	0.18	0.013	0.010	**8.88**	0.002	0.003	0.013
10.6 wt.% Mg	bal	0.41	0.18	0.012	0.011	**10.60**	0.002	0.004	0.012
12.1 wt.% Mg	bal	0.39	0.18	0.011	0.012	**12.10**	0.003	0.005	0.012
6.6 wt.% Si	bal	**6.61**	0.20	0.016	0.009	0.25	0.002	0.003	0.017
10.4 wt.% Si	bal	**10.37**	0.20	0.011	0.009	0.25	0.002	0.003	0.014
14.6 wt.% Si	bal	**14.60**	0.23	0.011	0.010	0.23	0.002	0.001	0.013

The software package Thermo-Calc (Thermo-Calc Software AB, Solna, Sweden), including the material database "TCAL6" for Al-based alloys, was used for the computer-aided calculation of thermodynamic properties in multi-component alloy systems. Equilibrium phase fractions and binary phase diagrams in the equilibrium state were calculated from this. These calculations served as a first approach to obtain an approximation of the potentially forming phases under equilibrium conditions in the custom-made Al alloys.

4.2 Substrate material: AA2024 Cu alloy (Al-Mg-Cu)

The substrate used for the FS process are plates of 300 x 130 x 8 mm from the Al alloy AA2024-T351. The precipitation hardenable Al-Cu-Mg alloy AA2024 is a high strength alloy widely used in aerospace and structural applications such as bridges, electric scooters, robotics, satellites etc. Precipitation hardening depends on Mg content and Cu/Mg ratio and occurs via the stable equilibrium phase, rhombohedral S-phase (Al_2CuMg), tetragonal θ-phase (Al_2Cu) or a mixture of both as described in the literature [96]. AA2024 is preferably used in its strain hardened condition (T3, T4) where high fracture toughness values and more favorable crack propagation behavior are present than in its artificially aged condition (T6, T8) [1]. The chemical composition of the used AA2024 sheets was measured by optical emission spectroscopy and is listed in Table 6.

Table 6: Chemical composition of the substrate material.

	substrate material								
	Al	**Si**	**Fe**	**Cu**	**Mn**	**Mg**	**Cr**	**Zn**	**Ti**
AA2024 (DIN EN 573, 2013)	bal	0.50	0.50	3.8-4.9	0.30-0.9	1.2-1.8	0.10	0.25	0.15
AA2024-T351	bal	0.08	0.114	4.46	0.509	1.383	0.004	0.095	0.032

4.3 FS processing & thermal cycle analysis

The process parameter window was elaborated on the custom-designed Friction Surfacing machine HLR-RAS (H. Loitz Robotik, Hamburg, Germany) shown in Figure 11. With a maximum capacity of 60 kN axial force, 200 Nm torque and 6000 min^{-1} rotational speed, this Friction Surfacing machine offers a wide range of parameter combinations as reported elsewhere [5] [97] [98]. The machine was operated force-controlled in z-direction and velocity-controlled in x-direction while the reaction forces, moments, and velocities were continuously recorded during the surfacing process.

Figure 11: Friction Surfacing machine.

Process temperatures were measured at three different positions along the center line of the coatings during their deposition process. For this purpose, thermocouples with a diameter of 0.5 mm (Type K, Conatex, St. Wendel, Germany) were guided from below through a hole in the substrate, so that the thermocouple tips are positioned 0.5 mm below the coating/substrate interface along the path of deposition. According to standard EN 60584-1, the measurement accuracy in the temperature range of -40 to 1200 °C is ± 0.0075 x $T_{measured}$ (measured temperature). The data acquisition system, including

the software by National Instruments (Austin, USA), provided sampling rates up to 100 Hz. Additionally, the process temperatures were recorded and evaluated by means of the infrared camera ImageIR 8300 and the corresponding data recording and evaluation software IRBIS 3.1 professional (Infra Tec GmbH, Dresden, Germany). The line of view of the infrared camera, calibrated between 150 °C and 650 °C, was oriented perpendicular to the welding direction, and the camera recorded the entire process at a sample rate of 25 fps. It must be taken into account that such temperature measurements have some uncertainties caused by reflection and variations in surface roughness and oxide layers. However, the surfacing process was repeated under similar conditions, so the measurement results can be compared with each other. The experimental setup with regard to temperature measurements is illustrated in Figure 12.

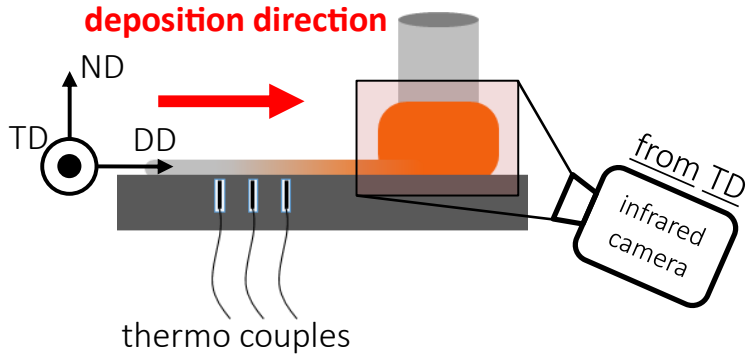

Figure 12: Experimental setup processing temperature.

Only the FS deposition processing of the initial alloy AA6060, the alloys with 2 wt.% and 3.5 wt.% Mg addition and the alloys with 6.6 wt.%, 10.4 wt.% and 14.6 wt.% Si addition was carried out on the HLR-RAS at the Helmholtz Center Hereon in Geesthacht (Germany) with its full measurement capabilities for process temperatures, reaction forces and torques. The alloys with 6.4 wt.%, 8.9 wt.%, 10.6 wt.% and 12.1 wt.% Mg addition were processed without additional measuring equipment using the Maho 700 universal milling machine (Maho, Pfronten, Germany). The machine was operated manually in z-direction and velocity-controlled in x-direction. A U2A force sensor (Hottinger Brüel & Kjaer GmbH, Darmstadt, Germany) calibrated from 500 N-10 kN was used to estimate the manually applied axial forces. In the latter investigations, the focus is on the microstructural analysis of the resulting deposited coatings. The resulting coating geometries, respectively the coating thicknesses and widths, were measured using a precision outside micrometer. For this purpose, at least 5 individual measurements were carried out for statistical evaluation.

4.3.1 Deposit characteristics & coating dimensions

Only mechanical energy is induced into the material during FS processing. The energy introduced (P) has a torsional component (P_T) as well as axial (P_z) and transverse (P_x) components as described in the following equation:

$$P = P_T + P_x + P_z = (2\,\pi\,n\,T) + (F_x\,v_x) + (F_z\,v_{CR}) \tag{10}$$

n is the rotational speed, T is the measured torque, and F_x and F_z are the reaction forces in x and z directions. The torsional component accounts for the largest contribution to the energy input, while the energy component from the translational motion, which mainly relates to the removal of the plasticized material from the stud tip and its deposition, accounts for less than 1% of the total energy [5]. Likewise, the energy component P_z, which results from the axial movement, contributes less than 1 % to the total energy. To estimate the specific energy input per deposited material unit volume (e_s), which is required for heating and plastic deformation of the consumed material, the following formula is used.

$$e_s = \frac{P_T + P_z}{\pi\,r_C\,v_{CR}} \tag{11}$$

During steady state FS, an offset between the outer radius of the stud in the translational direction and the beginning of the deposition can be detected on the thermogram shown in Figure 13, where d_{stud} is the diameter of the consumable stud, d_c is the corrected diameter, r_c is the corrected radius and d_{offset} is the deposition offset.

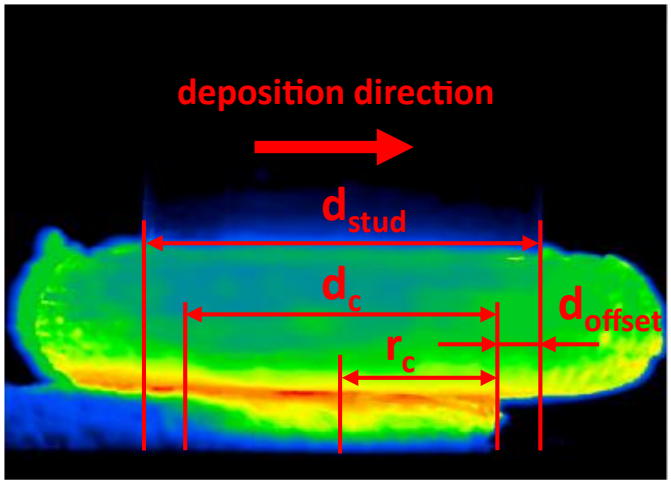

Figure 13: Thermogram of steady-state deposition in transverse observation direction. d_{stud} = diameter of the consumable stud, d_c = corrected diameter, r_c = corrected radius, d_{offset} = deposition offset.

This offset correlates with the calculated corrected radius according to the approach of Fukakusa [11]. The corrected radius r_c was substituted into equation e_s. From studies using marker material and filled studs, Fukakusa concludes that only the internal material that is deposited experiences the strong torsional shear deformation within what he calls the "real rotational contact plane". Hence, the corrected radius refers to the inner volume of the stud, which is deposited as coating, while the outer stud volume forms the flash. The corrected radius can be obtained by:

$$r_c = \sqrt{\frac{d\,w\,v_x}{\pi\,v_{CR}}} \tag{12}$$

where d is the coating thickness and w is the coating width. It is assumed that most of the shear flow induced by the rotational motion takes place within the inner volume of the stud with the corrected r_c while the surrounding material, which merges into the flash, undergoes significantly lower plastic strains. The deposition efficiency η is an additional relevant process characteristic. It expresses the ratio of the deposited material volume in the coating volume to the consumed stud volume, i.e., it indicates what fraction of the processed stud material was deposited as a coating and what was lost to the flash [2] [5]. Deposition efficiency η reads:

$$\eta = \frac{V_{deposited}}{V_{consumed}} 100\% = \frac{d\ w\ v_x}{\pi\ r^2\ v_{CR}} * 100\% \tag{13}$$

where d is the coating thickness, w is coating width and r is the stud radius (10 mm).

The resulting coating geometries respectively the coating thicknesses and widths were measured using a precision outside micrometer. For this purpose, at least 5 individual measurements were carried out for statistical evaluation.

4.3.2 Stop-action tests

The stop-action tests produce specimens in which the welding process is terminated in a controlled manner, by hitting an implemented safety switch, thus actively decelerating the machine axes' motion and gradually releasing applied forces. In these tests, the stud forms a solid connection with the substrate, and the resulting specimen reflects the deformation state of the ongoing process. Consequently, the coating, substrate and the plasticized stud are united in one sample. From this, the transitions between the different states of the initial material and the various process zones during FS can be reconstructed. The microstructure of the sheared zones, the bond zone, as well as the stud and coating material can all be investigated in the stop-action samples. The samples' microstructure is comparable to the steady-state generated coatings although some difference may arise from slightly different cooling conditions caused by the larger volume of heated material when the coating is still in contact with the stud.

4.4 Metallographic procedure

The sample preparation methods depend on which measurement or characterization method is to be used. An overview of the equipment, consumables and parameters used is shown in Table 7. All samples presented in this study were prepared using the methods and equipment listed here. In fact, the extended polishing steps were applied to the microscopy methods, OLM, SEM, TEM and the hardness measurements. For sample preparation for DSC and laser flash measurements, cutting and grinding methods were sufficient. More details about the specific sample preparation methods for each measurement method are given in the corresponding sections.

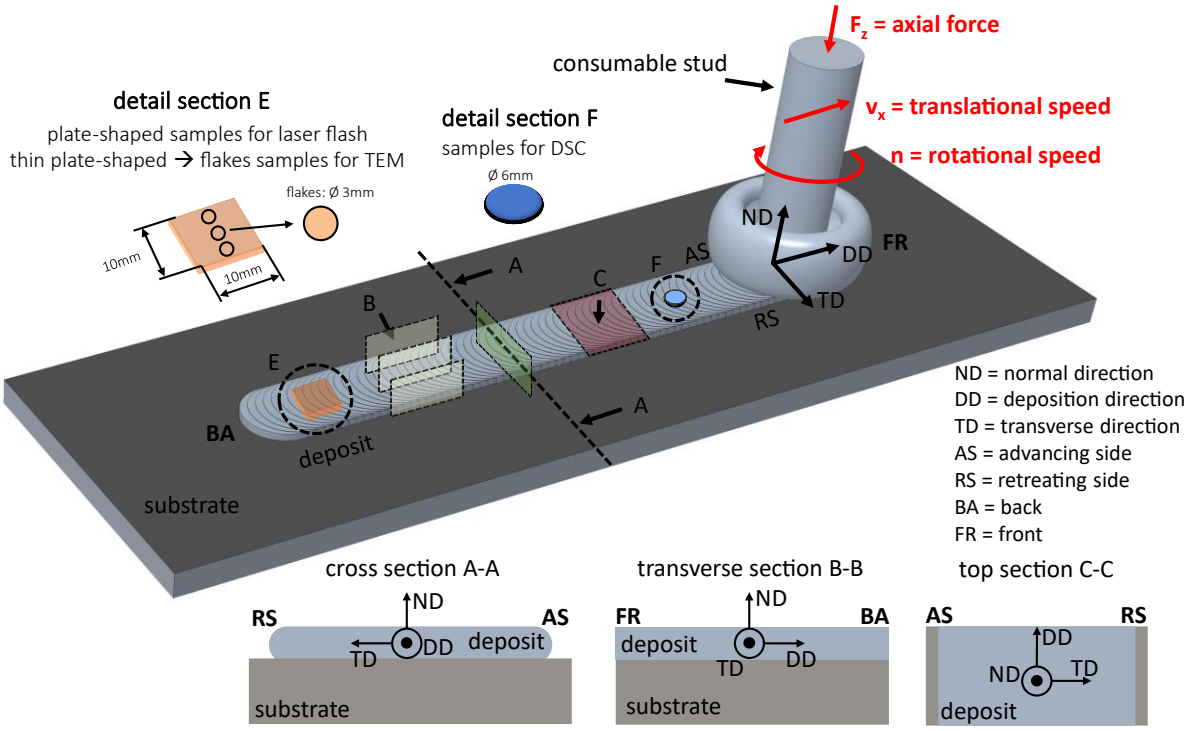

Figure 14: Schematic illustration of the Friction Surfacing process, coordinate settings of sample observation and sample extraction.

Table 7: Overview of all sample preparation steps used in this thesis – not all of them were required for each measurement technique (see details in corresponding sections).

Device	Material	Parameter
(A) cutting		
Wet cutting machine: Brilliant ATM (Mammelzen, Germany) Precision cutting machine: Accutom-100 (Struers GmbH, Willich, Germany)	cutting disc: corundum for low material hardness	n = 3200 rpm
	distilled water	feed rate = 2 mm/min
(B) embedding		
Mounting cups FixiForm (Struers GmbH, Willich, Germany)	EpoThin 2 Resin, EpoThin 2 Hardener Buehler, (Lake Bluff, IL, USA)	curing: 8-12 h
	Release agent	room temperature = approx. 20 °C
(C) grinding		
ATM (ATM Qness GmbH, Mammelzen, Germany) Phoenix 3000 Buehler, (Lake Bluff, IL, USA)	silicon carbide papers #220, #800	n = 150 rpm
		F = 10 N
	distilled water	t = 2 min
(D) polishing		
RotoPol.31 Struers (Willich, Deutschland) Phoenix 3000 Buehler (Lake Bluff, IL, USA)	MD-Largo; 9 µm diamond suspension	n = 150 rpm
	MD-Mol; 3 µm diamond suspension	F = 10 N
	DP-Lubricant Blue	t = 4-6 min
(E) final polishing		
RotoPol.31 Struers (Willich, Deutschland) Phoenix 3000 Buehler (Lake Bluff, IL, USA)	OP-Chem; colloidal silica 0.02 µm dioxide suspension 50% MasterMet 2 Buehler, (Lake Bluff, IL, USA)	n = 150 rpm
	50% H2O	F = 5 N
	distilled water	t = 5-8 min
(F) vibratory polishing (EBSD: Al-Mg: 5 h + electrolytical polishing; Al-Si: 12 h only)		
ATM Saphir Vibro (ATM Qness GmbH, Mammelzen, Germany)	IOTA; colloidal silica 0.02 µm dioxide suspension	frequency = 78.8 Hz
	30% MasterMet 2	intensity = 75%
	70% distilled water	t = 5-12 h
(G) electrolytical etching (only OLM)		
LectroPol -5 Struers (Willich, Deutschland)	etching reagent according to Barker: 5 ml HBF_4 (48%)	U = 20 V
		Q = 8 l/min
		T = 22 °C
	200 ml H_2O	t = 120-180 s
(H) electrolytical polishing (EBSD for Al-alloys with Mg additions)		
LectroPol -5 Struers (Willich, Deutschland)	electrolyte A2: 700 ml C_2H_6O	U = 30 V
		Q = 8 l/min
	200 ml distilled water	T = 22 °C
	100 ml $C_8H_{18}O_3$ 78 ml $HClO_4$	t = 12 s

4.5 Microstructural analysis

Samples were prepared from single layer coatings to examine the microstructure by optical light microscopy, scanning electron microscopy, and transmission electron microscopy. The three different methods used for sample characterization and their respective ways of preparing the samples are described in more detail in the following chapters.

4.5.1 Optical light microscopy

The examination of the microstructure of the sections by means of light microscopy is carried out in the etched (grain size, grain orientation, phase fractions and phase morphology) as well as unetched (pores, voids, cracks, inclusions, segregations, secondary phases) states. A compound-microscope is used, which allows increased magnification of 20x, 50x, 100x, 200x, 500x and 1000x. To produce polarized light, the light beam is passed through two polarizing filters (polarizer and analyzer). These are aligned at a 90° angle to each other. By using a compensator (platelet of anisotropic material), different colors are created. The light waves are slowed down and are offset by proportions of their wavelength xλ, so that interference occurs [99]. For the optical investigation, a light microscope by Olympus (Tokyo, Japan) of the type BX 41 TF is used in connection with the polarization filter U-P03 (Olympus, Tokyo, Japan) and the combined analyzer and compensator U-GAN (024) (Olympus, Tokyo, Japan). Creation and digital processing of images are performed using a Leica (Wetzlar, Germany) type DFC 420 camera and Image Access Standard 7 capturing software (Imagic Bildverarbeitung, Glattbrugg, Switzerland).

Sample preparation:

After the Al-Mg-Si samples have been prepared according to the preparation steps (A), (B), (C), (D) and (E) in Table 7, the special feature of this method is the preparation step (G), i.e., electrolytical etching. Samples were anodized in a Barker reagent (5 ml HBF_4 (48%) in 200 ml distilled water) at 22 °C for 120 s at a voltage of 20 V using the electrochemical etching device LectroPol-5 (Struers GmbH, Willich, Germany). The sample material serves as an anode, which leads to a roughening of the surface and an elliptical polarization effect [100]. Depending on their orientation, the crystals are affected by the etchant, so that differently oriented grains can be distinguished by color. Variations in composition within a grain are not visible.

4.5.1.1 Image processing

The images are digitally processed for further evaluation. Using the stitching program Image Composite Editor (Microsoft, Seattle, Washington USA) and the open-source panorama photo stitching and merging program hugin, single images are stitched to panoramic images. Images of the unetched structure are converted into 8-bit binary images in order to determine the fraction, size and distribution of phases. The processing is done with the open-source software Fiji (ImageJ) in several steps: converting to an 8-bit image, determining the threshold for the assignment of the color value, and determining the proportion of pixels below the gray value set as threshold. In order to analyze color-etched microstructures with regard to the average grain size, the line intersection method based on EN ISO 643 is applied. In the method chosen in this thesis, the number of intersections of a straight measuring line with the grain boundaries is selected as the basis for the calculation [101]. Fiji also offers the opportunity to analyze individual particles or grains with regard to their area content and aspect ratio.

4.5.2 Scanning electron microscopy (SEM)

Electron microscopy uses electrons instead of light waves to image objects, allowing higher magnifications with greater depth of focus. In this method, an electron beam consisting of primary electrons is focused by means of electrostatic and magnetic lenses and passed over the electrically conductive sample surface [102] [103]. The schematic operation of SEM is shown in Figure 15 (a). Primary electrons penetrate bulk material with a certain penetration depth. The penetration depth depends on the accelerating voltage and the atomic number of the atoms with which the primary electrons interact. Within different penetration depths (Figure 15 (c)), the primary electrons are scattered into both elastically backscattered electrons (BSE) (>50 eV) (Figure 15 (d.2)) and non-elastically secondary electrons (SE) (Figure 15 (d.1)) (<50eV) [104]. BSE are backscattered at an angle approaching 0° so that the BSE detector located around the pole piece can be used to image the material contrast of the sample. This method is used especially for elements of higher atomic numbers. By preparing the sample appropriately and tilting it by 70° (Figure 15 (b)), backscattered electrons can be used to identify crystal orientations, phases, etc. Secondary electrons have a lower energy level. SE can be detected using an Everhart-Thornley detector (SE2 detector), see Figure 15 (a), and used for surface topography analysis. Another method of elemental interactions with the primary electron beam used in this study is the emission of characteristic X-rays (Figure 15 (d.3)), which is employed for elemental analysis at the micrometer scale [102] [103].

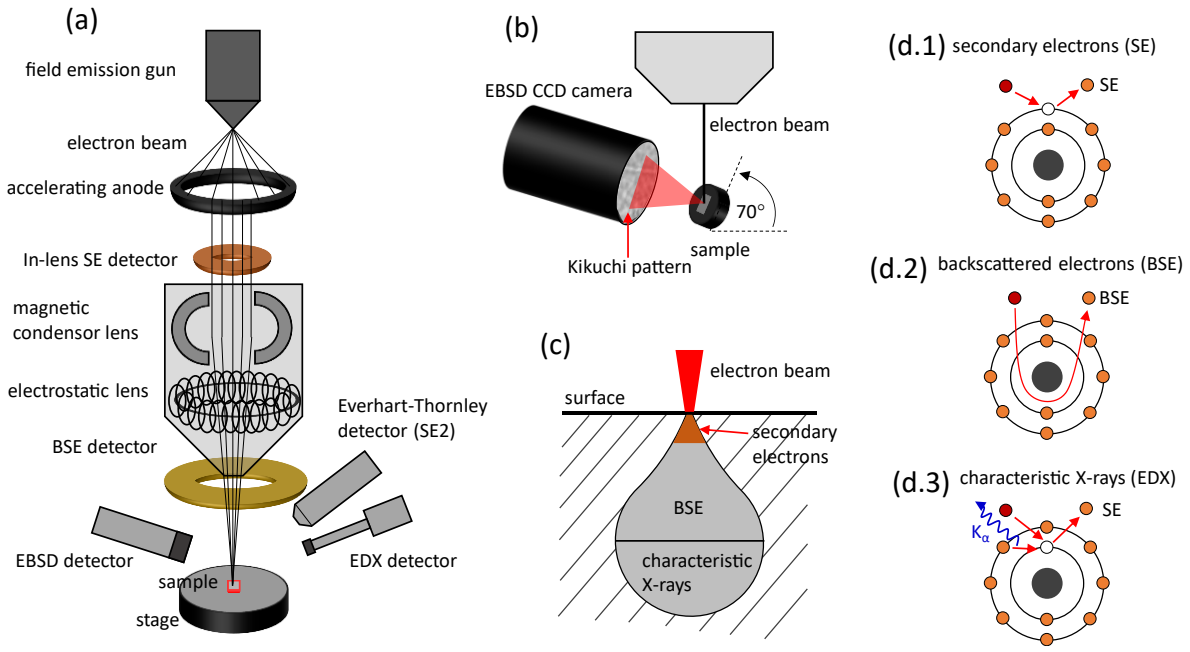

Figure 15: (a) Schematic illustration of SEM. (b) EBSD measuring setup. (c) Primary electron beam interactions and penetration depths. (d) Primary electron interactions: (d.1) Secondary electron release; (d.2) Backscattered electron release; (d.3) Characteristic X-ray release.

The analyses were carried out using a scanning electron microscope (LEO 1530 GEMINI, Carl Zeiss Microscopy GmbH, Munich, Germany) equipped with a field emission gun. For further analysis a combined microanalysis system (AMETEK-EDAX, Ametek GmbH, Wiesbaden, Germany) was used,

consisting of the Apollo X Silicon drift detector with TEAM 3.11 software for energy dispersive X-ray spectroscopy (EDX) and a Digiview IV CCD (couples charged device) camera for electron backscatter diffraction (EBSD). The evaluation is performed with the support of the analysis software OIM Data Collection™ and OIM Analysis™ 7.3.1 (AMETEK-EDAX, Ametek GmbH, Wiesbaden, Germany). The software includes a dataset of stored zone axes and angular relationships for selected phases, which are matched with the measured poles and thus identified.

Sample preparation:

For analyzing the imaging surface as well as determining the local chemical composition using EDX, the preparation steps (A), (B), (C), (D) and (E) according to Table 7 are sufficient for all Al-Mg-Si samples. For EBSD analysis, the Al-Mg alloys are vibration polished for 5 h (step (F)) and then electrolytically polished (step H) using A2 electrolyte (700 ml C_2H_6O, 200 ml distilled water, 100 ml $C_8H_{18}O_3$, 78 ml $HClO_4$) at 22 °C for 12 s at a voltage of 30 V. The Al-Si alloys are exclusively vibration polished for 12 h (step F), since the hard Si particles are not affected by the electrolytic polishing process.

4.5.2.1 Energy-dispersive X-ray spectroscopy (EDX)

By means of EDX, the elemental composition of a sample can be determined by analyzing characteristic X-ray radiation in the SEM. When the electron beam impinges on the sample, secondary electrons are generated by the inelastic scattering of primary electrons. When the primary electron beam strikes an atom, a secondary electron in one of the inner (lower-energy) shells is stimulated and ejected by the externally supplied energy (Figure 15 (d.3)). Since the most energetically favorable state is sought, an electron from one of the higher shells fills the space (shells M→L→K). As the electron sinks to a lower energy level, energy is released in the form of X-rays. In addition, the primary electrons in the atom's Coulomb field are decelerated, producing X-ray bremsstrahlung (braking radiation). This results in an X-ray spectrum, which is composed of the characteristic X-ray radiation and the X-ray bremsstrahlung. The wavelength and thus the energy of the radiation is specific for each element since the energy difference between the shells is element dependent. The element present can be determined by the position of the characteristic X-ray peaks in the spectrum, and the intensity of the X-ray peaks is determined by the element concentration present in the sample [105].

4.5.2.2 Electron backscattered diffraction (EBSD)

To determine grain orientations, grain sizes and misorientation angles, pole figure and phases, electron backscatter diffraction (EBSD) analyses were conducted in the SEM. EBSD is a high-resolution microstructural analysis technique in which elastically backscattered electrons are diffracted at the crystal lattice, resulting in Kikuchi patterns that provide information about crystal structure of the sample under consideration. The sample is clamped at a 70° tilt angle with respect to the primary electron beam direction as illustrated in Figure 15 (b) [102]. At 90° to the sample stage, a phosphor screen including an FSE detector (forward scattered electrons) and a CCD (charge coupled device) camera are located,

along with a detector attached to the phosphor screen for recording the backscattered electrons. The primary electrons of the wavelength λ incident on the sample are diffracted at the lattice planes of the crystal lattice; these planes are spaced apart by a distance d, with the Bragg angle θ_B, according to the Bragg equation [106]:

$$n_B\lambda = 2d_B \sin(\theta_B) \quad (14)$$

The diffraction order is given by n. The phosphor screen facing the sample forms a section plane with the diffraction cones of the respective lattice planes. This results in characteristic line patterns on the phosphor screen, so-called Kikuchi bands, each of which can be assigned to a lattice plane. The width of the respective Kikuchi band is determined by the wavelength of the backscattered electrons and the net plane spacing. The intersection points of several Kikuchi bands form zone axes. Thus, a Kikuchi pattern can be used to represent angular relationships of the crystal planes and to obtain information on the crystal symmetry and crystallographic orientation of the sample under investigation [102] [106].

Grain size, grain morphology & grain boundaries

Cross-sections perpendicular to the welding direction of the Mg- and Si-containing alloys processed with both identical and adjusted process parameters were analyzed by EBSD. Depending on the average grain size and the required degree of detail, the EBSD scans were recorded using different magnifications. The resolution was kept constant over the scan step size in µm corresponding to the magnification (magnification = scan step size): 100x = 2 µm; 150x = 1.5 µm; 250x = 1 µm; 500x = 0.5 µm; 1000x = 0.2 µm; 2500x = 0.1 µm. Software OIM Analysis™ 7.3.1 is used for representing the calculated orientation information maps, figure plots and diagram evaluations. Before creating the figure plots, the raw data must be pre-processed. Pattern indexing can be complicated by e.g., orientation identification at grain boundaries, superimposed diffraction patterns or triple points. Additionally, measurement errors can be caused by e.g. non-uniform topography of the sample surface. The cleanup methods of the software OIM Analysis™ generally adjust single data points based on the neighboring orientations, thus changing the raw measurement data. The following methods are used for this purpose:

- Grain dilation; The iterative grain dilation method; this method only affects points that do not belong to a grain but have neighboring points that do belong to a grain and consequently can be aligned.
- Confidence index (CI); The CI, which ranges from 0 to 1 and is calculated during the automatic indexing of the diffraction pattern. For a given diffraction pattern, several possible alignments can be found that correspond to the diffraction patterns determined by the data analysis routines and assigns alignments to them. Thus, for a CI of 1, 100% of the measurement point can be assigned to a particular diffraction pattern. In the CI standardization cleanup method, the CIs of all points in a grain are set to the maximum CI. This method essentially allows different points with low CI to be assigned to the corresponding similar orientations of neighboring points [107].

The following figure plots are calculated and analyzed from the measurement data:

- Pole figures (PF) & inverse pole figures (IPF); Mostly PFs and IPFs are employed for the orientation representation, which are based on the principle of the stereographic projection. In inverse pole figures, the orientation is plotted with respect to only one reference axis. This representation is thus suitable for samples of distinct reference [108]
- Image quality (IQ); The IQ is defined as the sum of the detected peaks in the Hough transformation and describes the quality of an electron backscatter diffraction pattern [109]. The quality of the EBSD-image depends largely on the quality of the Kikuchi patterns, and this quality is displayed in linear grayscale in IQ. To the lowest IQ value of the measurement is assigned the value black, and to the highest white.
- Kernel average misorientation (KAM); In KAM maps, which are also used in this thesis, a hexagonal grid is considered. The misorientation ΔgK is calculated based on the average deviation between a measurement point currently under consideration and the surrounding points ΔgAi in a previously self-determined radius. In addition, a maximum misorientation must be specified for the calculation of the average and the color-coded display [107] [108]. In this thesis, the local misorientation of a measurement point was correlated with the alignment of neighboring pixels, here up to a distance of 5 measurement points in all directions. The misorientation of each measurement point is limited to 5° of the misorientation angle θ (5° 5R) and is represented by a color gradation from white to blue ($0° \leq \theta < 5°$), with higher misorientation colored in blue.
- Grain boundaries; In addition, grain boundaries are defined as lines in the maps. Grain boundaries with small angles are displayed in red (LAGB = $5° \leq \theta < 15°$) and grain boundaries with large angles are represented in black (HAGB = $15° \leq \theta < 65°$). For further analysis, the height-to-width ratio of grains is mapped. This aspect ratio (AR) provides information about the length proportions between x and y of the grains in the deposited material. This determines whether the grain morphologies assume a more rounded or elongated shape.

4.5.2.3 Determination of ideal shear texture components

In this thesis, the approach of R.W. Fonda et al. [92] to describe ideal shear texture componants in friction stir welds is applied to Friction Surfacing coatings. The ideal shear texture components potentially occurring in fcc materials, under shear deformation, are considered on the basis of ECAP experiments from the study by Li et al.[93]. For this purpose, the EBSD data sets are such rotated that they are aligned according to the loading directions, following the reference texture frame with the shear direction (SD) where they point to the right or to the left and the shear plane normal (SPN) points up. This means that the rotation of the crystal reference frame is to be aligned with the local shear reference frame in a particular analyzed region [92]. Depending on both the distance between the center of the sample and the EBSD measurement section and the viewing direction, DD, TD or ND, the data sets are rotated. In Friction Surfacing, the shear direction (SD) is assumed to be tangential to the stud radius, to

which the shear plane normal (SPN), which is always coincident with the ND of the standard frame (SPN||ND), is perpendicular. At a particular location on the weld, the difference between the detected texture orientation and the local orientation of the shear plane can be represented by the angle α, which reflects the rotation of SD around the rotating stud. Subsequently, the alignment of the shear reference system with the EBSD crystal reference system is completed by additional rotations of 90° or 180° [92]. Figure 16 is intended to illustrate the shear loading conditions in Friction Surfacing.

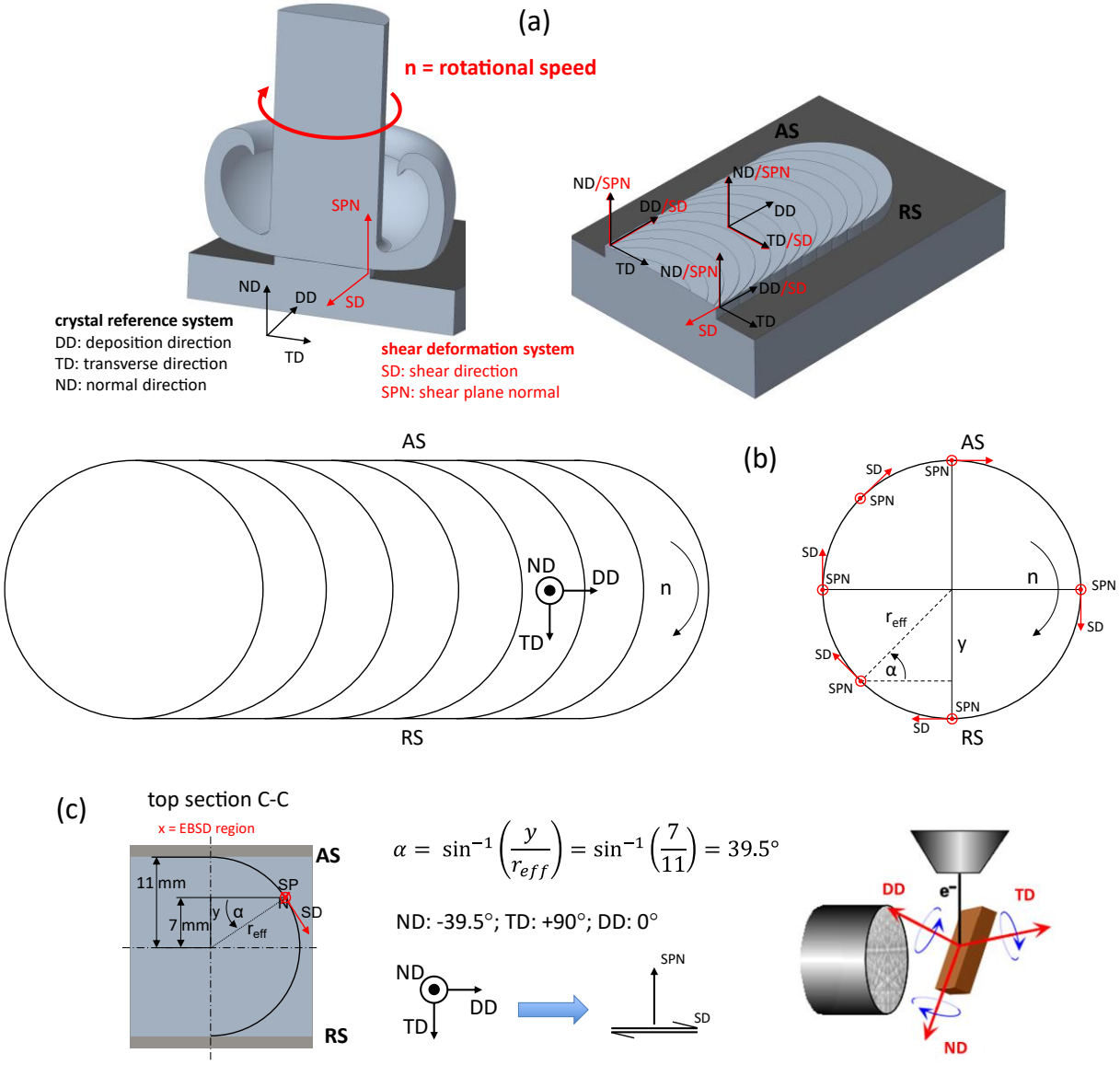

Figure 16: (a): Schematic relations between crystal reference system and shear deformation system in a model consisting of stud, coating and substrate. (b): Schematic top view of the shear surfaces generated during Friction Surfacing, showing the variations in shear directions [92]. (c): Calculation of the rotation angles of a data set at an example measuring point (x).

Figure 16 (a) illustrates the shear deformation system compared to the crystal reference system as a function of the local measurement region. Figure 16 (b) shows the sketch of an FS coating from the top view, adapted from [92]. The relationship of the orientation of the shear surface by the angle α is described. Figure 16 (c) demonstrates the example of a measuring point (x), which was measured on a

sample from top view, to determine the correct data rotation; this is required to be aligned with the desired shear deformation system. As described, the measurement data sets are rotated at an angle α

$$\alpha = \sin^{-1}\left(\frac{y}{r_{eff}}\right) \tag{15}$$

around the corresponding axes of the crystal reference system (DD, TD, ND) in such a way that the pole figures are aligned with respect to the ideal shear orientation.

4.5.3 Transmission electron microscopy (TEM)

The transmission electron microscope (TEM) is used to analyze lattice defects such as dislocations, stacking faults, twins, grain boundaries and precipitates. Primary electrons are released at the cathode (filament), and these electrons are then focused using condenser lenses as well as apertures and directed onto the sample as a parallel beam. When the electron beam passes through the sample, some of the electrons are scattered, while others pass through. The scattered electrons interfere with the unscattered electrons, producing a diffraction pattern of bright and dark areas on the detector. Samples with higher atomic numbers will scatter more electrons and produce a stronger diffraction pattern, which leads to better contrast in the TEM image. The resulting gray image is displayed on a fluorescent screen [102] [110]. Due to the strong electron absorption in solid materials, the samples to be transmitted by the electrons must be as thin as possible (< 300 nm). The transmission depends on the accelerating voltage and the atomic number of the elements. The high accelerating voltage of 100-400 kV allows a narrower primary electron beam and thus a higher resolution at high magnifications (up to 1,000,000x). Electron diffraction for selected regions in the TEM can be used to identify crystal structures and crystal defects [110].

In this study, TEM is used to detect possible substructures, dislocations, dislocation cells, stacking faults, grain boundaries and secondary phase particles/precipitates in bright field. A Phillips CM 200 transmission electron microscope equipped with a LaB_6 cathode at an accelerating voltage of 160 kV was used for the investigations (Philips Electronics Nederland B.V., Eindhoven, The Netherlands).

Sample preparation:

Plates of around 200 µm thickness were cut from coating material (see Figure 14). For grinding, samples were glued with a molten epoxy onto the plane surface of a steel holder. SiC paper was used, up to grit 1200, and polishing with diamond suspension was applied. Both sides of the cut samples were treated to achieve a smooth surface finish. When a thickness of 90 µm was reached, the samples were cleaned, and discs with a diameter of 3 mm were punched from the foils. Final thinning of the sample was performed by an electrochemical method to generate a hole in the center of the sample. The method applied was electrochemical jet polishing (TenuPol-3, Struers GmbH, Düsseldorf, Germany) using A2 electrolyte (700 ml C_2H_6O, 200 ml distilled water, 100 ml $C_8H_{18}O_3$, 78 ml $HClO_4$) (Struers GmbH, Willich, Germany). The edges of the generated hole should have a thickness of ≈ 100-200 nm to ensure transmission by the electron beam.

4.6 Thermal conductivity

Temperature-dependent thermal material properties were determined by means of the flash technique at the institute of Technology for Nanostructures (NST), University Duisburg-Essen, Duisburg, Germany. The front side of a plan-parallel sample is heated by a defined laser pulse, and then the temperature rise on the back side is determined over time using an IR detector. Laser flash measurements were performed with a NETZSCH LFA 457 MicroFlash (Erich Netzsch GmbH & Co. Holding KG, Selb, Germany) to assess the temperature-dependent thermal conductivity of Al-Mg-Si samples and investigate the influence of the alloying elements Mg and Si. The measurements were carried out in a temperature range from room temperature to 550 °C in temperature steps of 100 °C within a passive argon atmosphere to prevent reactions at elevated temperatures [111]. A total of 3 different alloys were measured by the laser flash technique: AA6060 as cast, 3.5 wt.% Mg and 10.4 wt.% Si.

Sample preparation:

Quadratic specimen with an edge length of 10 mm and a thickness of approx. 1 mm were taken from the consumable stud material (AA6060 as cast, 3.5 wt.% Mg and 10.4 wt.% Si) using the Accutom-100 precision cutting machine (Struers GmbH, Willich, Germany). The samples were then coated on both surfaces with graphite to evaluate the absorption/emission characteristics induced by the laser pulses.

4.7 Differential scanning calorimetry (DSC)

Differential scanning calorimetry (DSC) is a thermal analysis technique that measures the heat flux as a function of temperature that flows between an examined sample and a reference sample. This thermal analysis technique can determine various thermal parameters, heat capacities, melting and crystallization temperatures, heat of fusion, and various chemical reactions at a constant heating or cooling rate [112]. This technique has therefore been widely used to analyze precipitation and dissolution activities and to link microstructure to the processing and properties of age-hardenable Al-Mg-Si alloys [113].

In this thesis, the precipitation kinetics have been studied by means of DSC. Disc-shaped samples with a 6 mm diameter of the base material and of the coating material as well as of ultra-pure aluminum (reference sample) with a mass of approx. 180 mg were extracted from bulk material. The experiments were carried out by means of heat flow DSC (200 F3 Maia, Erich Netzsch GmbH & Co. Holding KG, Selb, Germany) and using DSC instrument (DSC 1, Mettler Toledo, Gießen, Germany). In this process, the sample is placed in the sample crucible, while an equal mass of pure aluminum is placed in the reference crucible. The cell containing both samples was heated from 30 °C to 550 °C in a dynamic nitrogen atmosphere at 10 K/min and then cooled to 30 °C with 10 K/min.

In order to obtain an evaluable DSC curve, it is necessary to eliminate the device-specific curvature from the raw measurement data. For this purpose, baseline measurements are taken with two high-purity aluminum reference samples. A baseline must be taken at the beginning and the end, as well as after every 3 measurements. The baseline is then subtracted from the sample measurements. The resulting

sample heat fluxes are converted to excess specific heat capacity caused by dissolution and precipitation reactions, and results are normalized with respect to sample masses. The formula for calculating the excess specific heat capacity c_p reads

$$c_p = \frac{\dot{Q}_{sample} - \dot{Q}_{baseline}}{m\ \beta} \tag{16}$$

where $\dot{Q}_{sample}$ is the heat flow of the sample, $\dot{Q}_{baseline}$ is the heat flow of the baseline. m reads the sample mass and β is the heating rate. Furthermore, isothermal areas of the obtained curve (reaction-free zones) do not lie at equal levels. By fitting the curve according to the zero-level polynomial method described by Osten [114], the DSC curve is polynomially corrected in such a way that the reaction-free zones lie at the zero line. The reaction-free zones reach from room temperature to 50 °C and in the higher range from ≈ 530-550 °C.

Sample preparation:

The DSC samples were separated into flakes of 1 mm thickness using the Accutom-100 precision cutting machine (Struers GmbH, Willich, Germany) and then manually processed into small cylinders of approximately 6 mm diameter using SiC paper. The deviation of the samples from the reference sample did not exceed ± 1 mg.

4.8 Hardness testing

During the hardness measurement of a material, a penetrating body is constantly pressed onto the material with a certain force. The hardness is defined as the mechanical resistance that the material offers to the mechanical penetration of the indenter. A local deformation occurs, which depends on the magnitude of the test force, the test duration, the shape of the indenter, and the hardness of the material to be tested. In Vickers hardness measurement, a pyramid-shaped diamond is pressed onto the material with a certain force. For the analysis of local hardness, hardness profiles and hardness distributions in this thesis, samples were extracted from different areas and observation directions (according to Figure 14) from the coating and substrate material, initial material as well as from the stop-action samples. All hardness measurements were performed in accordance with the ISO 6507-1:2005 standard, a test load of 1.961 N (HV0.2) and 9.807 N (HV1), respectively, and an exposure time of 10 s. Hardness maps were generated using the Vickers hardness method on both a Duramin-40 hardness tester (Struers GmbH, Willich, Germany) and a Carat 930 hardness tester (ATM Qness GmbH, Mammelzen, Germany). The individual indentations are generated automatically, measured, and evaluated optically via an image capture. This data can then be exported as a CSV file with included x and y coordinates of the indentations. A Zwick 3212 with textXpert V12.2 data acquisition software (Zwick Roell Gruppe, Ulm, Germany) was used to determine local hardness values and hardness profiles. Calibrated hardness reference plates were used for comparative measurements before each hardness measurement. For the purpose of statistical validation, at least 5 measured values were acquired to determine the local

hardness. The single impressions of the hardness profile measurements or hardness maps were generated in different step sizes, fine step size: 0.3 x 0.3 mm; coarse step size: 1 x 1 mm.

Sample preparation:

For hardness measurements, preparation steps (A), (B), (C), (D) and (E) have been performed according to Table 7 for all Al-Mg-Si specimens. Hardness measurements on polished surfaces are required for mainly two reasons. Homogeneous surfaces and high image contrasts are necessary for the automatic acquisition of hardness values during the generation a hardness map. Another reason is that at relatively low hardness values (approx. below 80 HV), as is often the case with Al alloys, grinding grooves can already cause local hardening effects and thus affect results.

5 Results

In this chapter, the results of the mechanical and thermal process characteristics, as well as the resulting coating properties, are presented. The focus lies on the microstructural characteristics and the development of the secondary phases. For this purpose, a comprehensive microstructural analysis of the Al-Mg-Si alloys in both base material state and FS coating material state is carried out. Furthermore, a detailed analysis of the precipitation evolution and microhardness development is presented.

5.1 Processing behavior & coating dimensions

The results presented focus on the influences the alloying elements Mg and Si have on aluminum. All other alloying elements, such as Fe, Mn, Cr, were neglected due to their minor variations. The relative position of stud and substrate, the spindle torque, and the forces in three directions are recorded and evaluated during FS. The process forces in the Z, X and Y directions, the positions in the Z and X directions, the torque and the consumption rate v_{CR} are recorded over the elapsed process time. The diagram in Figure 17 illustrates the recorded process characteristics of a single coating deposition of AA6060 in the as-cast state. The selected process parameters for this deposit are 4500 N, 4000 min^{-1}, 15 mm/s. The plot is classified into two sections. First, the plasticization phase, in which the material begins to plasticize due to the frictional heat. Secondly, the steady-state phase, in which the stationary coating deposition phase is reached by superimposing the translational feed rate. The red line describes the consumption rate v_{CR} and the velocity of the consumable stud in axial direction. v_{CR} is calculated through:

$$v_{CR} = \frac{\Delta s_z}{\Delta t} \tag{17}$$

where Δs_z is the consumed stud length difference during the corresponding time difference Δt.

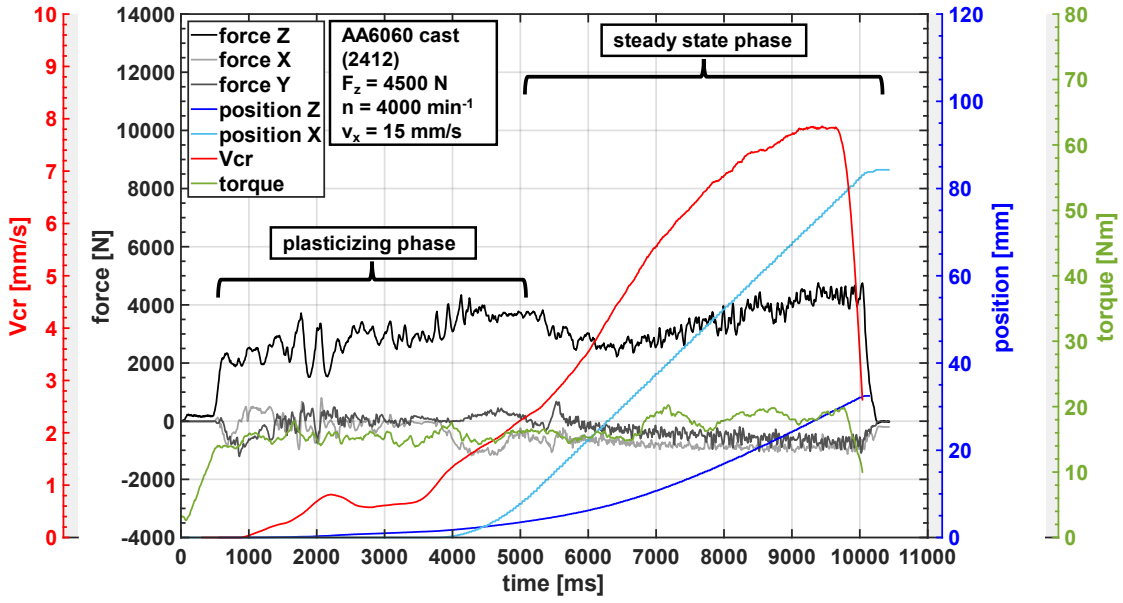

Figure 17: FS process diagram, including reaction forces in Z, X & Y directions; positions Z & X; the torque and the consumption rate v_{cr} integrating the two process stages plasticizing and stationary phase. Example welding of Al alloy AA6060 cast with the process parameters: F_z = 4500 N; n = 400 min^{-1}; v_x= 15 mm/s.

v_{CR} reaches its maximum in the steady state phase. In Figure 17, the gray and black lines respectively indicate the force curves, whereby black reflects the reaction forces in the Z direction, light gray the reaction forces in the X direction, and dark gray the reaction forces in the Y direction. Due to the highly dynamic processing conditions and the limited system stiffness, fluctuations occur within the reaction force curves. The green line describes the torque, which is also impacted on by dynamics. A stable torque is desired because it ensures to a high process stability. The light blue line describes the lateral position in X direction and the blue line the bolt position in axial Z direction. Stable process parameter windows were elaborated for the custom-made alloys by trial and error on the HLR-RAS (H. Loitz Robotik, Hamburg, Germany) in force control mode.

In this study, deposits for the customized alloys AA6060 cast, 2wt.% Mg, 3.5wt.% Mg, 6.6wt.% Si, 10.4wt.% Si, 14.6wt.% Si are first produced with a single set of process parameters, resulting in varying coating geometries. Subsequently, depositions were produced by means of varying parameters, adjusted as to achieve similar coating geometries for all alloys. The aim was to achieve homogeneous, defect-free coating widths of approximately stud diameter (20 mm) and coating thicknesses of several mm with high deposition efficiency. The investigations of the process and the coating properties were carried out focusing on steady-state material flow. For this purpose, the reaction moments and forces were first compared with the geometrically deposited coating in the steady-state region and examined for possible significant fluctuations. The two stable sets of process parameters developed are listed in Table 8. The addition of 2 and 3.5 wt.% Mg leads to a decrease in thickness while the process parameters remain the same. The thickness of the starting alloy AA6060 is reduced from 3.7 ± 0.34 mm to 1.1 ± 0.15 mm at 2 wt.% Mg and to 0.7 ± 0.13 mm at 3.5 wt.% Mg. This effect is more pronounced at higher Mg contents. The presence of Si also leads to smaller coating dimensions, which saturate or slightly increase again with increasing Si content. The addition of 6.6, 10.4 and 14.6 wt.% Si leads to a decrease in thickness to 1.2 ± 0.14 mm at 6.6 wt.% Si, to 1.4 ± 0.1 mm at 10.4 wt.% Si and to 1.5 ± 0.21 mm at 14.6 wt.% Si content while the process parameters remain identical. Still, the difference between 6.6 till 14.6% Si is not as pronounced as in the case of Mg.

Table 8: Suitable process parameters: identical parameters for all alloys resulting in dissimilar coating cross sections & adjusted parameters resulting in similar coating cross sections.

Material	Translational speed [mm/s]	Rotational speed [1/min]	Force [kN]	Coating cross section [mm²]
identical parameters, dissimilar coating cross sections				
AA6060-T6 wrought	15	4000	4.5	73.08
AA6060/cast	15	4000	4.5	71.04
2wt.% Mg	15	4000	4.5	19.44
3.5wt.% Mg	15	4000	4.5	7.32
6.6wt.% Si	15	4000	4.5	16.48
10.4wt.% Si	15	4000	4.5	19.41
14.6wt.% Si	15	4000	4.5	20.33
adjusted parameters, similar coating cross sections				
2wt.% Mg	12	1500	11	70.10
3.5wt.% Mg	8	1000	11	68.74
6.6wt.% Si	12	1800	9	76.98
10.4wt.% Si	12	1600	9	76.89
14.6wt.% Si	14	1500	9	77.17

For all alloys it was possible to generate coatings of similar thickness and width related to the original AA6060 alloy. As shown above in Table 8, it was necessary to adjust the process parameters. For both groups of alloys, the axial forces had to be increased, i.e., for Mg-addition to 11 kN and for Si-addition to 9 kN, in order to ensure a homogeneous material deposition. With a stable process control, the translatory movement can be used to control the thickness and width of the coating within a specific range. Generally, as the translational speed decreases, the width and thickness of the layer increase. Here, v_x had to be reduced from initially 15 mm/s to 12 mm/s for 2% Mg, and to 8 mm/s for 3.5% Mg. Regarding the translational speed, a small upward trend can be observed for the Si-alloys. For 6.6 and 10.4% Si, a v_x of 12 mm/s proved to be suitable, for 14.6% Si the v_x was increased to 14 mm/s. The most significant adjustments in process parameters were made with regard to rotational speed. An increase in the Si content requires a reduction in the rotational speed (6.6% Si: 1800 min^{-1}, 10.4% Si: 1600 min^{-1} and 14.6% Si: 1500 min^{-1}). For the Mg-alloys, this trend is more pronounced. This results in a rotational speed of 1500 min^{-1} for 2% Mg and a speed of 1000 min^{-1} for 3.5% Mg.

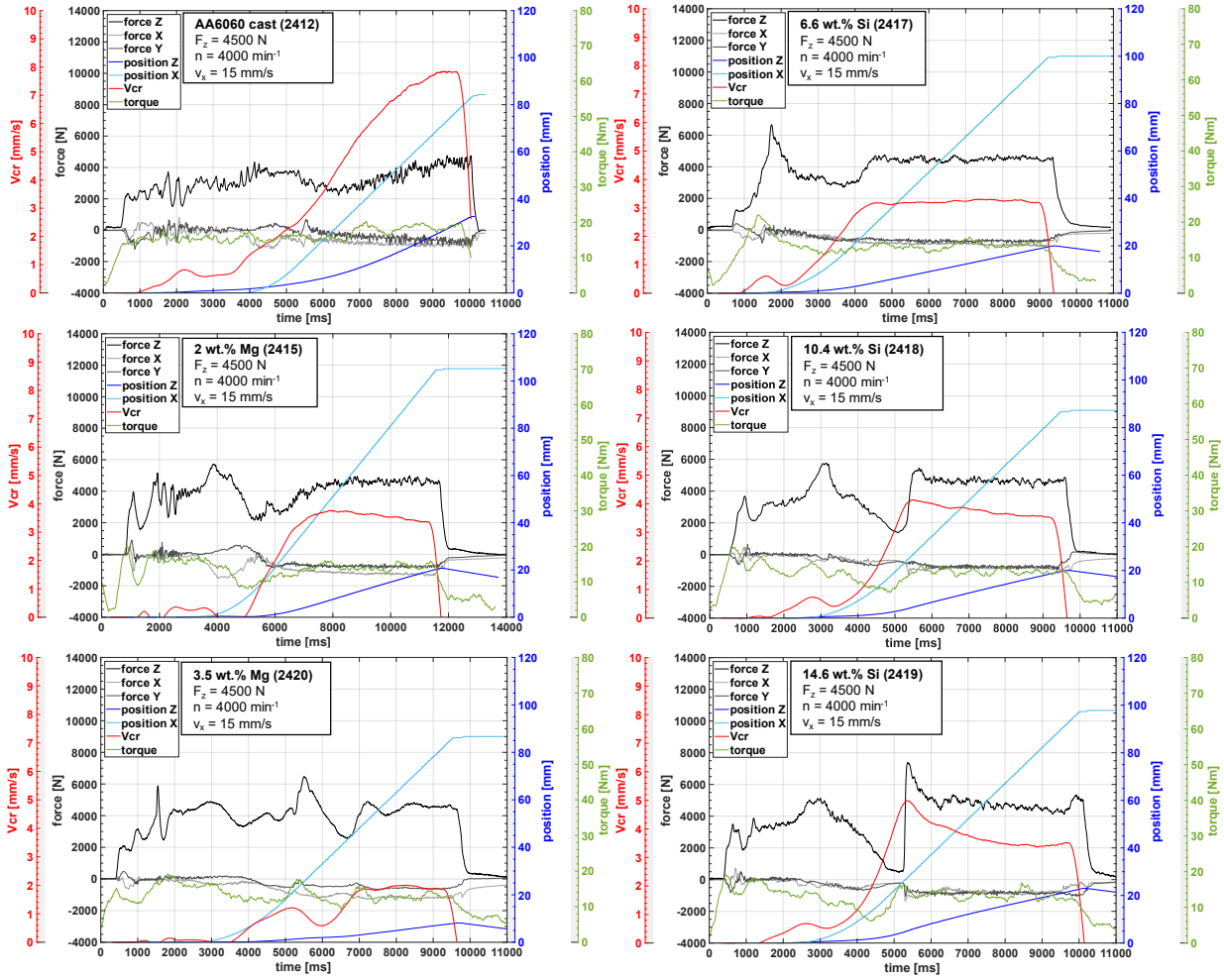

Figure 18: FS process diagrams of the customized Al-Mg-Si alloys applying identical parameters resulting in dissimilar coating cross sections.

Figure 18 shows the process diagrams of the investigated Al-Mg-Si alloys using identical process parameters of F_z = 4500 N; n = 4000 min^{-1}, and v_x = 15 mm/s. The following values focus on the steady-state area of the curves. Due to the low flexural strength of Al-Mg-Si alloys, the bending stiffnesses are insufficient. The length of the studs is related to the length of the lever arm and thus to the amount of bending moment that occurs. The smaller the lever arm, the lower the bending moment in both lateral directions X & Y. This enables a stable and homogeneous coating deposition. At the same time, less material is available for coating deposition. The lateral forces in the X and Y directions thus result from the initial stud length, which in turn influence the stiffness in the clamped stud during the process. These vary for the alloys processed in a range of -1267 N to -806 N in the X-direction and from -849 N to -599 N in Y-direction. The torque also stabilizes in the steady-state welding range for all alloys and lies in the range of 12.7 Nm to 18.6 Nm. With regard to the consumption rate v_{CR}, significant differences can be observed between the alloys used. With increasing Mg content, the average v_{CR} decreases from 7.8 mm/s for the initial alloy (AA6060 cast with 0.27 wt.% Mg) to a value of 1.9 mm/s for the alloy with 3.5 wt.% Mg, and thus a correspondingly lower amount of material from the stud is deposited as coating layer, and more material passes into the flash. With a less pronounced trend, a similar behavior

can be observed for the alloys with high Si content; the average v_{CR} for the alloy with 14.6 wt.% Si is 3.4 mm/s. The blue curves represent the positions in Z direction. v_{CR} is derived from the slope of the blue curves in the steady state region. With increasing Mg and Si content, the slope of the Z-position curve and thus also v_{CR} are reduced.

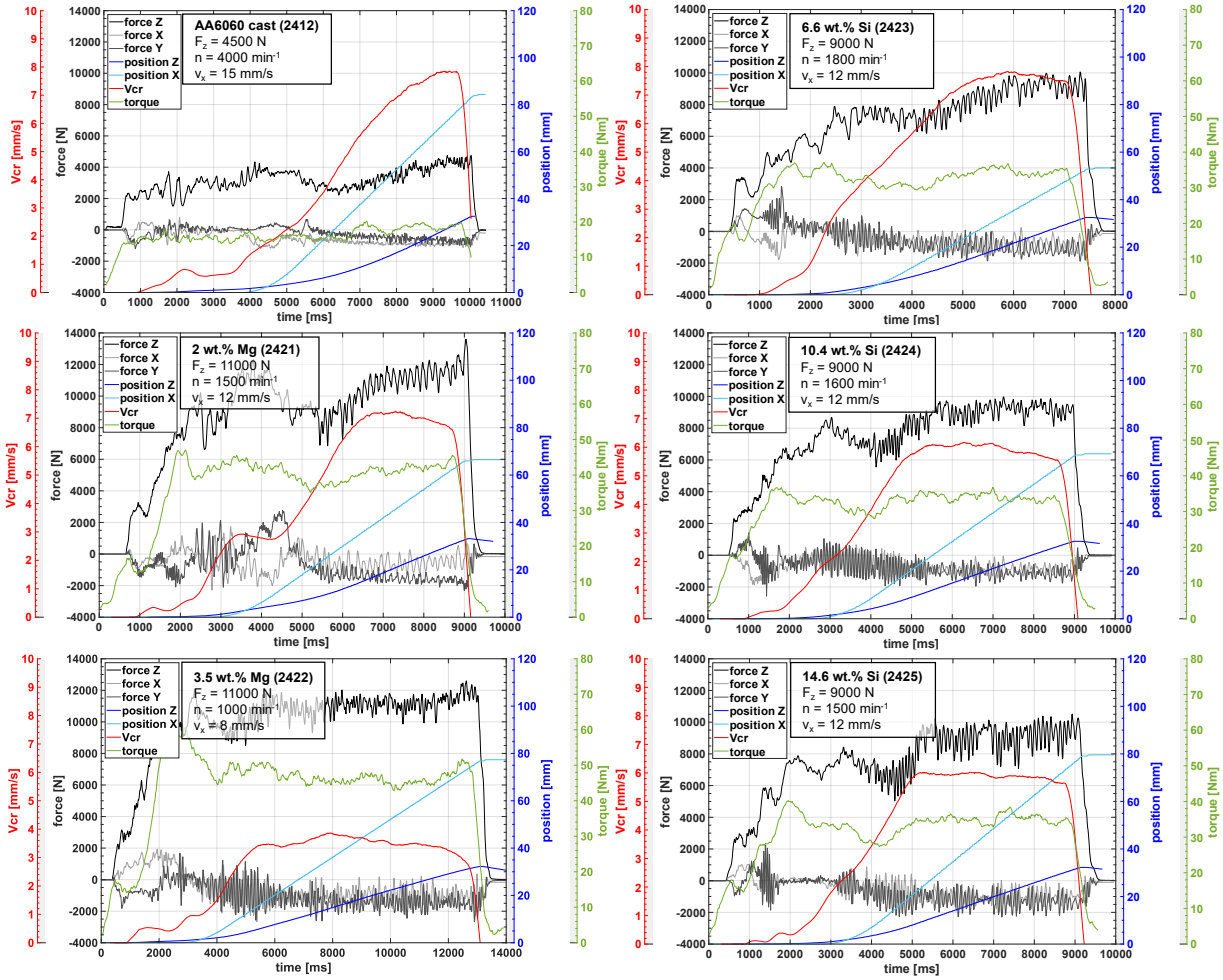

Figure 19: FS process diagrams of the customized Al-Mg-Si alloys applying adjusted parameters resulting in similar coating cross sections.

Figure 19 displays the process diagrams of the investigated Al-Mg-Si alloys deposited using adjusted parameters. Processing using adjusted parameters result in similar coating geometries in terms of coating width and thickness. The total length of the deposited coatings varies among the alloys, something which is quantified by the light blue position X curves. Despite the higher required axial forces of 11 kN for the Mg-rich and of 9 kN for the Si-rich alloys, the average shear forces during steady-state processing, being -1008 N to -869 N in the X-direction, are in a comparable range to those of lower axial forces (4.5 kN) previously applied. The average shear forces in the Y-direction show generally higher values of -1626 N to -618 N compared to those measured when applying the identical parameter set (Figure 18). However, higher oscillations are observed in the Z, X & Y force records in the plots in Figure 19. This observation may be due to non-ideal control parameter settings of the machine for the higher target forces in these depositions. Furthermore, higher average torques are the result, in the range of 42-44 Nm

for the Mg-rich alloys and around 34 Nm for the Si-rich alloys, compared to only 18.6 Nm for the initial AA6060. The average consumption rate v_{CR} for the alloy with 2 wt.% Mg is 6.8 mm/s. For the 3.5 wt.% Mg alloy, a slightly lower v_{CR} of 3.3 mm/s is obtained. Due to the lower translational feed rate of 8 mm/s (instead of 12 mm/s for the 2 wt.% Mg alloy), a comparable coating geometry is nevertheless obtained. Considered independently, the v_{CR} is not a sufficient indicator for the resulting cross-sectional dimensions of the coating. The average v_{CR} for the alloy with 6.6 wt.% Si is 7.8 mm/s, for that with 10.4 wt.% Si it is 5.9 mm/s, and for that with 14.6 wt.% Si it is 5.7 mm/s. From these values, no conclusive correlation between the alloying elements Mg or Si and the consumption rate v_{CR} can be determined.

The alloys with 6-12 wt.% Mg were processed on the Maho 700 universal milling machine (Pfronten, Germany), which is not equipped with adequate sensor technology. Only approximate process parameters can be given here, which are listed in Table 9. Therefore, shear forces in Z, X and Y directions, positions in Z and X directions, torque and consumption rates were not recorded. For these alloys, the focus is on the resulting coating microstructure.

Table 9: Suitable process parameters resulting in similar coating cross sections. The axial forces are estimated as described in section 4.3.

Material	Translational speed [mm/s]	Rotational speed [1/min]	Force [kN]
adjusted parameters, similar coating cross sections			
AA6060 cast	15	4000	4.5
6.4 wt.% Mg	5.25	800	approx. 6
8.9 wt.% Mg	5.25	800	approx. 6
10.6 wt.% Mg	3.3	800	approx. 6
12.1 wt.% Mg	2.7	800	approx. 6

5.1.1 Deposit characteristics & coating geometry

The following graphs in Figure 20 show the cross-sectional area of the deposits, the specific energy input, and the deposition efficiency as a function of the Mg or Si content as well as the process parameter set used. In the case of "adjusted parameters", these are the process parameters individually adjusted for each alloy as shown in the lower section of Table 8. In the case of "identical parameters", these are the unchanged parameter set listed in the upper section of Table 8.

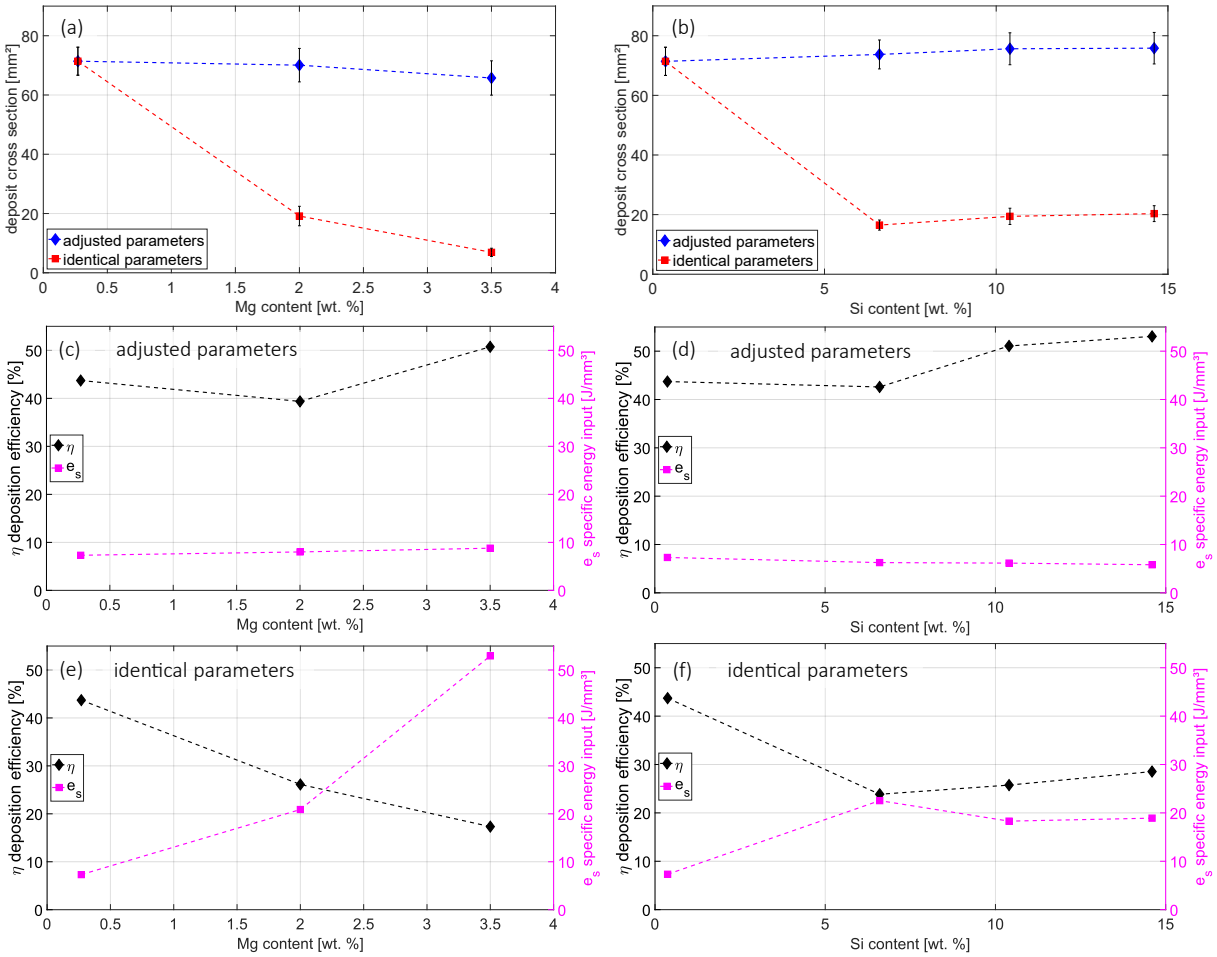

Figure 20: (a) & (b): Cross sectional area of deposited coatings for different Mg & Si contents obtained under identical process parameters (red squares) and using adjusted parameters (blue rhomboids). (c), (d), (e) & (f): Deposition efficiency η (blue rhomboids) and specific energy input per volume unit e_s (red squares) for different Mg & Si contents using identical parameters & adjusted parameters.

Figure 20 (a) & (b) depict the coating dimensions, starting from as-cast AA6060, as a function of Mg and Si content. Obviously, the addition of Mg to AA6060 at identical process parameters (F_z = 4.5 kN, v_x = 15 mm/s and n = 4000 min^{-1}) leads to a significant decrease in the amount of deposited material. An increase to 2 wt.% Mg leads to a reduction of the deposited material by ≈ 74 %, a further increase to 3.5 wt.% Mg even to a reduction of approx. 90 %; this can also be observed in the coating cross sections in Figure 22. The presence of Si also leads to smaller coating dimensions, which, however, do not decrease further with increasing Si content. Thus, 6.6 to 14.6 wt.% Si results in a reduction of the deposited material by about 73 to 76%.

Figure 20 (c), (d), (e) & (f) demonstrate the deposition efficiency η (blue rhomboids) and specific energy input per unit volume e_s (red squares) for different Mg and Si contents using identical and adjusted parameters. Deposition efficiency and specific energy input per unit volume show opposite trends. Thus, coatings with smaller dimensions produced with identical parameters result in lower efficiencies and higher energy input per deposited volume. For the coatings with larger volumes, higher efficiencies and lower energies per deposited volume are the result. The efficiencies for adjusted parameters are in the

range of 40-53% across all Mg-rich and Si-rich alloys, respectively, and the energies are in the range of 5.8-8.8 J/mm^3. With both increasing Mg content and Si content, the deposition efficiency for adjusted parameters increases slightly. Starting from the initial alloy (AA6060), η increases from 43% to 50% for the Mg-rich alloys and from 43% to 53% for the Si-rich alloys. The efficiencies with identical parameters decrease with the increasing Mg content to a value of 17%, and, simultaneously, increase in terms of the specific energy required per unit volume to 53 J/mm^3. For the Si-rich alloys using identical process parameters, efficiencies lie in a range of 24-28%, and specific energies per unit volume of 18-22 J/mm^3 are obtained. The efficiencies and energies of the coatings processed with both identical and adjusted parameters correlate with the corresponding coating geometries.

The coatings with different contents of the alloying elements Mg and Si are shown in Figure 21 from the top view. As described in chapter 5.1, Processing behavior & coating dimensions, process parameters were elaborated which led to a steady-state material deposition. The deposition direction of all coatings shown here is from left to right. In the coatings AA6060 cast and 2 wt.% Mg, an inhomogeneous material deposition can be observed in the plasticizing phase. The coatings produced with identical parameters also reveal defects and inhomogeneities in the plasticizing and transition regime. The focus of this study lies on the steady-state region, where the investigated samples exhibit stable behavior. This is the case for all coatings shown here. Based on the scale, which is the same for all images, it can be seen that the coatings produced with adjusted parameters give similar widths, whereas the width of the coatings produced using identical parameters is lower. The deposited coating length varies between the alloys. The reasons for this are the different stud lengths used, the varying consumption rates and other external conditions, e.g. a limitation of the substrate plate availability.

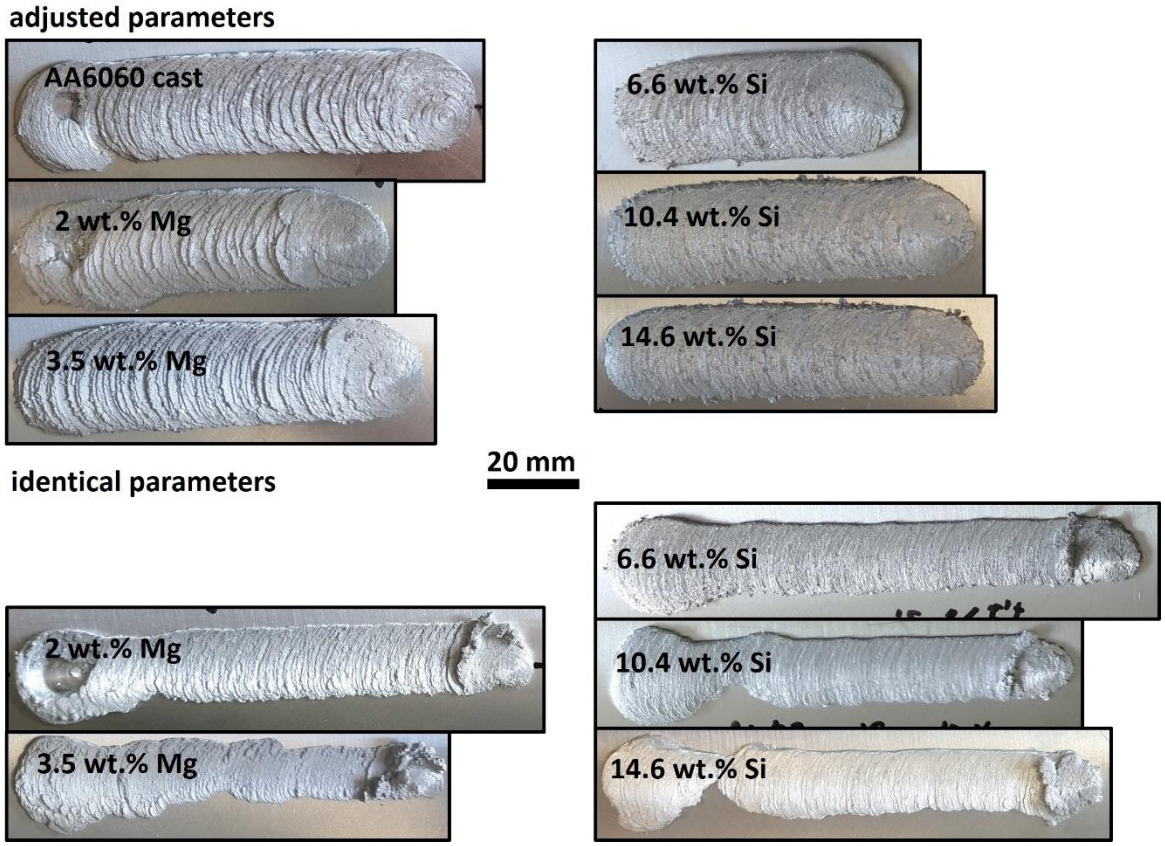

Figure 21: Top view of FS deposits produced using adjusted parameters (top section) and identical parameters (bottom section). All illustrations are scaled uniformly.

The determined cross-sectional areas have already been presented in the graphs in Figure 20 (a) & (b). Figure 22 displays light-optical micrographs (all at the same magnification) of cross sections through deposited FS coatings for the Mg- and Si-containing alloys, which were generated with both adjusted and identical parameters. Images were obtained from prepared cross-sectional samples anodized in Barker reagent and recorded using crossed polarized light and a sensitive tint filter. The coatings were extracted according to Figure 14 and are oriented in a way that the RS are on the left and the AS on the right. From these micrographs, the significant influences of Mg and Si to AA6060 at the same process parameters are evident. The addition of Mg leads to a significant decrease in the deposited coating geometry (compare Figure 22 (a) with (d) and (e)). The addition of Si also has the effect of clearly reducing the resulting coating width and height (compare Figure 22 (a) with (i), (j) and (k)). The use of adjusted process parameters obviously leads to adequate similarities in the coating geometry for the alloy with both Mg and Si addition (compare Figure 22 (a) with (b), (c) and with (f), (g), (h)). Nevertheless, it is observed that locally the cross-sectional areas of the coatings slightly vary especially in their height, even in the steady-state region. Essentially, a slight tendency of increasing coating thicknesses can be observed from the RS side (left) towards the AS side (right).

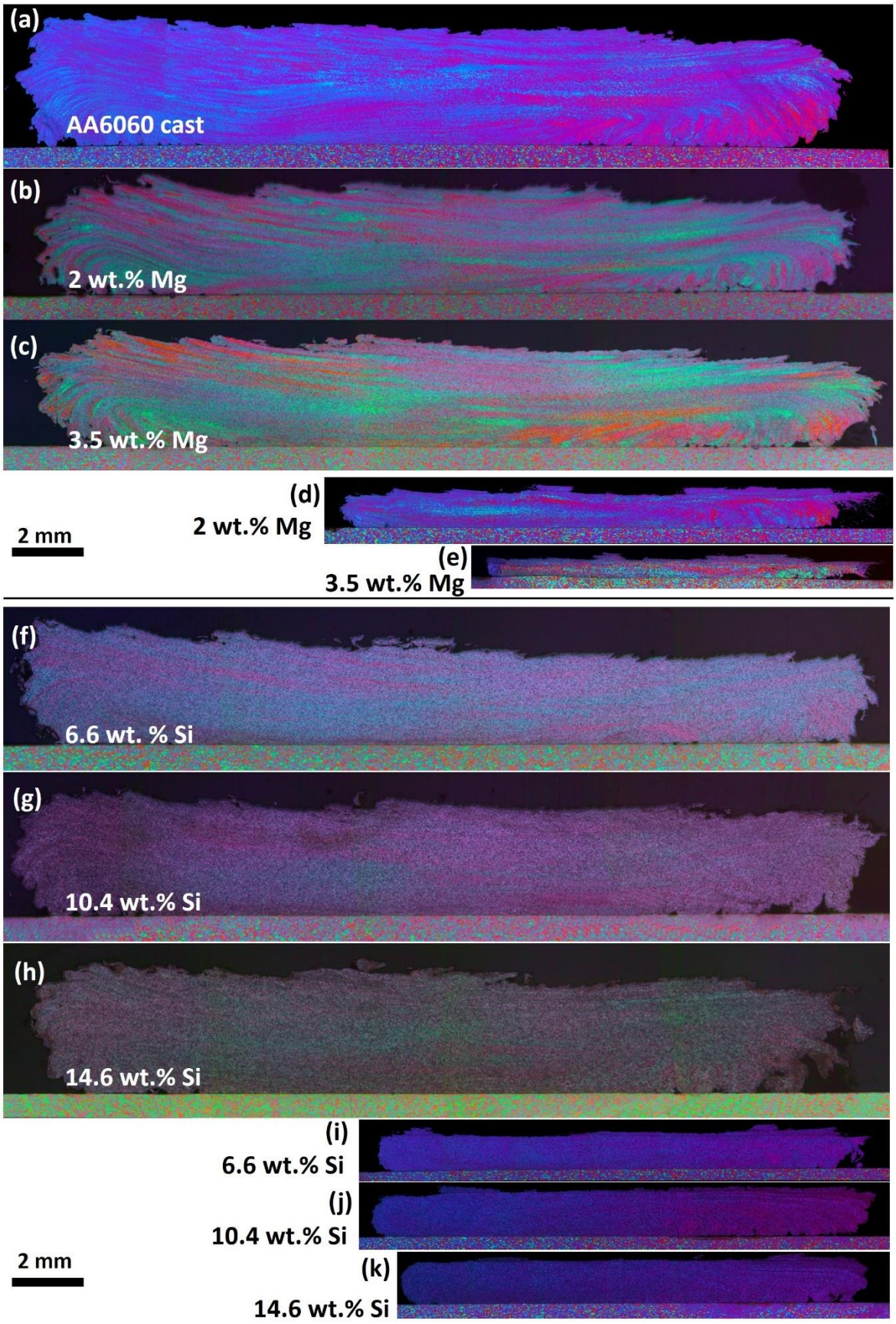

Figure 22: Light-optical micrographs of cross sections through deposited FS coatings: Adjusted parameters: cast (a), 2 wt.% Mg (b), 3.5 wt.% Mg (c), 6.6 wt.% Si (f), 10.4 wt.% Si (g), 14.6 wt.% Si (h). Identical parameters: cast (a), 2 wt.% Mg (d), 3.5 wt.% Mg (e), 6.6 wt.% Si (i), 10.4 wt.% Si (j), 14.6 wt.% Si (k). RS on the left side; AS on the right side.

Figure 23 illustrates that an offset of the stud forms in the direction of the RS of the deposit. The material in the deposit on the AS is thus not aligned under the rotating stud during deposition; instead, it is either next to it or below the flash. Therefore, this area does not experience the entire axial force and tilts a little upwards at the outermost AS edge of the coating. The RS of the coating is below the rotating stud during FS in the plane close to the stud's radius. Gandra et al. [115] show similar behavior for AA6082 over AA2024 and Sakihama et al. for AA5052 over AA5052 [116].

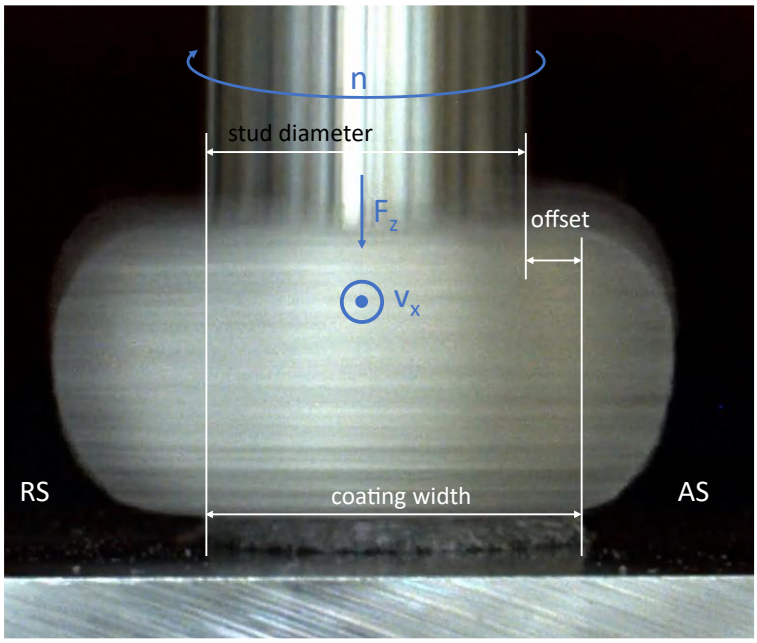

Figure 23: Photograph of running process with line of view parallel to the deposition direction (x-axis). Coating deposition occurs at an offset towards the advancing side.

5.1.2 Estimation of strain rates

On the solid-state joining process Friction Stir Welding (FSW), several approaches for determining the shear strain rates within the stir zone have been published. Morisada et al. [117] used tracer material to calculate the strain rates during FSW and measured the material flow rate. Morishige et al. [118] and Chang et al. [119] used a simplified model to estimate the shear strain rates within the stir zone during FSW. This simplified model for FSW was modified and was applied to the process FS. The model for estimating the shear strain rates for FS during deposition is derived from the time-dependent shear strain

$$\varepsilon(t) = \frac{\varphi(t)\, r_c}{d_{eff}} \tag{18}$$

where d_{eff} denotes the coating thickness, $\varphi(t)$ is the time dependent angle of rotation, and r_c is the corrected radius according to Fukakusa [11]. The shear strain rate results in

$$\dot{\varepsilon} = \dot{\varphi}\, \frac{r_c}{d_{eff}} = \frac{2\pi\, n\, r_c}{d_{eff}} \tag{19}$$

where n is rotational speed. The equation for the estimated shear strain rate adapted from Chang et al. [119] reads nearly identically:

$$\dot{\varepsilon}_{eff} = \frac{2\pi \ n_{mf} \ r_c}{d_{eff}} \tag{20}$$

where n_{mf} is the average material flow rate. For the FS process it can be assumed that the average speed of material flow from the rotational movement within the volume of the plasticized shear zone is lower than the stud rotational speed. For reasons of simplification in an attempt to estimate strain rates, the average material flow rate n_{mf} is assumed to be half the stud rotational speed n in this study. A comparable assumption is made for the calculations in [119] for FSW.

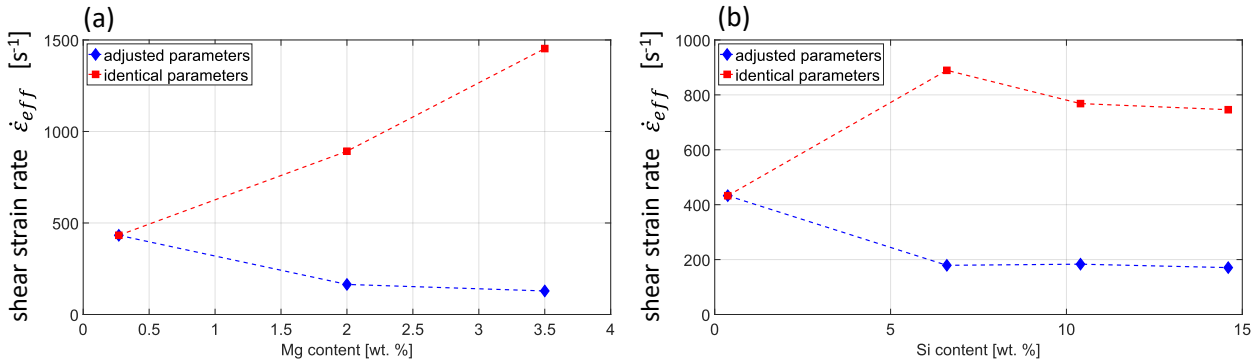

Figure 24: Estimated shear strain rate during FS calculated for different Mg (a) and Si (b) contents using the identical (red squares) and adjusted (blue rhomboids) process parameters.

Figure 24 illustrates the calculated shear strain rates for the FS deposits in this study. According to the applied model, the shear strain rate depends linearly on the rotational speed and inversely on the deposited thickness. For the thin coatings resulting from applying identical process parameters with increasing Mg content, very high effective shear strain rates of 892 s^{-1} at 2 wt.% Mg and 1453 s^{-1} for the 3.5 wt.% Mg alloy are obtained by this method. In contrast, the shear strain rates decrease for the adjusted parameters to obtain thicker coatings from 433 s^{-1} for 0.27 wt.% Mg down to 129 s^{-1} for 3.5 wt.% Mg. The effective shear strain rates for coating deposition using identical parameters is 890 s^{-1} for the alloy with 6.6 wt.% Si, 768 s^{-1} for 10.4 wt.% Si, and 745 $s^{-1}$for 14.6 wt.% Si. The effective shear strain rates with adjusted parameters are in the range of 170-183 s^{-1} for the Si-rich alloys. Due to the higher average material flow rate and the smaller effective deformed material volume, which yield the lower coating thicknesses resulting from using identical parameters, the effective shear strain rates for the Al-Mg and Al-Si alloys increase considerably compared to those generated using adjusted parameters.

5.2 Thermal cycle analysis & heat conductivity

Three thermocouples were positioned in the substrate material at a distance of 30 mm to each other along the x-axis and 0.5 mm underneath the substrate surface. The thermal cycle in this position during FS exhibits a distinct behavior with short exposure times to peak temperature, and high heating and cooling rates, something that is common for solid-state joining technologies. As the rotating stud moves just above the thermocouples, the temperature rises to its maximum values. Depending on the process parameters, especially the translational feed motion, this peak temperature dwells for a few seconds before the substrate and coating cool first rapidly and then gradually to room temperature according to Newton's law.

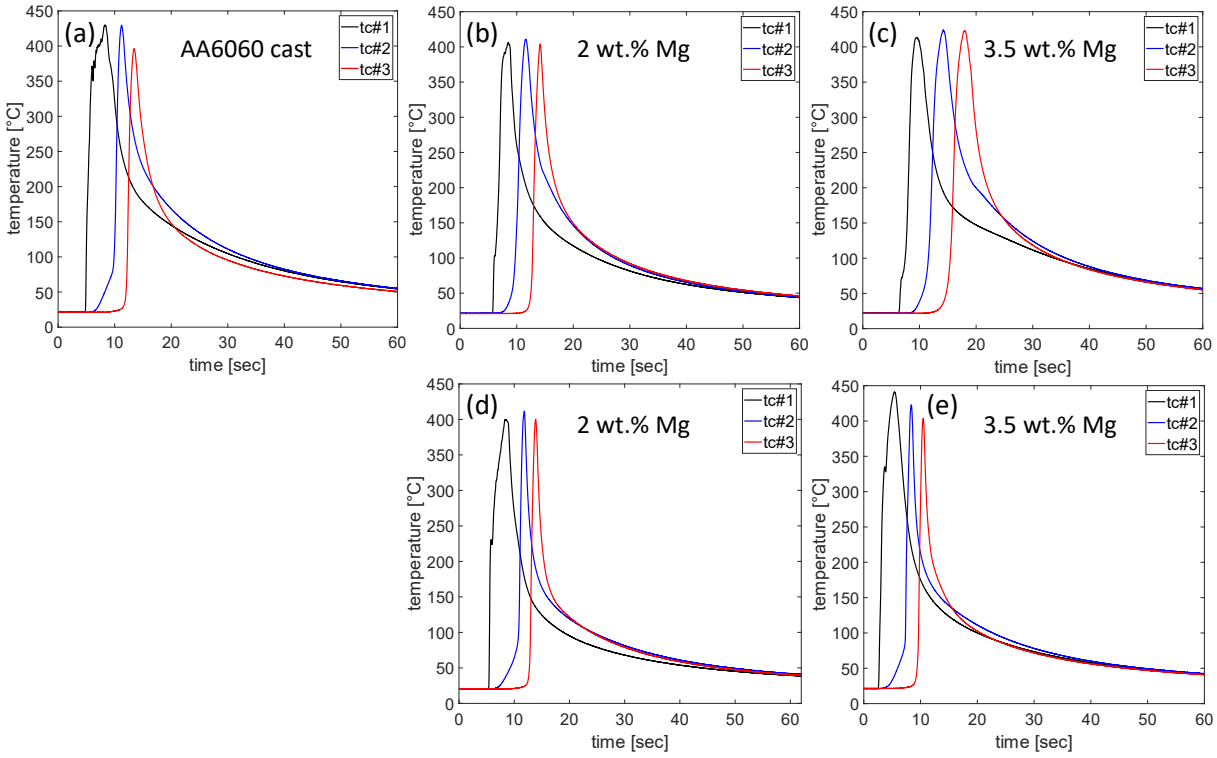

Figure 25: Temperature profiles during FS processing of Mg-rich alloys measured at 0.5 mm underneath the substrate surface. (a), (b) & (c): Adjusted parameters. (d) & (e): Identical parameters.

Figure 25 plots the temperature profiles versus process time for the Mg-containing alloys. The graphs in (a), (b) & (c) show the temperature profiles for FS using adjusted parameters, while (d) & (e) exhibit the temperature profiles for the produced coatings using identical parameters. Since the heating and cooling phases are not linear, heating rates and cooling rates were estimated qualitatively. Depending on the process parameters used, extreme heating rates of approx. 400 to 800 K/s and cooling rates of approx. -100 to -200 K/s can occur in the ranges before and after the peak temperature is reached. The highest heating and cooling rates result from the coatings produced with identical parameters due to the higher translation speed of 15 mm/s. For the same reason, the peak temperature dwell times are also lower for these than for the coatings generated with adjusted parameters.

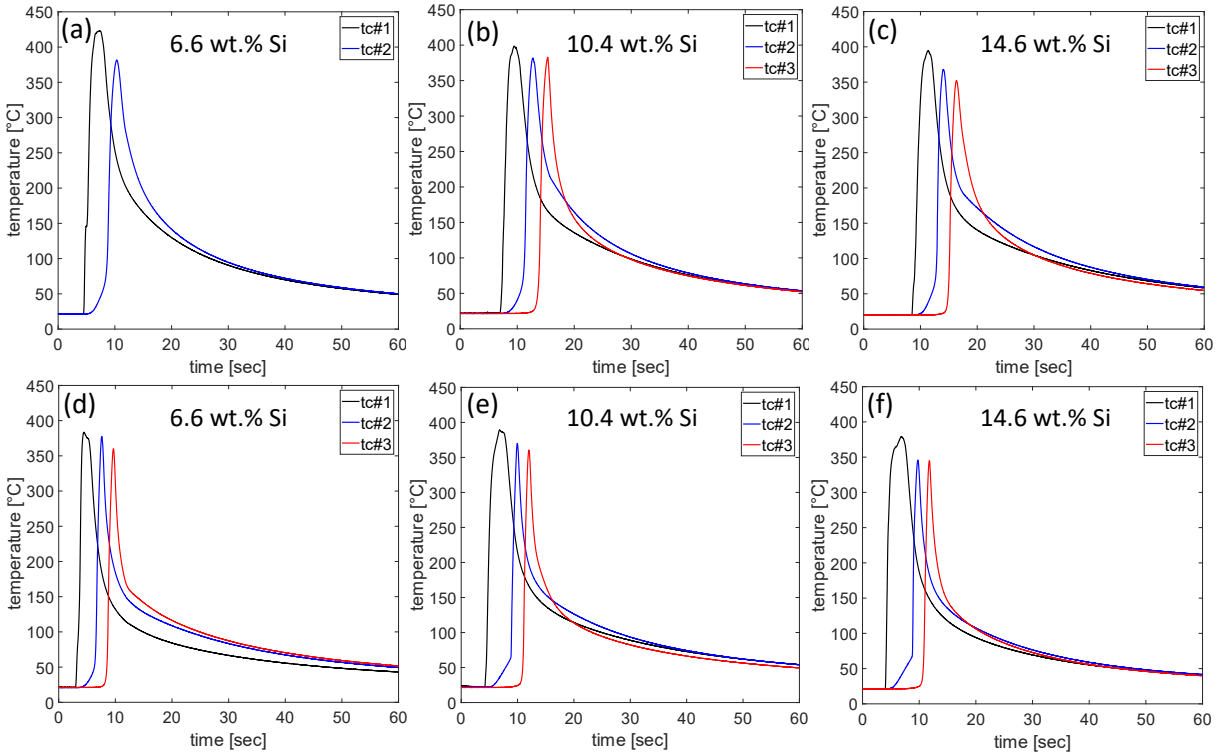

Figure 26: Temperature profiles during FS processing of Si-rich alloys measured at 0.5 mm underneath the substrate surface. (a), (b) & (c): Adjusted parameters. (d), (e) & (f): Identical parameters.

A similar behavior is observed for the Si-rich alloys (see Figure 26 & Figure 29). Apart from the maximum temperatures reached, the temperature curves behave similarly with respect to their heating and cooling rates. It appears that the Si-rich alloys produced by identical parameters (Figure 26 (d), (e) & (f)) (15 mm/s) show higher heating and cooling rates than those produced by adjusted parameters (Figure 26 (a), (b) & (c)). This behavior can be attributed to the increased translational feed rates of the coatings produced using identical parameters (15 mm/s). In addition, it is observed that the peak temperatures of the first thermocouples tc#1 exhibit the highest values in all measurements.

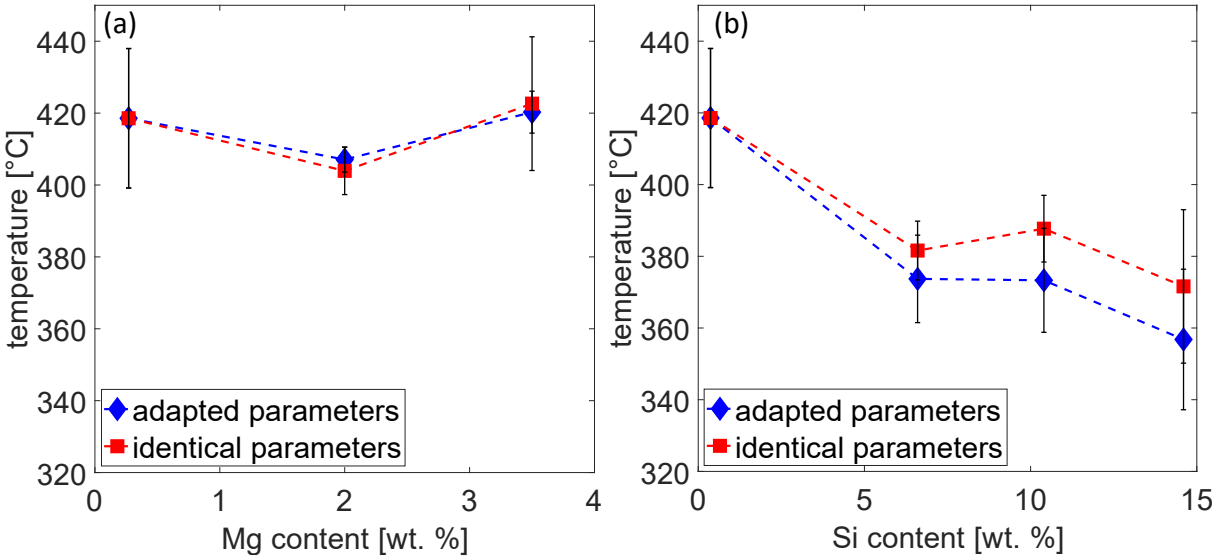

Figure 27: Average of maximum process temperature 0.5 mm underneath the substrate surface measured using three thermocouples type K.

The process peak temperatures obtained from the data shown in Figure 25 and Figure 26 are plotted in Figure 27 for the different Mg contents and Si contents. The maximum process temperatures of the Mg-rich alloys vary by about 15 °C between the different experiments; this is a small difference with respect to measurement scatter and could be due to variations in the positioning of the thermocouples. Regardless of the process parameters used, this study shows temperature saturation in the range of 400-420 °C. While no distinct correlations between the temperature evolution and the Mg content or the process parameters were found, patterns can be detected for the Si-containing alloys. Figure 27 (b) indicates that the maximum process temperatures of the Si-containing alloys are lower than those of both the initial AA6060 alloy and the alloys with Mg additions. Firstly, a slight downward trend in peak temperatures with increasing Si content can be observed. Thus, the peak temperatures for the 6.6 wt.% Si alloys are 374 °C (adjusted parameters) and 381 °C (identical parameters), and for the 14.6 wt.% Si alloy they are 357 °C (adjusted parameters) and 371 °C (identical parameters). Secondly, the alloys processed by means of adjusted parameters exhibit 8-14 K lower average maximum temperatures.

The results obtained with the infrared camera (Figure 28 & Figure 29) demonstrate that the highest temperatures occur at the interface or slip plane between the stud tip and the material already deposited below. Various measurement uncertainties can occur in the thermograms taken with the IR camera. Despite previous calibration reflection, surface roughness, oxide layers or measuring angle can affect the measured values. The temperature data are analyzed considering the resulting measurement uncertainties. The observed temperatures for the Mg-containing alloys are always in the range of 480-490 °C; this confirms that both the Mg content and the process parameters have only a minor or no influence on the process temperatures. For the high Mg content with adjusted process parameters (Figure 28 (e)), the low coating thickness prevents the clear observation of the shear zone. The maximum temperatures are higher, by about 30-40 °C, than the temperatures measured by the thermocouples under

the coatings. This is plausible since the shear volume within the stud tip seen in Figure 28, sliding on the already deposited material, is the heat source in the FS process.

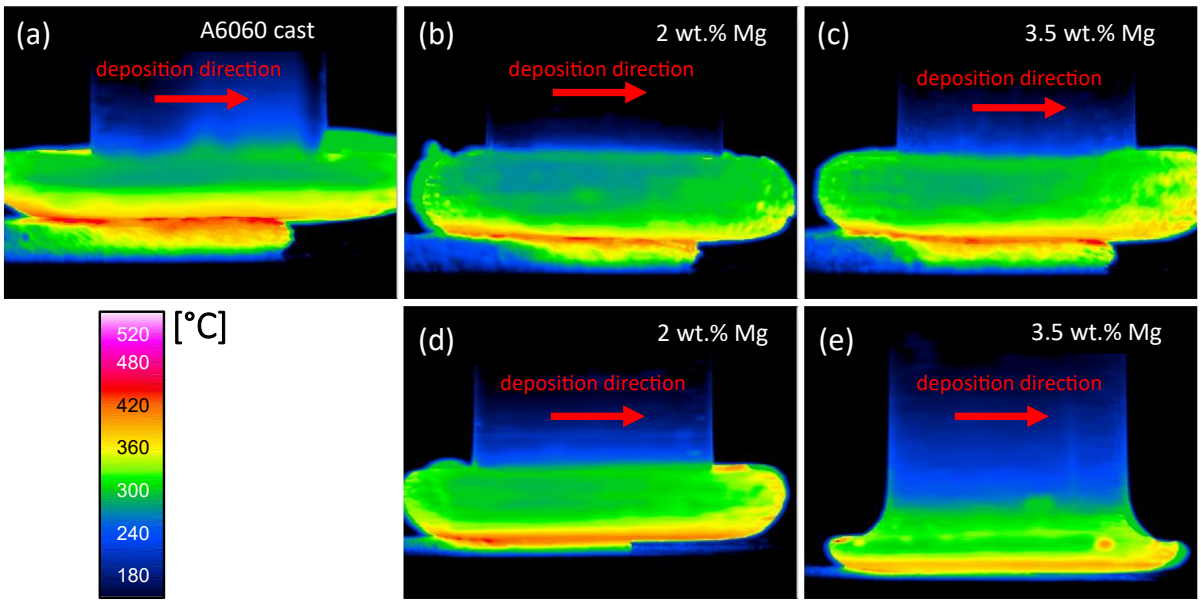

Figure 28: Thermograms showing the stud, the flash and the deposited material during the running FS process for different Mg contents. (a)-(c): Adapted process parameters; (d), (e): Identical process parameters as in (a).

The thermograms of the Si-containing alloys in Figure 29 indicate that the temperatures at adjusted parameters are slightly higher than at identical parameters; this finding opposes the trend observed in the thermocouple measurements. The welding temperatures are in the range of 460-470 °C. More heat is generated when processing the Mg-rich alloys than the Si-rich alloys, whether the parameters are kept constant or not. This behavior is reflected in both measurement methods, thermocouples (below the substrate) and thermograms (surface of the substrate, coating and stud).

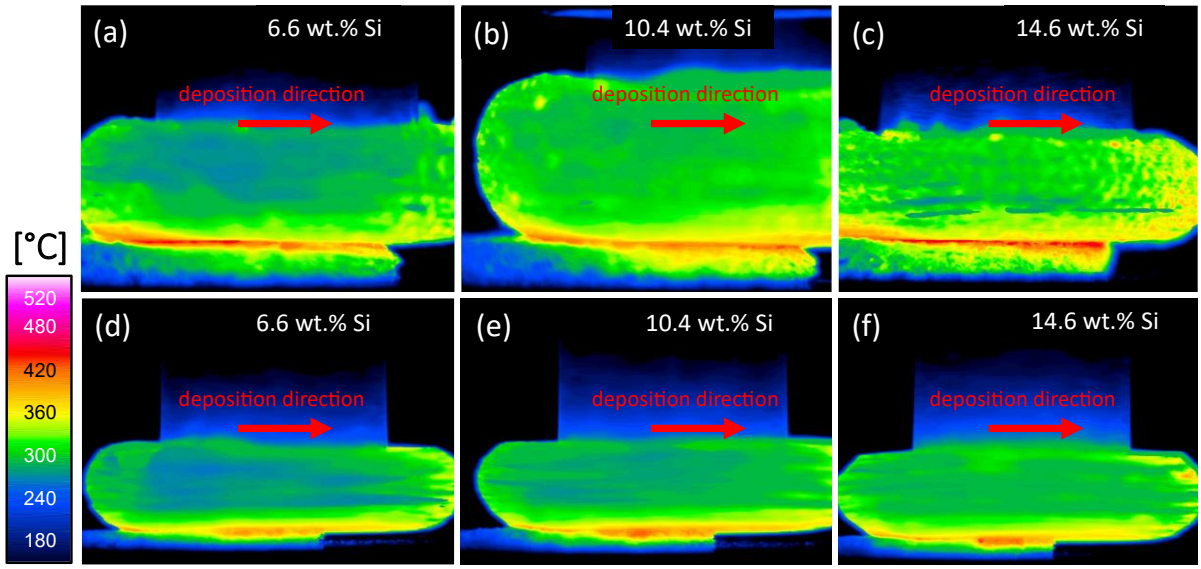

Figure 29: Thermograms showing the stud, the flash and the deposited material during the running FS process for different Si contents. (a)-(c): Adapted process parameters; (d)-(f): Identical process parameters as in (a).

In summary, it must be taken into account that many sources of uncertainties and influencing factors come into play, especially in temperature measurements. For this reason, significant correlations have to be elaborated.

Thermal conductivity describes how easily thermal energy is transferred through the material when there is a temperature difference between two locations. Materials with high thermal conductivity conduct heat quickly. Thermal conductivity is usually measured in units of watts per meter-Kelvin (W/(m·K)). Specific heat capacity is a measure of the amount of thermal energy required to raise the temperature of a unit mass of a material by one Kelvin. It describes how much energy is required to change the temperature of a material, with a high specific heat capacity indicating that the material requires more energy to change temperature. Specific heat capacity is measured in units of joules per kilogram Kelvin (J/(kg·K)). Thermal diffusivity, on the other hand, is a dimension of a material's ability to conduct heat over time. It describes how quickly a material can respond to a change in temperature, with a high thermal diffusivity indicating a fast response to temperature changes. Thermal diffusivity is calculated by dividing the material's thermal conductivity by its specific heat capacity and density, and it is usually measured in square meters per second (mm²/s).

For this purpose, a total of three alloys in the unprocessed as-cast state were used: AA6060 cast, 3.5 wt.% Mg & 10.4 wt.% Si. The results are given in Figure 30. In the graphs in Figure 30, heat conductivity and thermal diffusivity are plotted in blue on the left y-axis, and specific heat capacity is plotted in red on the right y-axis above the temperature on the abscissa. The temperature-dependent heat conductivity of the AA6060 alloy drops from ≈ 235 W/(m·K) at room temperature to approx. 214 W/(m·K) at 100 °C and rises to a plateau above 300 °C back to approx. 235 W/(m·K). The 10.4 wt.% Si alloy reveals similar characteristics, but at lower thermal conductivities from about 166 W/(m·K) at 100 °C to about 175 from 300 °C onwards. The heat capacity curve of the alloy with 3.5 wt.% Mg shows a slight continuous increase from ≈ 153 W/(m·K) at room temperature to about 176 W/(m·K) at 550 °C. The thermal diffusivity decreases slightly with increasing temperature for all three alloys. The calculated values are highest for the initial alloy AA6060 in a range of approx. 68-86 mm²/s. This is followed by the Si-rich alloy with a range of approx. 57-72 mm²/s and then the Mg-rich alloy with 54-60 mm²/s. The specific heat capacities increase for all alloys with increasing temperature. The highest values between the three materials compared here are obtained for the initial alloy from approx. 1 J/(g·K) at room temperature to approx. 1.3 J/(g·K) at 550 °C. Both alloys with Mg and Si additions display a similar trend with respect to the specific heat capacity, increasing from approx. 0.77 J/(g·K) at room temperature to approx. 0.9 J/(g·K) at 500 °C.

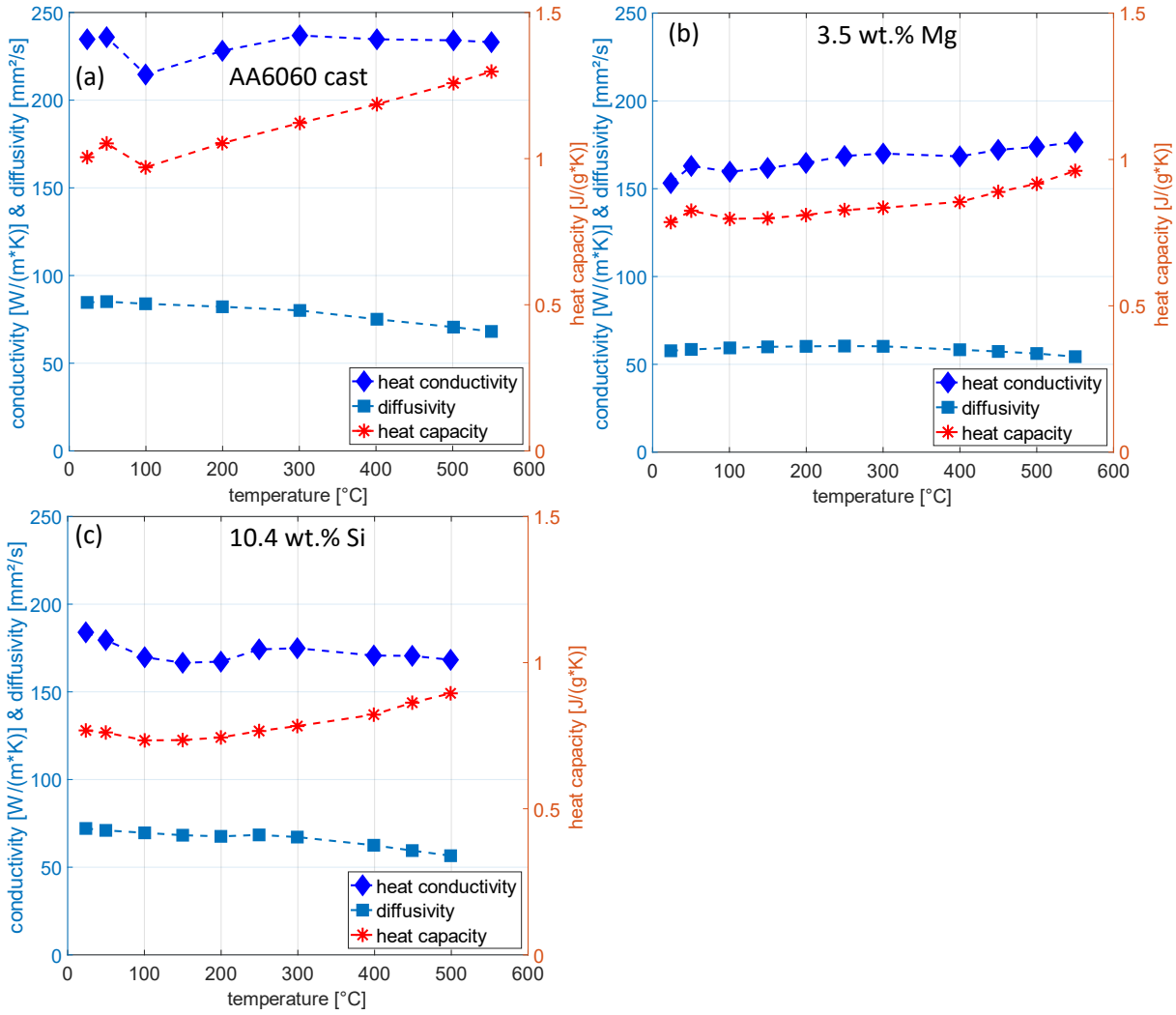

Figure 30: Temperature-dependent heat conductivity, thermal diffusivity & specific heat capacity for AA6060 cast (a), 3.5 wt.% Mg (b), and 10.4 wt.% Si (c).

The experiments demonstrate that additions of alloying elements Mg and Si in Al alloys change the temperature-dependent thermal material properties. The thermal conductivity of AA6060 is reduced by about 29% by 3.5 wt.% Mg addition and by about 27% by 10.4 wt.% Si addition. No significant differences were found between the Mg- and Si-containing alloys with regard to the thermal material properties. Factors influencing the thermal properties are, among others, the Mg/Si ratio as well as the Mg and Si excesses, which represent 3.31 wt.% for the Mg-containing alloy and 10.23 wt.% for the Si-containing alloy.

5.3 Microstructural analysis

In the following subsections, the results of the metallographic examinations are presented. For this purpose, samples of the cast material (base material) as well as the Friction Surfacing coating samples were extracted according to Figure 14 and prepared and analyzed according to the examination method as described in chapter 4, Materials and methods.

5.3.1 Particles in base & coating material

The factors determined are the percentage of particle volume fraction and the mean particle size in µm² on the surface of the section as a function of processing condition and Mg or Si content. The samples evaluated are the non-processed samples BMAA6060, BM2Mg, BM3.5Mg as well as BM6.6Si, BM10.4Si, BM14.6Si, and the processed samples FSAA6060, FS2Mg, FS3.5Mg as well as FS6.6Si, FS10.4Si, FS14.6Si. Furthermore, information on the arrangement, shape and quantity of the phases can be derived from the optical comparison. The following investigations were carried out on the FS coatings deposited using adjusted process parameters. From the optical images (Figure 31 & Figure 33), qualitative information about the shape, distribution and amount of the secondary phase particles can be derived.

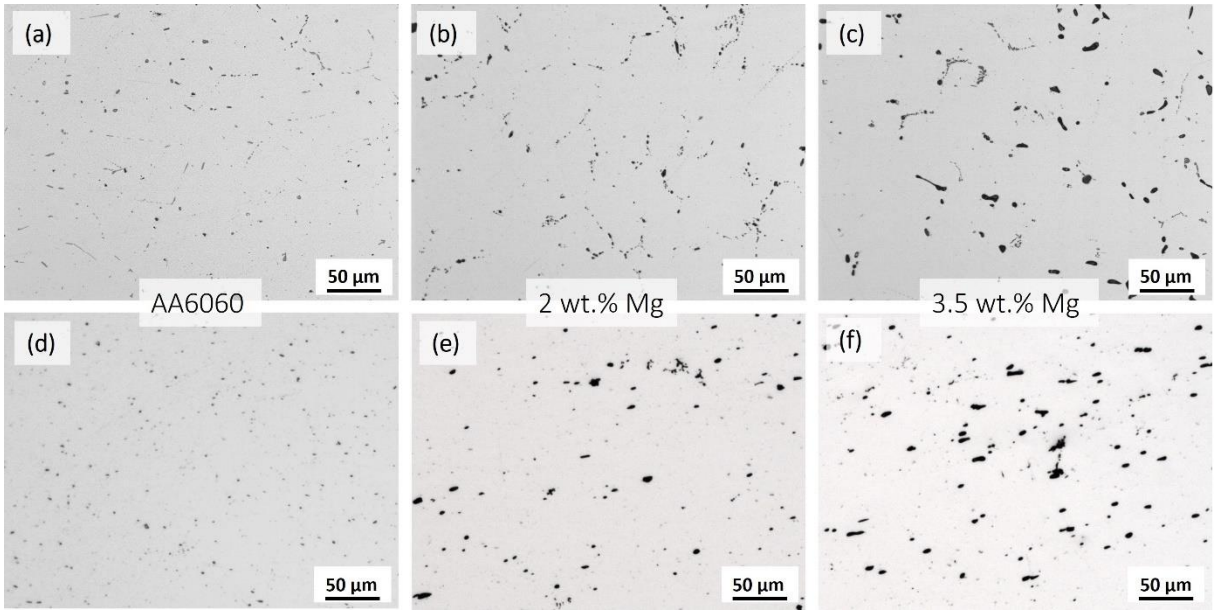

Figure 31: Light microscopic images showing the microstructures of the Al-Mg alloys. Base material (homogenized state): (a), (b), (c). FS coatings: (d), (e), (f).

Differences can be observed both between the material states and between the alloys investigated. The particle mean size and the number of phases which appear to be darker increase with increasing Mg content (see Figure 31). Due to differences in color intensity, it is difficult to estimate the absolute number of phases. Material defects (pores) can be detected primarily in the base material. Pores are observed in all base materials examined. In the homogenized state, a heterogeneous microstructure of the AA6060 cast alloy develops. This reveals major differences in the shape, size, color, and type of branching of the secondary particles visible in the microscope image. In the FS coatings, there is a more

homogeneous distribution of shape, size, and location of the particles. The quantitative image analysis of the microscope images is given in Figure 32. The base materials of the Mg-containing alloys generally have a higher proportion of secondary phases relative to the surface area than the corresponding processed FS variant (see Figure 31). The proportion of phases on the surface of the section increases with increasing Mg content. During FS, particles partially dissolve and change their morphology. However, the particle mean size is higher after the FS process for the alloys with Mg addition but remains almost the same for AA6060.

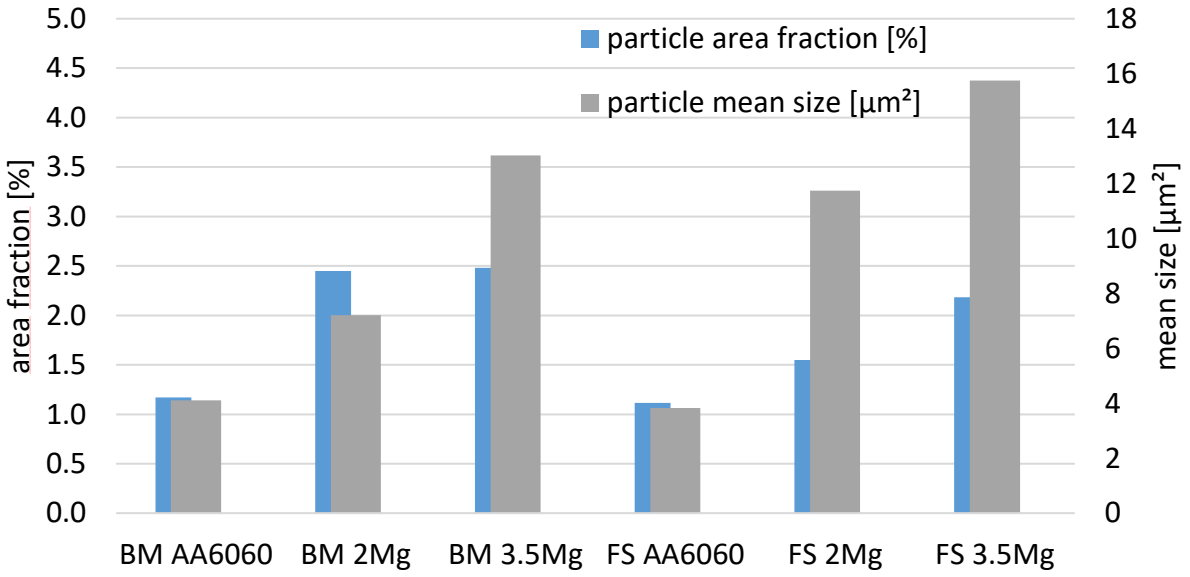

Figure 32: Area fraction in % of particles (blue) and average particle mean size in µm² (gray) of the different Mg-containing alloys in unprocessed base material (BM) & processed FS state.

The microstructure of the three processed Si-containing alloys in the base material state and after deposition as FS coatings is shown in Figure 33. In the cast and subsequently homogenized state of the base material, the Si particles are predominantly in needle-shaped form. Figure 33 (a) & (b) show the microstructure in the two hypoeutectic alloys (6.6 wt.% Si & 10.4 wt.% Si), while the hypereutectic alloy (14.6 wt.% Si) contains additional voluminous primary Si phase particles (Figure 33 (c)). The total volume fraction of Si particles changed within ±5% after the FS process (+1.86% for 6.6 wt.% Si, -2.65% for 10.4 wt.% Si, and -4.69 wt.% for 14.6 wt.% Si) and can be considered as not significantly changed (Figure 34). In addition, predominantly needle-shaped and oval Si particles have largely transformed into finely dispersed, almost spherical Si particles, while the larger primary Si particles in the hypereutectic alloy remain almost unchanged (Figure 33 (d) & (e)). Although the volume fractions differ only marginally in comparison before and after deposition, an increased number of smaller particles is observed from the optical analysis, which is supported by the decreasing particle mean size in Figure 34.

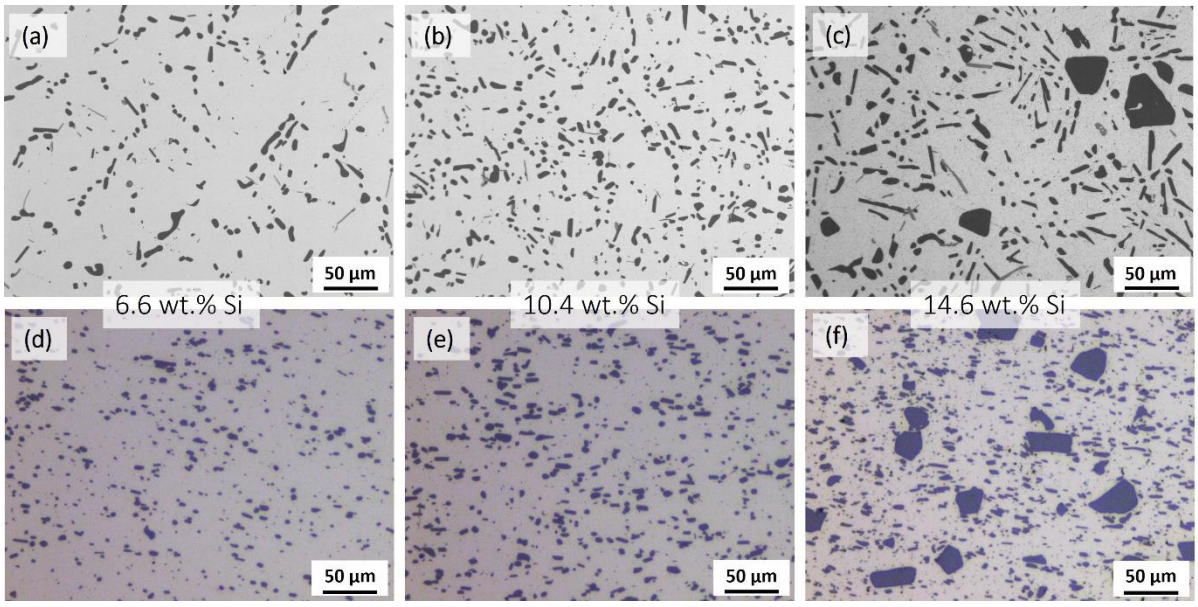

Figure 33 Light microscopic images showing the microstructure of Al alloys with increased Si content. Cast state base material: (a) 6.6 wt.% Si & (b) 10.4 wt.% Si, hypoeutectic; (c) 14.6 wt.% Si hypereutectic, Si needles, Si primary phase particles. FS coatings: (d) 6.6 wt.% Si & (e) 10.4 wt.% Si hypoeutectic, fine dispersed Si particles; (f) 14.6 wt.% Si hypereutectic, fine dispersed Si particles, Si primary phase particles.

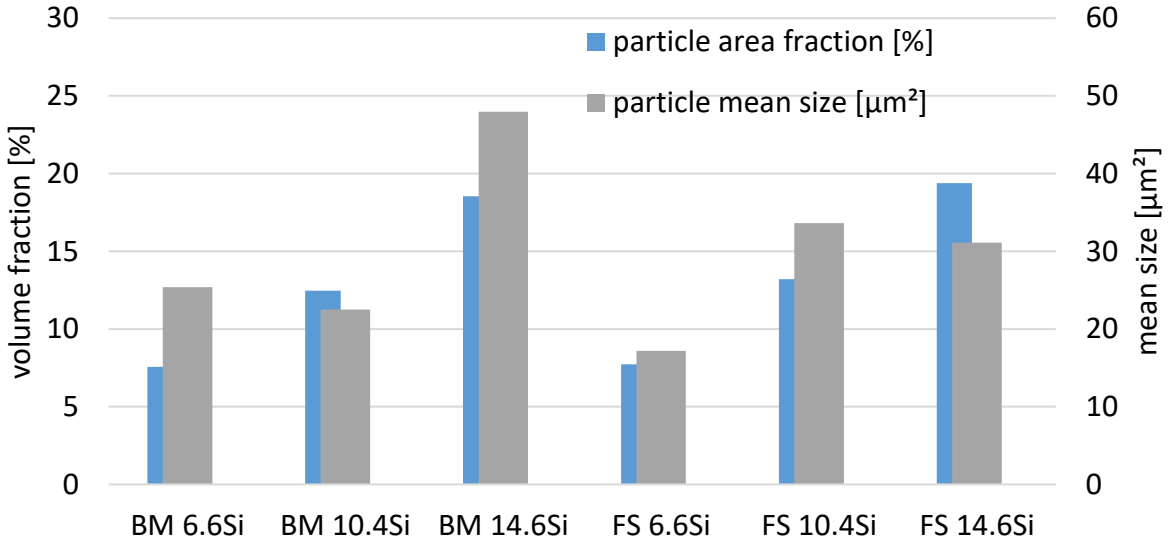

Figure 34: Area fraction in % of particles (blue) and average particle mean size in µm² (gray) of the different Si-containing alloys in unprocessed base material (BM) & processed FS state.

5.3.2 Recrystallization cycle & features of material flow

Figure 35 depicts a larger image section of the stop-action trial of the initial alloy AA6060. In the stop-action test, through controlled termination of the FS process, the stud is welded onto the coating and the substrate. From this, some characteristic microstructure zones can be determined, such as the shear-dominated and the compression-dominated parts of the thermo-mechanically affected zone (TMAZ), and the recrystallized areas within the coating and the area of the stud tip. To determine the microstructure zones, base material (BM), and heat-affected zone (HAZ), the polarized light microscope images are usually not sufficient. In this case, further investigations such as hardness measurements and

analysis of the precipitation distribution are required, which will be elaborated in later sections. Nevertheless, the BM & HAZ regions in both the stud material and AA2024 substrate have been labeled in Figure 35. The HAZ regions in the substrate were estimated and highlighted according to the study [120].

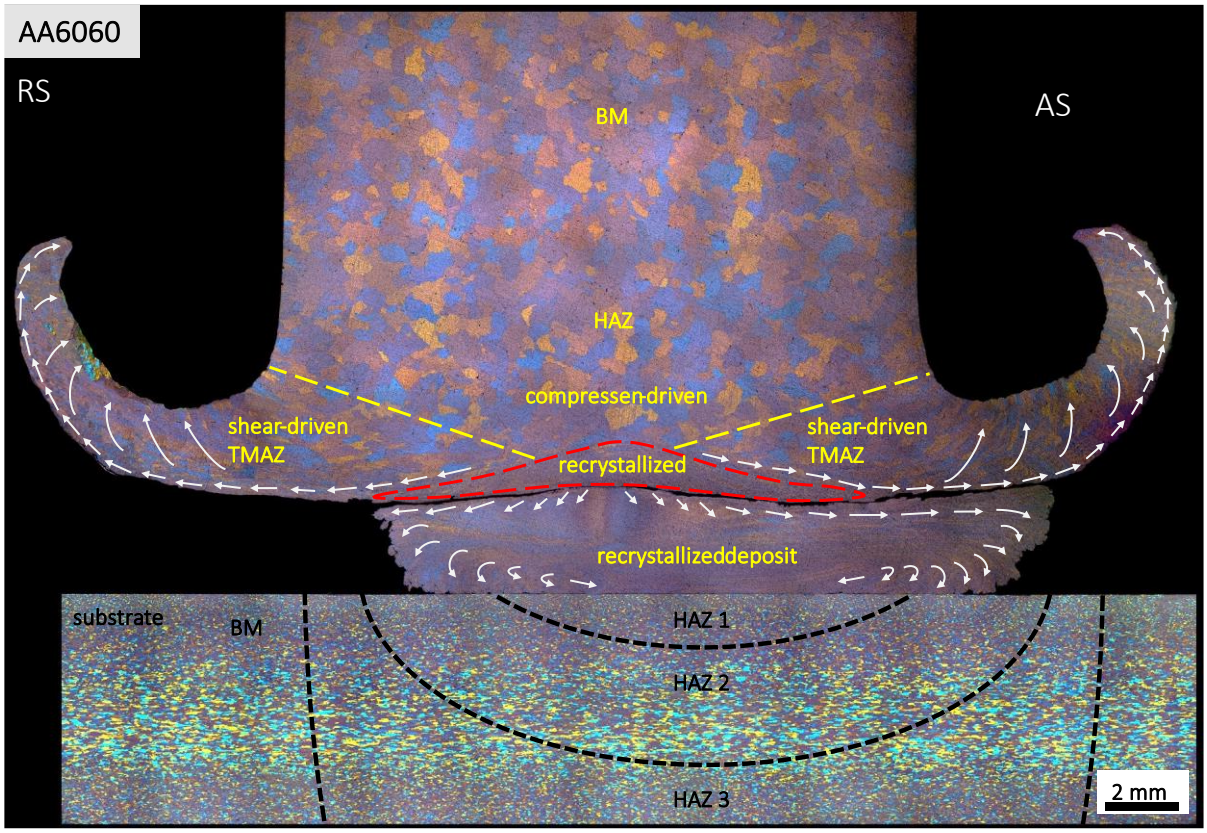

Figure 35: Light-optical micrograph of the stop-action sample from initial alloy AA6060 including characteristic FS microstructure zones.

The compression-dominated TMAZ is the region where the pressure introduced by the axial force begins to cause material flow. In an area of approx. 500µm above the recrystallized zone (dashed red line in Figure 35), a transition between spherical and elongated grain shape can be observed. The material begins to plasticize significantly. The shear-dominated TMAZ areas to the left and right in the image are mainly influenced by shear strain, which is initiated by torsion induced by the rotational movement of the stud. The "quasi-liquid layer" or shear zone known in the literature can be located in the area outlined by the dashed red line, where extreme viscoplastic conditions prevail. In this region, an almost complete dynamic recrystallization has taken place. The crescent-shaped sheared material to the left and right of the stud is part of the flash. From the top of the stud toward the coating, the grains stretch transversely in length. This is also observed in the transition to the flash, however, the grains continue to form into elongated crescent-shaped grains as the flash develops. The white arrows in Figure 35 symbolize the material flow estimated by means of the grain shape or the flow lines and vortices. Further overviews of the stop-action tests of the samples containing Mg and Si, including the characteristic FS zones, can be viewed in the Appendix (Figure 80, Figure 81, Figure 82, Figure 83 & Figure 84.

The microstructure of the coatings shows typical appearances of continuous dynamic recrystallization (cDRX). A pronounced grain refinement can be observed, shown for an exemplary sample of the 3.5 wt.% Mg alloy in Figure 36, from an average grain size of 450 to 12µm, which results approximately to a factor of 40. Homogeneously distributed equiaxed grains can be observed in the microstructure of the coating material. In addition, band structures in similar colors are evident after Barker etching, predominantly aligned parallel to the substrate surface. Towards the edges of AS and RS, these band structures bend and sometimes take on a vortex-like appearance. It is easy to imagine that these are indications of material flow during deposition as the material is sheared from the stud tip in the softened state, apparently affecting the local grain orientation to which the applied color etching technique is sensitive to. The bonding zone between the coating and the substrate is evident due to the different grain sizes. The integrity of the bond at this interface between the coating and the substrate is affected by discontinuities at the edges of the deposit. In the center, however, the bond is free of defects or voids.

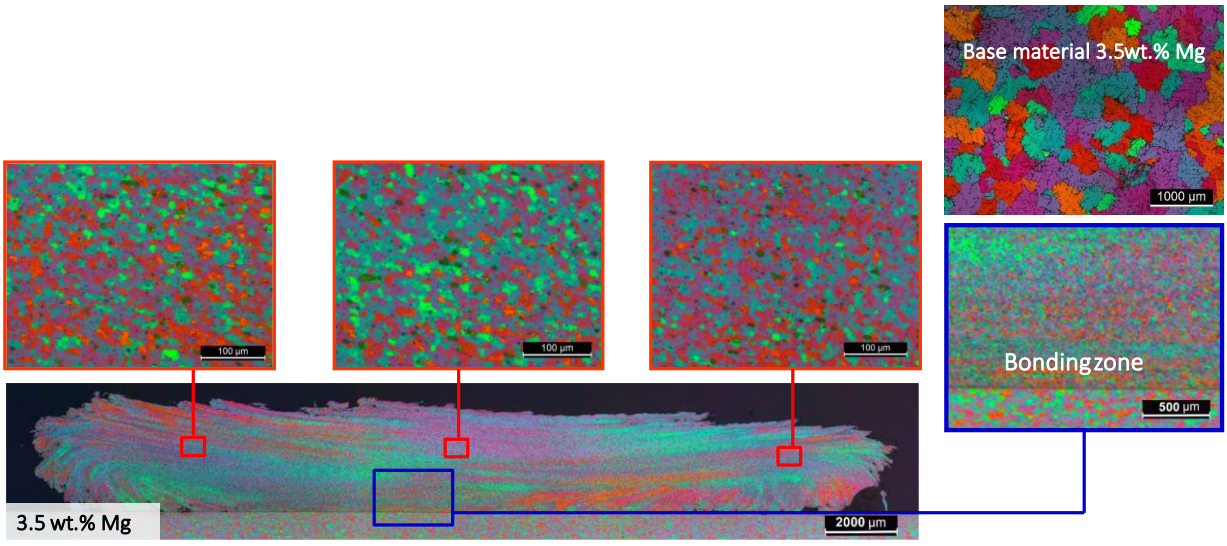

Figure 36: Light-optical micrograph of cross section through FS coating with 3.5 wt.% Mg.

Figure 37 displays micrographs of stop-action samples with different Mg or Si content which were produced with the adjusted process parameters. Shown are the cross sections of the stud tips, which are bonded to the coating material deposited underneath and also contain the flash. Areas of recrystallized microstructure of ultra-fine grain size are visible in the stud tips, resulting from severe shear deformation of the material. The recrystallization height of this deformed area within the studs decreases with increasing Mg content, from 1458 µm for the original alloy (0.27 wt.% Mg) to 675 µm for the sample containing 3.5 wt.% Mg. Similar behavior is observed for the samples with Si content, for which the recrystallization height is reduced to 435 µm for the alloy with 14.6 wt.% Si.

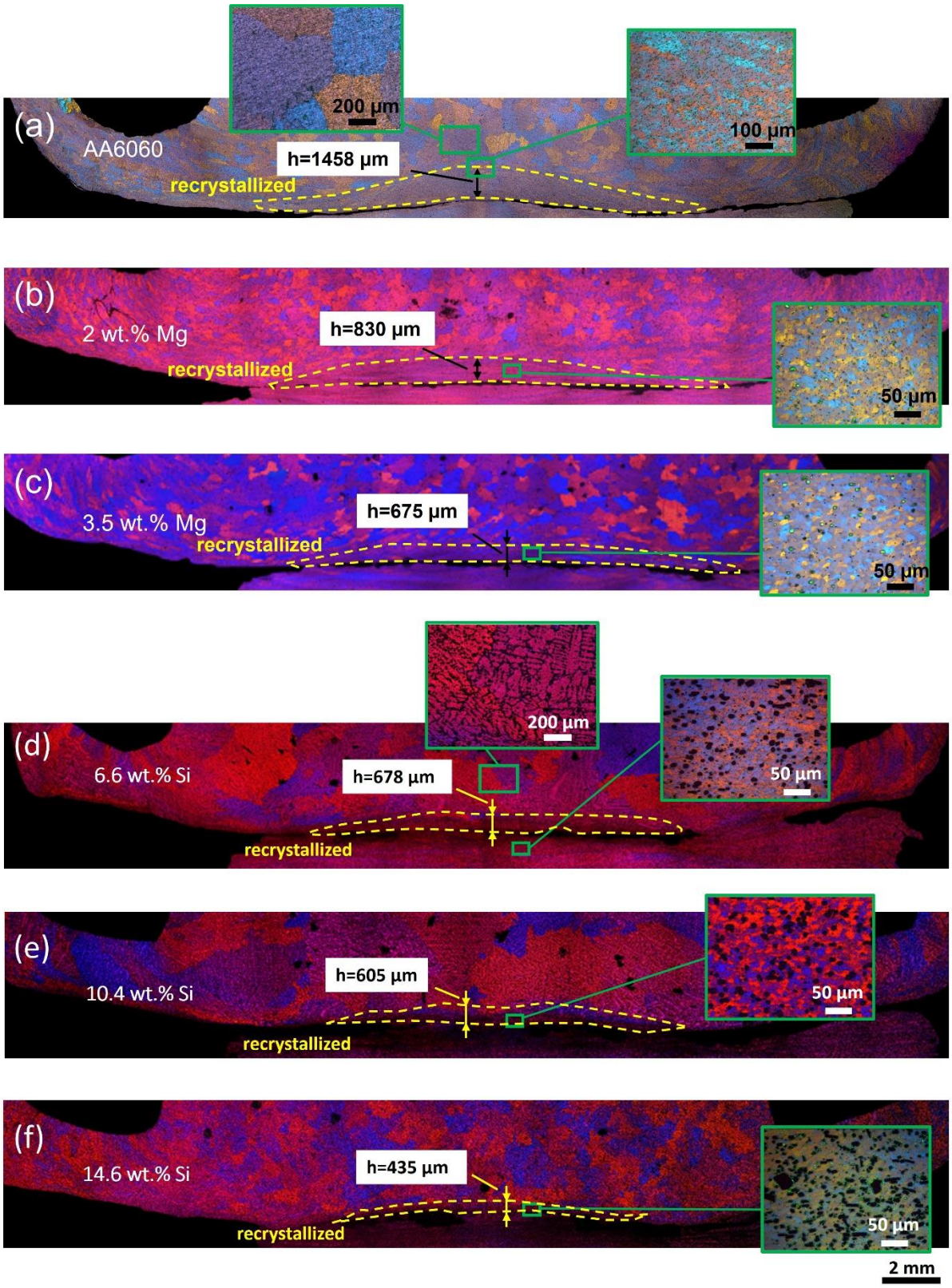

Figure 37: Light-optical micrographs of stop-action samples of FS coatings deposited using adapted parameters. The height of recrystallized microstructure within the studs is indicated. (a) 0.27 wt.% Mg; (b) 2 wt.% Mg; (c) 3.5 wt.% Mg; (d) 6.6 wt.% Si; (e) 10.4 wt.% Si; (f) 14.6 wt.% Si.

5.3.3 Grain structures of processed Al-Mg alloys

Figure 38 shows IPF maps of AA6060 in cast and FS processed state. The IPF maps reveal different grain sizes depending on the position within the deposit, with a much smaller grain size on the advancing side. Figure 39 shows IPF maps of the alloys with 2 and 3.5 wt.% Mg, in cast state and within FS coatings. In some measurements, textures can be observed in the IPF maps, e.g., the crystals of the 2 wt.% Mg sample deposited with adjusted process parameters (Figure 39 (b)) are mainly oriented in the [111] direction. This is due to the high magnification and thus the localized analysis of the EBSD measurements. The measurements were sometimes recorded from an area with a localized vortex or band structure where the grain orientations are predominantly oriented in one particular direction. Such macroscopic band structures are seen in all samples in Figure 22 and Figure 36, indicating non-uniform, shear-dominated material flow during FS. Figure 39 illustrates maps from the center of cross sections of coating with higher Mg contents, each deposited with the two sets of parameters. It can be seen that changing the process parameters has only a minor effect on the resulting grain size and morphology.

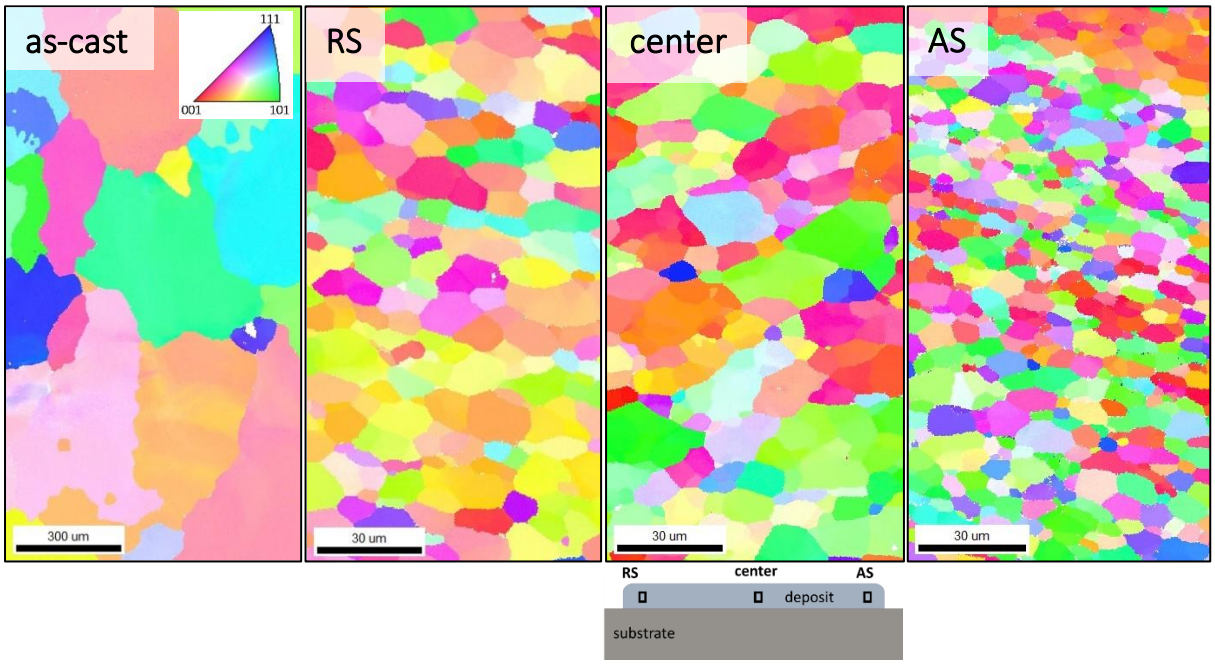

Figure 38: IPF maps of AA6060 (0.27 wt.% Mg) in cast state and within deposited coatings, obtained on RS, center and AS, as indicated in the schematic depiction.

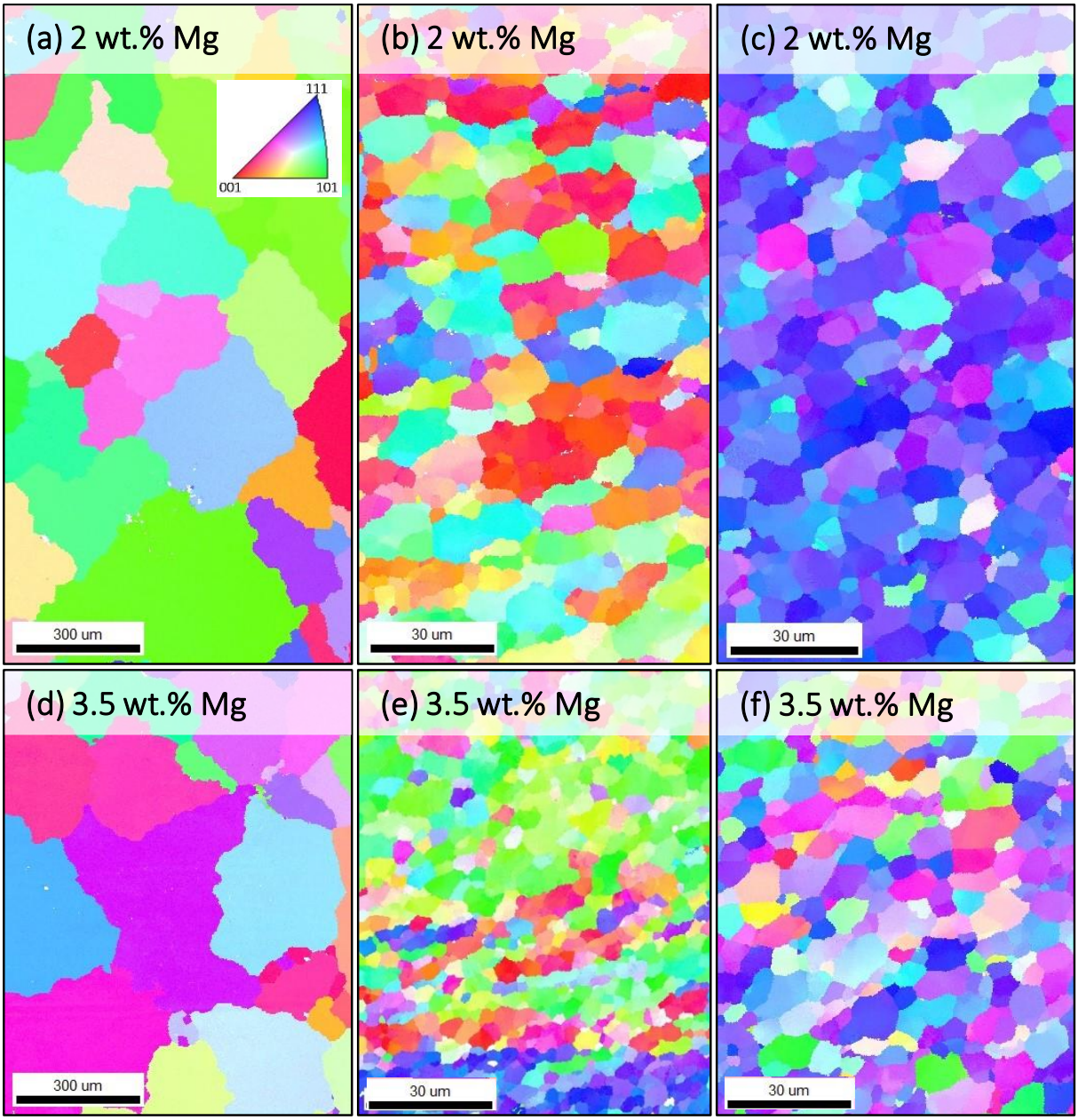

Figure 39: IPF maps of 2 & 3.5 wt.% Mg, in cast material state (a) & (d); in the center of deposited coatings, produced with (b) & (e) identical process parameters and (c) & (f) adjusted process parameters.

Figure 40 summarizes the average grain sizes at the different locations for the different deposits. The alloy with 0.27 wt.% Mg (AA6060) displays the highest average grain sizes, with a significantly reduced grain size (9.0 µm) on the advancing side, as mentioned above. The coatings with 2 wt. % Mg content display almost the same average grain size in the center of each coating (11.7 µm and 12.0 µm). Thus, the average grain size in the coatings' center is about 36% smaller than that of coatings with 0.27 wt. % Mg (18.9 µm). This tendency holds also for the alloy with the highest Mg content of 3.5 wt.%. The average grain size in the coatings' center even decreased to 9.1 and 6.7 µm for the two parameter sets, i.e. a grain size which is about 57% smaller than the grain size in the alloy with lower Mg content. This tendency for a lower grain size on the AS, compared to the center and the RS, shows in all alloys.

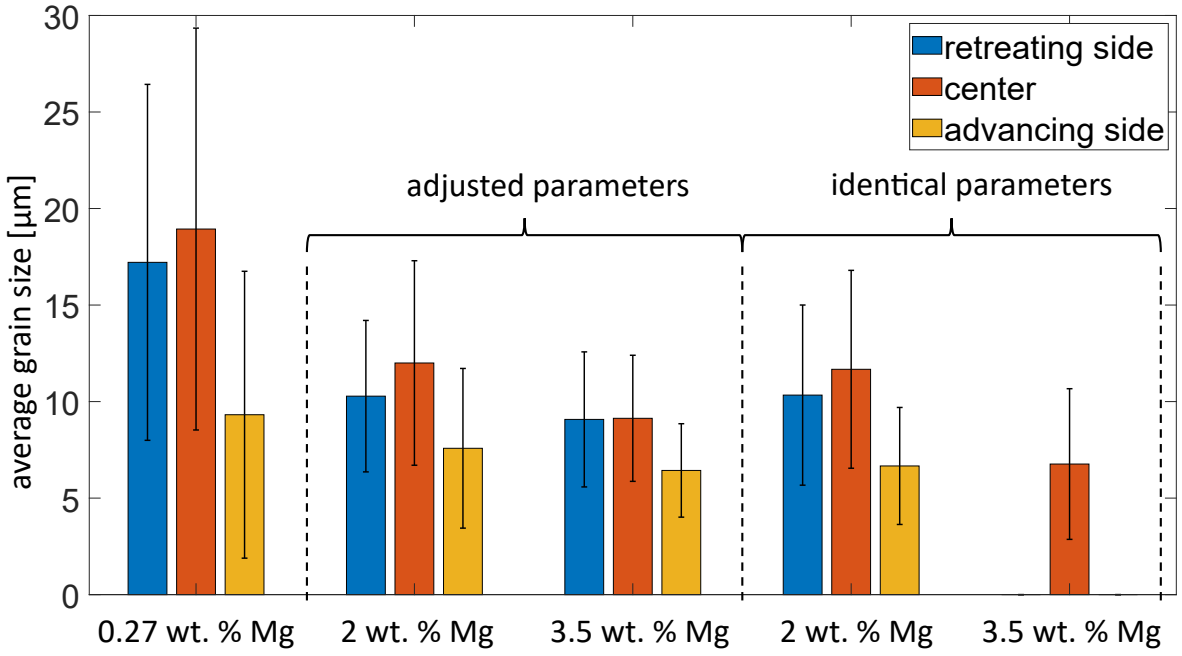

Figure 40: Average grain sizes in FS coatings from AA6060, 2 wt.% Mg & 3.5 wt.% Mg, deposited employing identical process parameters and using adjusted parameters.

As part of verifying the trend of decreasing grain size with increasing Mg content, the 4 additional Mg-containing alloys with 6.4, 8.9, 10.6 & 12.1 wt.% Mg, which were fabricated into similar FS coatings on the Maho 700 universal milling machine (Pfronten, Germany), were analyzed using EBSD. IPF maps of all Mg-rich alloys recorded in the center position are given in Figure 41.

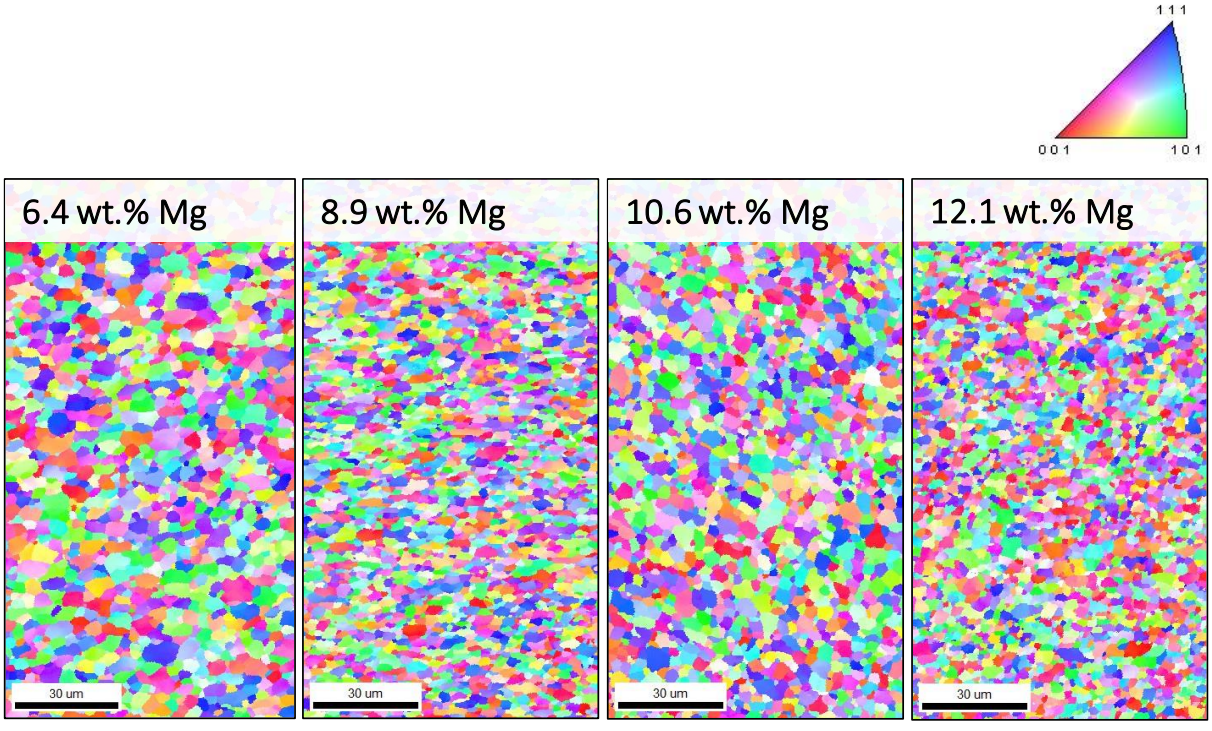

Figure 41: IPF maps of AA6060 and Mg-rich alloys (6.4 to 12.1 wt.% Mg), measured in the center of deposited coatings, produced with adjusted process parameters.

Comparing the different alloys in the IPF maps, it becomes clear that the average grain size decreases with increasing Mg content. Although the 10.6 % Mg coating seems to show a slightly higher grain size than the 8.9 % coating, this could be due to the selected area of data evaluation. In addition, it can be noted that the grains of alloys 6.4-12.1 wt.% Mg show less orientation in a particular direction and thus low texture development. It is possible that such differences appear due to the differences in FS processing, which was done for the four highest Mg contents on a conventional milling machine, and therefore under much less controlled conditions.

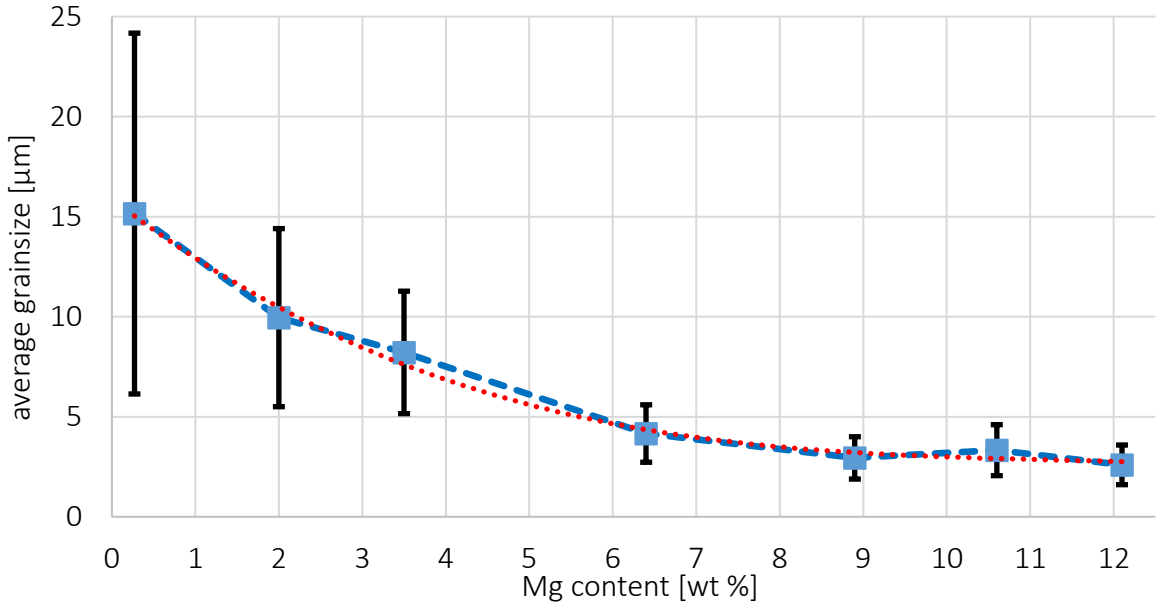

Figure 42: Grain sizes averaged from three measuring locations (RS, center, AS) in FS coatings with 0.27 wt.% Mg (AA6060) up to 12.1 wt.% Mg, deposited employing adjusted parameters.

A summary of the average grain sizes is plotted in Figure 42. To determine the mean grain sizes, three measuring locations (RS, center, AS) were averaged for each sample. A non-linear correlation between average grain size and Mg content can be determined, which appears to assume a saturation value for Mg contents of ≥ 9 wt.%. In the FS processed coating material of the initial alloy AA6060 with a Mg content of 0.27 wt.% Mg, an average grain size of 15.2 ± 9 µm is obtained. The lowest average grain size, with a value of 2.6 ± 1 µm, is obtained for the alloy with 12.1 wt.% Mg. Comparing the two alloys with the lowest and highest Mg content, the average grain size thus decreases by about 83%. In addition, the standard deviation of the measured grain sizes also decreases with increasing Mg content. From this finding, it can be deduced that a lower Mg content leads to a more inhomogeneous microstructure, with smaller and larger grains, while the Mg alloys from 6.4 wt.% Mg show a more homogeneous grain size distribution.

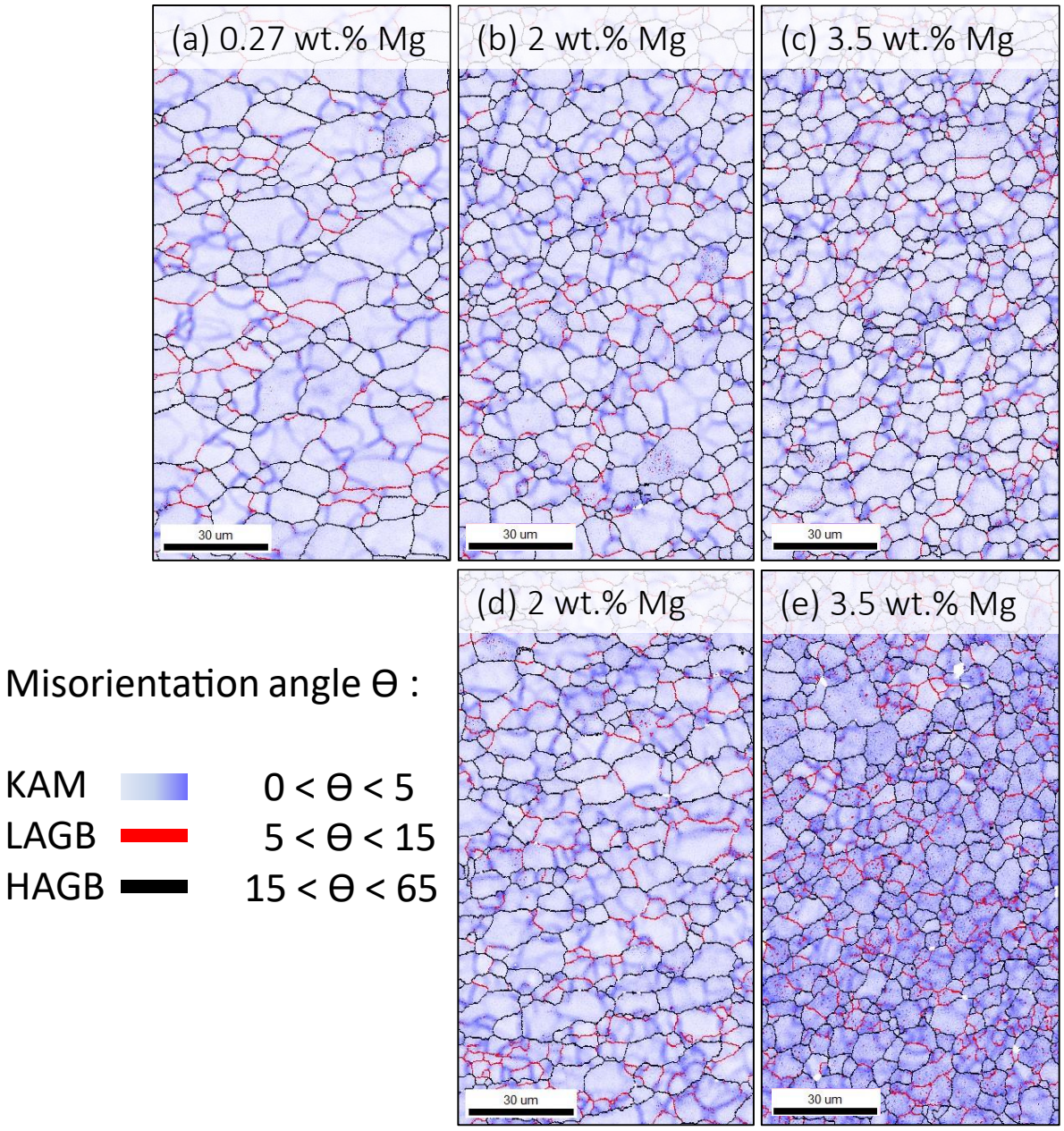

Figure 43: KAM and grain boundary maps of FS coatings from alloys with (a) 0.27 wt.% Mg, (b) 2 wt.% Mg, (c) 3.5 wt.% Mg produced with adjusted process parameters and (d) 2 wt.% Mg, (e) 3.5 wt.% Mg produced with identical process parameters as in (a). The white spots are non-measured areas and were not considered further.

The ESBD data were further analyzed in terms of grain boundaries and kernel average misorientation (KAM) of each measuring point limited to a 5° misorientation angle θ (5°|5R), and displayed by colour gradation from white to blue ($0° \leq \theta < 5°$). Additionally, low angle grain boundaries are displayed in red (LAGB = $5° \leq \theta < 15°$), and high angle grain boundaries in black (HAGB = $15° \leq \theta < 65°$). The combined representation of KAM, LAGBs and HAGBs is given in Figure 43 measurements with 1000x magnification. It can be seen that some larger grains are subdivided by LAGBs. Further, the KAM representation displays additional structures of high local misorientation, which also subdivide larger grains and subgrains. These structures can be assumed to consist of arranged dislocations which have not yet transformed into LAGBs. In Figure 44, the KAM maps for the samples with 6.4-12.1 wt.% Mg

were created from measurements with 2500x magnification to display more details of the fine microstructure. From the KAM maps, a higher percentage of HAGB is evident for these alloys compared to the alloys with 0.27-3.5 wt.% Mg.

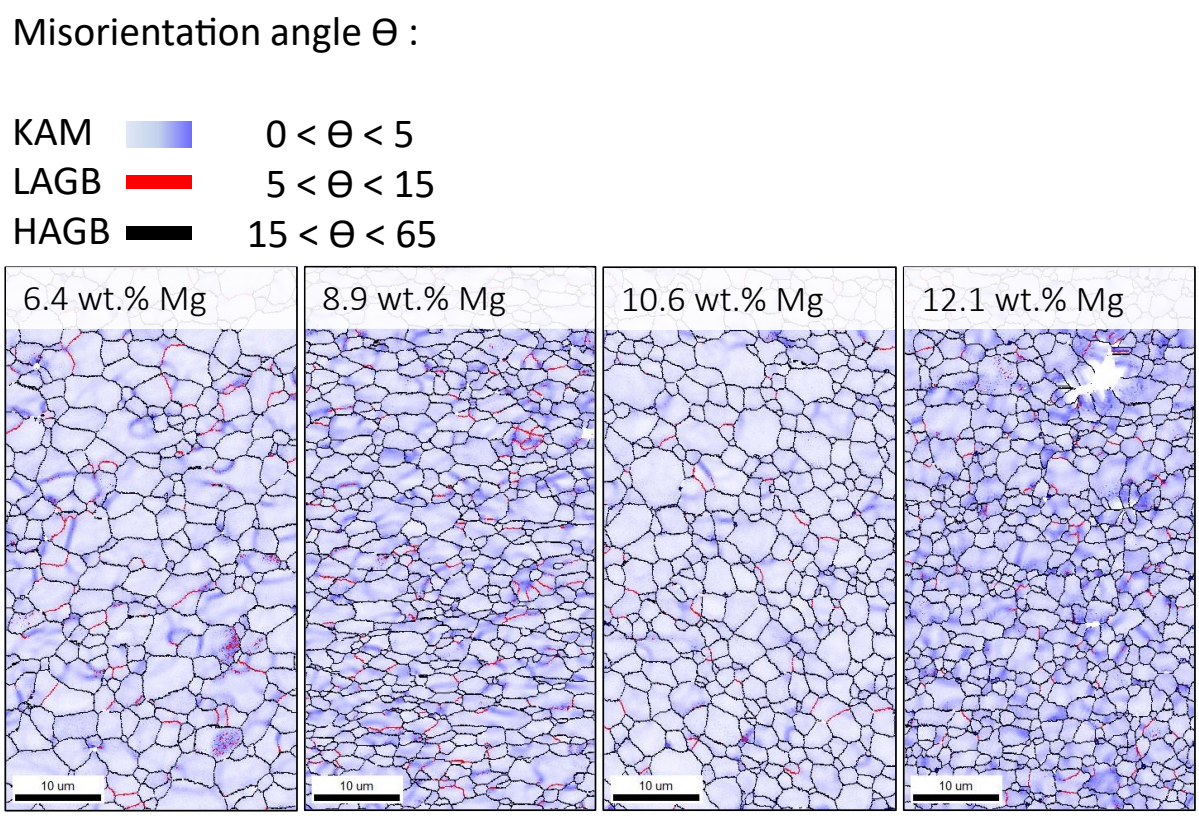

Figure 44: KAM and grain boundary maps of FS coatings from alloys with 6.4 wt.% up to 12.1 wt.% Mg produced with adjusted process parameters. The white spots are non-measured areas and were not further considered. Note the differences in image magnification.

The ratios of the absolute lengths of HAGBs and LAGBs in each measurement area of x µm by y µm were determined and plotted in Figure 45, allowing for a quantitative comparison. To determine the grain boundary ratios, three measurement areas (RS, center, AS) were averaged for each sample. The grain boundary ratio increases with increasing Mg content for both sets of process parameters, i.e. the length of HAGBs increases relative to that of the LAGBs. The grain boundary ratio for the alloy with 3.5 wt.% Mg increases by a factor of approximately 2 compared to 0.27 wt.% Mg. In sample 0.27 wt.% Mg the LAGBs length is comparably high. With increasing Mg content beyond 3.5 wt.%, the increasing grain boundary ratio trend continues. The ratio increases from 1.7 ± 0.3 for the alloy with 0.27 wt.% Mg to a ratio of 15.8 ± 3.1 for the alloy with 12.1 wt.% Mg. In percentage terms, this means that a ratio of 65% HAGB to 35% LAGB is formed in the microstructure of the FS processed 0.27 wt.% Mg alloy. In the alloy with 12.1 wt.% Mg, the ratio is 94% HAGB to 6% LAGB. However, it can be seen that the standard deviation also increases with higher Mg content.

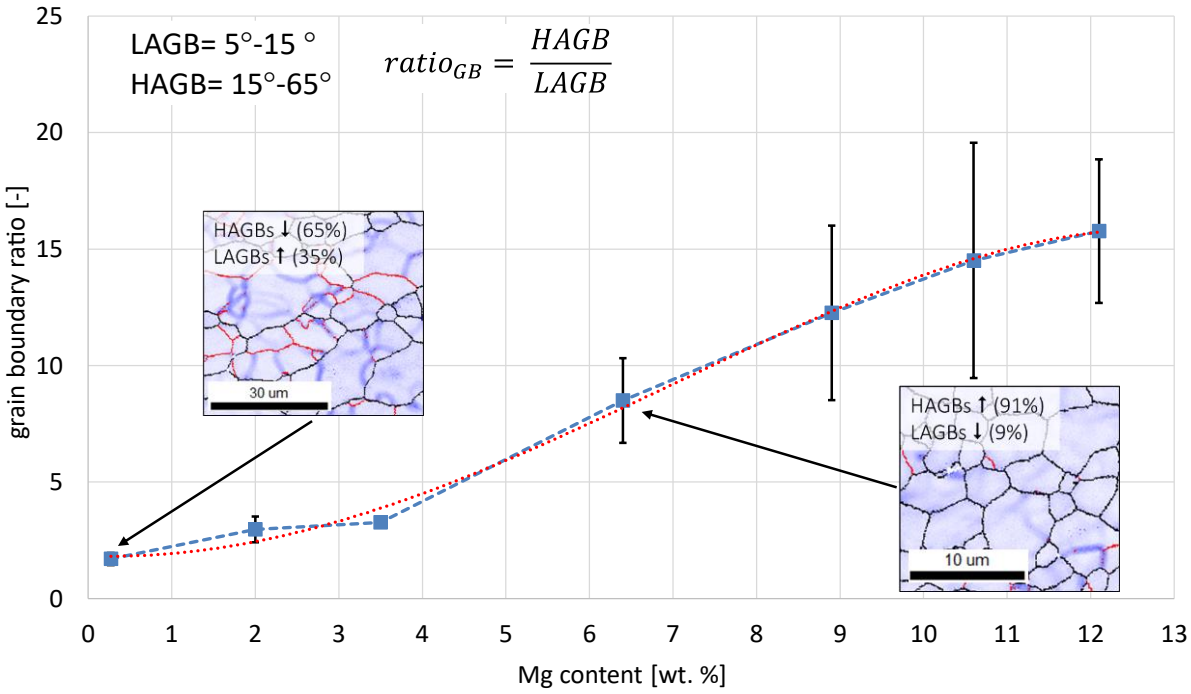

Figure 45: Grain boundary ratio depending on Mg content under adjusted parameters.

The unitless number fraction, describing the grain boundary length of a certain misorientation angle in relation to the sum of boundary length of all (sub-)grains, is plotted in Figure 46 and Figure 47 over the respective grain boundary misorientation angles. The area shaded in red, with misorientation angles of 5°-15°, represents the LAGBs colored in red in Figure 43 and Figure 44. In the initial alloy AA6060 with 0.27 wt.% Mg, the LAGB area is comparably high. Looking at Figure 46, with increasing Mg content, the number fraction of LAGBs decreases disregarding whether the process parameters were set identical or adjusted. The distribution of grain boundaries confirms the higher fractions of HAGBs with increasing Mg content. The misorientation angle distributions of the recrystallized coating materials reveal a similar course for all samples, regardless of the quantitative number fraction, and can be described as follows: steep drop in the fraction of LAGBs, followed by a less steep downward trend of HAGBs of low misorientation angles up to ≈ 30°-40°, followed by a rise in number fractions up to a higher level at ≈ 50°-55°.

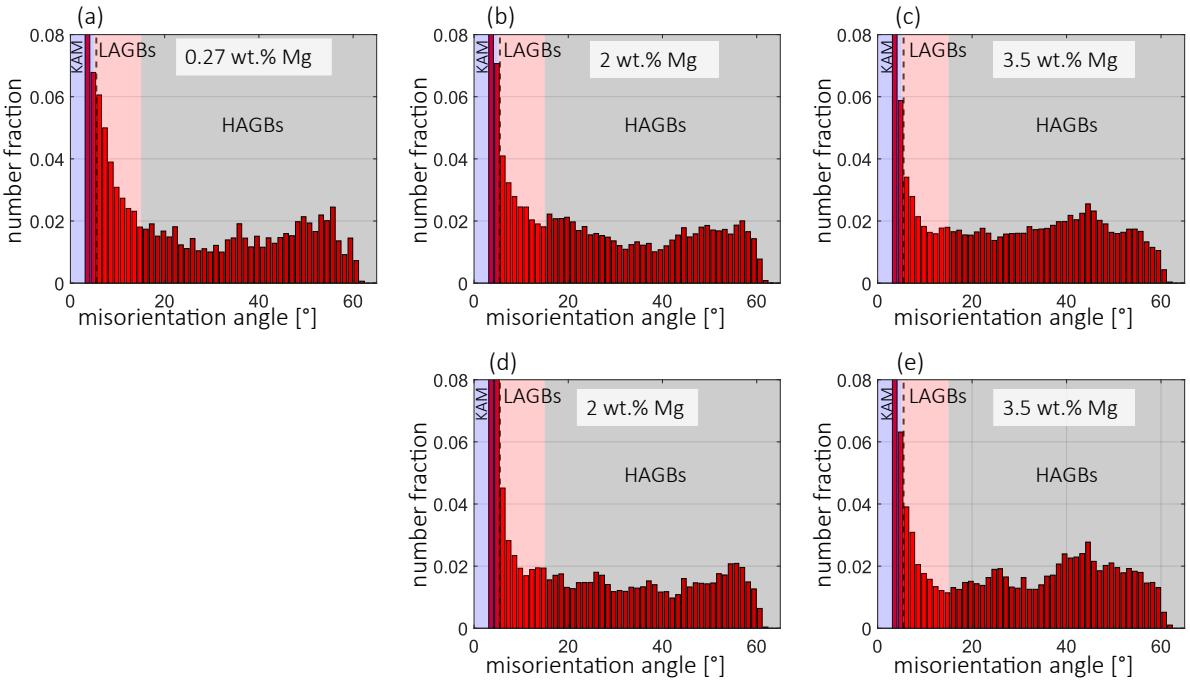

Figure 46: Distribution of grain boundary misorientation angles in FS coatings. (a) 0.27 wt.% Mg, (b) 2 wt.% Mg, (c) 3.5 wt.% Mg produced with adjusted process parameters and (d) 2 wt.% Mg, (e) 3.5 wt.% Mg produced with identical process parameters as in (a).

The three upper plots in Figure 47 are the same as in Figure 46, where all Mg-containing samples processed with adjusted parameters are compared. In the four alloys with 6.4 to 12.1 wt.% Mg, the number fractions of LAGBs are lower as shown before (Figure 46). For grain boundary misorientation angles ≥10°-15°, the number fraction of existing misorientations increase to a maximum at ≈ 45°. From this angle on, the number fractions drop to 0 at ≈ 60°. This results in a characteristic misorientation distribution, which could not be observed for the alloys with 0.27-3.5 wt.% Mg.

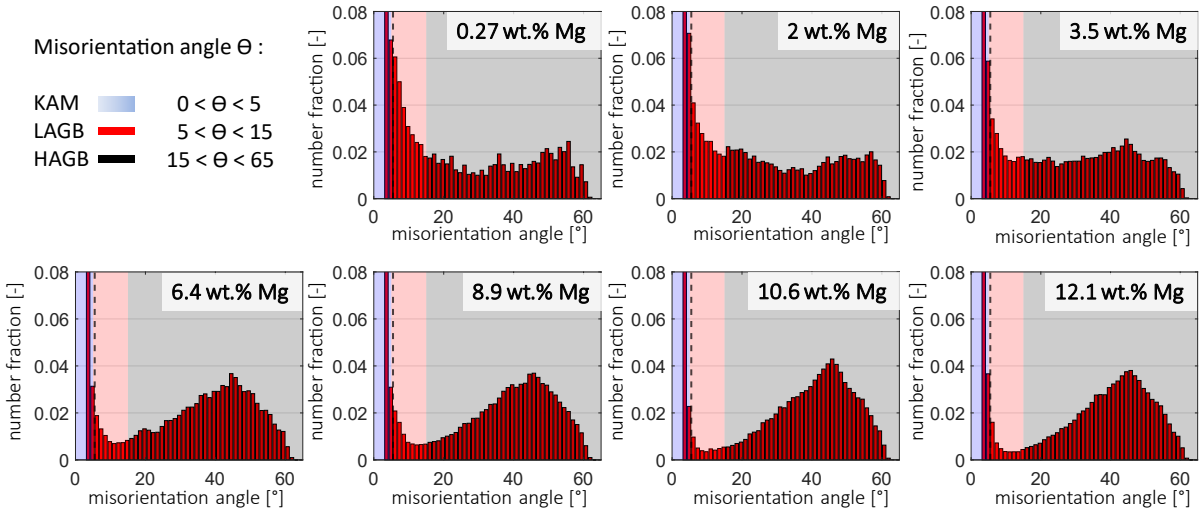

Figure 47: Distribution of grain boundary misorientation angles in FS deposits from alloys with 0.27 wt.% Mg up to 12.1 wt.% Mg, produced with adapted process parameters.

For further analysis, the height to width ratio of grains is evaluated. Figure 48 depicts the grain shape aspect ratio (AR) maps derived from the EBSD measurements. Here, the aspect ratios of the grains with HAGB are calculated and depicted by the color scale shown in the figure. As a result, the averaged aspect ratios lie in the range of 0.5. It can be observed that the subgrains stretch mainly laterally along the x-axis, something which is due to the shear strains. OIM Analysis™ 7.3.1 calculates the aspect ratios using exclusively grains with HAGBs. Subgrains with LAGBs are not considered. However, certain color-coded areas in the microstructures in Figure 48 consist of clusters of globulitic subgrains located in one HAGB grain stretched in the x-direction and thus exhibit a low aspect ratio of about 0.2-0.5.

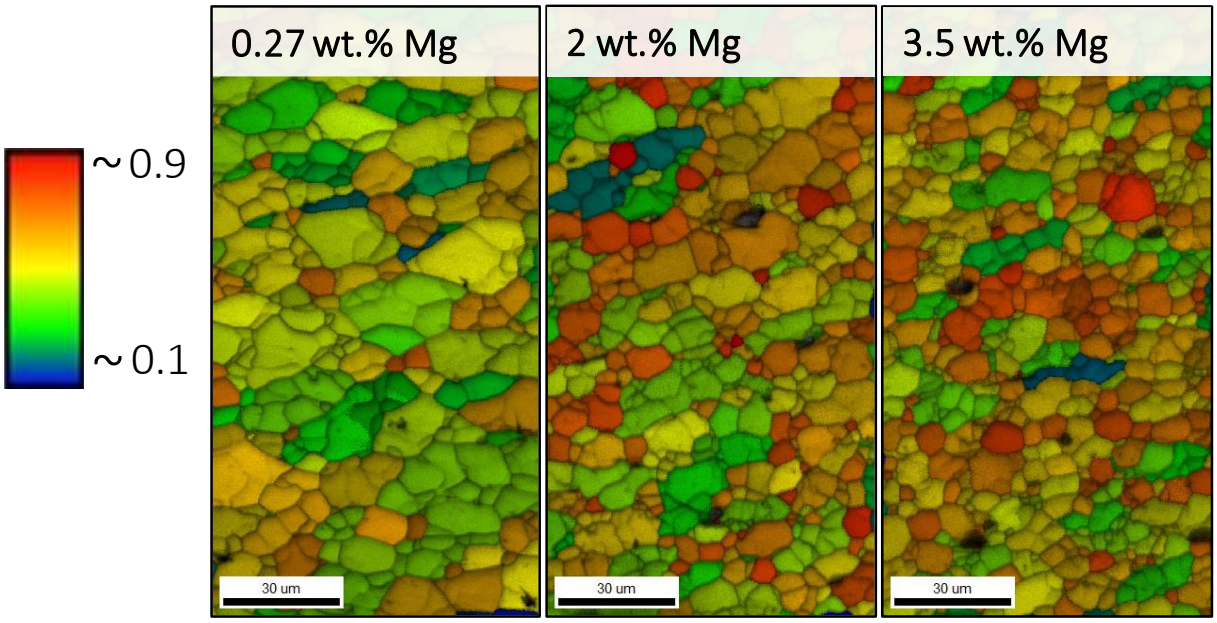

Figure 48: Aspect ratio maps of FS coatings from alloys with 0.27-3.5 wt.% Mg.

Color-etched light microscopy images were used to determine the aspect ratio of grains more specifically (see Figure 49). In these, all grains and subgrains are considered through manual selection. Using ImageJ analysis software, the heights and widths of the grains were determined for AA6060, 2 wt.% Mg and 3.5 wt.% Mg alloys. To account for the shape of the grains, which deviates from the equiaxed geometry, the measurement grid consists of both vertical and horizontal measurement lines. It should be noted that the ratio of height to width y/x does not exactly correspond to the anisotropy index since this requires that the principal axis of deformation is known [121]. Deviations of the aspect ratio of $\leq 3{:}1$ are considered not to deviate seriously from the equiaxed shape [121] (here: $\geq 1{:}3 = 0.33$). The farther away the ratio is from 1:1, the greater the deviation from the equiaxial form. Since multiaxial deformation occurs in FS, x and y are not aligned with the principal deformation axis but with the direction of the axially acting force F_z (with y(0°) and x(90°)). The determined aspect ratio of grains is nearly constant over all samples and observation fields, on average 0.756 ± 0.045 through all different alloys. As mentioned above, the differences in the results yielded by the methods used (1. EBSD + OIM AnalysisTM 7.3.1, 2. light microscopy + ImageJ) are due to the fact that subgrains are not taken into

account when using the first method. The subgrains within a HAGB usually form elongated clusters, something which leads to smaller aspect ratios.

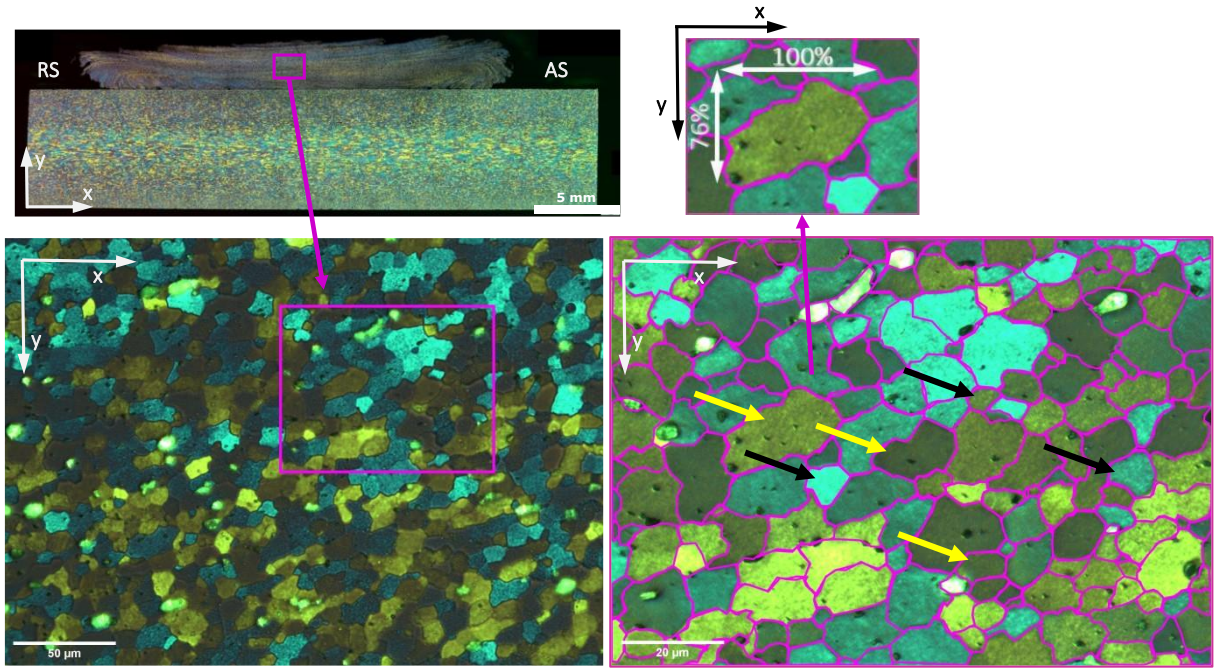

Figure 49: Light-optical micrographs of FS deposit from 3.5 wt.% Mg alloy (adjusted parameters). Grains made visible by etching. Left: 200x magnification with image detail in 500x magnification. Right: varying grain morphologies and sizes: yellow arrows: oval, tending to be larger; black arrows: nearly round, smaller.

5.3.4 Grain structures of processed Al-Si alloys

The analysis of grain sizes, orientation and grain boundaries is only feasible to a limited extent for the Si-rich alloys. Due to the presence of hard Si particles in the softer Al matrix, metallographic preparation is complicated. For example, in both mechanical vibration polishing and electrolytic polishing, the hard and brittle Si particles are ground off significantly less than the surrounding Al matrix. This results in height differences of the phases in the sample surface. Flatness and homogeneity of the sample surface are two important criteria for obtaining evaluable Kikuchi patterns. Different preparation methods were evaluated, and the one providing the highest sample quality is described in section 4.4, Metallographic procedure (Table 7). Figure 50 presents the IQ maps (top) as well as detail sections as IPF maps (bottom) of the FS coatings from the initial alloy with 0.37 wt.% Si (AA6060), 6.6, 10.4 & 14.6 wt.% Si produced using adjusted parameters. From the IQ maps, it appears that pronounced grain refinement by FS has occurred. In the IPF detail sections, it can be seen that some subgrains have also formed as can be clearly identified in the alloy with 6.6 wt.% Si. The areas marked with red arrows are Si particles. The grains in the surrounding Al matrix appear to be homogeneously recrystallized and predominantly globular. Due to the low data availability of sufficient pattern quality, no quantitative analyses with respect to grain size, grain boundaries or aspect ratio can be statistically validated from the EBSD investigations of the Si-containing alloys.

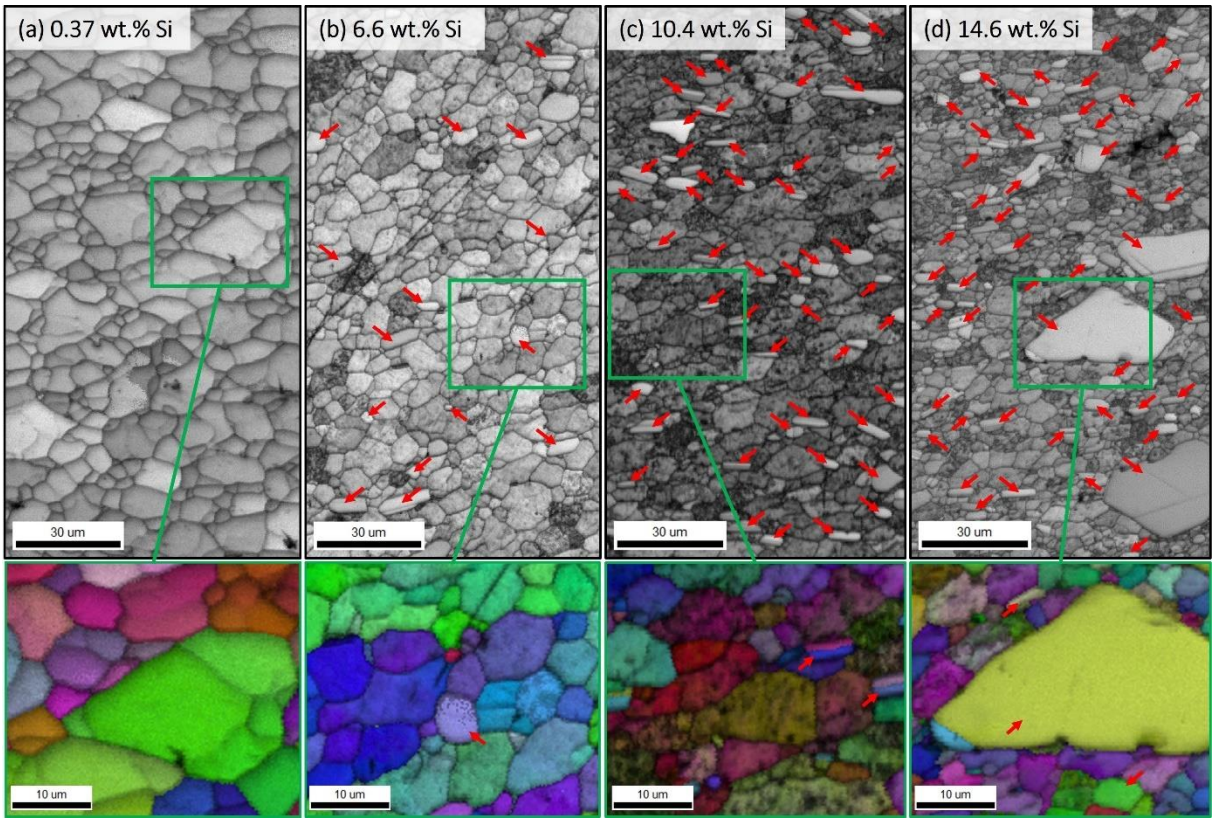

Figure 50: IQ maps (top) and detail IPF maps (bottom) of FS coatings from the initial alloy with 0.37 wt.% Si (AA6060), 6.6, 10.4 & 14.6 wt.% Si, produced using adjusted parameters.

However, the line intersection method based on EN ISO 643 can be applied to the light micrographs etched by Barker in order to determine the average grain size. In this method, the calculation is based on the number of intersections of a straight measuring line with the grain boundaries. The average grain size is obtained from the mean value of the line intersection segment [122]. Figure 51 shows light microscopic images of the color etched microstructure of the Si-rich alloys. The top line of images displays the microstructures in the base material state (20x magnification), while the bottom line illustrates the FS coating material (200x magnification) of the alloys AA6060 (0.37 wt.% Si), 6.6 wt.% Si, 10.4 wt.% Si, and 14.6 wt.% Si. Depending on their orientation, the crystals are affected differently by the etchant, so that differently oriented grains can be distinguished by color. Compared to EBSD evaluations, compositional variations within a grain are not visible here. Since there is no actual coloring of the material, color differences can only be perceived when observed through polarized light. After adjusting the polarization filters, settings are made in the digital image acquisition with regard to exposure time, gain factor, contrast and white balance in such a way that the grains in the microstructure can be determined with high contrast. For the best possible contrast, the color settings, such as in Figure 51 (b), (c) & (d), can also lean into red saturation. The microscope images of the coating material in Figure 51 (d) differ in terms of color and contrast from Figure 51 (f), (g) and (h) due to the settings of the polarization filters on the light microscope.

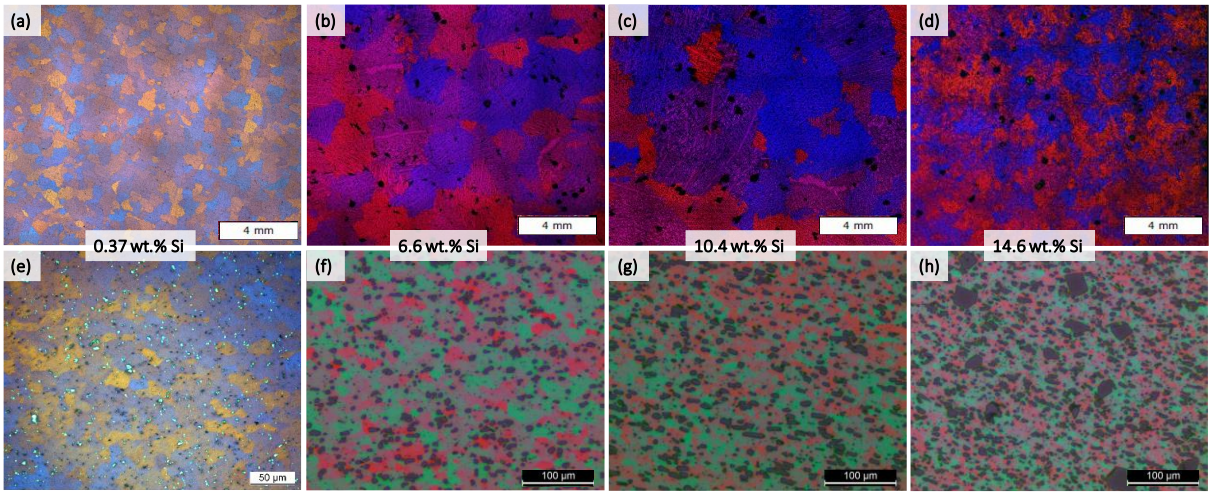

Figure 51: Light microscopic images showing color etched microstructure of the Si-rich alloys. Cast state base material: (a) 0.37 wt.% Si (b) 6.6 wt.% Si (c) 10.4 wt.% Si (d) 14.6 wt.% Si; FS coating material (adjusted parameters): (e) 0.37 wt.% Si (f) 6.6 wt.% Si (g) 10.4 wt.% Si (h) 14.6 wt.% Si.

The alloy with 10.4 wt.% Si (Figure 51 (c)) features the largest grain size in the base material state at 2157.7±155.2 µm. The size of crystals for cast alloys is generally determined by the cooling rate during the solidification process. Thus, gradual cooling means that the grains have more time to grow. The cast base material state displays high standard deviations of the average grain sizes. In addition, pores, which could be caused by gas inclusions during casting, are present in the Si-containing samples (black areas). Si particles could not be observed in the base material micrographs due to the low magnification of 20x used. The average grain sizes of the samples containing Si are summarized in Figure 52. To determine the mean grain sizes, three measuring points (RS, center, AS) were averaged for each sample. After an increase of the average grain size from 15.2 ± 9.0 µm for the 0.37 wt.% Si alloy to 20.8 ± 2.1 for the 6.6 wt.% Si alloy, the grain size decreases slightly to 13.5 ± 2.2 for the 14.6 wt.% Si alloy.

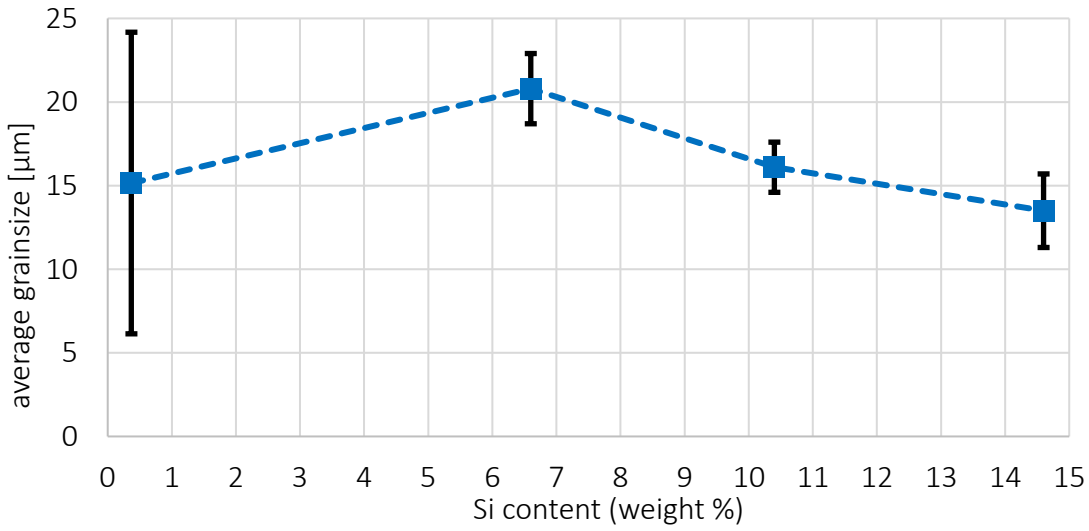

Figure 52: Grain sizes averaged from three measuring locations (RS, center, AS) in FS coatings with 0.37 wt.% Si (AA6060) up to 14.6 wt.% Si, deposited employing adjusted parameters.

5.3.5 Texture development

To analyze the recrystallized microstructure of the FS coatings with respect to potential preferential orientations, selected areas of the samples AA6060, 2 wt.% Mg generated by means of adjusted parameters & identical parameters are investigated as is the influence of the used process parameters as well as the content of the alloying element Mg (2 wt.%). The focus of the shear texture analysis lies in the flow lines developed in the microstructure, and these lines can be localized from etched light microscope images. Figure 53 illustrates pseudo 3D images of samples AA6060, 2 wt.% Mg adjusted parameters & identical parameters. For this purpose, the samples were extracted and prepared as shown in Figure 14 and then captured using an optical light microscope. The individual overview images of the three observation directions of the standard system, i.e., DD→ front view; ND→ top view and TD→ transverse view, were then assembled into a pseudo 3D image from three individual samples for illustration purposes. EBSD measurements were performed from all three observation directions. It should be noted that the individual samples were extracted at different locations in the coatings and thus do not reflect the real three-dimensional sample.

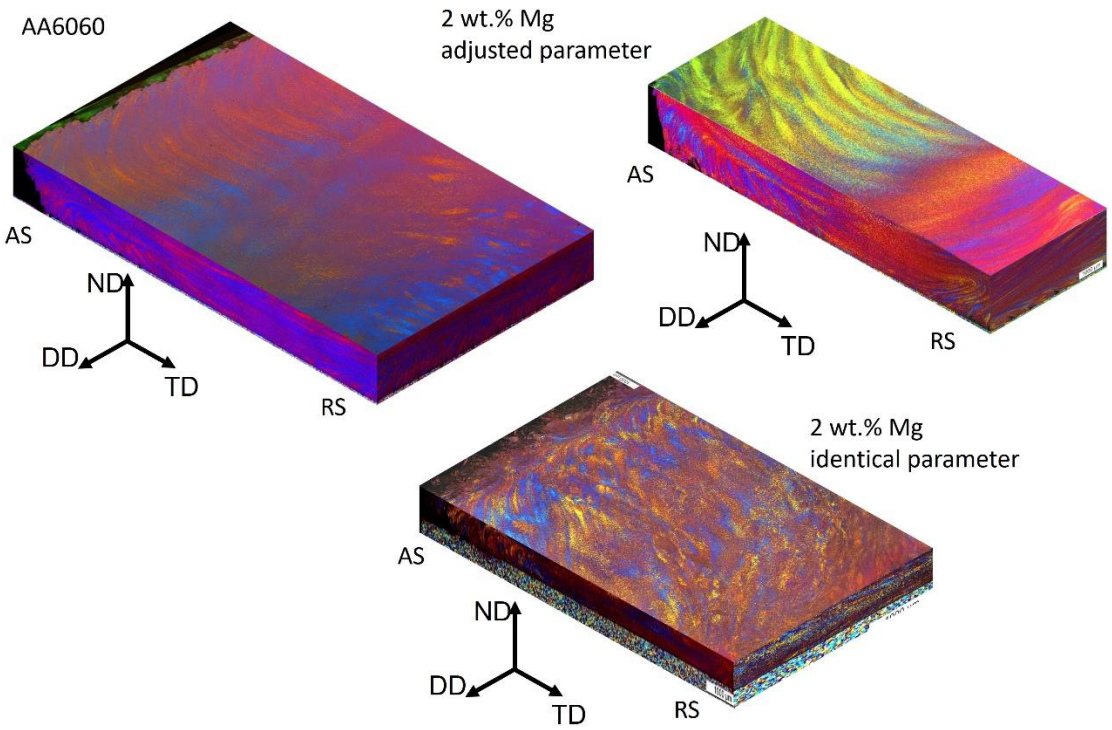

Figure 53: Pseudo 3D images of color etched samples AA6060, 2 wt.% Mg adjusted parameters & identical parameters. EBSD measurements were performed from all three observation directions of the standard system DD-> front view, ND-> top view and TD-> transverse view.

Figure 54 summarizes the investigations of ideal shear texture components by demonstrating selected results. The data sets of the PF plots were rotated according to the approach described above so that the SPN points upward, and the SD coincides with the horizontal. The highlighted areas of the IPF maps indicate for which measuring region the PF were plotted. Local preferred orientations were selected that occurred due to material flow and their investigation for ideal shear texture components.

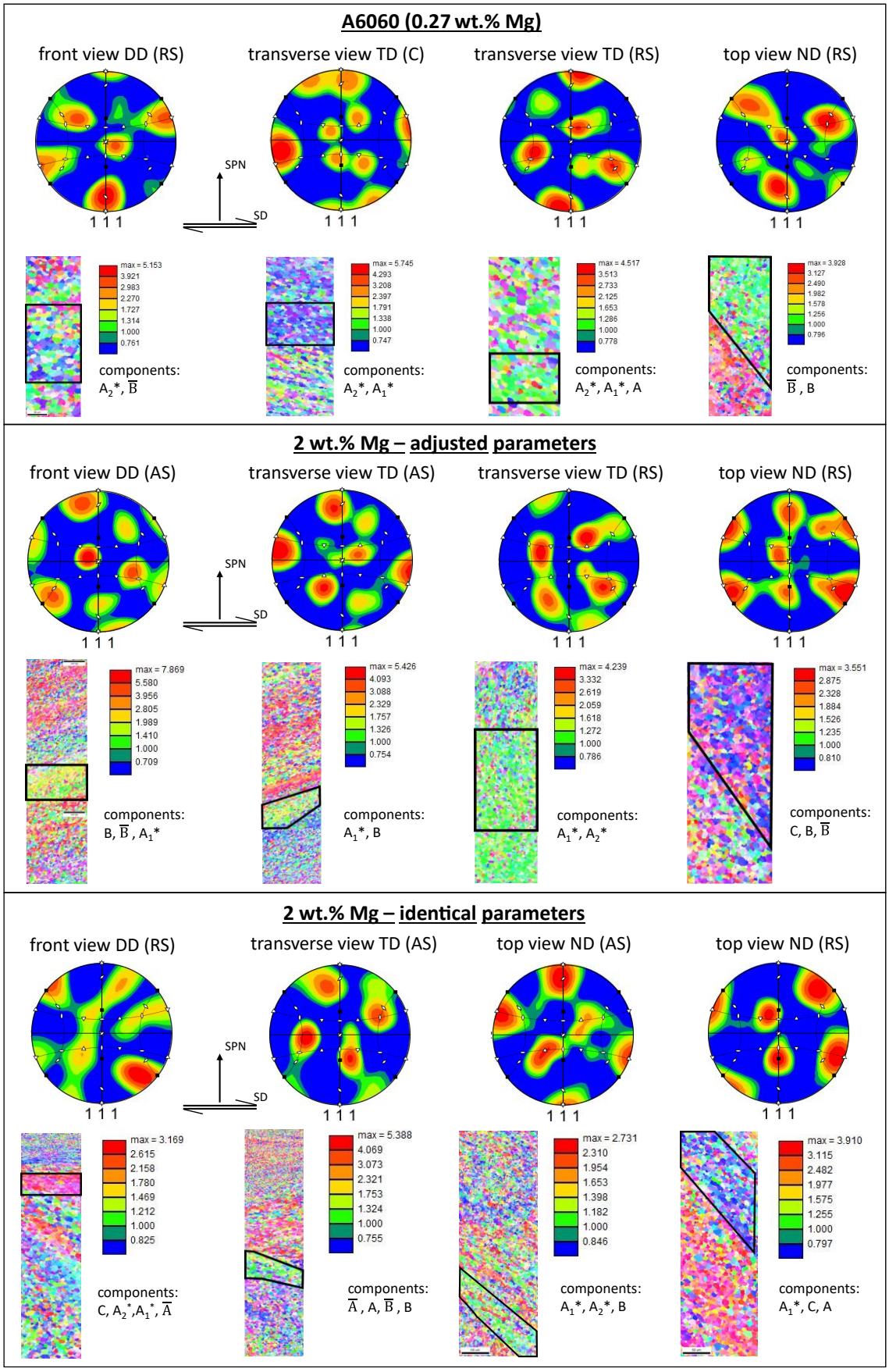

Figure 54: Rotated PF plots of three different FS coatings: top: Initial alloy AA6060; middle: 2 wt.% Mg adjusted parameters; bottom: 2 wt.% Mg identical parameters and each from different observation directions. In the PF plots, the SPN points upward, and the SD coincides with the horizontal.

It is assumed that during FS processing the shear direction is tangential to the stud radius, and the shear plane normal is orthogonal to the stud axis (axial force F_z direction). The corresponding rotated PF of the three investigated coatings, which were measured in the flow lines and vortices phenomena, confirm shear dominated material flow. The coatings were analyzed from three different observation directions in order to reconstruct local shear strain gradients or complex material flow effects. The results are analyzed with respect to the shear texture components and the texture intensity. The texture intensity is a quantitative indication of the degree of preferred crystallographic orientation in a material. It is understood as the ratio between the intensity of the preferred orientation and the intensity of the random orientation [107]. All ideal shear texture components (A_1*, A_2*, A, $\overline{A}$, B, $\overline{B}$, C) could be observed in the samples. In the initial AA6060 alloy, $\overline{B}$ components dominate, having an alignment of the $\{\bar{1}1\bar{2}\}$ slip plane with the shear plane normal and the $<\bar{1}\bar{1}0>$ slip direction with the SD (Figure 54 upper third). In addition, A_1* & A_2* components could be increasingly detected with {111}-slip planes and $<\bar{1}1\bar{2}>$-slip directions. The averaged maximum texture intensity, independent of the direction of observation, is 5.2 ± 0.9 for the AA6060 sample. In the coating with 2 wt.% Mg generated using adjusted parameters, components B & A_1* and also C dominate. The C component indicates a plane alignment in {001} and a directional alignment in <110> (Figure 54 middle third). With high texture intensity (7.9), B and $\overline{B}$ components can be identified in measurement "front view DD (AS)". The averaged maximum texture intensity of the sample 2 wt.% Mg, adjusted parameter, is 5.1 ± 1.5. However, the coating with 2 wt.% Mg, produced with identical parameters (Figure 54 lower third), yields the lowest average maximum texture intensity with 4.1 ± 1.2. From the rotated PF of this coating, no dominant components could be evaluated, something which correlates with the lower intensities.

5.3.6 Dislocation structures

For a further understanding of the microstructural constituents, the acting micromechanisms as well as the line and planar lattice defects analysis, measurements were carried out in the transmission electron microscope (TEM). For this purpose, the samples were taken from the coating material as shown in Figure 14 and prepared according to Table 7. For the same reasons as described in chapter 5.3.4, Grain structures of processed Al-Si alloys, the Si containing samples are more prone to preparation artifacts, therefore only the Mg containing samples are analyzed. It should be noted that TEM images provide only a highly localized view of the microstructure. Nevertheless, TEM images can support the findings of the EBSD investigations. Figure 55 presents TEM images showing details of the dislocation structures in coatings of alloys with different Mg contents. Dislocation tangles often form in areas of high dislocation density.

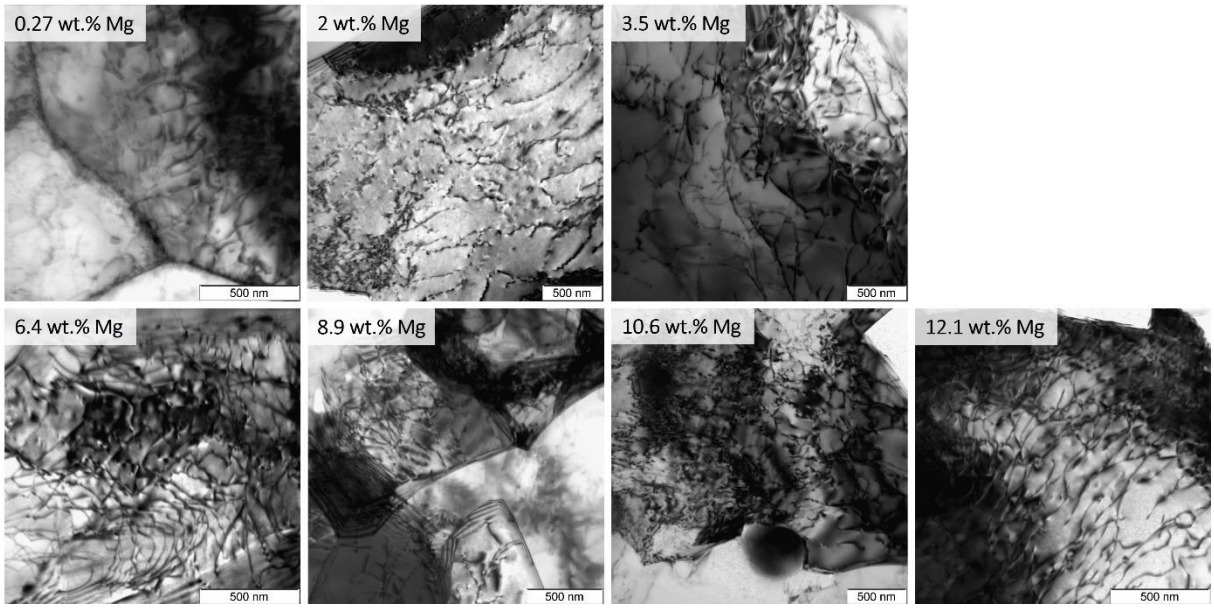

Figure 55: TEM images from FS coatings with different Mg content 0.27-12.1 wt.% processed using adjusted parameters showing grain boundaries & dislocation tangles.

The bright field images in Figure 55 reveal how dislocations accumulate to an increased density in different areas for the Mg-rich alloys. In Figure 55 (6.4 wt.% Mg) & (12.1 wt.% Mg) the characteristic features of bowed dislocation tangles can be detected quite distinctly. Dislocation tangles form when dislocations with the same Burgers vector interact and thus become entangled with each other. In Figure 55, (0.27 wt.% Mg) & (8.9 wt.% Mg) grain boundaries can be seen. Here, dislocations accumulate within the crystals. In a direct comparison of all TEM images from 0.27-12.1 wt.% Mg displayed here, the alloys appear to have a higher dislocation density within the crystals with increasing Mg content.

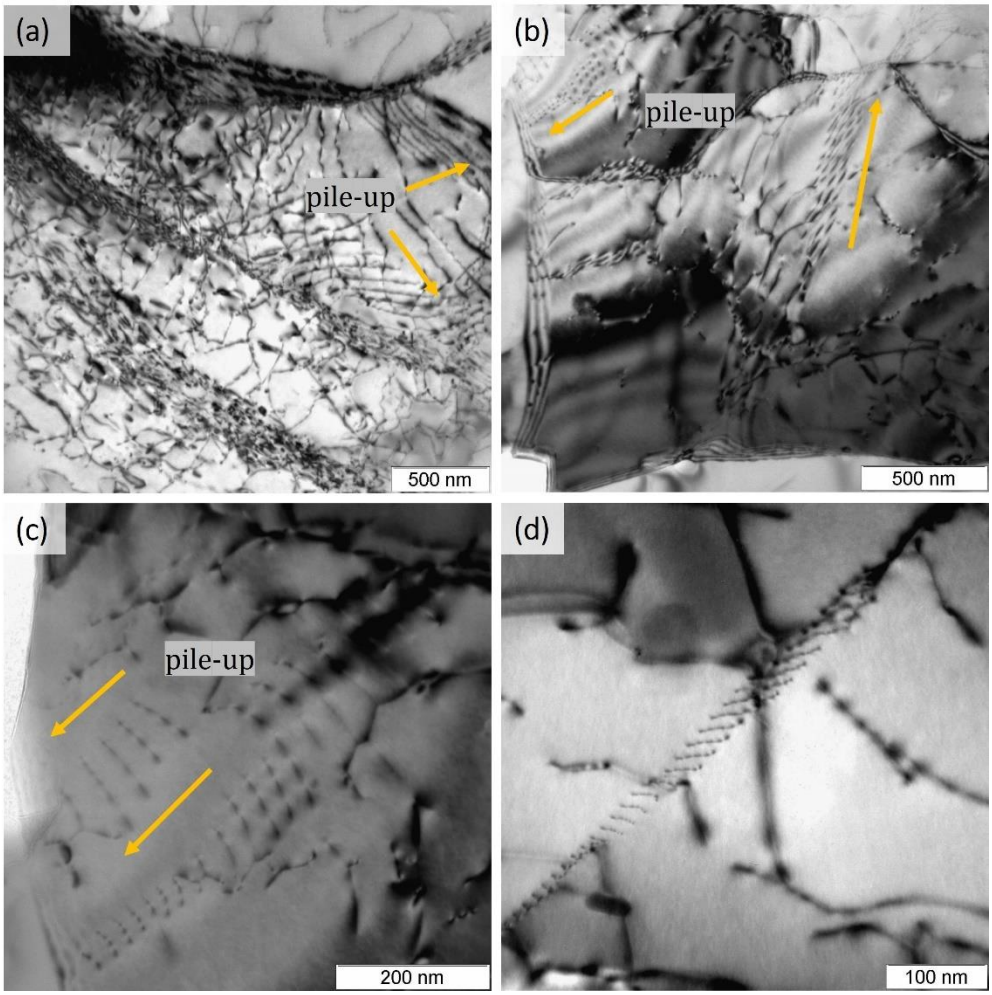

Figure 56: Selected TEM images from FS coatings: (a) 2 wt.% Mg alloy showing dislocation pile-up & dislocation tangles. (b) 12.1 wt.% Mg showing alloy showing dislocation pile-up. (c) 12.1 wt.% Mg alloy showing dislocation pile-up. (d) dislocation array of planar slip.

Figure 56 demonstrates selected brightfield images in which various lattice defects or microstructural appearances are visible. Figure 56 (a) & (b) show dislocations interacting with grain boundaries by forming arrangements of many dislocations oriented parallel to each other, piling up towards the grain boundary – therefore described in the literature as dislocation pile-ups [123]. Also, in Figure 56 (a) & (b) the densities of the dislocations within the dislocation pile-ups increase near the grain boundary. Presumably, the accumulations observed here can be attributed to the presence of a dislocation source (according to Frank-Read [19] [123]) from which the dislocations are generated [123]. In Figure 56 (c), these are presumably also dislocation pile-ups. However, these phenomena could represent dislocation arrays with planar slip as shown in Figure 56 (d). When dislocations move along the slip plane, they can leave a trail of new dislocations, resulting in the formation of a dislocation array. These do not accumulate near e.g. grain boundaries as in the case of pile-up.

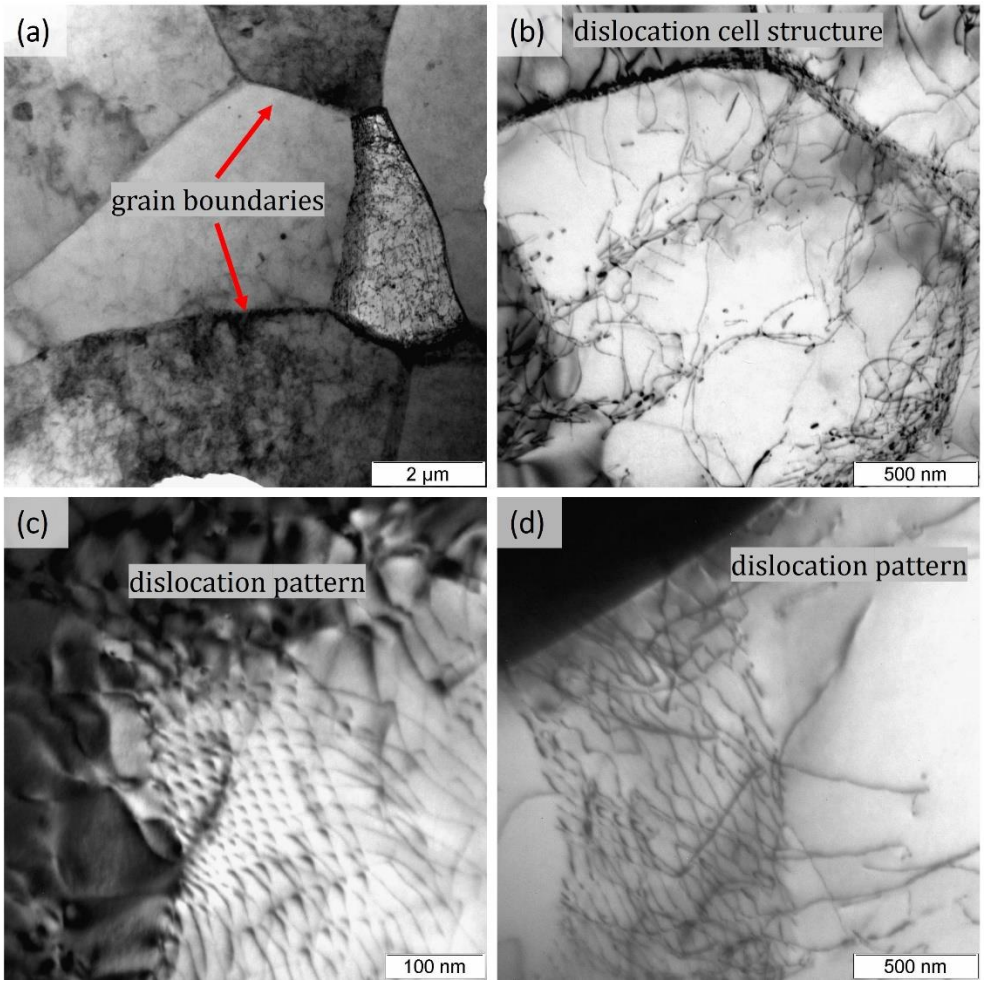

Figure 57: Selected TEM images from FS coatings: (a) 0.27 wt.% Mg showing grain boundaries. (b) 3.5 wt.% Mg showing the formation of cell structure. (c) 10.4 wt.% Mg showing formation of dislocation pattern. (d) 0.27 wt.% Mg showing formation of dislocation pattern.

Figure 57 reveals grain boundaries, dislocation cell structures, and dislocation patterns, all of which were found in all alloys. Fine recrystallized grains with distinct grain boundaries can be seen in Figure 57 (a). Figure 57 (b) illustrates the formation of a dislocation cell structure by dislocation accumulation. In Figure 57 (c) & (d) dislocation patterns can be observed. This could be part of the mechanism of grain subdivision, in which IDBs/dislocation walls form in the shape of planar dislocation patterns, something which is a sub-mechanism and an important indication of cDRX [20]. In general, the same dislocation mechanisms were observed in all alloys studied. It can also be observed that large secondary phase particles are not located at the grain boundaries but inside the grains. Fine Mg_2Si precipitates, e.g. GP-zones, β″ or β′-particles could not be detected by TEM. This is probably due to the lower atomic number of the Mg_2Si precipitates since elements with a low atomic number provide less of the contrast and are thus difficult to detect in the TEM. The intensity of the scattered electrons, and thus the resulting contrast, is proportional to the atomic number of the atoms locally present in the sample. Selected area electron diffraction on chosen large secondary phase particles also did not lead to reliable measurements due to the contrast deficits.

5.3.7 Secondary phase analysis

In identifying the phases contained in the Al-Mg-Si alloys, their chemical compositions are determined by means of EDX analysis as an average of several measurements and examined for matches with expected or plausible compounds. Primarily, the stoichiometric composition and, in inconclusive cases, additional criteria such as optics, arrangement and reaction kinetics are used to evaluate the composition. Potentially occurring phases are calculated with the software Thermo-Calc (Thermo-Calc Software AB, Solna, Sweden) for the multi-component system Al, Cr, Cu, Fe, Mg, Mn, Si, Ti, Zn (see Figure 58, Figure 59, Table 10). Not all the theoretically occurring phases can be detected within the scope of this thesis. This may be due to the fact that they are not formed in sufficient quantity or size to be detectable or measurable with SEM/EDX. The phase diagrams were simulated based on stable equilibrium conditions, which may differ from real conditions. In addition, the phase diagrams calculated by Thermo-Calc do not include oxidation processes. Oxide phases are analyzed by EDX.

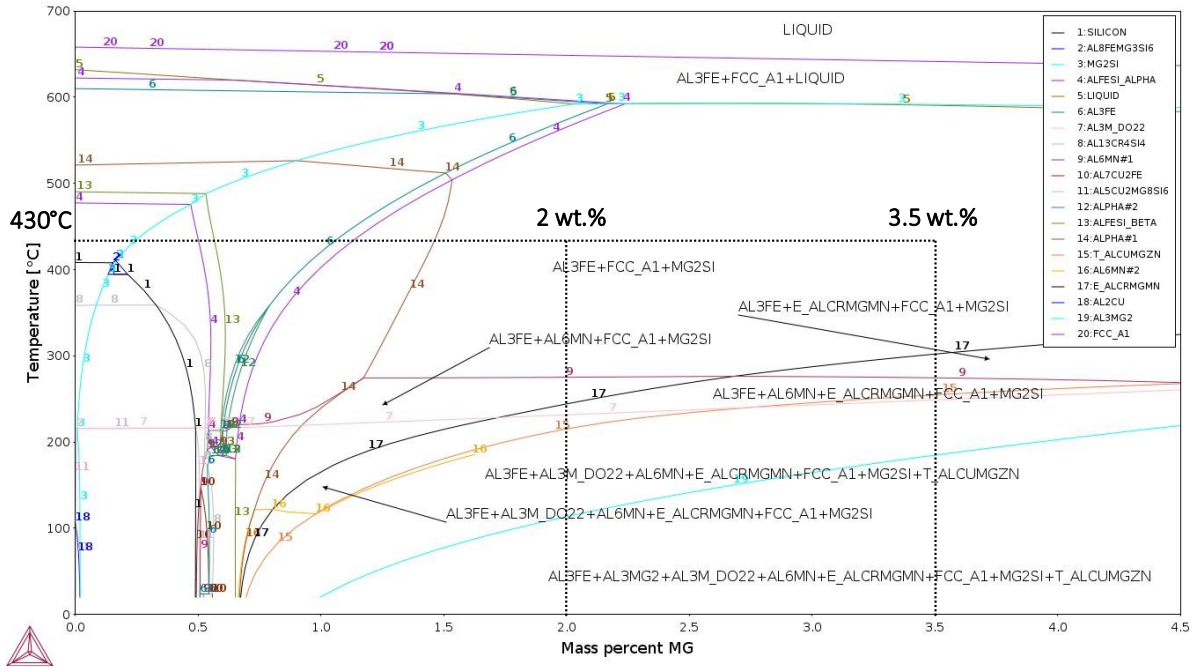

Figure 58: Al-Mg phase diagram for the multicomponent system Al, Cr, Cu, Fe, Mg, Si, Ti, Zn.

In the Al-Mg phase diagram, up to approx. 16 wt.% Mg can be dissolved in the α-matrix at a temperature of 430 °C (average maximum temperature occurring during FS). Note that the material is only heated to the maximum temperature for a few seconds.

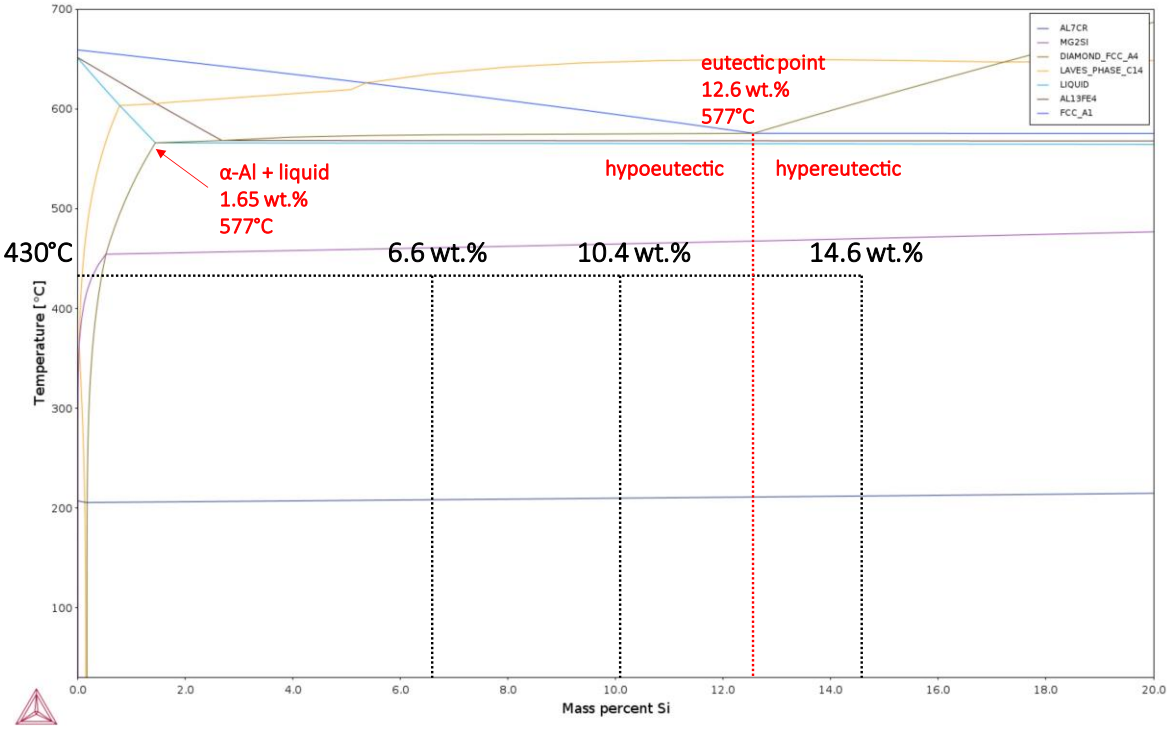

Figure 59: Al-Si phase diagram for the multicomponent system Al, Cr, Cu, Fe, Mg, Si, Ti, Zn.

The Al-Si phase diagram indicates that at the process temperature of 430 °C, a maximum of 0.8 wt.% Si can dissolve in the α-matrix. Table 10 lists the potentially occurring phases under equilibrium conditions for the multicomponent system depicted above [124]. Note that in the table only those phases are listed which are to be expected due to a high wt.% of various elements and taking into account the thermal exposure. Under ideal equilibrium conditions, other phases are possible (phases containing Cr, Mn, Ti and Zn), which are not considered in this thesis.

Table 10: Expected occurring phases for the multicomponent system Al, Cr, Cu, Fe, Mg, Si, Ti, Zn.

#	Thermo-Calc-Database	Phase
1	SILICON	Si
2	AL18FEMG3SI6	$Al_8FeMg_3Si_6$
3	MG2SI	Mg_2Si
4	ALFESI_ALPHA	α-AlFeSi
5	AL3FE	Al_3Fe
6	ALFESI_BETA	β-AlFeSi
7	AL2CU	Al_2Cu
8	AL3MG2	Al_3Mg_2(β)
9	FCC_A1	Al (fcc)
10	AL13FE4	$Al_{13}Fe_4$

5.3.7.1 α-Al matrix (EDX)

The Mg content in the α-matrix depends on the Mg-content of the respective alloy. This can be seen in the detailed EDX analyses in the area of the α-matrix (see inlets in images in Figure 60) as well as in the corresponding EDX maps, which were taken at 200x magnification. Visually, base material and

friction welded samples differ in phase morphology and α-Al. This is particularly evident in the alloys with 3.5 wt.% Mg and 10.4 wt.% Mg (see Figure 60 (b) & (e), (c) & (f)). In the EDX maps, the Mg-containing phases are mapped in red. A direct comparison reveals that the Mg phases in the base material are present in their needle-shaped or dendritic form and are distributed as finely distributed round Mg particles in the microstructure after the FS process. For the 10.4 wt.% Mg alloy in the BM state (Figure 60 (c)), 8.78% Mg was measured in the α-Al, while the same alloy in the FS state has 10.35 wt.% in the matrix. It is assumed that the EDX measurement area (blue frame) in Figure 60 (f) contains non-visible distributed Mg-containing phases. The α-Al of the alloys with 0.27 & 3.5 wt.% Mg reveals bright spots of varying size after the welding process, which do not significantly affect the measured chemical composition of the matrix areas. The cause of the optical differences is probably an inhomogeneous distribution of dissolved Mg [125]. Figure 60 displays selected exemplary SEM-EDX analyses/EDX maps only. The corresponding measurements of all Mg-containing alloys from 0.27-12.1 wt.% Mg are included in the appendix (Figure 85 & Figure 86). The secondary phases visible in the SEM images in Figure 60 are discussed in chapter 5.2.7.2, Secondary phases (EDX).

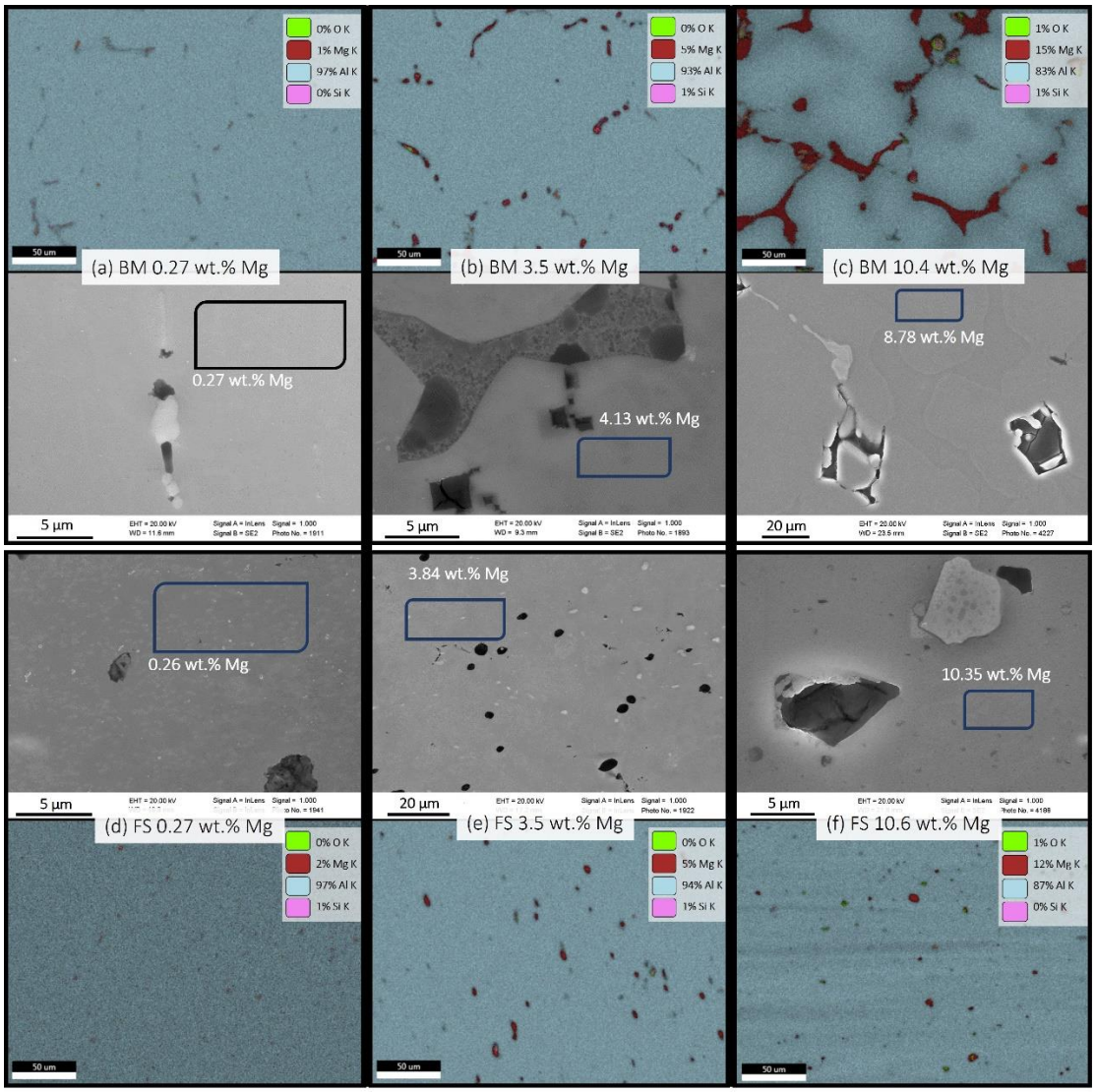

Figure 60: SEM-EDX analysis of α-Al phase & EDX maps in 200x resolution in base material (BM) state and Friction Surfacing (FS) state. BM: (a) 0.27 wt.% Mg, (b) 3.5 wt.% Mg, (c) 10.4 wt.% Mg. FS: (d) 0.27 wt.% Mg, (e) 3.5 wt.% Mg, (f) 10.6 wt.% Mg.

In the case of Si-rich alloys, on the other hand, where secondary phases form rapidly due to the low Si-solubility, low Si contents of 1.01-1.99 wt.% were measured in the detailed EDX micrographs in the α-Al (Figure 61). As expected, the EDX maps in Figure 61 indicate that with increasing Si content, the proportion of Si phases in the microstructure increases in a similar order of magnitude. In the BM state of the Si-containing alloys, it can be observed in both the SEM images and the EDX maps (Figure 61 (a), (b), & (c)) that the Si particles predominantly form needle shapes. The morphology of the Si particles in the microstructures in the FS state ((Figure 61 (d), (e), & (f)) is partly elongated, but mostly spheroidized by the process. However, the thermomechanical treatment by FS seems to have less influence on the shape of the large Si primary phases of the hypereutectic alloy with 14.6 wt.% Si. These adopt a similar morphology in both the BM and FS states (Figure 61 (c) & (f)). As in the analyzed light microscope images in chapter 5.3.1, Particles in base & coating material, it can be observed in the EDX

maps that the Si secondary phases are finely distributed and almost spherical in the FS material state. Optical differences with regard to the α-Al could not be identified in the Si-rich alloys.

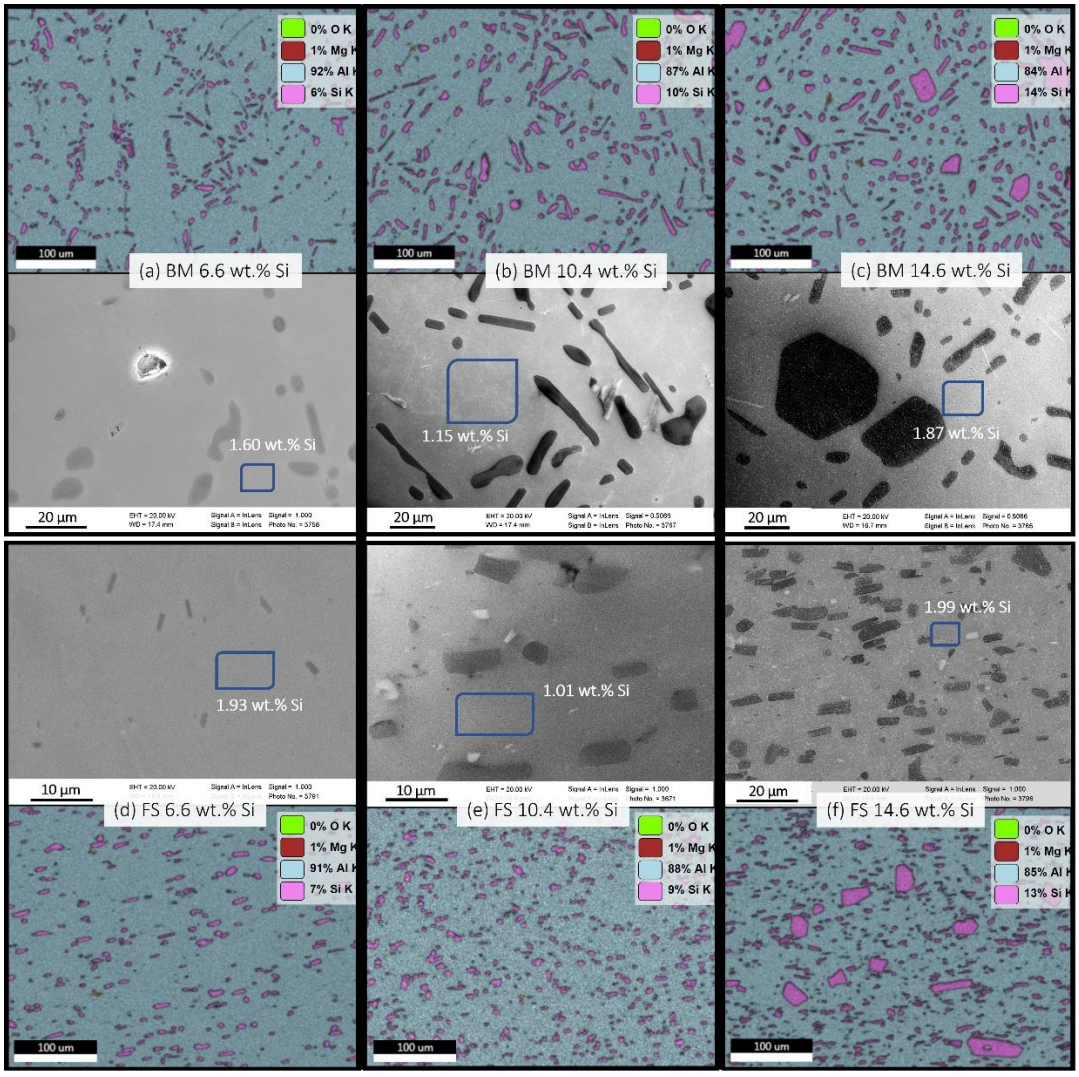

Figure 61: SEM-EDX analysis of α-Al phase & EDX maps in 400x resolution in base material (BM) state and Friction Surfacing (FS) state. BM: (a) 6.6 wt.% Si, (b) 10.4 wt.% Si, (c) 14.6 wt.% Si. FS: (d) 6.6 wt.% Si, (e) 10.4 wt.% Si, (f) 14.6 wt.% Si.

5.3.7.2 Secondary phases (EDX)

The amount of Al analyzed is difficult to quantify due to the high proportion of Al in the surrounding α-Al matrix. Therefore, elements that are not measured in the matrix material or in strongly deviating amounts are of particular interest. For 6000 series aluminum alloys, the formation of the AlFeSi phase is an important aspect of the microstructure. This can occur as α-AlFeSi or β-AlFeSi phase. β-AlFeSi is characterized by a plate-like appearance and can negatively influence the mechanical properties. Furthermore, the α-AlFeSi or β-AlFeSi phases can adopt different stoichiometries, which can be determined by the measured Fe/Si ratio of the respective phase. On this basis, the atomic ratio of iron to silicon (Fe/Si) β-AlFeSi can be used. α-AlFeSi phases exhibit a higher Fe/Si ratio than β-AlFeSi phases [126]. For example, an α-Al_8Fe_2Si (2/1) or β-Al_5FeSi (1/1) phase can be derived in a measuring range from the chemical percentages of Al, Fe, Si measured by EDX. From studies on the alloy AA6063, it

appears that β-Al_5FeSi dissolves or remains as α-Al_8Fe_2Si rest from homogenization (585 °C, up to 720min) [127]. Figure 61 provides selected microstructures with the determined secondary phases of the Mg-containing alloys in the BM and FS states. Since the base materials were homogenized under similar parameters (535 °C, 72h), and the averaged Fe/Si ratio of 1.8 is significantly greater than 1/1, the Al-Fe-Si containing secondary phases appear to be α-Al_8Fe_2Si.

In the FS samples, Al-Fe-Si can be found in the initial alloy AA6060 at 0.27 wt.% Mg with an Fe/Si ratio of 0.684 (Figure 61 (a) & (e)). This composition matches the phase β-Al_5FeSi. Phases containing Mg and Si were identified only sporadically. The Al_3Fe phase could be identified in both the BM and the FS state alloys, as none of the other phases determined by Thermo-Calc corresponds to the determined chemical composition. In the BM, it can be described as a "Chinese script"-like form of appearance (see Figure 61 (c) & (d)). In the FS state, Al_3Fe phases have a more compact form with an aspect ratio closer to 1 (see Figure 61 (f)). It is assumed that, due to the low Mg_2Si excess and the solubility of Mg_2Si in α-Al at 430 °C of approx. 0.3-0.5 wt.%, the majority of this phase is either dissolved in the α-Al matrix or has formed as finely distributed precipitates in the nm range. Only in Figure 61 (a), in the initial alloy with 0.27 wt.% Mg, secondary phases could be classified as Mg_2Si. However, further secondary phases containing MgSi were measured by EDX, but the Mg/Si ratio did not match Mg_2Si. These phases were labelled accordingly and can be observed as MgSi containing secondary phases in Figure 61 (b) & (f). Al_3Mg_2 could be detected in the alloys with Mg content of 8.9 wt.% and above. For the alloy with 10.6 wt.% Mg BM, Al_3Mg_2 was determined in Figure 61 (c). Phase analysis in the FS samples proved to be more difficult due to the shearing of the phases that occurred as a result of the thermomechanical treatment during the process. As a consequence, they are present in the microstructure in a finely dispersed (stirred) or transformed form. For example, the Al_3Mg_2 phase could only be detected in the alloys above 8.9 wt.% Mg in the BM state.

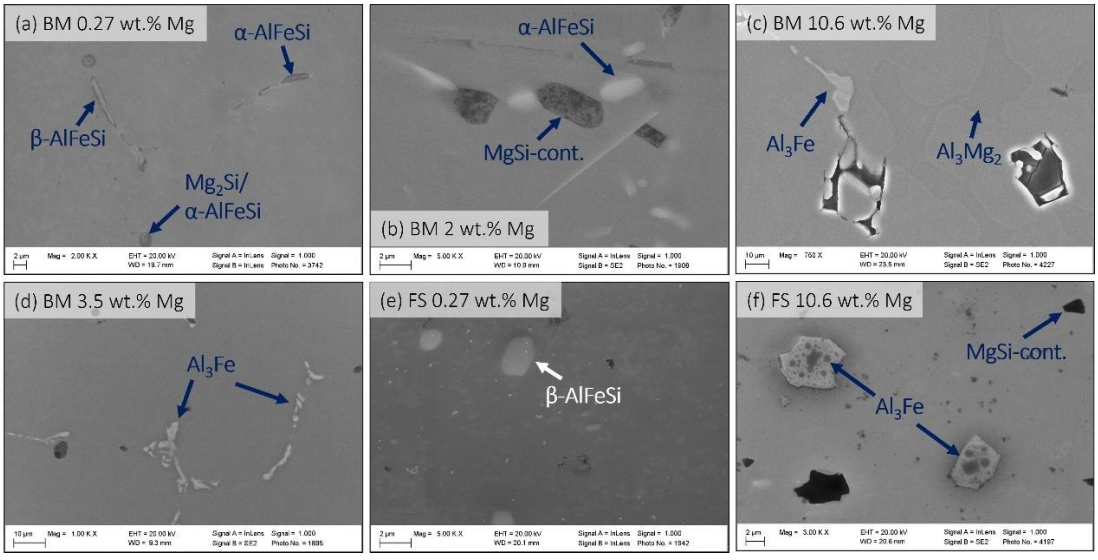

Figure 62: SEM-EDX analysis of occurring secondary phases in the microstructure for selected Mg – containing alloys in base material (BM) state and Friction Surfacing (FS) state. BM: (a) 0.27 wt.% Mg, (b) 2 wt.% Mg, (c) 10.6 wt.% Mg, (d) 3.5 wt.% Mg. FS: (e) 0.27 wt.% Mg, (f) 10.6 wt.% Mg.

Figure 62 presents selected microstructures with the identified secondary phases of the Si-containing alloys in the BM and FS states, a finding which is representative of the EDX analyses of the Si-containing alloys. Regardless of the material state (BM & FS), finely distributed Si particles could be detected in all samples containing Si. In the two hypoeutectic alloys (6.6 wt.% Si & 10.4 wt.% Si), the Si particles are exclusively finely distributed in the microstructure (see Figure 62 (a), (b) & (c)). In the hypereutectic alloy (14.6 wt.% Si), on the other hand, large primary Si particles are also found in the microstructure in addition to fine Si particles (Figure 62 (d)). Similar to the Mg-containing alloys, AlFeSi phases could also be determined. However, in the Si-containing alloys, only β-AlFeSi with a lower Fe/Si (1/1) ratio could be detected in the analyzed phases. In the BM materials, these take on needle-shaped configurations (Figure 62 (b)), but also "Chinese script"-like configurations (Figure 62 (a) & (c)). In the FS state, the AlFeSi phases are finely distributed with a higher aspect ratio (close to 1). Al_3Fe phases could not be detected in the Si-containing samples. The other phases expected from Thermo-Calc diagrams for the multi-component system, such as phases containing Cu, Cr, Mn, Zn, for instance, could not be detected within the EDX analysis. Possible reasons for this could be the low wt.% of the respective elements of multi-component phases or that not enough EDX measurements were carried out for them to be found.

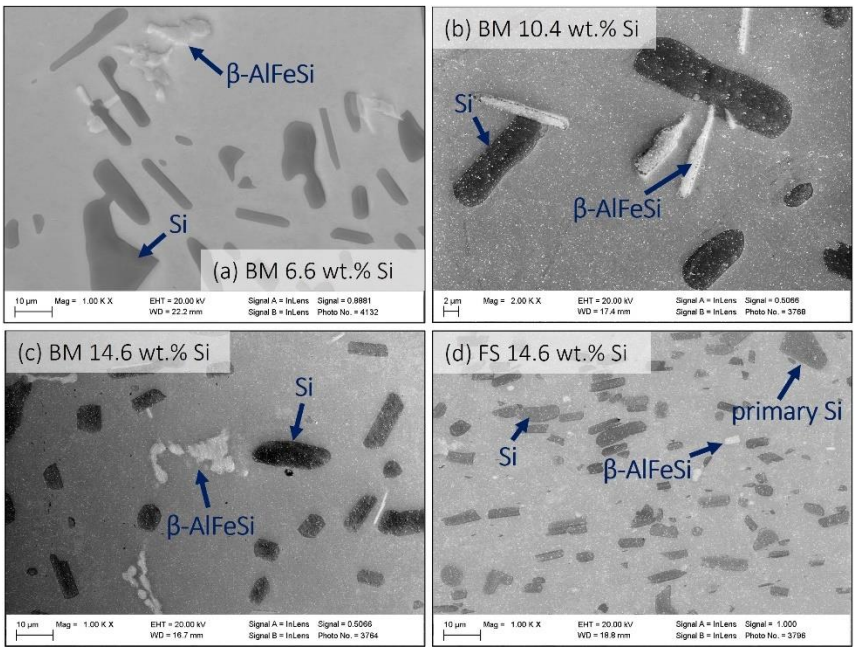

Figure 63: SEM-EDX analysis of occurring secondary phases in the microstructure for selected Si – containing alloys in base material (BM) state and Friction Surfacing (FS) state. BM: (a) 6.6 wt.% Si, (b) 10.4 wt.% Si, (c) 14.6 wt.% Si. FS: (d) 14.6 wt.% Si.

5.3.7.3 Oxides in Al-Mg-Si (EDX)

All further identified phases are affected by the presence of oxygen. Thus, their composition differs from the phases determined by Thermo-Calc. Moreover, O_2 is not considered in the database used by Thermo-Calc [124]. In general, the EDX analysis of oxygen also has higher inaccuracies than other elements because the characteristic K-transition of oxygen (O K) is outside the usual calibration range

for the energies used to identify the elements. In addition, the photon energy peaks of O K are particularly low and may exhibit non-linear behavior [128]. Conventionally, the wavelength-dispersive spectroscopy (WDS) or X-ray diffraction (XRD) techniques are used to determine oxide phases in metallic microstructures. In order to be able to make valid statements with regard to O-containing phases despite the issues described, the oxygen content is not considered in isolation, but it is put into relation with other samples. If a phase can be identified as particularly rich in oxygen, the stoichiometric composition is roughly inferred based on the ratios to the other elements contained in the phase. This is compared with known compounds occurring in a similar context. In Al-Mg-Si alloys, the oxide inclusions Al_2O_3, SiO_2, MgO, $MgAl_2O_4$ (spinel) are observed. Al_2O_3 does not have a fixed crystal structure but can exist as μ-, γ-, δ-, θ- and α-Al_2O_3 depending on the conditions and time of formation [129]. The oxidation tendency of the material increases depending on the Mg content [129]. In the investigation, three Si-containing oxide phases can be identified, which are similar in composition (Figure 64 (a), (c) (b)). Compared to the surrounding matrix, the Si content and the oxygen content are increased. Based on the O/Si ratio, the oxygen compounds can be identified as SiO_2 (↑O, ↑Si), Al_2O_3 (↑O, ↓Si), and a mixed phase of Al_2O_3 and SiO_2. The O/Si ratio of the mixed phase corresponds to that of silicate or aluminosilicate. Since silicates are not described as a common oxidation product in Al alloys, the mixed phase is assumed to be Al_2O_3, which is formed from reaction with SiO_2 as follows [130]:

$$3\ SiO_2 + 4\ Al \rightarrow 2\ Al_2O_3 + 3\ Si$$

as well as directly from Al:

$$4\ Al + 3\ O_2 \rightarrow 2\ Al_2O_3$$

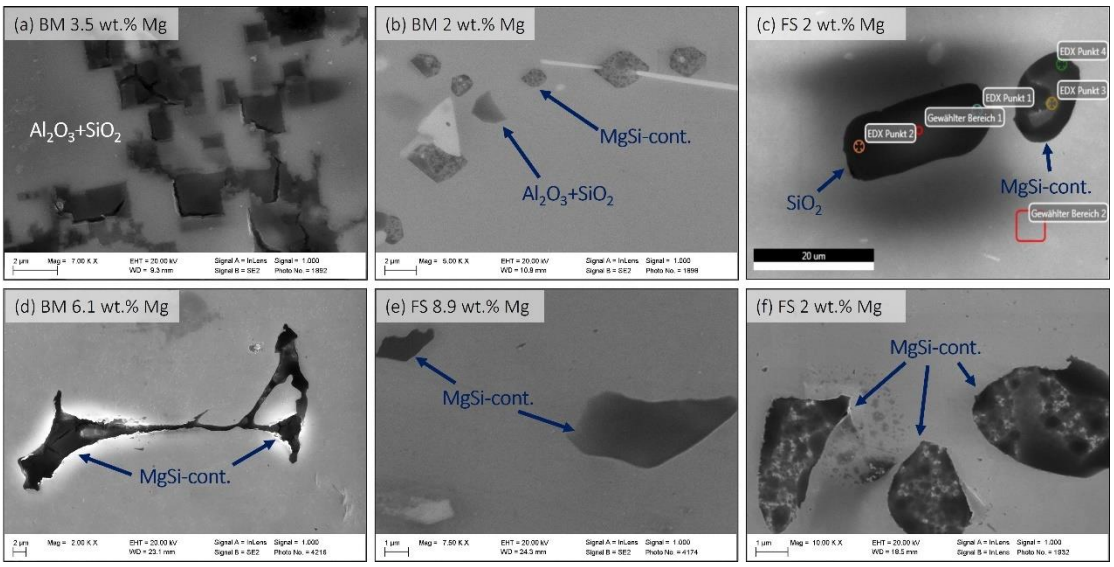

Figure 64: SEM-EDX analysis of occurring oxide phases in the microstructure for selected alloys in base material (BM) state and Friction Surfacing (FS) state. BM: (a) 3.5 wt.% Mg, (b) 2 wt.% Mg, (d) 6.1 wt.% Mg. FS: (c) 2 wt.% Mg, (e) 8.9 wt.% Mg, (f) 2 wt.% Mg.

Furthermore, phases with increased Mg and Si concentration were identified, which can be Mg_2Si. These phases are composed of several optically distinguishable parts (Figure 64 (d), (e) &(f)). The presence of oxygen impairs the formation of Mg_2Si, and the reaction of pure Mg with Si does not take place primarily, but the oxidation of Mg to MgO does. Pure Mg_2Si is synthesized via the reduction of SiO_2. Depending on the reaction time, reaction temperature and stoichiometric composition, the reaction proceeds in favor of one of the following products [131]:

$$2\ Mg + Si \rightarrow Mg_2Si$$

$$SiO_2 + 2\ Mg \rightarrow Si + 2\ MgO \qquad \text{(Si excess)}$$

$$SiO_2 + 4\ Mg \rightarrow Mg_2Si + 2\ MgO \qquad \text{(Mg excess)}$$

The constituents of the phase to be identified are allocated to the preferentially formed intermediates, reactant or product by means of their chemical composition and the ratios of Mg, Si and O since it is assumed that the reaction has not proceeded completely. The EDX-maps in Figure 65 reveal phases in the 3.5 wt.% Mg alloy, which are composed of parts of MgO, Mg_2Si, Si and SiO_2. Figure 65 (a) displays the distributions of the elements within a single secondary phase particle at 8kx magnification. In Figure 65 (b), several multi-material phases containing oxides can be seen in 1000x magnification, and additional Al_3Fe phases can be detected.

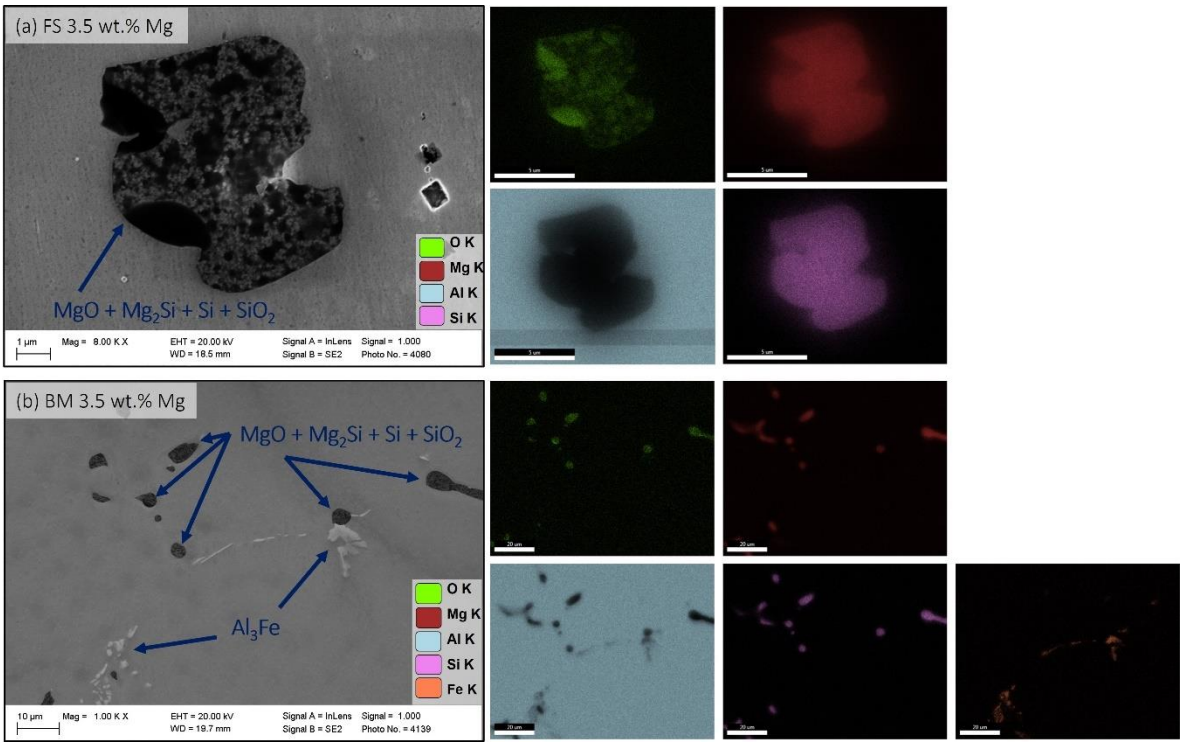

Figure 65: SEM-EDX analysis / EDX maps of occurring oxide phases for selected alloys in base material (BM) state and Friction Surfacing (FS) state. BM: (a) 3.5 wt.% Mg. FS: (b) 3.5 wt.% Mg.

Oxide-containing phases could be detected in all Mg-containing alloys regardless of the state. Significantly fewer oxide-containing phases were detected in the Si-containing alloys. Only in the alloy

with 6.6 wt.% Si BM and in the one with 14.6 wt.% Si FS portions of SiO and Al_2O_3 were distinctly detectable. The secondary phases and intermetallics or oxide compounds for all alloys, both in BM and FS state, identified by means of EDX investigations, are summarized in Table 11.

Table 11: Summary of all identified phases

	Si	α-AlFeSi	β-AlFeSi	Al_3Fe	Al_3Mg_2	Mg_2Si	SiO_2/ Al_2O_3	MgO/ (Mg_2Si)/ SiO_2
BM								
AA6060		x						x
2 wt.% Mg		x		x		x	x	x
3.5 wt.% Mg		x		x			x	x
6.4 wt.% Mg				x				x
8.9 wt.% Mg				x	x			x
10.6 wt.% Mg				x	x			x
12.1 wt.% Mg				x	x			x
6.6 wt.% Si	x		x				x	
10.4 wt.% Si	x		x					
14.6 wt.% Si	x		x					
FS								
AA6060			x					x
2 wt.% Mg				x			x	x
3.5 wt.% Mg				x			x	x
6.4 wt.% Mg				x				x
8.9 wt.% Mg				x	x			x
10.6 wt.% Mg				x	x			x
12.1 wt.% Mg				x	x			x
6.6 wt.% Si	x		x			x		
10.4 wt.% Si	x	x				x		
14.6 wt.% Si	x		x				x	

5.3.7.4 Formation of β (Mg_2Si) precipitates (DSC)

The corresponding reaction directions are highlighted in the diagrams with an arrow "exo" for exothermic. For instance, even if a part of the curve lies in the endothermic range and produces a peak in the direction of exothermic, this is to be assigned to an exothermic reaction. The following DSC curves are interpreted based on the directions of the respective peaks and their characteristics rather than on absolute values. The temperature-dependent excess-specific heat capacity curve for the initial alloy AA6060 base material and FS state is shown in Figure 66. The curve starts with a small exothermic peak A at 90 °C. This peak is generally considered to be the formation of Si/Mg co-clusters. In this process, supersaturated solid solution Si and Mg atoms rapidly diffuse in the pre-generated vacancies, forming small Si- and Mg-clusters. Peak B is not clearly recognizable in Figure 66. Edwards et al. [132] found, that weak exothermic reactions occur in a wide temperature range from room temperature to 180 °C, which is due to the formation of GP(I) zones. In addition, it is assumed that the exothermic excess heat capacity is caused by the formation of precipitates of still unknown structure and/or vacancy condensation of the co-clusters [132]. This is followed by the endothermic peak C at approx. 215 °C, which indicates the dissolution of previously formed clusters, and is indicated for the red curve (AA6060 FS) in Figure 66. Instead, the black curve (AA6060 BM) indicates an early exothermic double peak in this temperature range, which results in the D peak. Thus, the endothermic peak C cannot be identified for the black curve. The exothermic peak D at 250 °C includes the formation of GP(I) zones and β" precipitates. The fine, coherent, needle-shaped β" precipitate is responsible for most of the hardness increase. In the case of pre-aging, the formation of β" precipitates is favored over GP(I) zones [1].

During the transition from SSSS to β" precipitation, additional intermediate and transitional phases can form; the occurrence of these strongly depends on the proportion of vacancies [1] [81]. It is assumed that the two following exothermic peaks at 300 °C (peak E) and at approx. 370 °C (peak F) are related to the formation of β′, U1, U2, B′ [133] [134]. According to Matsuda et al. [134], the first peak E is related to the formation of β′ and peak F is due to β′, U1, U2, B′. The endothermic peak G at approx. 400-450 °C is probably caused by the dissolution of previously formed phases β′, U1, U2, B′. The less distinct exothermic peak at approx. 470-490 °C (peak H) is related to the precipitation of the equilibrium phase β. In the literature, dissolution reactions of all previously formed phases are expected at temperatures above 500 °C [135]. This endothermic peak I is not clearly detectable in Figure 66. In summary, the DSC curves of the initial AA6060 alloys in the BM and FS states differ in their peak positions and in the expression of their peaks. Peak A & B are almost not recognizable in both conditions. From about 160 °C to about 215 °C, the red curve indicates an endothermic reaction (peak C) which can be attributed to Si/Mg co-cluster dissolution. This is not pronounced in the BM state, instead an early (from approximately 200 °C) GP(I) zone and β″ precipitates formation takes place. In general, the peaks shift to higher temperatures as the heating rate increases.

Although all experiments were performed at the same heating & cooling rate, there seems to be a shift of the D peak of the BM alloy to lower temperatures. The high maximum welding temperatures of about

450 °C cause the dissolution of small β″ precipitates. Thus, more dissolved elements are present in total for subsequent re-precipitation in the FS alloy. As a result, the D & E peaks are more pronounced in the FS alloy. At the same time, the larger precipitates begin to grow, leading to the formation of β′, U1, U2, B′ in the temperature range from 250 to 400 °C.

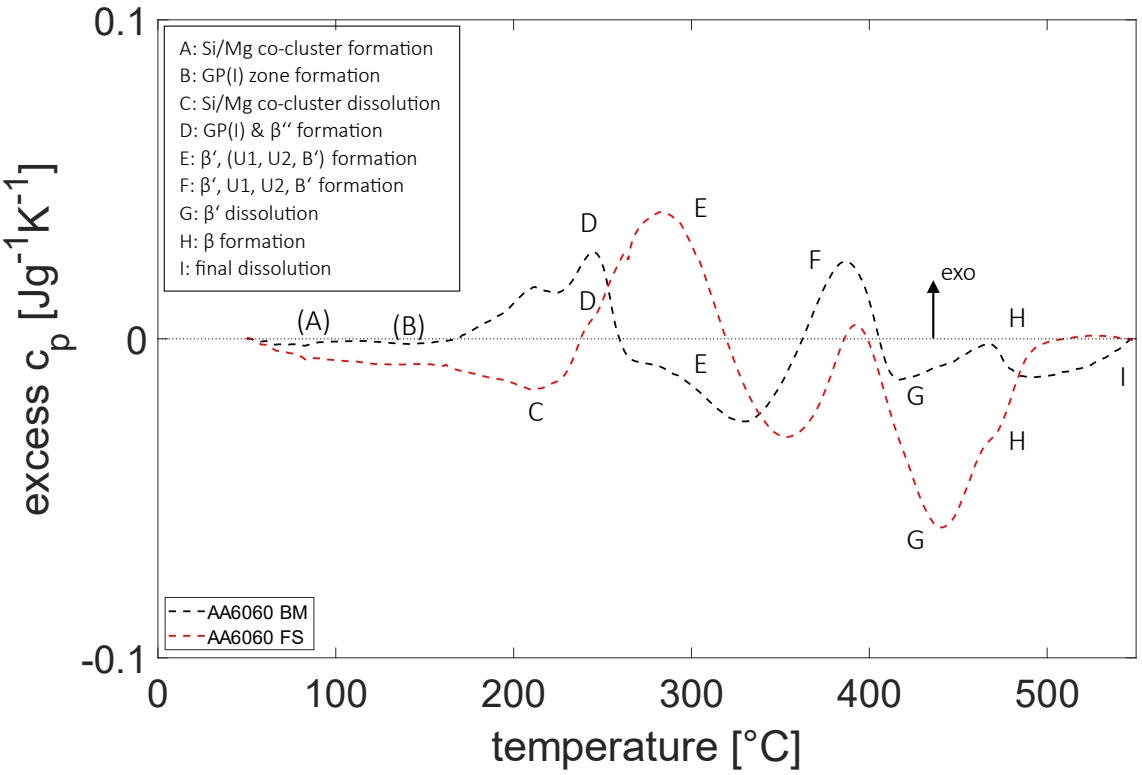

Figure 66: DSC curves of AA6060 in the BM (black) and FS (red) conditions.

DSC curves for each of the three Si-rich alloys before and after the FS process are presented in Figure 67. The precipitates of the metastable phases β″ and β′, which are described by the exothermic peak D and the exothermic peak E, are noticeable. In the alloys with 6.6 wt.% Si and 10.4 wt.% Si, these are only pronounced as double peaks in the FS state. Gaber et al. have demonstrated [136] that when the atomic ratio of Mg to Si is greater than 1.25, the two exothermic peaks of the β″- and β′-precipitates have a large overlap and are therefore difficult to distinguish. When the Si content increases, the difference between the two exothermic peaks of the β″- and β′-precipitates becomes more distinct [137]. A lower atomic ratio of Mg to Si results in the exothermic peaks of the β″- and β′-precipitates being formed by two separate peaks. The exothermic peak D of the β″ phase decreases after the FS process, while the exothermic peak E of the β′ phase increases significantly after the FS process. This indicates that part of the β″-phase has been converted to the β′-phase during the FS process.

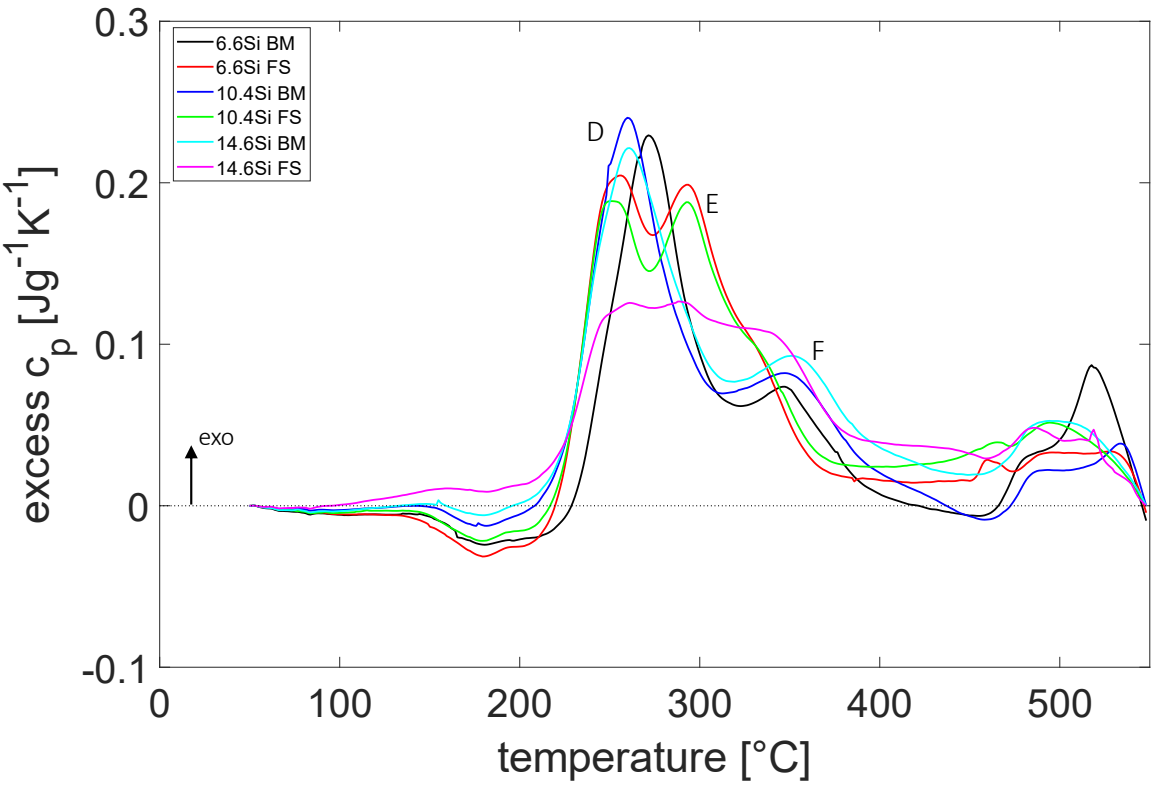

Figure 67: DSC curves of 6.6 wt.% Si, 10.4 wt.% Si, & 14.6 wt.% Si alloys in the BM and FS conditions.

Analogously, the DSC curves of the Mg-containing alloys with 2 wt.% and 3.5 wt.% in the BM and FS state are analyzed in Figure 68. The precipitates of the metastable phases β″ and β′, which are described by the exothermic peak D, the exothermic peak E and the exothermic peak F, are compared. According to [136], at high atomic ratios of Mg to Si, the two exothermic peaks of the β″ and β′ precipitates will exhibit less overlap, which the alloys display exclusively in the BM state. Firstly, the peaks E (β′ precipitation) in both alloys are not detectable in the FS state. Secondly, the peaks D (β″ precipitation) seem to be more pronounced in both alloys in the FS state than in the BM state. Thirdly, the peaks F (β′, U1, U2, B′ formation) are significantly more prominent for the alloys in the FS state. In summary, due to the high maximum welding temperatures of about 450 °C, the dissolution of small β″ precipitates with subsequent re-precipitation (peak D) after welding is expected. Simultaneously, the larger precipitates begin to grow, leading to β′, U1, U2, B′ formation in the temperature range from 250 to 450 °C. Above a maximum welding temperature of 450 °C, complete dissolution of the β″ precipitates can be assumed.

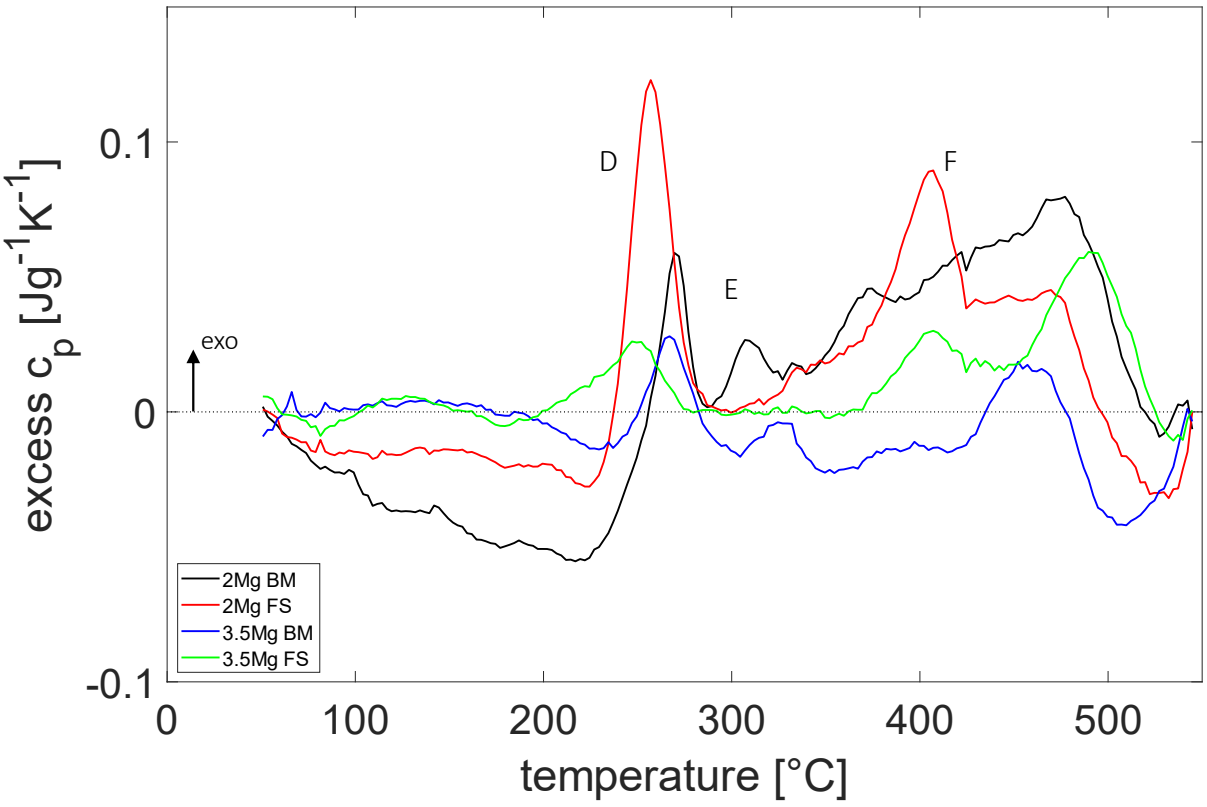

Figure 68: DSC curves of 2 wt.% Mg & 3.5 wt.% Mg alloys in the BM and FS conditions.

5.3.8 Microhardness evolution

The mean hardness values of the FS samples are compared with those of the corresponding base material of the various Mg-rich and Si-rich alloys. For this purpose, average values with standard deviations were calculated for FS coatings via hardness maps on the cross-section (DD direction); for the base materials, 5 data points were measured from the cast stud materials. Figure 69 & Figure 70 present the hardness values versus the content of alloying element Mg and Si. With increasing Mg content in the aluminum base alloy, the hardness increases. Moreover, the alloys in the FS condition exhibit a higher hardness values compared to the BM state. At 0.27 wt.% Mg in the BM condition, the hardness is 35±2.6 HV0.2 while the FS condition has a hardness value of 41.2±1.3 HV0.2. At 12.1 wt.% Mg, the highest hardness is reached in both the BM (with 95.9±6.3 HV0.2) and FS (with 113.8±1.6 HV0.2) states. The hardness in the FS condition is approx. 15-23.5% higher than in the BM condition, depending on the Mg addition (see Figure 69).

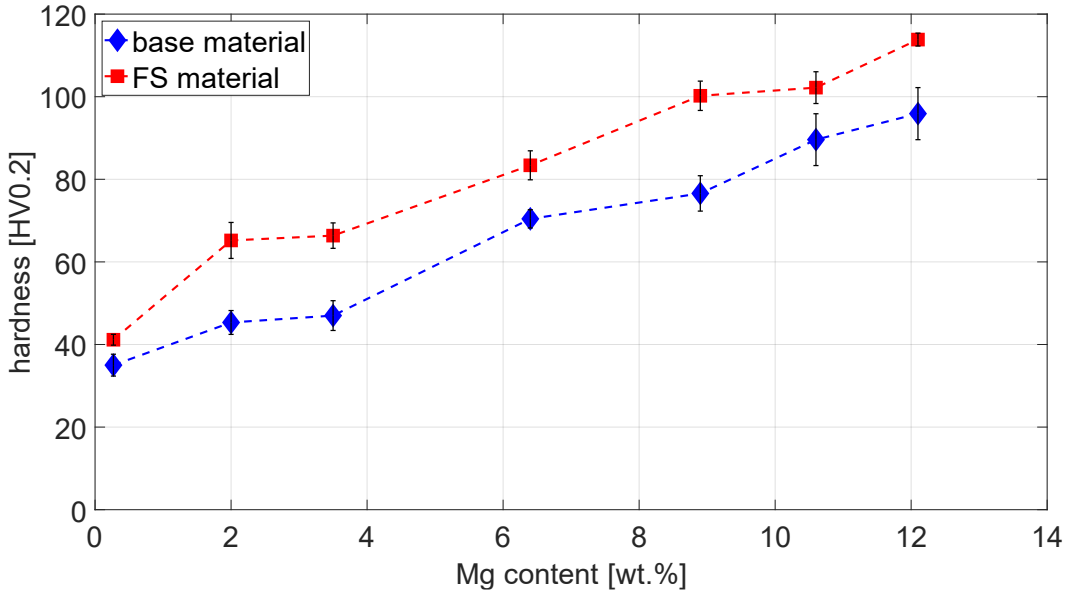

Figure 69: Hardness versus Mg content for base material (BM) and Friction Surfacing material (FS) condition.

Figure 70 illustrates the hardness versus Si content for the alloy in the BM and FS states. Similar to the Mg-containing alloys, the hardness increases with increasing weight percent of the alloying element Si, i.e. from 0.37 wt.% Si with a hardness in the BM condition of 35±2.6 HV0.2 and in the FS condition of 41.2±1.3 HV0.2, to 76±2.1 HV0.2 in the BM and 83.4±3.5 HV0.2 in the FS condition at 14.6 wt.% Si. The hardness differences between BM and FS condition are less pronounced in the Si-rich alloys. For example, the alloy with 10.6 wt.% Si in the BM condition displays a hardness value about 4 HV0.2 higher than the same alloy in the FS condition.

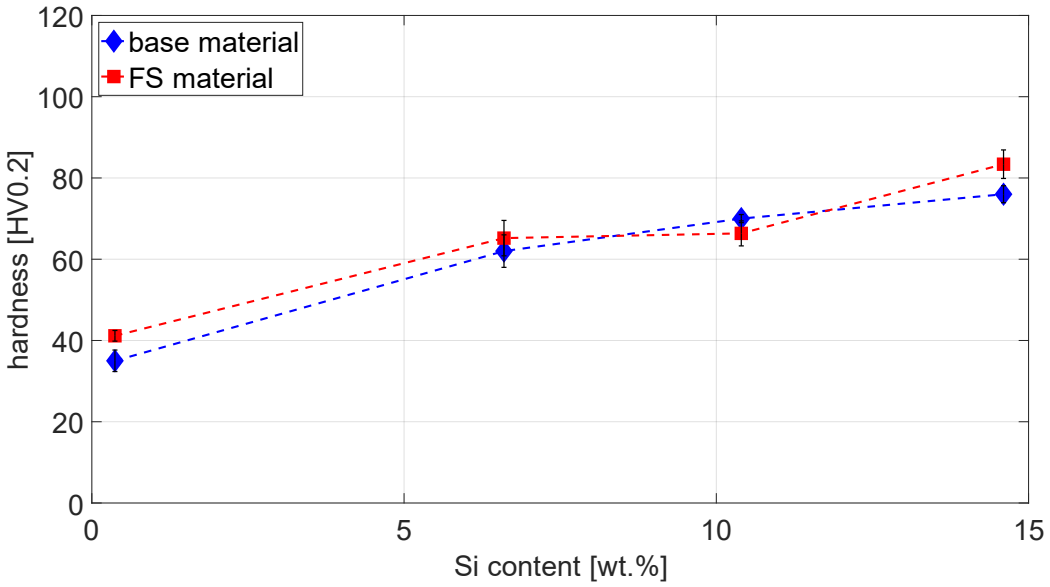

Figure 70: Hardness versus Si content for base material (BM) and Friction Surfacing material (FS) condition.

The distribution of the microhardness over the cross-section of the coating is illustrated in Figure 71 (a). This figure can be considered as representative for all processed alloys since the different hardness zones and trends are always comparable. The graphs exemplify the hardness contour plot as well as the hardness profiles from RS to AS (Figure 71 (b)) and from bottom to top (Figure 71 (c)) of the deposited coating for the initial alloy AA6060. The hardness indentations were placed at high resolution in measurement points at a distance of 0.3mm x 0.3mm to each other. The zone of minimum hardness of the 3.2±0.16 mm thick deposited coating lies in the center with hardness values of approx. 39 HV0.2. The highest hardness values can be observed in the contour plot around the upper part of the coating with around 44 HV0.2. The hardness progression from the RS to the AS (Figure 71 (b)) follows a fluctuating curve, which levels off at hardness values between 40and41.5 HV0.2. This trend could not be confirmed for all alloys. However, tendencies of higher hardness values were observed in the edge areas of AS and RS compared to the center. The hardness profile measured in the center, from the bottom to the top of the coating (Figure 71 (c)), seems to display a slightly increasing trend, which is recognizable in all samples. The maximum hardness for the sample illustrated lies at a range of 42.8±0.8 HV0.2 in the upper area.

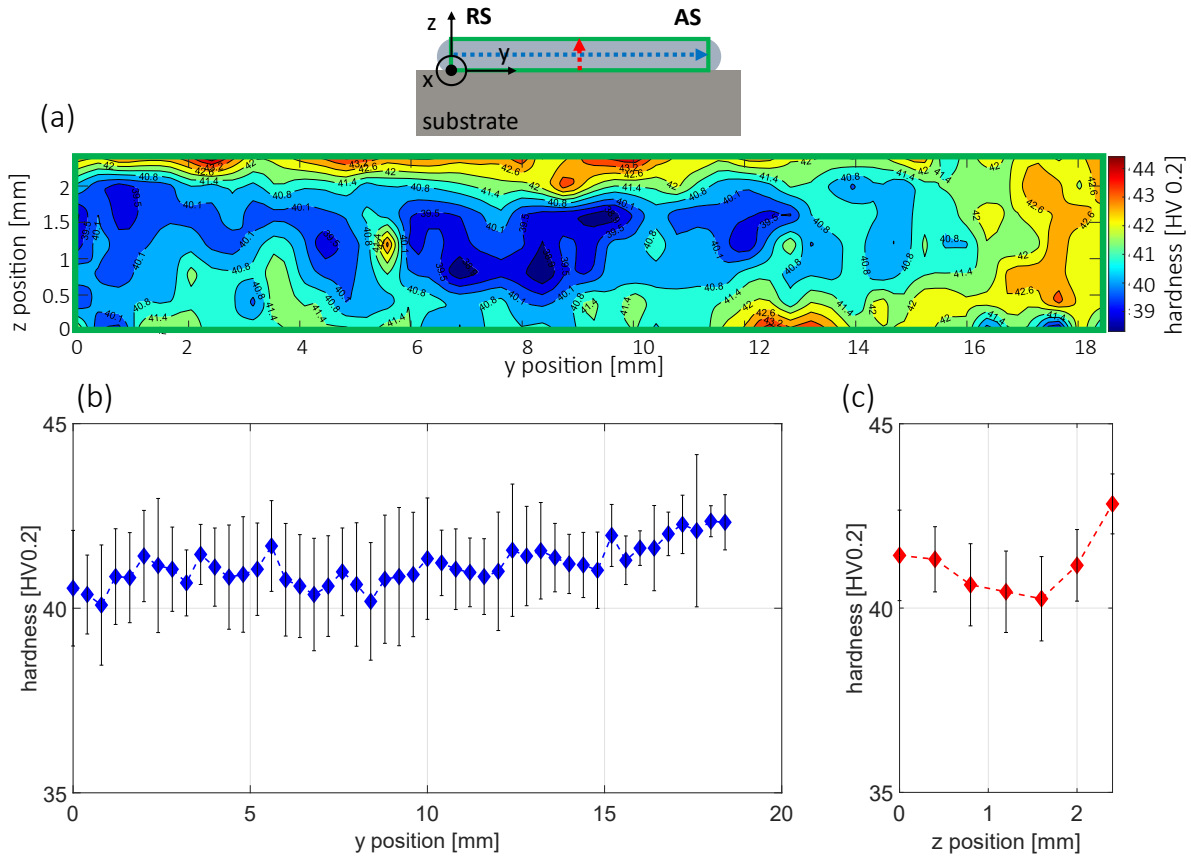

Figure 71: Distribution of microhardness over the cross-section of a AA6060 coating as contour plot (a). Averaged hardness profiles measured at half height of the coating from RS to AS (b) and in the center from bottom to top (c) for the initial alloy AA6060.

Figure 72 depicts in (a) the schematic diagram of a stop-action trial in cross-section view of the AA6060 alloy, highlighting therein the measuring ranges for the hardness profile plots in the area of the stud (green) and the coating (red) as well as the averaged hardness profile from the top edge of the stud to the bottom edge of the coating (dashed blue line). The resolution of the hardness indentations is 1mm x 1mm. The regions of the flash are not included in the diagram. Likewise, the hardness values of the substrate, consisting of the high-strength aluminum alloy AA2024, are not the subject of this study and therefore not included in the evaluation.

Figure 72 (b.1) presents the hardness contour diagram of the stud. The average hardness of the as-cast stud, which was heated by the FS process but not mechanically processed, appears to settle at 40–45 HV0.2. Apart from this, individual zones of higher hardness can be observed, such as at z = 9 mm; y =9 mm or z = 15; y = 8 mm. In these areas, hardness values of up to approx. 60 HV0.2 were measured. These local hardness data are obtained by measurements near accumulations of intermetallic phases or segregations or unfavorable hardness indentations near voids or pores. Representative of the alloys processed in this study, it can be stated that only a slight tendency of decreasing hardness can be observed towards the deposited coating or in the not yet recrystallized area of the stud. Figure 72 (b.2), on the other hand, illustrates the hardness contour diagram of the coating. As in Figure 71, it shows the as-cast AA6060 alloy in the deposited coating condition. Here, a lower resolution of the hardness

indentations was used (1mm x 1mm), so the tendencies described above are less apparent. The average hardness values are approximately 44-47 HV0.2. As described above, a slight trend towards decreasing hardness in the coating bottom area is also evident. The averaged hardness profile from the upper edge of the stud (green shaded) to the lower edge of the coating (red shaded) is plotted in Figure 72 (c). To calculate the curve, the values of 7 hardness indentations shown in Figure 72 (a) were averaged along the centerline of the stud and coating and then plotted. Due to the defects such as pores within the microstructure, the hardness values fluctuate between 42 and 47 HV0.2. For all stop-action specimens (AA6060, 2 wt.% Mg, 3.5 wt.% Mg, 6.6 wt.% Si, 10.4 wt.% Si, 14.6 wt.% Si), a slight hardness decrease was observed in the heat-affected zone of the stud, which starts about 4 mm above the coating. For the alloy AA6060, which is representatively illustrated here, the values lie in the range 41.8-43.2 HV0.2. In the recrystallized coating material, the average hardness values increase again to approximately 45.5 HV0.2. As it is common in welding processes or solid-state joining technologies, heat-affected zones (HAZ) occur near the welding regions. The HAZ in the stud material during stop-action tests is close to the deposited coating. However, the entire consumable stud is heated over the full duration of the process time, so that no clearly outlined HAZ region can be detected.

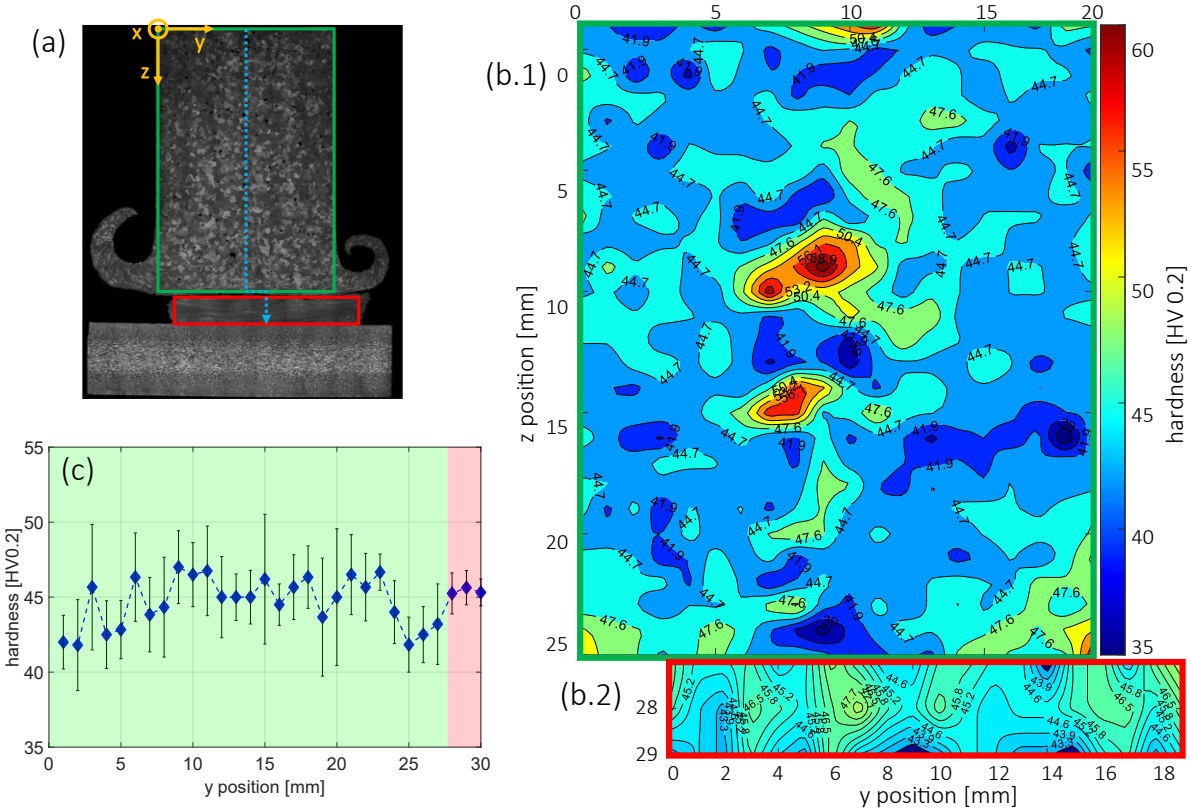

Figure 72: (a) Photograph of the cross-section of stop-action test sample of AA6060; measured area for the hardness contour plots in the stud (green) and coating (red) as well as the hardness profile from the upper edge of the stud to the lower edge of the coating (blue dashed line) are indicated. (b.1) Hardness contour plot of the stud, (b.2) Hardness contour plot of the coating. (c) Averaged hardness profile stud.

6 Discussion

The influence of the alloying elements Mg and Si in Al alloys on the processing behavior, in particular the development of the microstructural features, is discussed in detail in this chapter. The theoretical fundamentals regarding dynamically recrystallized microstructures, effective micromechanisms and secondary phase formation are contrasted with the results from the detailed microstructure analysis. In addition, a concise overview of the influence of FS on the mechanical properties is provided.

6.1 Influence of process temperatures on material deposition

Al alloys with higher content of an alloying element, either Mg or Si, exhibit lower thermal softening at higher temperatures [138]. At the same temperatures in the stud tips, Al alloys with higher Mg or Si content retain higher strength, which can lead to more localized plastic slip and smaller plasticized volume. This can be seen in the recrystallized layer in the stud tips of the stop-action trials (Figure 37). This layer represents the actual process zone where the shear flow of the plasticized material is localized before the coating is deposited. Obviously, increasing the Mg and Si content leads to more pronounced flow localization and plasticization of a smaller volume of material. Since less plasticized volume is available for deposition, high process speeds, i.e., 4000 min^{-1} and 15 mm/s, lead to very thin and narrow coatings (cf. Figure 22). If the process speeds are reduced, e.g., to 1000 min^{-1} and 8 mm/s (3.5 wt.% Mg) or to 1600 min^{-1} and 12 mm/s (10.4 wt.% Si), a larger volume can be deformed and subsequently deposited due to the longer process times. This is a possible explanation why lower translational speeds are required to obtain coatings of the same thickness with higher contents of Mg and Si. Since the thermal material properties are governed by the Mg/Si ratio through the formation of Mg_2Si precipitates, the addition of the alloying elements Mg and Si in Al alloys alters the temperature-dependent thermal material properties. The temperature-dependent thermal conductivity, specific heat capacity and the thermal diffusivity are all reduced by adding alloying elements (Figure 30). Thus, material with a higher fraction of saturated Mg_2Si precipitates softens more gradually due to the reduced thermal diffusivity processes. However, there is no obvious explanation for a correlation between the required low rotation speed and the less pronounced thermal softening of Al alloys with increased Mg or Si content since the process temperatures differ only marginally within both the Mg-rich and the Si-rich alloys.

It is understandable that the properties of the plasticized material within the (viscoplastic) volume of the shear zone are determined by the flow stress of the dynamically recrystallizing material. This observation cannot be easily related to general properties of the material determined for deformation without DRX, such as the thermal softening rate according to [139].

Additionally, the high content of Si secondary phase particles, with hardness values of about 1200 HV0.2, were expected to act as a further source of internal friction during plastic deformation in steady state, thus causing a higher temperature and higher flow stresses during the process. However, it was shown that for both identical parameters and adjusted process parameters, the process temperatures remain even below the Mg-rich alloys. Excessive magnesium content can lead to the formation of brittle

intermetallic compounds such as Mg_2Al_3, which reduce the ductility of the alloy and increase its susceptibility to brittle fracture [1]. In this thesis it was demonstrated that by adjusting the process parameters, in particular reducing the rotational speed and translational speed, it is possible to deposit low defect coatings at even very high Mg contents (6.4 wt.% Mg, 8.9 wt.% Mg, 10.6 wt.% Mg and 12.1 wt.% Mg). However, during the trial-and-error phase to identify stable process parameters at higher rotational speeds and feed rates of the Mg-rich alloys, stud breakage occurred more frequently. Also, a more pronounced development of short chips was observed on the Mg-rich alloys during FS.

Deposition efficiencies and specific energy inputs per unit volume behave reciprocally. Thus, coatings with smaller dimensions produced with identical parameters generally lead to lower efficiencies and require a higher energy input. Within the coatings deposited with identical parameters, the width and thickness dimensions vary depending on the alloying element content. These variations also correlate with efficiency and energy consumption, since coatings with slightly larger volumes also result in higher efficiencies and lower energies. On the other hand, the coatings produced with adjusted parameters and comparable deposit cross sections display comparable values for η and e_s for all alloys (Figure 20).

A decisive driver for steady-state temperatures of the FS process is the heat sink. It is essential for a stationary FS process to ensure that the heat flux away from the process zone is sufficient to prevent heat accumulation. At lower translational movement speeds, and with unsatisfactory heat dissipation, the process could overheat, resulting in oversoft stud material and ending in stud breakage. Instead, the temperatures in the process zone assume a level at which the material can be sheared under DRX conditions without defect formation and, at the same time retain, sufficient strength not to be squeezed too quickly into the flash. Shinoda and Li [15] have shown that the process heat is dissipated into the substrate and that the deposition efficiency depends on the thermal conductivity and the amount of material, i.e., substrate and backing plate thickness, beneath the deposition. Dovzhenko [140] has shown that deposition on 2 mm thick substrates made of AA2024 requires a heat sink consisting of a 10 mm thick AA2024 backing plate in order to ensure sufficient heat dissipation. Deposition efficiency increases with thicker substrate/backing plates and thereby with larger heat sinks. Furthermore, cooling the substrate and backing plate (to -120°C) before deposition leads to an increase in deposition efficiency of ~10% compared to room temperature deposition [140]. In general, the deposition efficiency of FS increases when heat is more effectively dissipated from the consumable stud [140] while simultaneously the heat dissipation is controlled by the process parameters used.

In this current study, 8 mm thick sheets of Al alloy AA2024 with a thermal conductivity of 140 W/mK were used as substrates, and these sheets were positioned on a second sheet (also 8 mm, AA2024) as a backing plate. So, the heat sink properties were kept constant for all depositions and can therefore be excluded from considerations about the influencing factors on obtained coating and process properties.

6.2 Microstructural alterations

6.2.1 Material flow & shear texture evolution

The calculated effective shear strain rates (Figure 24) are approximations of an average value for the material flow during FS deposition. In reality, the material flow along the coating thickness and width, as well as in the shear zone, is non-uniform and certainly does not follow the rotational shear plane exclusively. The complex three-dimensional nature of the shear surfaces (see e.g. Figure 36) occurring during FS contain also loading increments from axial and lateral directions. According to the applied model, the shear strain rate depends linearly on the rotational speed and inversely on the deposited thickness. For the thin coatings resulting from applying identical process parameters with increasing Mg content, very high shear strain rates of 892 s^{-1} at 2 wt.% Mg and 1453 s^{-1} for the 3.5 wt.% Mg alloy are obtained by this method. A different picture would be drawn if, instead of the deposited coating thickness, the height of the shear zone was used for d_{eff} as visible in the cross sections from stop-action samples presented in Figure 35. Here, a decrease in d_{eff} with increasing alloying element content would also be obtained for adapted parameters. Still, the estimated strain rates would be even higher. By adding particles as marker material to the studs, Belei et al. [141] demonstrated that the material is transported from different locations in the stud to different locations in the coatings and that the material flow during deposition is quite complex. In addition, it must be assumed that a significant fraction of the shear flow during the ongoing process occurs within the shear zone in the stud tip material before it is deposited [55].

According to equation (7), the effective shear strain rates and coating geometries are linked via the coating thickness and the corrected radius. Despite the considerable differences in the theoretical effective shear strain rates and the associated higher stress concentration on a smaller coating area, the average grain sizes of the coatings of a certain alloy produced with identical and adjusted parameters are in a similar order of magnitude. For example, for the 2 wt.% Mg with identical parameters in the center of the coating, the average grain size is 10.3 ± 4.6 µm, and for adjusted parameters 12.0 ± 5.3 µm (Figure 40). Rather, the alloy element content Mg or Si has an influence on the resulting coating grain size and on the grain boundaries as reported in Grain structures of processed Al-Mg alloys. However, it was found that, regardless of the process parameters used, lower average grain sizes occur on the AS and RS followed by the center of the cross-section coating. For the 3.5 wt.% Mg produced with identical parameters, grain size measurement was not possible on either the AS or RS due to the low coating geometry. Uneven material flow can lead to local differences in grain size. Another reason for the lower grain size at the sides of the coating (AS & RS) can be caused by different cooling rates at the edges of the deposits [55]. The influence of the particle size on DRX is discussed in chapter 6.2.3, Dynamic recrystallized microstructure.

In the microstructure of all FS-processed aluminum alloys, flow lines and band structures of different characteristics occur. These are mostly narrow and very fine-grained structures in which a preferred crystallographic orientation is clearly observed. The flow lines, which are for the largest part oriented

parallel to the substrate surface, bend towards the edges of AS and RS and sometimes take on a vortex-like appearance. Bending of the flow lines towards the sides of the deposit and within the deposit close to the substrate can also be seen in Figure 73 (a) & (b), indicating an inhomogeneous material flow.

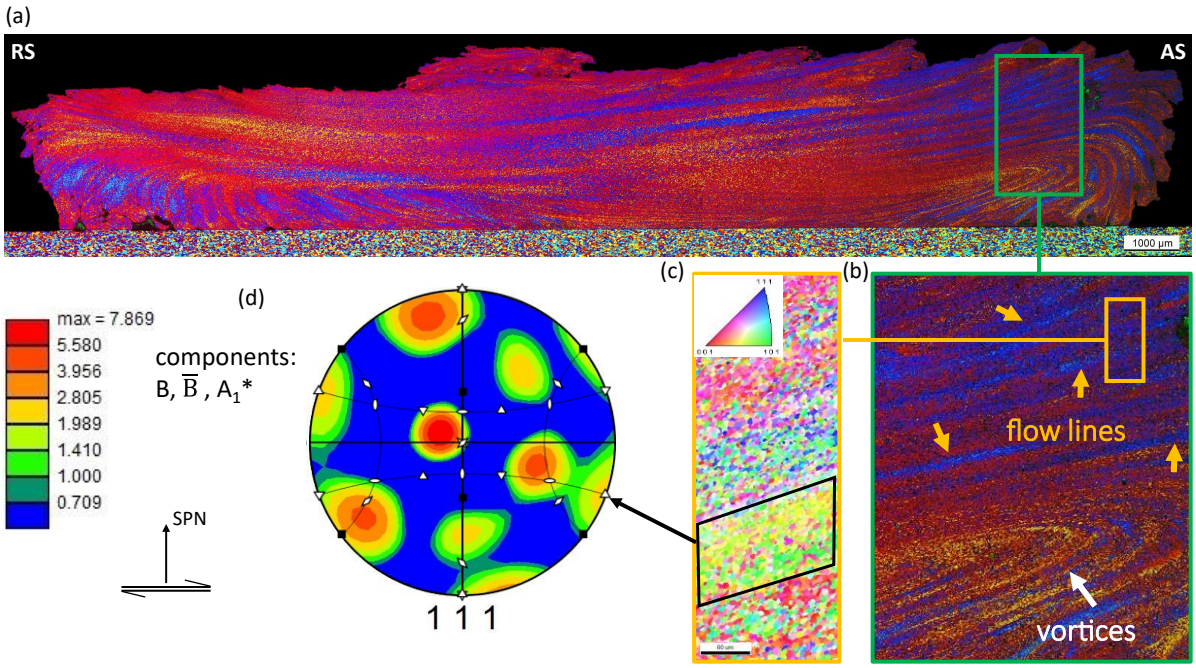

Figure 73: 2 wt.% Mg alloy deposited using adjusted parameters: (a) Color-etched light-optical cross section image (front view DD); (b) Flow lines and vortices appearances; (c) EBSD measurement of selected flow line; (d) Rotated PF including dominant ideal shear texture components.

The material flow can be particularly clearly observed on the pseudo-3D microstructure representation of the initial alloy AA6060, 2 wt.% Mg with adjusted and identical parameters. Rafi et al. showed in [142] that the material flow during FS is mainly controlled by the rotational speed of the consumable stud while assuming that the material flow rate is about half of the stud rotational speed.

It is known that rotational solid state joining technologies are based on shear deformation, and the texture variation can be related to ideal shear deformation. Fonda et al. [92] had proposed a systematic method for aligning the texture analysis reference frame with the ideal shear reference frame at a certain location of an FSW weld. Furthermore, Prangnell et al. [143] analyzed shear textures in FSW samples "frozen" using stop-action technique. Shen et al. [144] presented shear textures during refill friction stir spot welding of Al-Mg-Sc alloys. Suhuddin et al. [94] showed by textural analysis that the material flow in the measured areas during FS is close to simple-shear deformation. Similar to the observations in this study, there are zones in which, based on the texture analysis, a shear-dominated material flow seems to have taken place, and intermediate areas in which the texture intensity is lower due to recrystallization. Thus, in this study, FS is assumed to be a shear-dominated process which forms areas of ideal shear textures during the material flow [145]. The crystallographic planes {hkl} and directions <uvw> are aligned with the shear plane and direction. Studies have shown that {112} <110> textures develop preferentially in fcc metals or aluminum alloys processed by FSW, corresponding to those of the B and

$\overline{B}$ components of the ideal shear texture [92]. These shear texture components are aligned with the SD along the close-packed <110> direction and lie on the close-packed {111} plane [92].

In the EBSD measurements of selected flow lines in various deposits, evidence of ideal shear texture components was detected at different texture intensities (Figure 55). The grains have a uniform orientation distribution when the maximum texture intensity is below 2 [146]. In other words, a preferential grain orientation is referred to as texture when texture intensity is greater than 2. In the initial AA6060 alloy, the $\overline{B}$ components as well as A_1* & A_2* components dominate (Figure 55). The averaged maximum texture intensity is 5.2 ± 0.9 regardless of the observation direction. In the coating with 2 wt.% Mg produced by adjusted parameters, the B & A_1* components and also C components dominate. In addition, B and $\overline{B}$ components could be identified in the measurement even at high texture intensity (7.9) (Figure 55). This is exemplified in Figure 73 (c), which shows the EBSD measurement of a selected flow line. In Figure 73 (d), the rotated PF is presented, aligned with the shear texture frame including dominant ideal shear texture components. However, the averaged maximum texture intensity of the sample with 2 wt.% Mg, adjusted parameters was found to be 5.1 ± 1.5. The coating with 2 wt.% Mg produced with identical parameters revealed no dominant components and exhibited the lowest averaged maximum texture intensity of 4.1 ± 1.2. With increasing rotational and translational speeds, and the associated reduced deposition volume, material flow is localized to a smaller volume, and higher strain rates are assumed. This eventually leads to a weakening of the texture intensities. Rahmati et al. [147] also described a similar phenomenon in their research: The shear texture intensity in the coating decreases with increasing feed rate. However, the weakening of the texture may also be related to DRX processes. Due to the predominant cDRX micromechanism, in which grain rotations play an important role, less pronounced flow lines are formed. Thus, the shear texture intensity could be reduced by recrystallization. Another reason for discrepancies between FS textures to the ideal shear orientations could be the imprecise alignment of the shear texture frame over the rotation angle α_i. If necessary, the shear texture frame would have to be rotated by an additional angle by which the stud is laterally inclined in the feed direction during deposition. Fonda et al. [148] rotate the data sets by a tilt angle (analogous to TD), in which the tool is inclined in the translational direction at FSW. The exact orientation of the shear deformation frame would need to be aligned with that of the sample frame, something which is difficult to achieve due to the fluctuations in terms of torques and forces in addition to the 3D material flow.

6.2.2 Zener-Hollomon equivalence for FS

In this chapter, the application of the Zener-Hollomon equivalence is discussed exemplarily for the alloy with 2 wt.% Mg deposited with identical and adjusted parameters.

The Zener-Hollomon model [62] [117] can be applied to estimate grain size resulting from dynamic recrystallization based on strain rates, temperatures, lattice activation energy and gas constant. The Zener-Hollomon parameter can be calculated according to equation (7). For hot working processes, usually the activation energy for lattice self-diffusion is applied to Q since it is related to dislocation motion and correspondingly reflects the mechanisms that control DRV and DRX [67]. Q depends on the Mg content in Al-alloys and is assumed to be in a range of 122-126 kJ mol^{-1} [149] for the Mg-rich alloys used in this study. The Z-value for the FS deposits with 2 wt.% Mg, produced with adjusted parameters, can be calculated using the estimated strain rate from section 5.1.2, Estimation of strain rates, something which results in a value of Z = 6.05E+11. This coating displays an average grain size of around 9.9 µm. Processing this alloy with an identical parameter set leads to a Z value of Z = 2.97E+12. The experimentally determined average grain size is around 9.6 µm. Although the experimental process parameters for these two cases differ significantly, a difference which is reflected by the considerably different Z values, the grain sizes are quite similar. While estimated strain rates vary for the two parameter sets for the different alloys, the grain size shows no significant differences. In contrast to studies on FSW of AA5083 & AA5052 [65], in the current study no correlation between the resulting grain size of the deposit and the Zener-Hollomon parameter could be found for FS on any of the studied alloys.

Even accepting that the estimated strain rates are not calculated correctly, it is not probable that the equal grain size in the coatings deposited by different process parameters is a result of equal strain rates. Possibly, the effect of temperature outweighs the effects of strain rates under the extreme conditions the materials encounter during FS. For FS of Ti-6Al-4V, it was found in [150] that up to a certain rotational speed, a rise in process temperatures resulted in an increase of grain size despite an increasing strain rate while for further increasing rotational speeds very little changes in the resulting grain size were found [150]. Additionally, changes in the DRX mechanisms may lead to variations in the activation energy value Q. A given Q value is valid only within a range of thermomechanical conditions. In the case of several mechanisms operating simultaneously, the activation energy is considered to be an "effective activation energy" that must be averaged [20]. Assuming that different DRX modes operate simultaneously or sequentially during FS, the activation energy may distort the calculated Z values. Another factor could be post-dynamic recrystallization and grain growth. Even at the high cooling rates, grain growth can already take place, a process which could lead to a saturation of grain size for the deposition temperature which is similar for all alloys in this study. This may especially be the case after deformation at large strain rates where recrystallization driving force is high. These and possibly more factors are the reason why the resulting grain size cannot be correlated to the Zener-Hollomon parameter in this study.

6.2.3 Dynamic recrystallized microstructure

Figure 74 highlights the onset of DRX during the FS. In the center of Figure 74, an overview image is provided with enlargements of the stop-action test of the initial alloy AA6060 in which the EBSD measurements (blue, red & green frames) were carried out. Figure 74 (a) & (b) illustrate IPF maps of the measured EBSD sections (blue & red frames). In these, arrows are depicted which are associated with the misorientation profiles in (a.1) & (a.2) and (b.1). The misorientation profiles of the presented stop-action sample of AA6060 indicate a strong local misorientation within the initial grains shortly before they undergo DRX/grain subdivision. Misorientation profiles in show a misorientation angle of max. 35.5° in (a.1), and up to max. 10.4° in (a.2) as well as (b.1) with up to max. 43.4° point-to-origin misorientation angle within a single grain. Based on the IPF-maps and the corresponding misorientation profiles in Figure 74 (a), (a.1), (a.2) & (b), (b.1), it can be concluded that after reaching a material specific critical strain as well as critical dislocation density within the initial grain, recrystallization is initiated. Furthermore, in the area of the compression-driven TMAZ in the stud material, a compression-dominated pinching of the initial grains seems to take place (see Figure 74 (c.1) & (c.2). Similar to the study by Suhuddin et al. [60], signs of gDRX were detected in this FS zone. Typical appearances are serrated grain boundaries which are depicted by the short red arrows in Figure 74 (b). At higher resolution, serrated grain boundaries are shown in both the IPF map in Figure 74 (c.1) and the KAM map (c.2), here indicated by short black arrows. The HAGB impingements typical of gDRX were not found. It is suggested that gDRX has a small effect on recrystallization in the early stages of DRX during FS and then transitions to the cDRX mechanism. According to Figure 6, a possible DRX sequence might be grain elongation without HAGB impingements in the first step, followed by progressive cell structure/subgrain formation, subsequent subgrain rotation, and the final recrystallized microstructure. The two related processes cDRX and gDRX usually occur preferentially in materials with high SFE at elevated temperatures. However, cDRX is observed at high strain rates and gDRX at rather low strain rates [20]. Thus, gDRX is a possible mechanism that would be expected in areas of lower local strain rates, as is the case in compression-driven TMAZ, and that is substituted by cDRX as strain rates increase in the area below. In alloys with a fine initial grain size, dDRX may be more pronounced as the fine grains have more grain boundaries that serve as potential nucleation sites for new grains [20]. Furthermore, the presence of numerous grain boundaries promotes grain boundary migration and recrystallization. Due to the latter aspect, cDRX, in which the deformed grains are gradually replaced by newly formed grains during hot working, could also be accelerated by a fine initial grain size. However, a possible influence of the initial grain size on the resulting DRX grain size could not be validated in this study and remains subject to scientific investigation.

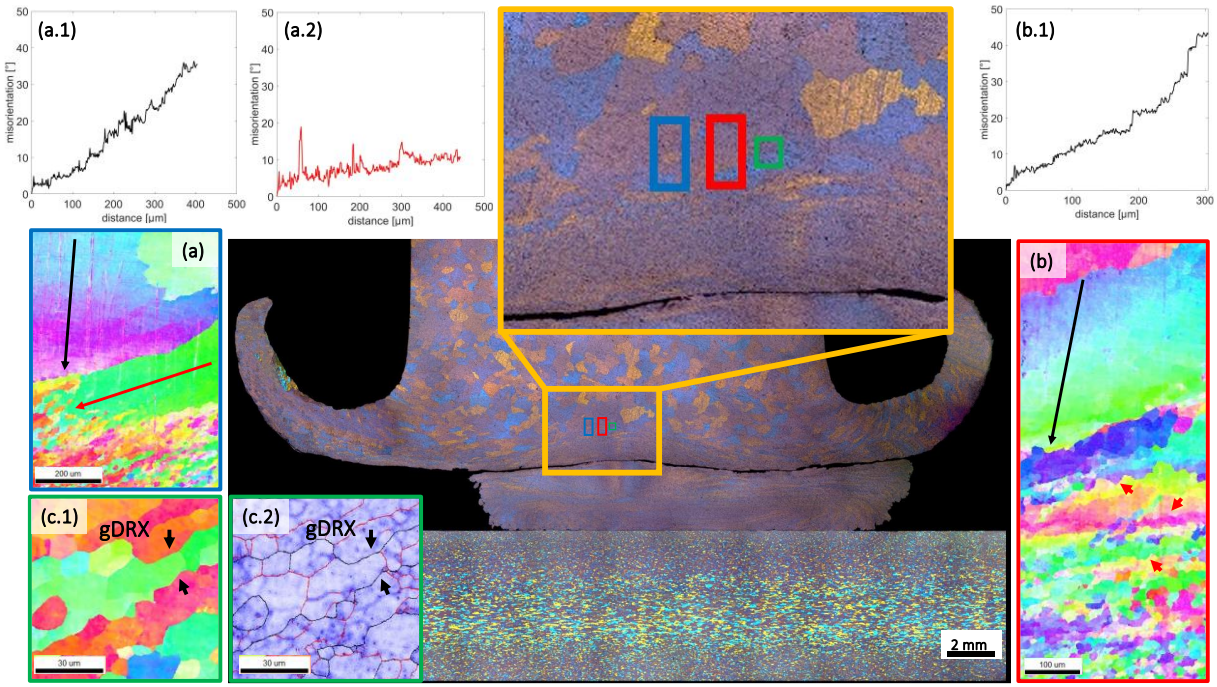

Figure 74: Onset of DRX during FS. (a): IPF map with MO profiles within parent grains; black arrow: (a.1), red arrow: (a.2). (b): IPF map with serrated grain boundaries highlighted with short red arrows. black arrow: (b.1) MO profile within parent grain. IPF map (c.1) and KAM map (c.2) with serrated grain boundaries highlighted with short black arrows which indicate gDRX.

Since high SFE-alloys like Al alloys are assumed to recrystallize dynamically via continuous dynamic recrystallization (cDRX) [20], dislocation cells are initially formed within larger grains at the onset of deformation, which are transformed into LAGBs by the continuous accumulation of dislocations. Further transformation of LAGBs into equiaxed HAGB grains is achieved by further intake of dislocations as a result of ongoing deformation [52] [151]. Typically, a microstructure formed by cDRX exhibits an equiaxed grain morphology consisting of proportions of LAGB grains and HAGB grains homogeneously distributed throughout the material. The analyzed cDRX sequence can be reconstructed by means of the TEM investigations and is summarized in Figure 75. Accumulations of dislocations form tangles, and with further deformation the dislocations accumulate at the grain boundaries through pile-ups and then form so-called dislocation cell structures [55].

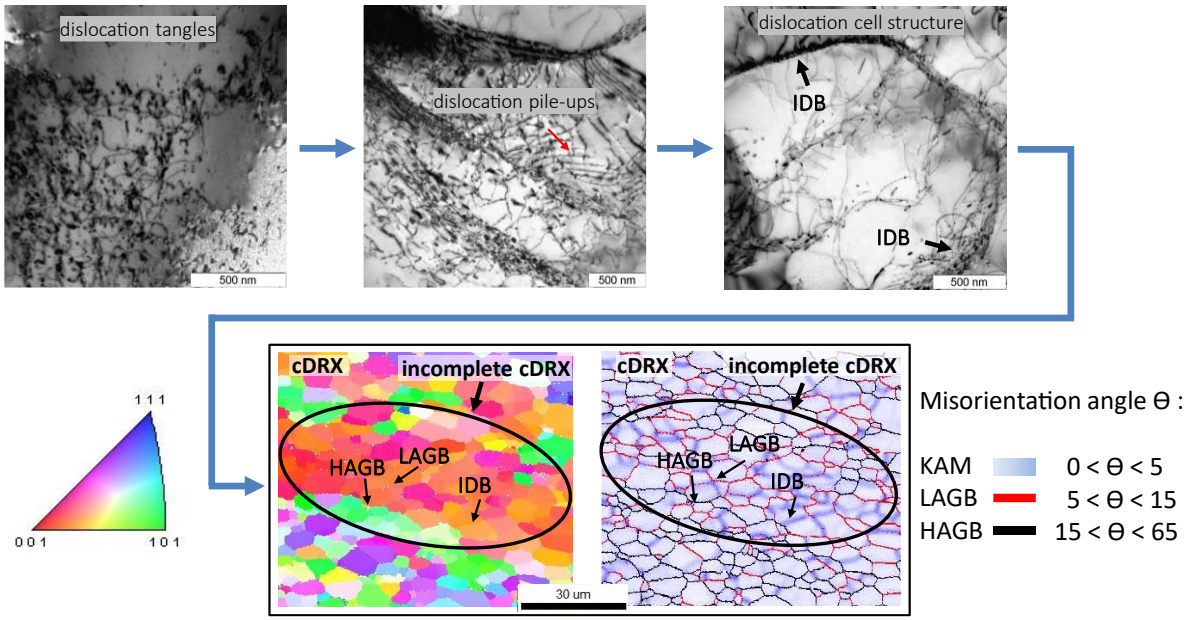

Figure 75: Appearances of cDRX sequence in the microstructure. TEM: dislocation tangles → dislocation pile-ups → dislocation cell structure formation; EBSD: IPF map & KAM & grain boundary map including IDBs (sub LAGBs), LAGBs & HAGBs.

Figure 75 illustrates a section of an EBSD measurement of a coating with 0.27 wt.% Mg (AA6060), showing an area with incomplete cDRX. Within the highlighted area, LAGB (red lines) grains are visible within a larger parent grain, all of which still exhibit minor misorientation differences. In the KAM map in Figure 75, the blue, slightly blurry lines with localized misorientation below 5° can be classified as dislocation walls respectively IDBs, which represent the boundaries of the dislocation cell structures. These substructures can be considered as a pre-stage of LAGB. It is known that substitutionally dissolved alloying element atoms can reduce the SFE in fcc metals. In general, the SFE in Al alloys decreases with increasing dissolved elements Mg and Si [49] [65]. However, the influence of Si is much lower because the maximum solubility of Si in Al in the solid state is limited to 1.65 wt.%. In contrast, Mg can be dissolved in Al up to 14.9 wt.% in the solid state [1]. For this reason, the influence of the SFE on DRX during FS is discussed exemplarily for the Mg-containing alloys. The SFE can be determined in different ways, including X-ray diffraction (XRD), high-resolution scanning transmission electron microscopy (HR-STEM), or by ab-initio calculation e.g. using density functional theory (DFT). SFEs of Al-Mg alloys are derived from the work of Edalati et al. [149] and Morishige et al. [65]. The SFEs of the alloys used in this study were interpolated based on the Mg content and are illustrated in Figure 76. All other alloying elements, e.g. Si, Fe, Mn and Cr, were neglected due to their low content and minor differences between the alloys [55].

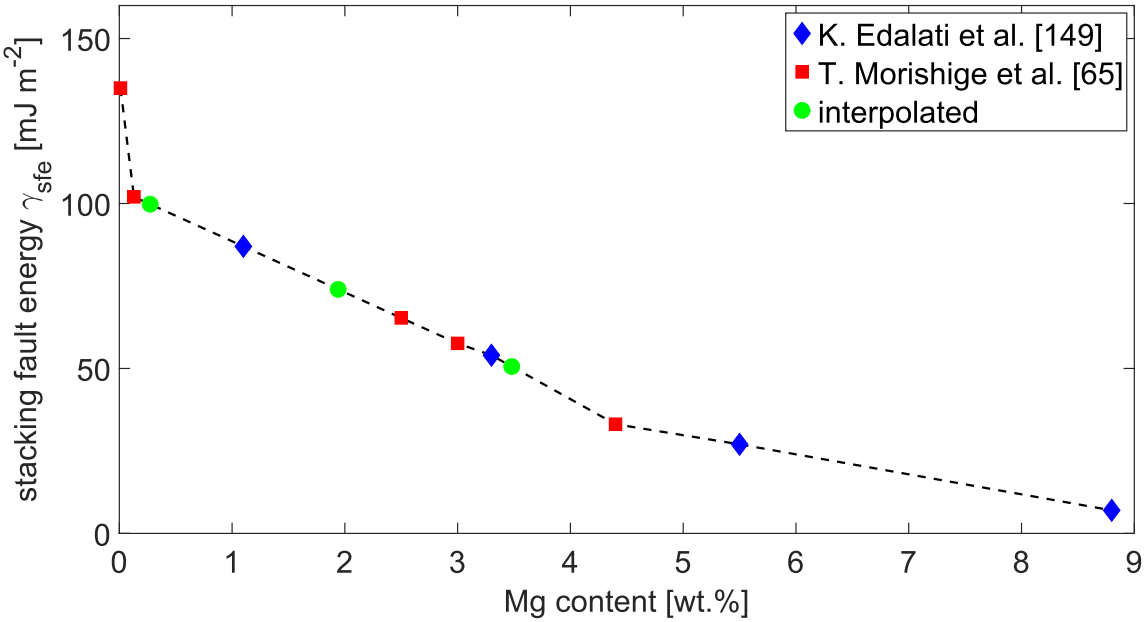

Figure 76: Stacking fault energy γ_{sfe} depending on the Mg-content in Al-alloys.

In materials with a low SFE, the stacking fault distance, or rather the distance between the Shockley partial dislocations, is larger, something which hinders cross slip and climbing of dislocations. This means that dislocation annihilation is less effective and, therefore, dynamic recovery (DRV) is delayed. In contrast, recovery is more effective in materials with higher SFE as dislocation annihilation is accelerated. During SPD, this results in a lower number of dislocations available to form dislocation cell structures, and eventually higher proportions of IDBs and LAGBs remain [20]. LAGBs in the microstructure of a material after processing under cDRX conditions are therefore a pre-stage of the final HAGB grains that would have formed upon further deformation. Thus, a microstructure with a high proportion of HAGBs is indicative of a more complete recrystallization state than a microstructure with a higher proportion of IDBs and LAGBs [55]. The initial alloy AA6060 with 0.27 wt.% Mg has a SFE of ≈ 100 mJm^{-2} according to Figure 76 and the alloy with 8.9 wt. % Mg has a SFE of ≈ 7 mJm^{-2}. The SFE of the alloys with 10.4 wt.% Mg and 12.1 wt.% Mg lies in the range of ≈ 2-4 mJm^{-2} [65]. According to Sakai et al. [52], materials with low SFE can experience dDRX during hot working. However, no typical indications of dDRX, such as necklace-like grains, are found in the microstructures of the coatings, and both EBSD and TEM analyses indicate cDRX even in the alloys with very high Mg content (8.9-12.1 wt.%). This could be due to the fact that the SFE in Al alloys increases with increasing temperature [67]. With increasing Mg content, the grain size in the microstructure of the coatings decreases (Figure 42). Based on the present data, it is reasonable to assume that the availability of a higher number of dislocations for the formation of dislocation cell structures in cDRX leads to their reduced grain size. In the TEM images in Figure 55, a tendency towards larger amounts of dislocation tangles was observed for the alloys with higher Mg content, an observation which supports this assumption. It must be considered though that the TEM results do not allow for a statistically relevant analysis. With higher Mg content and lower SFE, the proportion of HAGBs also increases relative to

LAGBs, indicating a higher degree of recrystallization in the final microstructure. This trend is supported by the distribution of the misorientation angles (Figure 46 & Figure 47). With increasing Mg content, the proportion of misorientation angles above 15° increases significantly. Furthermore, the KAM maps reveal that a lower proportion of lines of high local misorientation (IDBs or cell structures) was observed in the alloys with high Mg content (Figure 43 & Figure 44).

The presence of a higher number of dislocations during cDRX may also lead to higher yield stresses during shear deformation for alloys with higher Mg content. This is closely related to the requirement for lower process speeds and higher axial forces during FS in order to produce a sufficiently plasticized material volume and to deposit thick coatings in a stable FS process [55].

Theoretically, materials with high SFE deform predominantly by slip of dislocations. Screw dislocations can cross-slip because there are only few stacking faults. Low SFE materials, on the other hand, form crystal twins when there are not enough slip systems available and partial dislocations instead of screw dislocations, which cannot slip across stacking faults [19]. Despite the expected low SFE in the alloys with very high Mg content, no twinning and no indications of dDRX could be detected in the microstructures.

PSN occurs when particles or inclusions act as preferential sites for nucleation and promote the formation of new grains in their surroundings. The presence of particles or inclusions can lead to a finer grain structure by increasing the number of nucleation sites and the recrystallization rate [152]. Zener pinning occurs when the nm-sized second phase precipitates or dispersoids act as obstacles or barriers to the movement of dislocations or grain boundaries. The effect of Zener pinning on DRX depends on particle size, distribution, composition, and spatial arrangement, as well as deformation conditions and temperature. The dislocations tend to be pinned in position, something which restricts their movement and effectively inhibits grain growth. As a result, nucleation and growth of new grains are constrained, reducing the degree of DRX. The pinning effect can lead to less grain refinement during the deformation process [70].

Indications of PSN and also Zener pinning could be identified in bright-field TEM images, some of which are shown in Figure 77. Figure 77 (a) reveals a particle of ≈ 500 nm in size in an AA6060 coating, potentially inducing PSN, since it is surrounded by dislocations. A more distinct indication is shown in Figure 77 (b). Here, in the 6.4 wt.% Mg alloy, a potential PSN particle which acts as a dislocation source was found. Demny [123] describes in his research that piles of dislocations can be attributed, for example, to the presence of a dislocation source. In contrast to edge dislocations, screw dislocations can have different slip planes at low temperatures and thus cross-slip occurs. In this case, screw dislocations leave their original slip plane and continue to slip on a different one. In the bright-field image, cross-slip is detected by the slip trace of a dislocation movement, which suddenly changes direction [123]. In Figure 77 (c) (3.5 wt.% Mg), orthogonal kinks are visible in the slip traces of screw dislocations, which is a significant indication of cross-slip. Figure 77 (d) (blue arrows) shows evidence of Zener pinning,

which can be observed on e.g. very fine dispersoids or precipitates [20] [123]. In this case, the dislocations migrating through the crystal are stuck at nm-sized semi-coherent or incoherent particles, and a kind of dragging effect is obtained [70]. In the bright field image, the dislocation pattern, which is disturbed by nm-sized particles, can be observed.

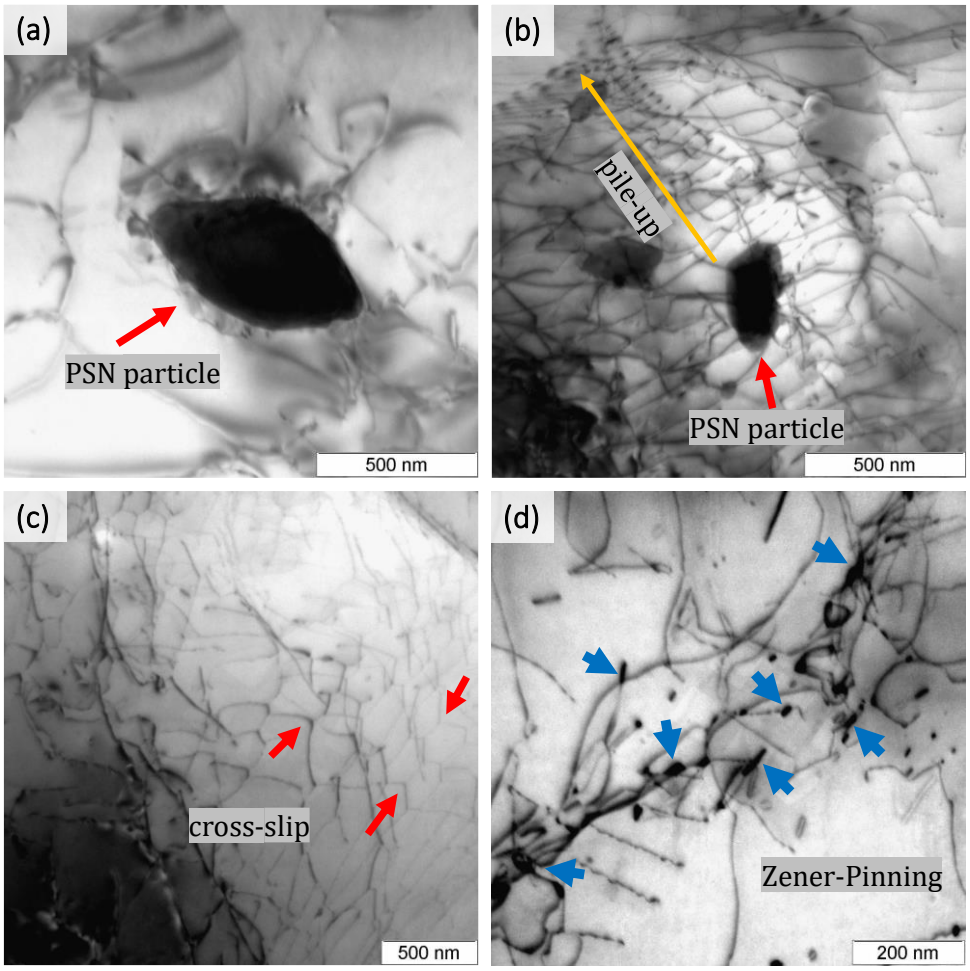

Figure 77: Bright-field TEM images. (a): AA6060 alloy: potential PSN particle surrounded with dislocations. (b): 6.4 wt.% Mg: potential PSN particle promoting pile-ups as a dislocation source. (c): 3.5 wt.% Mg: cross-slip dislocations (red arrows) with orthogonal inflections. (d): 3.5 wt.% Mg: potential Zener pinning (blue arrows).

The influence of the addition of Mg or Si in Al alloys on the DRX process and the associated grain size is outlined in the following points:

1. As the SFE decreases with increasing Mg or Si content, cross-slip and climbing of dislocations are impeded, which in turn hinder the dislocation annihilation and delay dynamic recovery. Thus, more dislocations remain in the material, something which promotes DRX. Note that due to the higher solubility of Mg in Al compared to Si in Al, the influence of Mg is much more significant.

2. The higher the Mg or Si content, the more secondary phase particles occur in the alloys. More particles mean increased opportunities for PSN events, which lead to more nucleation sites for dislocation cell structures in particular, thereby promoting DRX. It is assumed that this effect is dominant in Si alloys due to the low solubility of Si in Al (see Figure 77 (b)).

3. With increasing Mg or Si content, more nanoscale Mg_2Si precipitates form in the microstructure. However, due to the stoichiometry, the Mg/Si ratio plays a major role. Once, after saturation, one of the alloying elements is no longer available, the other is precipitated separately in the form of further secondary phases. However, depending on the Mg/Si ratio, the precipitates present act as obstacles to the dislocations. Dislocations can be pinned by the nm large precipitates, a process known as Zener Pinning. This means that DRV is impeded and less dislocation cells can be formed, leading to a delay in DRX (see Figure 77 (d)).

It is obvious that the influence of the chemical composition outweighs the effects of the different strain rates for the different process parameters during FS. The influence of the alloying elements on the resulting microstructure is divided into the three main influencing factors: SFE, secondary phase particles, and precipitates, as summarized in Figure 78.

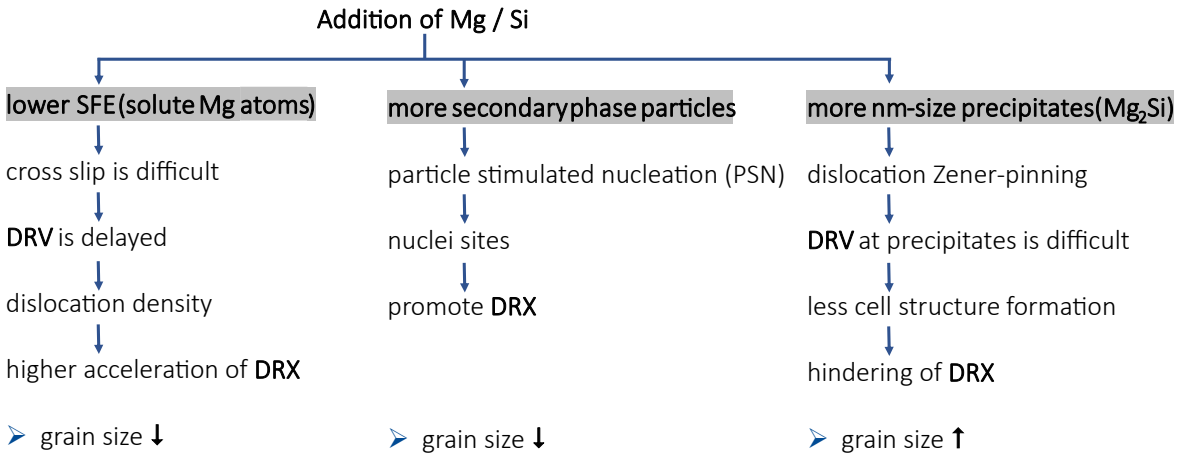

Figure 78: Summary of the factors influencing the alloying elements Mg/Si on DRX with the associated sub-micro mechanisms.

6.2.4 Secondary phases and precipitation during FS

The discussion of the evolution and transformation of secondary phases and precipitates during FS is divided into the following three subsections: phase development, precipitation kinetics and dynamic precipitation.

Phase development:

The proportion of secondary phases, determined based on surface area in metallographic cross sections, increases with increasing Mg or Si content. This is due to the fact that an increased amount of alloying element is available to form phases other than α-Al. After FS, the phases differ in shape and amount from the BM. The decrease of the secondary phase fraction on the surface can be explained by the heat influence during FS, which causes phases to partially dissolve. In addition, large Al_3Mg_2 phases in the Mg-rich alloys, for instance, are refined by shear deformation at high strain rates (compare Figure 60 (c) with (f)). Further, dynamically formed precipitates are too small to be identified by optical light microscopy or EDX. Based on the elemental composition, the alloys studied can be classified according

to whether there is an excess of Si or Mg. The Mg/Si ratio affects the potential phases formed and the maximum possible amount of Mg_2Si precipitates that can be developed (Table 12).

Table 12: Excess of Si, Mg and max. Mg_2Si

	ratio Mg/Si	Mg_2Si [wt.%]	excess Si [wt.%]	excess Mg [wt.%]
AA6060	0.85	0.43	0.21	x
2 wt.% Mg	5.90	1.04	x	1.78
3.5 wt.% Mg	10.31	1.07	x	3.31
6.4 wt.% Mg	20.11	1.01	x	6.28
8.9 wt.% Mg	25.03	1.12	x	8.70
10.6 wt.% Mg	29.88	1.12	x	10.42
12.1 wt.% Mg	35.85	1.07	x	11.93
6.6 wt.% Si	0.04	0.79	6.47	x
10.4 wt.% Si	0.03	0.79	10.23	x
14.6 wt.% Si	0.02	0.73	14.47	x

The maximum amount of Mg_2Si to be attained in the initial alloy AA6060 with 0.43 wt.% Mg_2Si can be increased but is limited by the fact that the Mg or Si contents are not increased in parallel. Most of the additional Mg or Si added is in the form of excess Mg or Si, which is not involved in the formation of Mg_2Si. The phases identified in the alloys investigated are directly related to the alloy composition or the Mg or Si excess and the FS process. Beyond that, no fundamentally different phases could be identified before and after FS. First and foremost, the quantity and morphology change. Some of the phases simulated by Thermo-calc could not be identified. This may be due to the fact that Thermo-calc simulates on the basis of equilibrium states, and this is not the case during FS. Furthermore, other phases could simply not be identified with the methods used in this study as these may exist in too small quantities or are outside the range of the measurement resolution. In Al-Mg-Si, the formation of the Al_3Fe as well as the AlFeSi phase is an important aspect in the microstructure. Both Al_3Fe and AlFeSi reduce the corrosion resistance [1] and have negative effects on the mechanical properties [127]. AlFeSi can occur as α-AlFeSi or as β-AlFeSi phase. It is desired to convert especially the needle-shaped β-AlFeSi phases into spheroidal α-AlFeSi by the homogenization treatment [153]. Besides, there are different morphologies and stoichiometries of AlFeSi phases such as Al_5FeSi, $Al_{21}Fe_3Si_5$, Al_8Fe_2Si etc. which can be specified by the Fe/Si ratio of the respective phase composition [154]. In the alloys with Si excess, segregated Si secondary phases are transformed from their original needle-shaped morphology into a globular one by heat treatment or thermo-mechanical treatment using FS (Figure 33 & Figure 61). In the alloys with Mg excess, Al_3Fe is formed predominantly in both the BM and the FS state (Figure 62). This suggests that in these alloys the Si reacts elsewhere with Mg during FS, so that AlFeSi can no longer be formed. Since Al_3Fe was formed from the initial AlFeSi in the BM during or after FS, it can be assumed that the Si involved dissolves or forms phases with Mg or O. In the alloys with Si excess, predominantly β-AlFeSi phases are detected (Figure 63). Al_3Fe could not be detected in

these alloys due to the increased affinity of Si to Fe. It is noticeable that especially the Fe-rich phases occur in the BM and coating material after FS in all alloys in close proximity to Mg-rich or Si secondary phases (e.g. Figure 62). The rate at which both AlFeSi and Mg_2Si dissolve when subjected to heat is related to the grain size. Small grains accelerate the dissolution process [127]. Since heat exposure occurs during FS and a correlation exists between grain size and the rate of phase transformation and dissolution behavior [127], it can be assumed that parts of the Mg-rich phases go into solution in a short time during FS, resulting in local reactions between Mg, Si and O. The size of the phases varies significantly between the BM and the coating material. However, there is a tendency to detect smaller phases in the coating material than in the BM, which can be observed especially for the MgSi containing phases Mg_2Si, MgO, SiO_2 and Si. The small phase size and changed arrangement are caused by exposure to high temperatures and resulting diffusion as well as the extreme plastic deformation of the material.

Oxide-containing phases can be identified in all alloys investigated in this study, regardless of whether there is an excess of Si or Mg. After FS, a slightly increased amount of oxides tends to be found in all alloys (Figure 64 & Figure 65). The following oxide types are classified: Al, Si, O and Mg, Si, O containing phases. The latter are not formed in the alloy with Si excess. Depending on the local element concentrations, Mg, Si, O-containing oxides form predominantly in the presence of phases containing Fe. Al, Si, O-containing oxides predominantly form square shapes with straight edges. These phases do not appear in the same quantity in all samples examined. Either the oxide is introduced directly during melting, or it is introduced during FS at the contact surface with air due to increased temperatures and reaches the material inside through the material flow. The identified oxides, however, do not correspond in their composition to the expected MgO and $MgAl_2O_4$, which, in addition to Al_2O_3, appear primarily as an oxidation product in Al-Mg-Si alloys [155]. The determined Si concentration is significantly higher, which is due to SiO_2 as a solid oxygen source [156] caused by e.g. introduced contaminants. Oxidation by FS is already known – the use of a protective inert gas during deposition can prevent this phenomenon [2].

Precipitation kinetics:

The peak temperatures prevailing during the process were measured by means of an infrared camera positioned orthogonally to the coating deposition, as well as by thermocouples placed in the substrate below the deposition. Temperatures of max. 450-470 °C were found for the Mg-containing alloys and max. 440-460 °C for the Si-containing alloys by the infrared camera. It should be noted that the maximum temperatures encountered within the shear zone may be higher. It is assumed that most of the strength enhancing precipitates, i.e., predominantly β″, but also β′, U1, U2, B′, dissolve during the thermal cycle. It follows that a larger amount of solutes is present in the material inside the matrix in deposited coatings, compared to the BM state. Subsequently, re-clustering or precipitation formation takes place due to natural aging. In this post-FS state, β″, β′, U1, U2, B′ precipitates can obviously form to a higher degree in the following DSC analysis, since the associated D (β″) and E (β′) peak is clearly

pronounced in the DSC curves in both the Mg-rich and Si-rich alloys (Figure 67 & Figure 68). However, with respect to the D (β″) and E (β′) peaks, the two alloy groups Mg-rich and Si-rich differ from each other. As Gaber et al. have demonstrated in their study [136], when the atomic ratio of Mg/Si exceeds 1.25, the two exothermic peaks of the β″ and β′ precipitates strongly overlap and are thus difficult to distinguish. On the other hand, when the Si content increases, the difference between the two exothermic peaks of the β″- and β′-precipitates becomes more pronounced [137]. Thus, a lower atomic ratio of Mg/Si leads to the exothermic peaks of the β″ and β′ precipitates consisting of two separate peaks. However, in the DCS curves of the Si-rich alloys the D (β″), E (β′) double peaks appear exclusively for the FS coatings while in the BM state only the D (β″) peak seems to be highly pronounced. In addition, the F peak seems to be much less pronounced (Figure 67). This suggests that either the higher expected fraction of particles available for reaction in the post-FS coatings causes these different reaction kinetics, or the DRX grain size has an accelerating effect on the reaction kinetics. A similar phenomenon can be observed in the Mg-rich alloys. Here, a pronounced D (β″) peak is present in the respective DSC curve of the post-FS materials, while in the BM state both a D (β″) peak and a separate less pronounced E (β′) peak can be identified (Figure 68). For the Mg-rich alloys, the DSC curves are more variable in appearance, making it difficult to draw conclusions about the exact reaction kinetics. It is assumed that the temperature and primarily the exposure time during FS processing are not sufficient to form coarse β precipitates. β″ or β′ precipitates could not be detected in this study due to the limited resolution in the TEM.

Dynamic precipitation:

When dislocations move through the material during plastic deformation, dislocation-dislocation interactions occur in which jogs are generated. Moving dislocations will drag the generated jogs, something which bends the dislocations and leaves vacancies [85]. Furthermore, dislocation loops form as a result of condensation of vacancies generated through plasticity at elevated temperatures during FS, and have a contribution to strength. These formed dislocation loops are an indication of the localized vacancy generation and could be detected in the TEM investigations of this study; they are exemplarily shown in Figure 79.

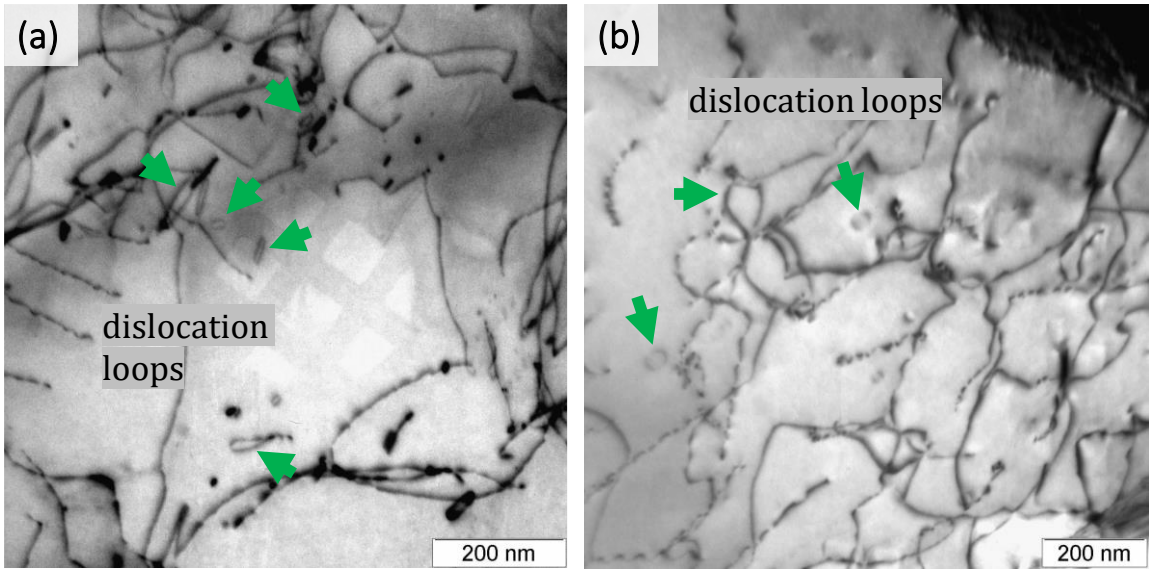

Figure 79: Bright-field TEM images showing dislocation loops (green arrows) in a 3.5 wt.% Mg alloy FS coating.

These generated vacancies can facilitate mass transfer and thus lead to accelerated precipitate growth and formation [85] [86]. For a more accurate detection of dynamic precipitation during FS, *in-situ* small angle x-ray scattering measurements would be necessary.

6.3 Influence of FS on mechanical properties

The analysis of the mechanical properties in this thesis is primarily limited to hardness measurements and hardness maps. In summary, the hardness increases with increasing proportions of alloying elements Mg or Si, a process which is to be expected considering the acting strengthening mechanisms. With increasing content of soluble alloying elements, first solid solution strengthening and, second, precipitation strengthening increase in precipitation hardening alloys. Furthermore, additional particle strengthening may occur due to intermetallic phases or dispersoids [19]. If the BM of one alloy composition is subjected to thermo-mechanical FS treatment, the hardening increments of grain boundary hardening and strain hardening through additional dislocations play a significant role. According to Hall-Petch [19] [32], the strength increases with smaller grain size or higher absolute grain boundary length. In addition, FS increases the dislocation density inside the material. However, due to the material′s exposure to high temperatures during FS, precipitates contributing to the strength such as β″ or β′ are dissolved or partially coarsen, resulting in a less favorable ratio of strength-increasing precipitates. Hence, the strengthening is achieved by grain boundary and dislocation strengthening. Nevertheless, in the Mg-containing alloys, the hardness values in the FS condition are about 15-23.5% higher than those for alloys in the BM condition. For the Si-containing alloys, the difference is not clearly observed; this may be due to the lower solubility of Si in Al and the consequently higher SFE. The higher SFE promotes recovery, resulting in a lower dislocation density remaining in the material after FS than for the Mg-containing alloys. The hardness maps within the coatings' cross sections are relatively homogeneous. On average, slightly increased hardness values were detected only at the edges of RS and AS, an observation which correlates with the smaller grain size in these areas. From the

hardness maps of the stop-action tests, no conclusions can be drawn regarding a precise classification into separate welding zones.

Within this project, but not presented as part of this thesis, additional investigations regarding the wear mechanisms of Friction Surfacing coatings of the Si containing alloys have been conducted. Lubricated sliding wear tests were carried out on a pin-on-disc tribometer; in this test, the Si-rich alloys in as-cast BM and FS condition were subjected to wear as pins sliding against 42CrMo4 steel discs. The FS-induced changes in the microstructure lead to an improvement in wear resistance. In the alloys with 6.6 wt.% Si and 10.4 wt.% Si, the spheroidization of the Si-particles improved the wear rates by a factor of up to $\approx$ 6. The dominant wear mechanisms on the Al alloy counterparts are micro-ploughing and breakout of Si phase particles. Details on these investigations are published in [47].

7 Summary and Conclusions

The focus of this thesis has been to elucidate the materials' response to FS processing, i.e. SPD at elevated temperatures, and their microstructural evolution in dependence of alloy composition. This includes the investigation of the effects on the processing behavior and on the resulting DRX microstructure when a single alloying element, Mg or Si, is replaced in an Al-based alloy. This novel approach is based on the assumption that in otherwise similar alloys, especially the SFE as well as the secondary phases are decisive for the FS process properties, the coating characteristics, and the recrystallized microstructure all driven by DRX mechanisms. For this purpose, aluminum alloy AA6060 (0.27 wt.% Mg; 0.37 wt.% Si), and, additionally, six alloys with different Mg contents (2, 3.5, 6.4, 8.9, 10.6 & 12.1 wt.%) and three with different Si contents (6.6, 10.4 & 14.6 wt.%) were processed using FS. For all Al alloys used, FS coatings could be generated under steady-state deposition.

Below, a summary of the main findings and conclusions drawn are divided into process development and coating characteristics, microstructure evolution and mechanical properties:

Process development and coating characteristics

- The maximum process peak temperatures of the Mg-containing alloys lie in the range of 460-480 °C, while the temperatures of the Si-containing alloys reach 440-460 °C. Obviously, the effect of alloying elements on process temperatures is very limited in the scope of this thesis.
- The temperature-dependent thermal conductivity, specific heat capacity, and the thermal diffusivity are all reduced by the addition of alloying elements Mg or Si, resulting in a slower softening of the material due to the higher proportion of saturated Mg_2Si precipitates. Increasing the Mg or Si content thus results in a reduced thermal softening rate. For the FS process, this means that more pronounced flow localization and plasticization of a smaller volume of material within the shear zone occur, leading to thin and narrow coatings when process parameters are not adjusted to the alloys' thermal properties.
- Small additions of Mg (2 and 3.5 wt.%) reveal significantly stronger effects on reduction of coating dimensions and required adjustments of process parameters than additions of higher amounts of Si (6.6-14.6 wt.%). Process speeds must be reduced for alloys with increased content of alloying elements – the Mg-rich alloys require a stronger reduction than the Si-rich alloys in order to achieve similar coating characteristics.
- An approach was presented for calculating effective shear strain rates during FS. Shear strain rates are estimated from theoretical considerations. They are high and vary strongly between the different alloys and process parameters. It appears that the necessary assumptions for the calculations simplify the process too much, in order to obtain quantitatively meaningful results. Especially the material flow during FS is difficult to approximate for calculations since it is complex and appears to vary with different process parameters.

Microstructure evolution

Macrostructure and texture

- Narrow and extremely fine-grained flow lines or band structures with preferred crystal orientation have been observed, mainly aligned parallel to the substrate surface. Towards the edges of AS and RS they tend to bend and sometimes take on a vortex-like appearance. This implies that the local grain orientation (texture) is affected by the material flow in terms of direction and strain rate although the grain size is rather homogeneous. For all process parameters, a minimum average grain size occurs at the AS and RS, followed by the center of the cross-section coating, due to the local differences in material flow conditions during FS.
- Using identical parameters with high rotational and translational speeds (4000 min^{-1}; 15mm/s) and the thus reduced deposition volume, a more localized material flow with higher strain rates is assumed, which leads to a weakening of the texture intensities within the flow lines.
- On average, the components B and $\overline{B}$ of the ideal shear texture dominate in the analyzed flow lines of the alloys AA6060 & 2 wt.% Mg. B and $\overline{B}$ components represent the slip planes {111} and slip directions <110> in the fcc crystal indicating a shear-dominated material flow at high texture intensities. A_1* & A_2* are also represented more than average in the microstructures. Regions beyond the flow lines and vortices exhibit lower texture intensities due to a more complete recrystallization.

Grain size and boundaries

- With increasing Mg content, the proportion of misorientation angles above 15° increases significantly with higher Mg content. The proportion of HAGBs also increases relative to LAGBs, indicating a higher degree of recrystallization in the final microstructure. The grain size generally decreases with higher content of alloying elements.
- As the SFE decreases with increasing Mg or Si content, cross-slip and climbing of dislocations are impeded; this process hinders dislocation annihilation, which in turn means that dynamic recovery is delayed. Thus, more dislocations remain inside the material, and these are active in DRX and result in the lower grain size.
- The higher the Mg or Si content, the more secondary phase particles occur in the alloys. More particles imply more opportunities for PSN events, which lead to more nucleation sites, in particular for dislocation cell structures to form, and thereby promote DRX and a lower resulting grain size.
- With increasing Mg or Si content, more nanoscale precipitates (Mg_2Si) are present in the microstructure. Dislocations can get stuck by the precipitates/dispersoids through Zener pinning. This means DRV is more difficult, and less dislocation cell structure formation is possible; the result is a delay of DRX and a counteraction of further grain refinement.

DRX mechanisms

- No correlation between DRX grain size and the Zener-Hollomon parameter was found. This may be due to several reasons: the estimated strain rates are not calculated correctly; temperature outweighs the effects of strain rates under the extreme conditions during FS; changes in the DRX mechanisms may lead to variations in the activation energy value Q and post dynamic recrystallization and grain growth may affect the grain size after processing.
- cDRX has been identified as the major acting mechanism. The complete cDRX process, as described in the pertinent literature, has been observed in the FS coating materials. First, accumulation of dislocations in clusters takes place, which further accumulate at the grain boundaries with ongoing deformation and subsequently form IDBs and dislocation cell structures. Second, with continuous accumulation of dislocations, these dislocation cell structures are transformed into LAGBs and finally into HAGBs.
- In the transition TMAZ to the recrystallized microstructure, the onset of DRX occurs during the deformation process, indicated by internal misorientation of the initial grains and serrated grain boundaries. These grain boundaries reveal compression-dominated pinching of the initial grains, indicating grain subdivision and signs of gDRX. It is assumed that gDRX gradually transitions to the cDRX mechanism in the early stages of DRX.
- Materials with low SFE undergo dDRX during hot working. However, no typical appearances of dDRX, such as necklace-like grains, were found in the microstructures of the coatings, even in alloys with very high Mg content (8.9-12.1 wt.%).

Secondary particles

- The volume fraction of the secondary phases increases with increasing Mg or Si content. The volume fraction is lower after FS since phases are dissolved in the α-Al solid solution during the FS process.
- The acting shear strains during FS shear off the larger Mg-rich or Si-rich phase particles and, in combination with the elevated temperatures, spheroidization takes place.
- The formation of phases is influenced by the presence of an excess of Mg or Si in the alloy. α-AlFeSi is transformed by FS to β-AlFeSi in the presence of an Si excess, and to Al_3Fe in the presence of an Mg excess. FS processing leads to spheroidization of needle-shaped β-AlFeSi and edged Al_3Fe phases.
- Oxides are formed due to externally introduced SiO_2 particles and/or by contact with oxygen at elevated temperature during casting or the FS process. From a thermodynamic point of view, the formation of oxides (Mg, Si, O-containing phases) is preferred to the formation of Mg_2Si due to the larger negative change in the Gibbs free energy ΔG. This leads to higher proportions of oxides instead of excess Mg_2Si phases in the microstructure after processing.

- It is assumed that most of the strength-enhancing precipitates, i.e., predominantly β″, but also β′, U1, U2, B′, are being dissolved during the thermal cycle. It follows that a larger amount of solutes is present within the α-Al in the deposited coating material compared to the BM state. As a result, re-clustering or precipitation occurs due to natural ageing. Consequently, the β″ and β′ peaks in the DSC curves are more pronounced for both the Mg-rich and the Si-rich alloys, implying that an unfavorable ratio of strength-increasing precipitates is present in the coating material after processing.
- Dislocation loops are created by FS resulting from the condensation of vacancies. These generated vacancies can promote mass transfer and thus lead to strain-induced accelerated growth and formation of precipitates, a phenomenon which is referred to as dynamic precipitation. This accelerates the formation of small precipitates in the FS coatings.

Mechanical properties

- Precipitation hardening & particle hardening, grain boundary hardening, and dislocation hardening all determine the resulting hardness in the coating material. Due to the unfavorable ratio of strength-increasing precipitates in the coating material (DSC analyses), particle hardening, grain boundary hardening, and dislocation hardening dominate.
- For the Mg-containing alloys, the hardness values in the FS state are about 15-23.5% higher than for the alloys in the BM state. It is assumed that the increase in strength was due to the highly recrystallized microstructure by grain boundary hardening, as well as increased dislocation density by dislocation hardening.
- In the case of Si-containing alloys, the difference between BM and FS is not significant. The finely distributed hard Si particles in the microstructures of the Si-containing samples both before and after the processing are responsible for the resulting hardness. Thus, it is assumed that particle hardening dominates here, and the remaining strengthening shows only a minor effect on the resulting hardness.

The presented results highlight the influence of the alloy composition on the thermal softening rate and shear strain rates caused by different Mg and Si contents in Al-base alloys and thus validate the investigated assumption: If only one of the alloying element Mg or Si is modified in aluminum alloys, the FS process behavior, the localized material flow during plastic deformation, the resulting microstructures and mechanical properties vary extensively, due to the influence of the alloying elements on the acting micromechanisms, particularly driven by the SFE and secondary phases.

References

[1] F. Ostermann; Anwendungstechnologie Aluminium, 2nd ed. Berlin, Heidelberg: Springer-Verlag Berlin Heidelberg, 2007. DOI: 10.1007/978-3-662-05788-9

[2] Gandra, J.; Krohn, H.; Miranda, R.; Vilaça, P.; Quintino, L. & dos Santos, J. Friction surfacing—A review Journal of Materials Processing Technology, Elsevier BV, 2014, 214, 1062-1093, DOI: 10.1016/j.jmatprotec.2013.12.008

[3] Shen, J.; Hanke, S.; Roos, A.; dos Santos, J. F. & Klusemann, B. Fundamental study on additive manufacturing of aluminum alloys by friction surfacing layer AIP Conference Proceedings 2113, 150015 (2019), DOI: 10.1063/1.5112691

[4] Edalati, K.; Bachmaier, A.; Beloshenko, V. A.; Beygelzimer, Y.; Blank, V. D.; Botta, W. J.; Bryła, K.; Č\ižek, J.; Divinski, S.; Enikeev, N. A.; Estrin, Y.; Faraji, G.; Figueiredo, R. B.; Fuji, M.; Furuta, T.; Grosdidier, T.; Gubicza, J.; Hohenwarter, A.; Horita, Z.; Huot, J.; Ikoma, Y.; Janeček, M.; Kawasaki, M.; Král, P.; Kuramoto, S.; Langdon, T. G.; Leiva, D. R.; Levitas, V. I.; Mazilkin, A.; Mito, M.; Miyamoto, H.; Nishizaki, T.; Pippan, R.; Popov, V. V.; Popova, E. N.; Purcek, G.; Renk, O.; Révész, Á.; Sauvage, X.; Sklenicka, V.; Skrotzki, W.; Straumal, B. B.; Suwas, S.; Toth, L. S.; Tsuji, N.; Valiev, R. Z.; Wilde, G.; Zehetbauer, M. J. & Zhu, X., Nanomaterials by severe plastic deformation: review of historical developments and recent advances, Materials Research Letters, Informa UK Limited, 2022, 10, 163-256, DOI: 10.1080/21663831.2022.2029779

[5] S. Hanke, J.F. dos Santos, Comparative study of severe plastic deformation at elevated temperatures of two aluminium alloys during friction surfacing, J. Mater. Process. Technol. 247 (2017) 257–267. DOI:10.1016/j.jmatprotec.2017.04.021.

[6] H. Klopstock und A. R. Neelands, An Improved Method of Joining or Welding Metals. Vereinigtes Königreich Patent 572789, 17 Oktober 1941.

[7] E. Seidi, S.F. Miller, A Novel Approach to Friction Surfacing: Experimental Analysis of Deposition from Radial Surface of a Consumable Tool, Coatings. (2020) 1–17. DOI:10.3390/coatings10111016.

[8] H.K. Rafi, G.D.J. Ram, G. Phanikumar, K.P. Rao, Surface & Coatings Technology Friction surfaced tool steel (H13) coatings on low carbon steel : A study on the effects of process parameters on coating characteristics and integrity, Surf. Coatings Technol. J. 205 (2010) 232–242. DOI:10.1016/j.surfcoat.2010.06.052.

[9] Hanke, S.; Sena, I.; Coelho, R. S. & dos Santos, J. F., Microstructural features of dynamic recrystallization in alloy 625 friction surfacing coatings, Materials and Manufacturing Processes, Taylor & Francis, 2018, 33, 270-276, DOI: 10.1080/10426914.2017.1291947

[10] J.J.S. Dilip, S. Babu, S.V. Rajan, K.H. Rafi, G.D.J. Ram, B.E. Stucker, Materials and Manufacturing Processes Use of Friction Surfacing for Additive Manufacturing Use of Friction Surfacing for Additive Manufacturing, Mater. Manuf. Process. (2013) 37–41. DOI:10.1080/10426914.2012.677912.

[11] Fukakusa, K., On the characteristics of the rotational contact plane - a fundamental study of friction surfacing Welding International, Taylor & Francis, 1996, 10, 524-529, DOI: 10.1080/09507119609549043

[12] Liu, X. M.; Zou, Z. D.; Zhang, Y. H.; Qu, S. Y. & Wang, X. H., Transferring mechanism of the coating rod in friction surfacing, Surface and Coatings Technology, 2008, 202, 1889-1894, DOI: 10.1016/j.surfcoat.2007.08.024

[13] Batchelor, A. W.; Jana, S.; Koh, C. P. & Tan, C. S., The effect of metal type and multi-layering on friction surfacing, Journal of Materials Processing Technology, 1996, 57, 172-181, DOI: 10.1016/0924-0136(95)02057-8

[14] Box, G. E. P. & Behnken, D. W., Some New Three Level Designs for the Study of Quantitative Variables, Technometrics, Informa UK Limited, 1960, 2, 455-475, DOI: 10.1080/00401706.1960.10489912

[15] T. Shinoda and al. et. Effect of process parameters during friction coating on properties of non-dilution coating layers. Surface Engineering, 14:211–216, 1998. Doi: 10.1179/sur.1998.14.3.211

[16] Sakihama, H., Tokisue, H., Katoh, K., 2003. Mechanical properties of friction surfaced 5052 aluminum alloy. Materials Transactions 44, 2688–2694.

[17] Fitseva, V.; Hanke, S. & dos Santos, J. F., Influence of rotational speed on process characteristics in friction surfacing of Ti-6Al-4V, Materials and Manufacturing Processes, Informa UK Limited, 2016, 32, 557-563, DOI: 10.1080/10426914.2016.1257799

[18] Hornbogen, E.; Eggeler, G. & Werner, E.; Werkstoffe; Springer Berlin Heidelberg, 2012, DOI: 10.1007/978-3-642-22561-1

[19] G. Gottstein; Physikalische Grundlagen der Materialkunde, 3rd ed. Berlin, Heidelberg: Springer-Verlag Berlin Heidelberg, 2007. DOI: 10.1007/978-3-662-09331-3

[20] K. Huang; R.E. Loge; A review of dynamic recrystallization phenomena in metallic materials, Materials & Design, 111 (2016) 548–574. DOI: 10.1016/j.matdes.2016.09.012.

[21] Zhao, Y.; Liao, X.; Zhu, Y.; Horita, Z. & Langdon, T. Influence of stacking fault energy on nanostructure formation under high pressure torsion, Materials Science and Engineering: A, Elsevier BV, 2005, 410-411, 188-193, DOI: 10.1016/j.msea.2005.08.074

[22] Aerts, E.; Delavignette, P.; Siems, R. & Amelinckx, S., Stacking Fault Energy in Silicon, Journal of Applied Physics, AIP Publishing, 1962, 33, 3078-3080, DOI: 10.1063/1.1728570

[23] Hull, D. & Bacon, D., Introduction to Dislocations, Elsevier, 2011, 85-107, DOI: 10.1007/s40195-020-01064-6

[24] Edalati, K. & Horita, Z. A review on high-pressure torsion (HPT) from 1935 to 1988 Materials Science and Engineering: A, Elsevier BV, 2016, 652, 325-352, DOI: 10.1016/j.msea.2015.11.074

[25] Bridgman, P. W., Effects of High Shearing Stress Combined with High Hydrostatic Pressure Physical Review, American Physical Society (APS), 1935, 48, 825-847, DOI: 10.1103/physrev.48.825

[26] Iwahashi, Y.; Wang, J.; Horita, Z.; Nemoto, M. & Langdon, T. G., Principle of equal-channel angular pressing for the processing of ultra-fine grained materials, Scripta Materialia, Elsevier BV, 1996, 35, 143-146, DOI: 10.1016/1359-6462(96)00107-8

[27] Saito, Y.; Tsuji, N.; Utsunomiya, H.; Sakai, T. & Hong, R., Ultra-fine grained bulk aluminum produced by accumulative roll-bonding (ARB) process, Scripta Materialia, Elsevier BV, 1998, 39, 1221-1227, DOI: 10.1016/S1359-6462(98)00302-9

[28] Beygelzimer, Y.; Orlov, D. & Varyukhin, V., A New Severe Plastic Deformation Method: Twist Extrusion, Ultrafine Grained Materials II, John Wiley & Sons, Inc., 2013, 297-304, DOI: 10.1002/9781118804537.ch35

[29] Thomas, W.M., Friction Stir Butt Welding. International Patent, Application No PCTrGB92 Patent Application No.9125978.8, 1991

[30] Thomas, W.M. & Nicholas, E., Friction stir welding for the transportation industries, Materials & Design, Elsevier BV, 1997, 18, 269-273, DOI: 10.1016/s0261-3069(97)00062-9

[31] dos Santos, J. F., Solid-State Joining Processes, Booklet, 2016

[32] Zehetbauer, M.; Kohout, J.; Schafler, E.; Sachslehner, F. & Dubravina, A., Plastic deformation of nickel under high hydrostatic pressure, Journal of Alloys and Compounds, Elsevier BV, 2004, 378, 329-334, DOI: 10.1016/j.jallcom.2004.01.039

[33] Kumar, K.; Swygenhoven, H. V. & Suresh, S., Mechanical behavior of nanocrystalline metals and alloys, The Golden Jubilee Issue—Selected topics in Materials Science and Engineering: Past, Present and Future, edited by S. Suresh, Acta Materialia, Elsevier BV, 2003, 51, 5743-5774, DOI: 10.1016/j.actamat.2003.08.032

[34] Hornbogen, E. & Warlimont, H., Allgemeiner Überblick, Metallkunde: Aufbau und Eigenschaften von Metallen und Legierungen, Springer Berlin Heidelberg, 2001

[35] R.Z. Valiev, I.V. Alexandrov, Y.T. Zhu, T.C. Lowe: Paradox of strenght and ductility in metals processed by severe plastic deformation. Journal of Materials Research. Vol.17, No 1 (2002) 5-8, DOI: 10.1557/JMR.2002.0002

[36] Pippan, R.; Wetscher, F.; Hafok, M.; Vorhauer, A. & Sabirov, I., The Limits of Refinement by Severe Plastic Deformation, Advanced Engineering Materials, Wiley, 2006, 8, 1046-1056, DOI: 10.1002/adem.200600133

[37] Zhang, H.; Huang, X. & Hansen, N., Evolution of microstructural parameters and flow stresses toward limits in nickel deformed to ultra-high strains, Acta Materialia, Elsevier BV, 2008, 56, 5451-5465, DOI: 10.1016/j.actamat.2008.07.040

[38] Tsuji, N.; Gholizadeh, R.; Ueji, R.; Kamikawa, N.; Zhao, L.; Tian, Y.; Bai, Y. & Shibata, A., Formation Mechanism of Ultrafine Grained Microstructures: Various Possibilities for Fabricating Bulk Nanostructured Metals and Alloys, MATERIALS TRANSACTIONS, Japan Institute of Metals, 2019, 60, 1518-1532, DOI: 10.2320/matertrans.mf201936

[39] Gholizadeh, R.; Shibata, A. & Tsuji, N. Global view for grain refinement in ultra-low-C IF steel during high-strain deformation at various temperatures and strain rates Materialia, Elsevier BV, 2019, 6, 100262, DOI: 10.1016/j.mtla.2019.100262

[40] T. Hebesberger, H.P. Stüwe, A. Vorhauer, F. Wetscher, and R. Pippan: Structure of Cu deformed by high pressure torsion. Acta Materialia, 53(2): (2005) 393–402, DOI: 10.1016/j.actamat.2004.09.043

[41] Kaveh Edalati, Tadayoshi Fujioka, Zenji Horita: Microstructure and mechanical properties of pure Cu processed by high-pressure torsion. Materials Science and Engineering A 497 (2008) 168–173, DOI: 10.1016/j.msea.2008.06.039

[42] Y.T. Zhu, T.G. Langdon: The fundamentals of nanostructured materials processed by severe plastic deformation. JOM 56(10) (2004) 58–63, DOI: 10.1007/s11837-004-0294-0

[43] Skripnyuk, V.; Rabkin, E.; Estrin, Y. & Lapovok, R., The effect of ball milling and equal channel angular pressing on the hydrogen absorption/desorption properties of Mg–4.95 wt% Zn–0.71 wt% Zr (ZK60) alloy, Acta Materialia, Elsevier BV, 2004, 52, 405-414, DOI: 10.1016/j.actamat.2003.09.025

[44] Dobatkin, S.; Gubicza, J.; Shangina, D.; Bochvar, N. & Tabachkova, N., High strength and good electrical conductivity in Cu–Cr alloys processed by severe plastic deformation, Materials Letters, Elsevier BV, 2015, 153, 5-9, DOI: 10.1016/j.matlet.2015.03.144

[45] Nishizaki, T.; Lee, S.; Horita, Z.; Sasaki, T. & Kobayashi, N., Superconducting properties in bulk nanostructured niobium prepared by high-pressure torsion, Physica C: Superconductivity, Elsevier BV, 2013, 493, 132-135, DOI: 10.1016/j.physc.2013.03.046

[46] Gao, J.; Guan, S.; Ren, Z.; Sun, Y.; Zhu, S. & Wang, B., Homogeneous corrosion of high pressure torsion treated Mg–Zn–Ca alloy in simulated body fluid, Materials Letters, Elsevier BV, 2011, 65, 691-693, DOI: 10.1016/j.matlet.2010.11.015

[47] Schütte, M. R.; Ehrich, J.; Linsler, D. & Hanke, S., Effects of Microstructure Modification by Friction Surfacing on Wear Behavior of Al Alloys with Different Si Contents, Materials, MDPI AG, 2022, 15, 1641, DOI: 10.3390/ma15051641

[48] Hanke S.; Microstructural Alterations of Commercial Metallic Alloys by Friction Surfacing, PhD Thesis, Duisburg, Universität Duisburg-Essen (2014).

[49] Sakai T.; Dynamic Recrystallization Microstructure Under Hot Working Conditions, Journal of Materials Processing Technology, 53 (1995) 349-61. DOI: 10.1016/0924-0136(95)01992-n

[50] Doherty, R.; Hughes, D.; Humphreys, F.; Jonas, J.; Jensen, D.; Kassner, M.; King, W.; McNelley, T.; McQueen, H. & Rollett, A., Current issues in recrystallization: a review, Materials Science and Engineering: A, Elsevier BV, 1997, 238, 219-274, DOI: 10.1016/S0921-5093(97)00424-3

[51] Haasen, P.; Physikalische Metallkunde. Springer Berlin Heidelberg, 1994. DOI: 10.1007/978-3-642-87849-7

[52] Sakai, T.; Belyakov, A.; Kaibyshev, R.; Miura, H. & Jonas, J. J. Dynamic and post-dynamic recrystallization under hot, cold and severe plastic deformation conditions, Progress in Materials Science, 2014, 60, 130-207. DOI: 10.1016/j.pmatsci.2013.09.002.

[53] Sabirov, I.; Murashkin, M. Y. & Valiev, R. Z.; Nanostructured aluminium alloys produced by severe plastic deformation: New horizons in development, Materials Science and Engineering: A, 2013, 560, 1-24, DOI: 10.1016/j.msea.2012.09.020

[54] Zhilyaev; A. P. & Langdon, T. G.; Using high-pressure torsion for metal processing: Fundamentals and applications, Progress in Materials Science, 2008, 53, 893-979, DOI: 10.1016/j.pmatsci.2008.03.002

[55] Ehrich, J.; Roos, A.; Klusemann, B. & Hanke, S.; Influence of Mg content in Al alloys on processing characteristics and dynamically recrystallized microstructure of friction surfacing deposits, Materials Science and Engineering: A, Elsevier BV, 2021, 819, 141407, DOI: 10.1016/j.msea.2021.141407

[56] Lv, J.; Zheng, J.-H.; Yardley, V. A.; Shi, Z. & Lin, J. A Review of Microstructural Evolution and Modelling of Aluminium Alloys under Hot Forming Conditions, Metals, MDPI AG, 2020, 10, 1516, DOI: 10.3390/met10111516

[57] McQueen, H.; Development of dynamic recrystallization theory. Materials Science and Engineering: A, Elsevier BV, 2004, 387-389, 203-208. DOI: 10.1016/j.msea.2004.01.064

[58] McQueen, H.. Dynamic Recovery and Recrystallization, Encyclopedia of Materials: Science and Technology, Elsevier, 2001, 2375-2381, DOI: 10.1016/b0-08-043152-6/00419-8

[59] Henshall, G.A.; Kassner, M.E.; McQueen, H.J. Dynamic restoration mechanisms in Al-5.8 At. Pct Mg deformed to large strains in the solute drag regime. Met. Mater. Trans. A 1992, 23, 881–889, DOI: 10.1007/BF02675565

[60] Suhuddin, U.; Mironov, S.; Krohn, H.; Beyer, M. & Santos, J. F. D., Microstructural Evolution During Friction Surfacing of Dissimilar Aluminum Alloys, Metallurgical and Materials Transactions A, Springer Science and Business Media LLC, 2012, 43, 5224-5231, DOI: 10.1007/s11661-012-1345-8

[61] Liu, X.; Sun, Y.; Nagira, T.; Ushioda, K. & Fujii, H. Effect of Stacking Fault Energy on the Grain Structure Evolution of FCC Metals During Friction Stir Welding, Acta Metallurgica Sinica (English Letters), Springer Science and Business Media LLC, 2020, 33, 1001-1012, DOI: 10.1007/s40195-020-01064-6

[62] Zener, C. & Hollomon, J. H., Effect of Strain Rate Upon Plastic Flow of Steel, Journal of Applied Physics, AIP Publishing, 1944, 15, 22-32, DOI: 10.1063/1.1707363

[63] Dialami, N.; Cervera, M. & Chiumenti, M., Numerical Modelling of Microstructure Evolution in Friction Stir Welding (FSW), Metals, MDPI AG, 2018, 8, 183, DOI: 10.3390/met8030183

[64] Chang, C. I.; Lee, C. J. & Huang, J. C., Relationship between grain size and Zener-Holloman parameter during friction stir processing in AZ31 Mg alloys, Scripta Materialia, 2004, 51, 509-514

[65] Morishige, T.; Hirata, T.; Uesugi, T.; Takigawa, Y.; Tsujikawa, M. & Higashi, K., Effect of Mg content on the minimum grain size of Al-Mg alloys obtained by friction stir processing, Scripta Materialia, 2011, 64, 355-358

[66] Kuhlmann-Wilsdorf, D., The Connection between Recovery and Glide Type in Aluminum and Al-Mg, Materials Science Forum, Trans Tech Publications, Ltd., 2000, 331-337, 689-702, DOI: 10.4028/www.scientific.net/msf.331-337.689

[67] Gallagher, P. C. J., The influence of alloying, temperature, and related effects on the stacking fault energy, Metallurgical Transactions, 1970, 1, 2429-2461, DOI: 10.1007/BF03038370

[68] Engler, O. & Hirsch, J., Texture control by thermomechanical processing of AA6xxx Al–Mg–Si sheet alloys for automotive applications—a review, Materials Science and Engineering: A, Elsevier BV, 2002, 336, 249-262, DOI: 10.1016/s0921-5093(01)01968-2

[69] Humphreys, F., The nucleation of recrystallization at second phase particles in deformed aluminium, Acta Metallurgica, Elsevier BV, 1977, 25, 1323-1344, DOI: 10.1016/0001-6160(77)90109-2

[70] E. Nes, N. Ryum, O. Hunderi, On the zener drag, Acta Metall. 33 (1985) 11–22. DOI:10.1016/0001-6160(85)90214-7.

[71] Huang, K.; Wang, N.; Li, Y. & Marthinsen, K., The influence of microchemistry on the softening behaviour of two cold-rolled Al–Mn–Fe–Si alloys, Materials Science and Engineering: A, Elsevier BV, 2014, 601, 86-96, DOI: 10.1016/j.msea.2014.02.037

[72] Roven, H. J.; Liu, M. & Werenskiold, J. C., Dynamic precipitation during severe plastic deformation of an Al–Mg–Si aluminium alloy, Materials Science and Engineering: A, Elsevier BV, 2008, 483-484, 54-58, DOI: 10.1016/j.msea.2006.09.142

[73] Dogan, E.; Wang, S.; Vaughan, M. & Karaman, I., Dynamic precipitation in Mg-3Al-1Zn alloy during different plastic deformation modes, Acta Materialia, Elsevier BV, 2016, 116, 1-13, DOI: 10.1016/j.actamat.2016.06.011

[74] Su, J.-Q.; Nelson, T.; Mishra, R. & Mahoney, M., Microstructural investigation of friction stir welded 7050-T651 aluminium, Acta Materialia, Elsevier BV, 2003, 51, 713-729, DOI: 10.1016/S1359-6454(02)00449-4

[75] Guo, F.; Zhang, D.; Yang, X.; Jiang, L. & Pan, F., Strain-induced dynamic precipitation of Mg17Al12 phases in Mg–8Al alloys sheets rolled at 748 K, Materials Science and Engineering: A, Elsevier BV, 2015, 636, 516-521, DOI: 10.1016/j.msea.2015.03.112

[76] Su, J.; Kaboli, S.; Kabir, A. S. H.; Jung, I.-H. & Yue, S., Effect of dynamic precipitation and twinning on dynamic recrystallization of micro-alloyed Mg–Al–Ca alloys, Materials Science and Engineering: A, Elsevier BV, 2013, 587, 27-35, DOI: 10.1016/j.msea.2013.08.019

[77] H.-J. Bargel and G. Schulze, Werkstoffkunde: Mit 85 Tabellen, 9th ed. Berlin, Heidelberg: Springer, 2005

[78] M. Cabibbo, E. Evangelista, and M. Vedani, “Influence of severe plastic deformations on secondary phase precipitation in a 6082 Al-Mg-Si alloy,” Metall and Mat Trans A, vol. 36, no. 5, pp. 1353–1364, 2005, DOI: 10.1007/s11661-005-0226-9.

[79] B. Leszczyńska-Madej, M. Richert, A. Wąsik, and A. Szafron, “Analysis of the Microstructure and Selected Properties of the Aluminium Alloys Used in Automotive Air-Conditioning Systems,” Metals, vol. 8, no. 1, p. 10, 2018, DOI: 10.3390/met8010010.

[80] Marioara, C. D.; Andersen, S. J.; Stene, T. N.; Hasting, H.; Walmsley, J.; Helvoort, A. T. J. V. & Holmestad, R. The effect of Cu on precipitation in Al–Mg–Si alloys Philosophical Magazine, Informa UK Limited, 2007, 87, 3385-3413, DOI: 10.1080/14786430701287377

[81] Vissers, R.; van Huis, M.; Jansen, J.; Zandbergen, H.; Marioara, C. & Andersen, S. The crystal structure of the upbeta′ phase in Al–Mg–Si alloys Acta Materialia, Elsevier BV, 2007, 55, 3815-3823, DOI: 10.1016/j.actamat.2007.02.032

[82] R. N. Lumley, Fundamentals of aluminium metallurgy: Production, processing and applications. Oxford, Philadelphia: Woodhead Pub, 2011. [Online]. Available: http://search.ebscohost.com/login.aspx?direct=true&scope=site&db=nlebk&db=nlabk&AN=680662

[83] C. Genevois, A. Deschamps, Quantitative investigation of precipitation and mechanical behaviour for AA2024 friction stir welds, Acta Mater. 53 (2005) 2447–2458. DOI:10.1016/j.actamat.2005.02.007.

[84] K. Huang, K. Marthinsen, Q. Zhao, R.E. Logé, The double-edge effect of second-phase particles on the recrystallization behaviour and associated mechanical properties of metallic materials, Prog. Mater. Sci. (2018). DOI:10.1016/j.pmatsci.2017.10.004.

[85] Hutchinson, C.; de Geuser, F.; Chen, Y. & Deschamps, A., Quantitative measurements of dynamic precipitation during fatigue of an Al–Zn–Mg–(Cu) alloy using small-angle X-ray scattering, Acta Materialia, Elsevier BV, 2014, 74, 96-109, DOI: 10.1016/j.actamat.2014.04.027

[86] Deschamps, A.; Fribourg, G.; Bréchet, Y.; Chemin, J. & Hutchinson, C., In situ evaluation of dynamic precipitation during plastic straining of an Al–Zn–Mg–Cu alloy, Acta Materialia, Elsevier BV, 2012, 60, 1905-1916, DOI: 10.1016/j.actamat.2012.01.002

[87] Engler, Olaf, and Valerie Randle. Introduction to texture analysis: macrotexture, microtexture, and orientation mapping. CRC press, 2009.

[88] Hans-Joachim Bunge, Texture Analysis in Materials Science Elsevier, 1982.

[89] G. Gottstein, „Kristallographische Orientierung,“ in Materialwissenschaft und Werkstofftechnik - Physikalische Grundlagen, Berlin/Heidelberg, Springer Vieweg, 2014, pp. 44-51.

[90] G. Gottstein, „Kristallographische Texturen,“ in Materialwissenschaft und Werkstofftechnik - Physikalische Grundlagen, Berlin/Heidelberg, Springer Vieweg, 2014, pp. 60-67.

[91] Saiyi, Zhang Xinming Li. "Research of Textures in Metallic Materials and ITS Development [J]." Bulletin of National Science Foundation of China 3 (1995)

[92] R. W. Fonda und K. E. Knipling, „Texture development in friction stir welds,“ Science and Technology of Welding and Joining, pp. 288-294, 12 Januar 2011.

[93] Saiyi Li, Irene J. Beyerlein, Mark A.M. Bourke, Texture formation during equal channel angular extrusion of fcc and bcc materials: comparison with simple shear, Materials Science and Engineering A 394 (2005) 66–77, DOI: 10.1016/j.msea.2004.11.032

[94] Suhuddin, U., et al. "Microstructural evolution during friction surfacing of dissimilar aluminum alloys." Metallurgical and Materials Transactions A 43.13 (2012): 5224-5231.

[95] Field, David P., et al. "Heterogeneity of crystallographic texture in friction stir welds of aluminum." Metallurgical and Materials Transactions A 32.11 (2001): 2869-2877

[96] J. Kozieł, L. Błaz, G. Wloch, J. Sobota, P. Lobry, Precipitation Processes during Non-Isothermal Ageing of Fine-Grained 2024 Alloy, Arch. Metall. Mater. (2016). DOI:10.1515/amm-2016-0030.

[97] Zhilyaev, A. P. & Langdon, T. G., Using high-pressure torsion for metal processing: Fundamentals and applications, Progress in Materials Science, 2008, 53, 893-979

[98] Ehrich, J.; Roos, A. & Hanke, S., Effect of Mg and Si Content in Aluminum Alloys on Friction Surfacing Processing Behavior, Light Metals 2019, Springer International Publishing, 2019, 357-363

[99] J. Sanderson, Understanding light microscopy. Hoboken, NJ: John Wiley & Sons, 2019.

[100] W. F. Gale and T. C. Totemeier, Smithells metals reference book, 8th ed. Amsterdam: Elsevier/Butterworth-Heinemann, 2004. [Online]. Available: http://www.sciencedirect.com/science/book/9780750675093

[101] Stahl –Mikrophotographische Bestimmung der erkennbaren Korngröße (ISO/DIS 643:2017); Deutsche und Englische Fassung prEN ISO 643:2017, DIN Deutsches Institut für Normung e.V., Berlin: Beuth Verlag GmbH, 2017

[102] B. Mitevski; „Untersuchungen zum mechanischen Verhalten von oligokristallinem X2 CrNiMo 18-15-3“, Doktorarbeit, Brandenburgischen Technischen Universität Cottbus –Senftenberg, 2018

[103] E. Macherauch, H.W. Zoch; “Praktikum in Werkstoffkunde“, Springer Fachmedien Wiesbaden, 2014, S. 57-64, DOI: 10.1007/978-3-658- 05038-2

[104] C. Colliex, H. Kohl; „Elektronenmikroskopie: eine anwendungsbezogene Einführung“, Wiss. Verlag-Ges. Stuttgart, 2008.

[105] A. Polini and F. Yang, “5 - Physicochemical characterization of nanofiber composites,” in Woodhead publishing series in biomaterials, Nanofiber composites for biomedical applications, M. Ramalingam and S. Ramakrishna, Eds., Duxford, Cambridge, MA, Kidlington: WP Woodhead Publishing an imprint of Elsevier, 2017, pp. 97–115. [Online]. Available: http://www.sciencedirect.com/science/article/pii/B9780081001738000053

[106] H. Biermann und L. Krüger, „Moderne Methoden der Rasterelektronenmikroskopie,“ in Moderne Methoden der Werkstoffprüfung, Weinheim, WILEY-VCH Verlag GmbH & Co. KGaA, 2015, pp. 217-237.

[107] OIM DataAnalysisTM (OIM Analysis 5.3) Manual, Ametek GmbH, EDAX Division, Kreuzberger Ring 6, D-65205 Wiesbaden, 2012. (Veröffentlichungsjahr: 2007)

[108] S. Weiß, “Einfluss der Wenigkristallinität auf das Verformungsverhalten von Werkstoffen und Bauteilen der Medizintechnik” Habilitation Thesis, University of Duisburg-Essen (2008) VDI-Fortschr. Bericht Reihe 5 Nr. 734 VDI-Verlag, Düsseldorf, Germany (2008)

[109] Tao, Xiaodong, and Alwyn Eades. "Alternatives to image quality (IQ) mapping in EBSD." Microscopy and Microanalysis 8.S02 (2002): 692-693

[110] E. Hornbogen, B. Skrotzki; “Mikro- und Nanoskopie der Werkstoffe“, 3ed., Springer-Verlag Berlin Heidelberg, 2009.

[111] Neises, J.; Scheld, W. S.; Seok, A.-R.; Lobe, S.; Finsterbusch, M.; Uhlenbruck, S.; Schmechel, R. & Benson, N. Study of thermal material properties for Ta- and Al-substituted Li7La3Zr2O12 (LLZO) solid-state electrolyte in dependency of temperature and grain size. Journal of Materials Chemistry A, Royal Society of Chemistry (RSC), 2022, 10, 12177-12186, DOI: 10.1039/d2ta00323f

[112] Menczel, J. D., Judovits, L., Prime, R. B., Bair, H. E., Reading, M., & Swier, S. (2009). Differential scanning calorimetry (DSC). Thermal analysis of polymers: Fundamentals and applications, 7-239.

[113] Birol, Y. (2006). DSC analysis of the precipitation reactions in the alloy AA6082: Effect of sample preparation. Journal of thermal analysis and calorimetry, 83(1), 219-222.

[114] Osten, J., Milkereit, B., Schick, C., & Kessler, O. (2015). Dissolution and precipitation behaviour during continuous heating of Al–Mg–Si alloys in a wide range of heating rates. Materials, 8(5), 2830-2848.

[115] J. Gandra, D. Pereira, R.M. Miranda, R.J.C. Silva, P. Vilaça, Deposition of AA6082-T6 over AA2024-T3 by friction surfacing - Mechanical and wear characterization, Surf. Coatings Technol. 223 (2013) 32–40. DOI:10.1016/j.surfcoat.2013.02.023.

[116] H. Sakihama, H. Tokisue, K. Katoh, Mechanical properties of a friction surfaced 5052 aluminum alloy., J. Japan Inst. Light Met. 52 (2002) 346–351. DOI:10.2464/jilm.52.346.

[117] Morisada, Y.; Imaizumi, T. & Fujii, H., Determination of strain rate in Friction Stir Welding by three-dimensional visualization of material flow using X-ray radiography, Scripta Materialia, 2015, 106, 57-60

[118] Morishige, T.; Hirata, T.; Uesugi, T.; Takigawa, Y.; Tsujikawa, M. & Higashi, K., Effect of Mg content on the minimum grain size of Al-Mg alloys obtained by friction stir processing, Scripta Materialia, 2011, 64, 355-358

[119] Chang, C. I.; Lee, C. J. & Huang, J. C., Relationship between grain size and Zener-Holloman parameter during friction stir processing in AZ31 Mg alloys, Scripta Materialia, 2004, 51, 509-514

[120] Ehrich, J.; Staron, P.; Karkar, A.; Roos, A. & Hanke, S., Precipitation Evolution in the Heat-Affected Zone and Coating Material of AA2024 Processed by Friction Surfacing, Advanced Engineering Materials, Wiley, 2022, 2201019, DOI: 10.1002/adem.202201019

[121] Designation: E112 − 12. Standard Test Methods for Determining Average Grain Size, ASTM International, West Conshohocken: Center For Library Initiatives,2013

[122] Stahl –Mikrophotographische Bestimmung der erkennbaren Korngröße (ISO/DIS 643:2017);Deutsche und Englische Fassung prEN ISO 643:2017, DIN Deutsches Institut für Normung e.V., Berlin: Beuth Verlag GmbH, 2017

[123] Demny, J. Gitterfehler und ihre Beobachtung: II. Bewegungen von Versetzungen, Stapelfehler, Leerstellenkondensation Physik Journal, Wiley, 1962, 18, 61-71

[124] TCAL6:TCSAl-basedAlloyDatabase, Thermo-Calc Software AB, Solna, Schweden, http://www.thermocalc.com

[125] B. B. Straumal, B. Baretzky, O. A. Kogtenkova, A. B. Straumal, and A. S. Sidorenko, “Wetting of grain boundaries in Al by the solid Al3Mg2 phase,” J Mater Sci, vol. 45, no 8, pp. 2057–2061, 2010, DOI: 10.1007/s10853-009-4014-6.

[126] Rosefort, M.; Matthies, C.; Buck, H. & Koch, H. Using SEM and EDX for a Simple Differentiation of upalpha- and upbeta-Alfesi-Phases in Wrought Aluminum Billets Light Metals 2011, Springer International Publishing, 2011, 711-716, DOI: 10.1007/978-3-319-48160-9_124

[127] K. Uttarasak, W. Chongchitnan, K. Matsuda, T. Chairuangsri, J. Kajornchaiyakul, and C. Banjongprasert, “Evolution of Fe-containing intermetallic phases and abnormal grain growth in 6063 aluminum alloy during homogenization,” Results in Physics, vol. 15, p. 102535, 2019, DOI: 10.1016/j.rinp

[128] D. E. Newbury and N. W. M. Ritchie, “Is scanning electron microscopy/energy dispersive X-ray spectrometry (SEM/EDS) quantitative?,” Scanning, vol. 35, no. 3, pp. 141–168, 2013, DOI: 10.1002/sca.21041

[129] X. CAO and J. CAMPBELL, “OXIDE INCLUSION DEFECTS IN Al-Si-Mg CAST ALLOYS,” Canadian Metallurgical Quarterly, vol. 44, no. 4, pp. 435–448, 2005, DOI: 10.1179/cmq.2005.44.4.435.

[130] V. M. Sreekumar, N. Hari Babu, D. G. Eskin, and Z. Fan, “Structure–property analysis of in-situ Al–MgAl2O4 metal matrix composites synthesized using ultrasonic cavitation,” Materials Science and Engineering: A, vol. 628, pp. 30–40, 2015, DOI: 10.1016/j.msea.2015.01.029.

[131] N. Hayati-Roodbari, R. J. F. Berger, J. Bernardi, S. Kinge, N. Hüsing, and M. S. Elsaesser, “Monolithic porous magnesium silicide,” Dalton transactions (Cambridge, England: 2003), vol. 46, no. 27, pp. 8855–8860, 2017, DOI: 10.1039/c7dt00571g

[132] Edwards, G.; Stiller, K.; Dunlop, G. & Couper, M. The precipitation sequence in Al–Mg–Si alloys. Acta Materialia, Elsevier BV, 1998, 46, 3893-3904, DOI: 10.1016/S1359-6454(98)00059-7

[133] Takeda, M.; Ohkubo, F.; Shirai, T. & Takeda, M. Stability of metastable phases and microstructures in the ageing process of Al–Mg–Si ternary alloys Journal of Materials Science, Springer Science and Business Media LLC, 1998, 33, 2385-2390, DOI: 10.1023/A:1004355824857

[134] Matsuda, K.; Ikeno, S.; Terayama, K.; Matsui, H.; Sato, T. & Uetani, Y. Comparison of precipitates between excess Si-type and balanced-type Al-Mg-Si alloys during continuous heating Metallurgical and Materials Transactions A, Springer Science and Business Media LLC, 2005, 36, 2007-2012, DOI: 10.1007/s11661-005-0321-y

[135] M. Reimann; „Keyhole repair in precipitation hardening aluminum alloys using refill friction stir spot welding“, Doktorarbeit, Technischen Universität Hamburg, 2018

[136] Gaber, A.; Afify, N.; Mostafa, M. & Abbady, G., Effect of heat treatment on the precipitation in Al–1at.% Mg–xat.% Si (x=0.6, 1.0 and 1.6) alloys, Journal of Alloys and Compounds, Elsevier BV, 2009, 477, 295-300, DOI: 10.1016/j.jallcom.2008.11.009

[137] Tsai, M. S., Sun, P. L., Kao, P. W., & Chang, C. P. (2009). Influence of severe plastic deformation on precipitation hardening in an Al-Mg-Si alloy: microstructure and mechanical properties. Materials transactions, 50(4), 771-775

[138] Eskin, D.; Suyitno & Katgerman, L., Mechanical properties in the semi-solid state and hot tearing of aluminium alloys, Progress in Materials Science, Elsevier BV, 2004, 49, 629-711

[139] Cleveland, R. M.; Ghosh, A. K. & Bradley, J. R., Comparison of superplastic behavior in two 5083 aluminum alloys, Materials Science and Engineering: A, 2003, 351, 228-236

[140] Dovzhenko, G.; “Characterization of Residual Stresses in Friction Surfacing of Ti and Al Alloys“, Doktorarbeit, Universität Hamburg, 2020

[141] C. Belei, V. Fitseva, J.F. dos Santos, N.G. Alcantara, S. Hanke, TiC particle reinforced Ti-6Al-4V friction surfacing coatings, Surf. Coating. Technol. 329 (2017) 163–173.

[142] Rafi, H. Khalid, et al. "Microstructural evolution during friction surfacing of austenitic stainless steel AISI 304 on low carbon steel." Metallurgical and Materials Transactions A, 44.1 (2013): 345-350.

[143] Prangnell, P. & Heason, C. Grain structure formation during friction stir welding observed by the `stop action technique' Acta Materialia, Elsevier BV, 2005, 53, 3179-3192

[144] Shen, J.; Lage, S. B. M.; Suhuddin, U. F. H.; Bolfarini, C. & dos Santos, J. F., Texture Development and Material Flow Behavior During Refill Friction Stir Spot Welding of AlMgSc, Metallurgical and Materials Transactions A, Springer Science and Business Media LLC, 2017, 49, 241-254

[145] Fonda, R. W., D. J. Rowenhorst, and K. E. Knipling. "3D material flow in friction stir welds." Metallurgical and Materials Transactions A 50.2 (2019): 655-663.

[146] Chun, Y. B., et al. "Distribution characteristics of in-grain misorientation axes in coldrolled commercially pure titanium and their correlation with active slip modes." Metallurgical and Materials Transactions A 41.13 (2010): 3473-3487.

[147] Rahmati, Zahra, et al. "Microstructural, tribological, and texture analysis of friction surfaced Al-Mg-Cu clad on AA1050 alloy." Surface and Coatings Technology (2020): 125980

[148] Fonda, R. W.; Knipling, K. E. & Rowenhorst, D. J., EBSD Analysis of Friction Stir Weld Textures, JOM, Springer Science and Business Media LLC, 2013, 66, 149-155

[149] Edalati, K.; Akama, D.; Nishio, A.; Lee, S.; Yonenaga, Y.; Cubero-Sesin, J. M. & Horita, Z., Influence of dislocation-solute atom interactions and stacking fault energy on grain size of single-phase alloys after severe plastic deformation using high-pressure torsion, Acta Materialia, 2014, 69, 68-77

[150] Fitseva, V.; Hanke, S.; dos Santos, J.; Stemmer, P. & Gleising, B. The role of process temperature and rotational speed in the microstructure evolution of Ti-6Al-4V friction surfacing coatings, Materials & Design, Elsevier BV, 2016, 110, 112-123, DOI: 10.1016/j.matdes.2016.07.132

[151] Musin, F.; Belyakov, A.; Kaibyshev, R.; Motohashi, Y.; Itoh, G. & Tsuzaki, K., Microstructure evolution in a cast 1421AI alloy during hot equal-channel angular extrusion, Reviews on Advanced Materials Science, 2010, 25, 107-112

[152] Peng, P.; Zhang, K.; She, J.; Tang, A.; Zhang, J.; Song, K.; Yang, Q. & Pan, F., Role of second phases and grain boundaries on dynamic recrystallization behavior in ZK60 magnesium alloy, Elsevier BV, 2021, 861, 157958, DOI: 10.1016/j.jallcom.2020.157958

[153] S. Belmares-Perales, A. A. Zaldívar-Cadena, “Addition of iron for the removal of the β-AlFeSi intermetallic by refining of α-AlFeSi phase in an Al–7.5Si–3.6Cu alloy,” Materials Science and Engineering: B, vol. 174, 1-3, pp. 191–195, 2010, DOI: 10.1016/j.mseb.2010.03.032

[154] Ma Qian, J.A Taylor, J.Y. Yao, M.J Couper, D.H. StJohn, “A practical method for identifying intermetallic phase particles in aluminium alloys by electron probe microanalysis,” Journal of light Metals, 2001.

[155] A. Jalar, N. A. Che Lah, N. K. Othman, R. Shamsudin, A. R. Daud, and S. R. Sayd Bakar, “Characterization of Oxide Growth on Surface of Al-Mg-Si Welded Joint,” Advances in Materials Science and Engineering, vol. 2014, pp. 1–10, 2014, DOI: 10.1155/2014/272804

[156] X. Zhu, H. Yang, X. Dong, and S. Ji, “The effects of varying Mg and Si levels on the microstructural inhomogeneity and eutectic Mg2Si morphology in die-cast Al–Mg–Si alloys,” J Mater Sci, vol. 54, no. 7, pp. 5773–5787, 2019, DOI: 10.1007/s10853-018-03198-6.

Appendix

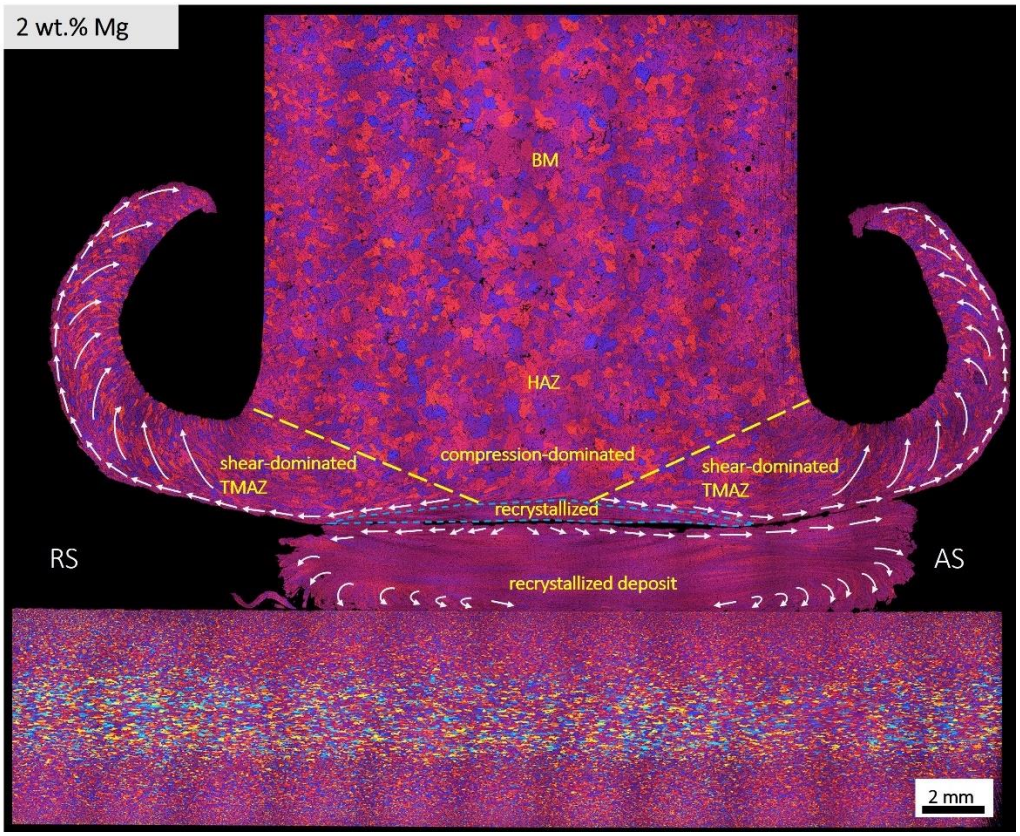

Figure 80: Light-optical micrograph of the stop-action sample from 2 wt.% Mg including FS characteristically microstructure-zones.

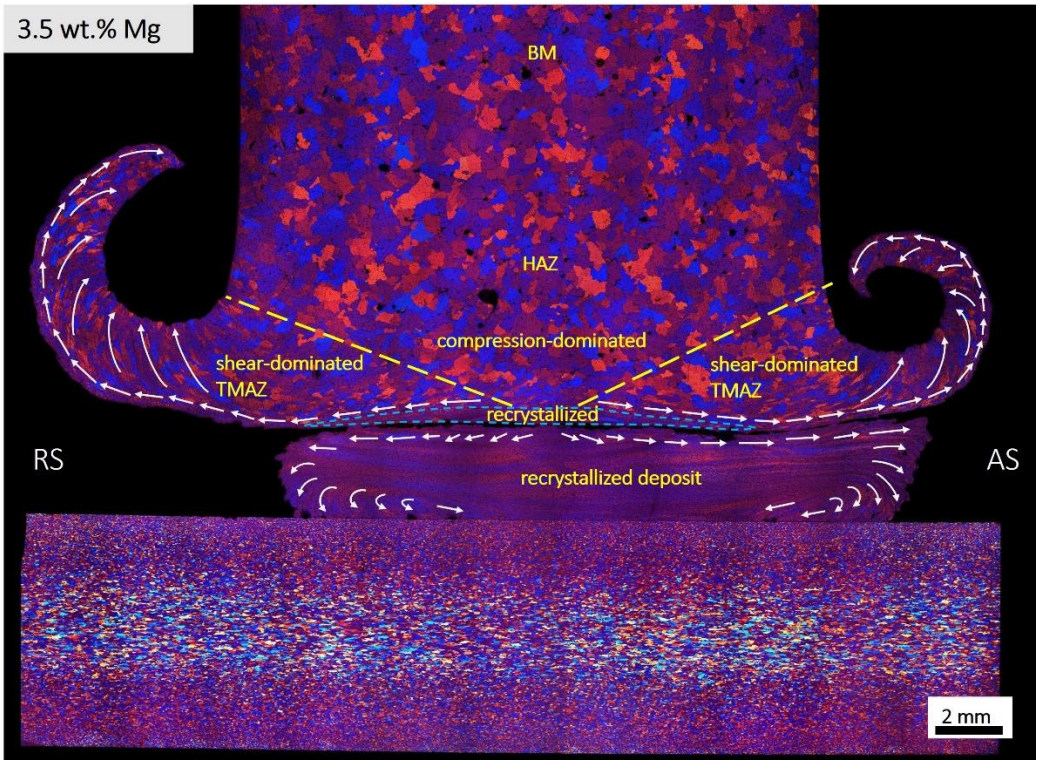

Figure 81: Light-optical micrograph of the stop-action sample from 3.5 wt.% Mg including FS characteristically microstructure-zones.

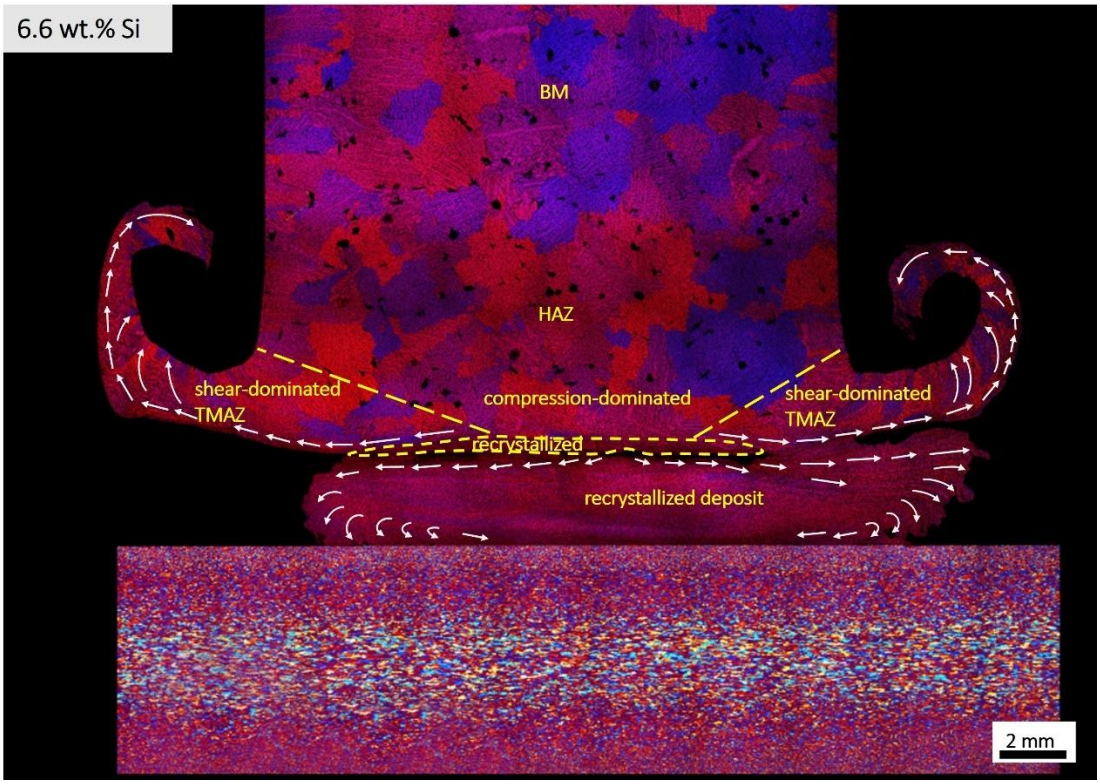

Figure 82: Light-optical micrograph of the stop-action sample from 6.6 wt.% Si including FS characteristically microstructure-zones.

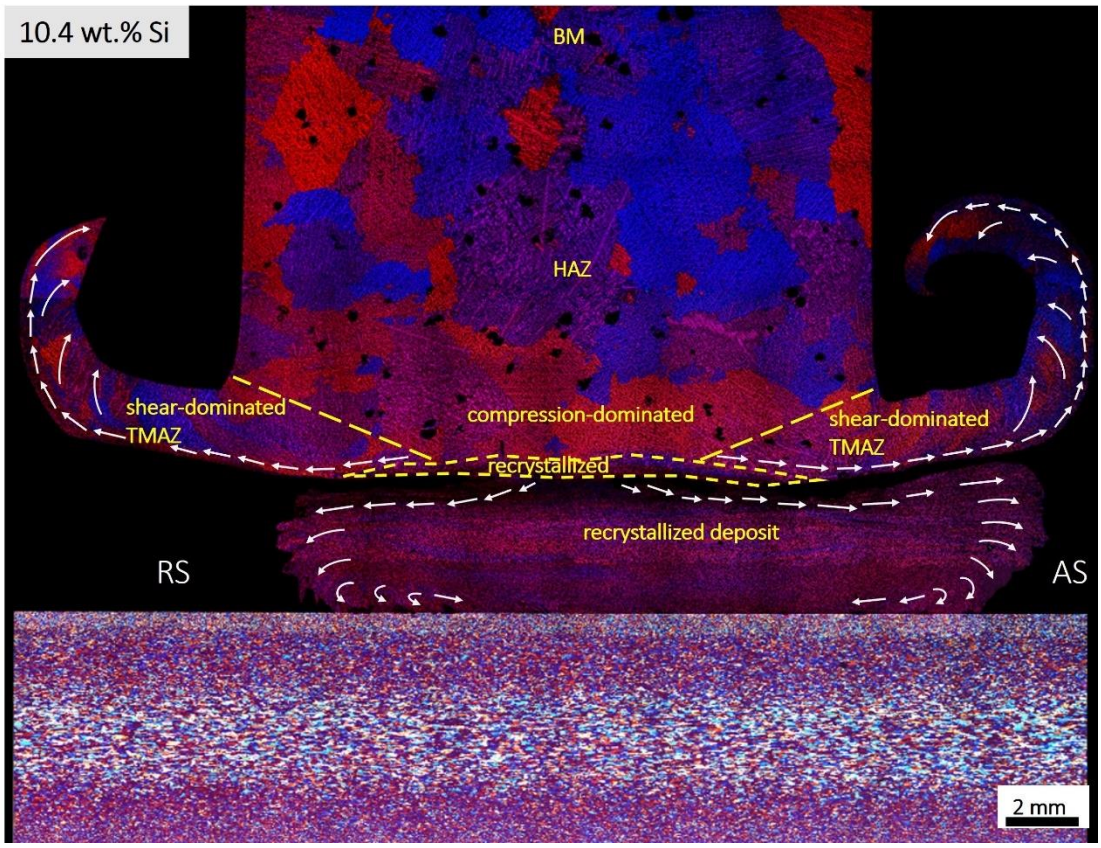

Figure 83: Light-optical micrograph of the stop-action sample from 10.4 wt.% Si including FS characteristically microstructure-zones.

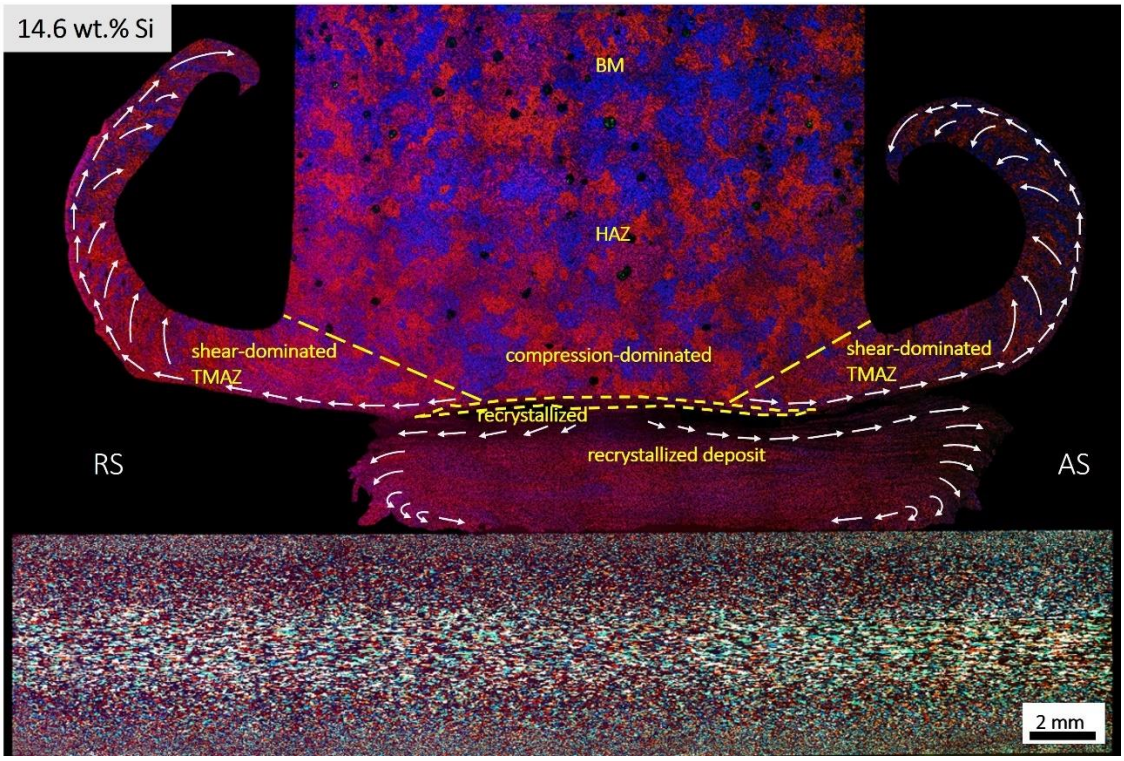

Figure 84: Light-optical micrograph of the stop-action sample from 14.6 wt.% Si including FS characteristically microstructure-zones.

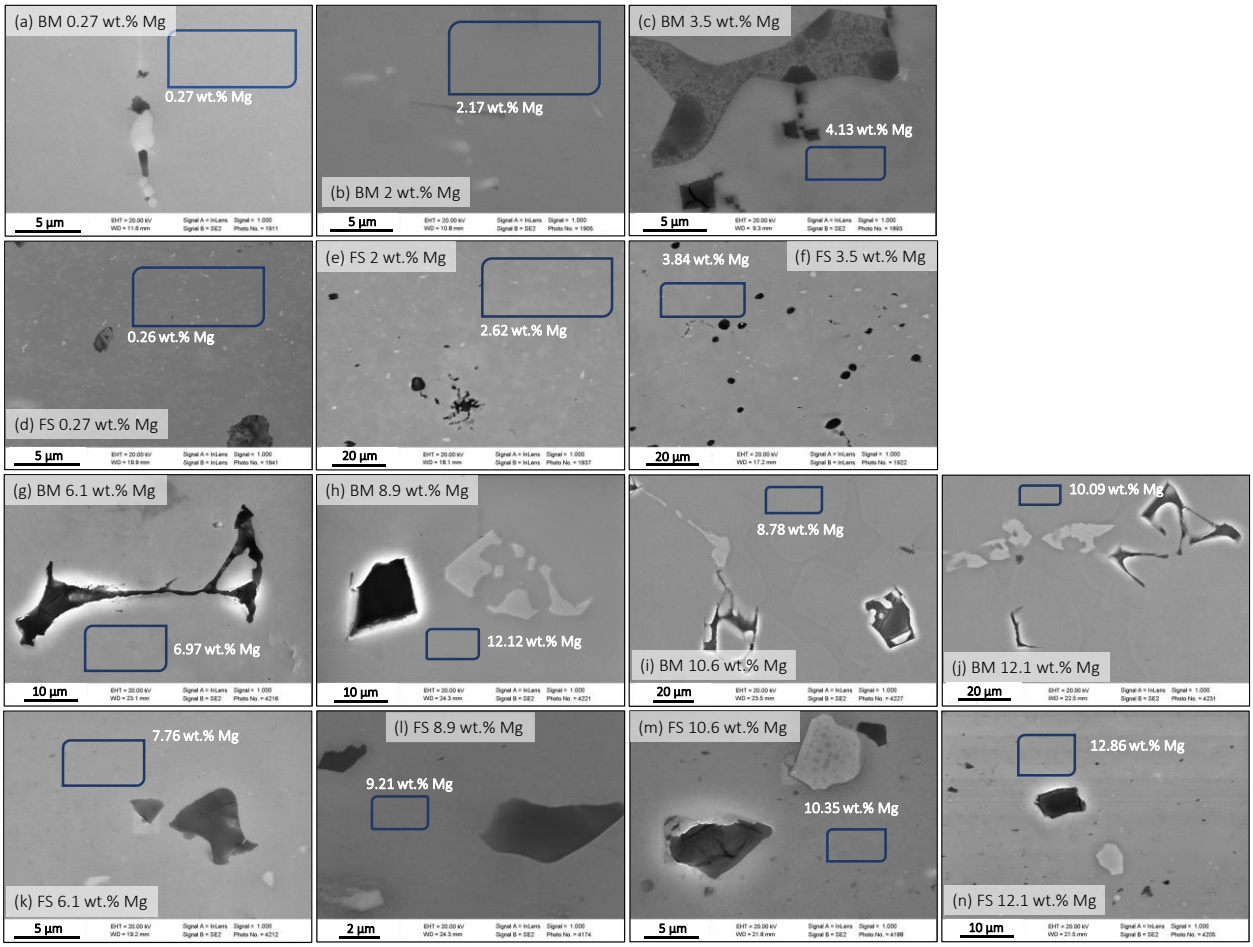

Figure 85: SEM-EDX analysis of α-Al phase areas in base material (BM) state and Friction Surfacing (FS) state. BM: (a) 0.27 wt.% Mg, (b) 2 wt.% Mg & (c) 3.5 wt.% Mg, (g) 6.1 wt.% Mg, (h) 8.9 wt.% Mg, (i) 10.6 wt.% Mg, (j) 12.1 wt.% Mg. FS: (d) 0.27 wt.% Mg, (e) 2 wt.% Mg & (f) 3.5 wt.% Mg, (k) 6.1 wt.% Mg, (l) 8.9 wt.% Mg, (m) 10.6 wt.% Mg, (n) 12.1 wt.% Mg.

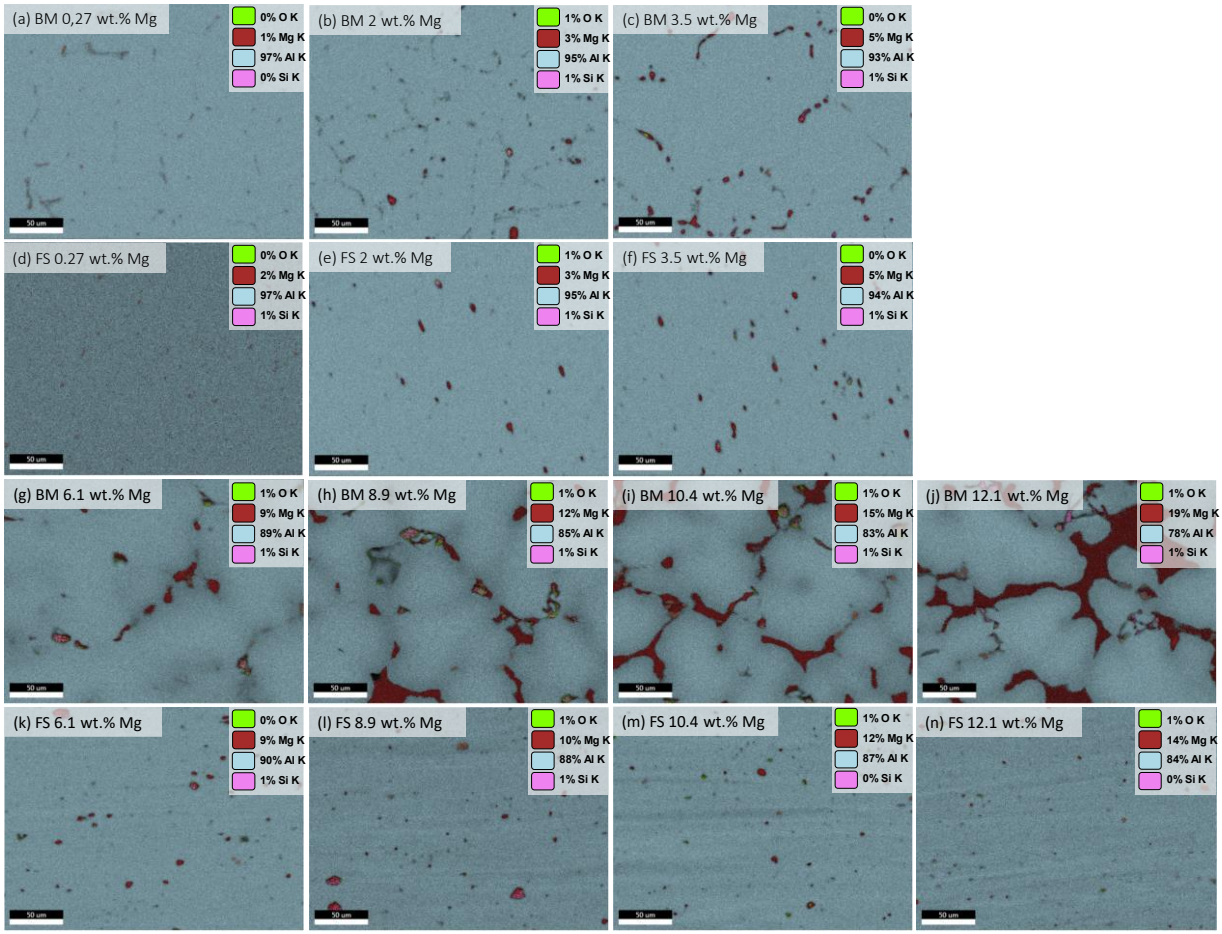

Figure 86: SEM-EDX maps in base material (BM) state and Friction Surfacing (FS) state. BM: (a) 0.27 wt.% Mg, (b) 2 wt.% Mg & (c) 3.5 wt.% Mg, (g) 6.1 wt.% Mg, (h) 8.9 wt.% Mg, (i) 10.6 wt.% Mg, (j) 12.1 wt.% Mg. FS: (d) 0.27 wt.% Mg, (e) 2 wt.% Mg & (f) 3.5 wt.% Mg, (k) 6.1 wt.% Mg, (l) 8.9 wt.% Mg, (m) 10.6 wt.% Mg, (n) 12.1 wt.% Mg.

List of figures

List of tables

DOI: 10.17185/duepublico/79068
URN: urn:nbn:de:hbz:465-20231019-105544-1